Nanodiamonds:

From Biology to Engineering

Joseph Orin Welch

This thesis is submitted for the degree of Doctor of Philosophy

London Centre for Nanotechnology/Department of Electronic and Electrical Engineering

University College London

Declaration

The work in this thesis is the result of research carried out at

University College London, London Centre for

Nanotechnology/Department of Electronic and Electrical Engineering,

Diamond Electronics Group.

I declare it to be my own work unless referenced contrary in the text.

Acknowledgments

I used to like curry. However, Professor Richard Jackman's excessive generosity, combined with the surprisingly low standard of the local eating establishments, may have resulted in some form of operant conditioning. It is necessary to point out that Richard's generosity extends well beyond tandoori cooking, and I owe him a great deal of gratitude in my development from an excited 2nd year undergraduate to a weary final year PhD. Richard, I could not have asked for a better supervisor, both in the academic and pastoral roles you constantly shift between, I have no doubt our friendship will last the test of time. My introduction into the diamond electronics group was at an unusually early stage and therefore I have had the great pleasure of knowing many members of the diamond family (a term I do not use loosely here), too many to list in full, although a special high five to Robert Edgington and Aysha Chaudhary for their help in collecting data and writing this thesis. Within UCL there are several names that require recognition; Tom Hamer at the EEE workshop for his amazing work in transforming painfully vague ideas into concrete (or more usually 304 steel) reality, Steve Hudziak for his help acquiring AFM data and in developing an aversion to any form of long distance running, Mark Turmaine in his patient teaching in the use of the SEM, and Tony Kenyon as my second supervisor and all-round nice guy. EEE undergraduate students have come and gone with varying degrees of success, but Jason Plumb deserves special mention as a particularly talented chap with a bright future (long live your micro mullet!). Turning to those external to UCL, Gert Nutzel and Pascal Lavoute of Photonis for their technical expertise, funding, friendship and belief that the next big breakthrough was always 'only 6 months away'. The top is most definitely the top. Philippe Bergonzo of CEA and his highly professional,

supremely talented troop of “cheese-eating surrender monkeys”. From my personal life, I would (literally) not be here without my loving parents, Karen and Phil, thank you both for getting me to where I am today – your encouragement and support mean the world to me. James and Hester, my wonderful siblings, the same goes for you – much love. My thanks to Tasha Lyons, my partner in life, your love gave me the strength to overcome anything that came my way and I will always treasure you. My friends, for being my first line of defence when tough times arose, providing a great deal of comic relief and so many good times along the way – possibly too many good times, on reflection. Last and certainly most least, George Gabriel for no particular reason other than he offered me a pint to get on this list. Mine’s a Budvar mate.

Abstract

Whilst diamond nanoparticles have been synthesised by the detonation method since the middle of the 20th century, it was not until the development of their fully dispersed form in 2008 that the hugely varied array of potential applications opened up. These prospective uses are described in chapter 2, spanning the breadth of the sciences; from the chemical (ion sensors and electrochemical electrodes), the biological (drug delivery and intracellular monitoring), to the physical (composite materials and growth nucleation seeds). Highlighting this versatility, chapter 5 of this thesis covers the use of ND as a neuronal biomaterial, investigating for the first time the role of the size, production method and surface functionalisation on neurite extension, where it was found that the only significant variable was the size of the ND used, suggesting the curvature of particle is of high importance. A patterned ND surface was also fabricated and this resulted in the successful growth of neuronal networks along the ND patterning, down to ND track widths of 10 μm. Chapter 6 presents a study into the electrical characteristics of nanodiamond. Here for the first time, ND layers with various surface terminations were produced and verified using Fourier transform infrared spectroscopy. These layers were then probed using impedance spectroscopy to obtain modelled values of the layers' resistance and capacitance as a function of measurement temperature. This data was manipulated into Arrhenius plots to extract activation energies of the observed conduction paths. The hydrogen terminated ND layers were shown for the first time to be stable for short heating durations up to 475°C, although longer heating duration at this temperature did cause permanent damage to the ND layer. Oxygen terminated ND was found to be less stable when heated in atmospheric conditions, with permanent degradation occurring at 200°C. However when measured in vacuum, these layers showed

resilience similar to that seen on the hydrogen terminated ND, suggesting the hydrogen termination is providing protection against oxidative degradation in atmospheric conditions. The next chapter documents the attempts to fabricate thin, conformal layers of ND within the channels of a microchannel plate (MCP) – the electron amplification stage of a night vision device. This work resulted in the first successful seeding of ND throughout the first 60 μm of the MCP channel, as requested by the industrial sponsor of this work, Photonis. This chapter also presents the iterative designs of a custom cooler and sample mount for the microwave plasma enhanced chemical vapour deposition chamber used for low temperature diamond growth both in this chapter and the final experimental chapter. The last experimental chapter details a novel investigation into the optimal conditions for ND to be grown into a thin film for use as a secondary electron emitter. The results presented include Raman spectroscopy (for film quality assessment), scanning electron micrographs (to provide topographical information), atomic force microscope line scans (to estimate film thickness) and finally secondary electron yield experiments upon each of the films. It was found that the films grown with the highest applied microwave power - resulting from the most aggressive cooling - gave the highest secondary electron emission yield, slightly under 10 (meeting the objective set by Photonis) along with a sharper sp^3 peak at $1333cm^{-1}$.

Contents

Glossary

AFM	Atomic Force Microscopy
AM	Attachment Medium
ATR	Attenuated Total Internal Reflection
CCD	Charge Coupled Device
CMOS	Complementary Metal-Oxide-Semiconductor
CVD	Chemical Vapour Deposition
D.I.	De-Ionised water
DIV#	# Days *In Vitro*
DND	Detonation Nanodiamond
ECM	Extra Cellular Protein
EDR	Equivalent Disc Radius
f	Fixed (short growth step)
FBS	Fetal Bovine Serum
FET	Field Effect Transistor
FTIR	Fourier Transform Infrared Spectroscopy
GFP	Green Fluorescence Protein
HeLa	Henrietta Lacks (cancer cell line)
HFCVD	Hot Filament CVD
HPHT	High Pressure High Temperature
IBM	International Business Machines
IS	Impedance Spectroscopy
ISFET	Ion-Sensitive Field-Effect Transistor
IUPAC	International Union of Pure and Applied Chemistry
LEI	Lower Electron Image Mode
LN	Laminin
MAP2	Microtubule-associated protein 2
MCP	Microchannel plate
MEA	Micro Electrode Array
MEM	Medium Essential Medium
MEMS/NEMS	Micro/Nano Electromechanical Systems
MM	Maintenance Medium
MPECVD	Microwave Plasma Enhanced CVD
N	Seeding Density
NCD	Nano Crystalline Diamond
ND	Nanodiamond
NEA	Negative Electron Affinity
NV	Nitrogen vacancy

ODA	Octadecylamine
PBS	Phosphate Buffered Solution
PDDAC	Poly-Diallyldimethylammonium Chloride Polymer
PEA	Positive Electron Affinity
p-ORN	Poly-Ornithine
PVA	Polyvinyl Alcohol
RDX	Research Department Explosive
RGD	Arginylglycylaspartic acid
RIE	Reactive Ion Etching
RMS	Route Mean Squared
RT	Room Temperature
SC	Spin Coating
SCD	Single Crystal Diamond
S.E	Standard Error
SEE	Secondary Electron Emission
SEI	Secondary Electron Imaging Mode
s.e.m	Standard Error Of The Mean
SEM	Scanning Electron Microscope
SEY	Secondary Electron Yield
siRNA	Small Interfering Ribonucleic Acid
TNL	Total Neurite Length
TNT	Trinitrotoluene
UNCD	Ultra Nano Crystalline Diamond
US	Ultrasonication
UV	Ultraviolet

Chapter 1: Introduction

It is unusual for a completely new class of material to become available within a well established material system. However, the introduction of nanodiamonds (ND) as a novel form of diamond has spurred considerable interest into areas of possible use. ND has a particularly unique advantage in that it combines the extreme and versatile properties of bulk diamond with nanoscale dimensions, allowing for a diverse range of potential roles as a material for biological, [1,2] chemical, [3,4] mechanical [5,6] and electronic engineering.[7,8] Whilst several applications for ND have already been utilised,[9,10] a critical problem for the exploitation of the ND is the lack of understanding of the electrical properties, of both as received and surface functionalised particles, to date there are very few publications in this area. Additionally, although the problem is not as severe, the successful use of ND in varied engineering scenarios has not materialised. Therefore there are many areas currently unexplored. As a result this thesis presents efforts to more completely understand and exploit this material and to this end, headway has been made in both of these respects (see below).

Chapter 2 gives an introduction to diamond, its properties and methods of production. Doping of diamond is also discussed, along with the difficulties encountered in making a very wide bandgap semiconductor sufficiently conductive. The implications for electronic devices taken into account. This is then followed by a review of surface conductivity and highlighted research results. The breadth of applications for bulk diamond is then evaluated and specific examples given. A similar treatment of ND follows, where the formation, purification and functionalisation is described. ND surface functionalisation is then introduced, along with an overview of the range of ND applications reported to date.

Chapter 3 begins with an introduction into neurons, briefly covering their anatomy and function. In addition, an explanation of the use of murine embryonic hippocampal cells in Chapter 5 is given. Finally, a description of neuronal biomaterials and their use in diamond is given. For the second half of Chapter 3, a review of image intensifiers is given. Here, the concept of photomultiplication is introduced along with insight into the operating principles of the photomultiplier tube. The photomultiplier tube is then compared against other sensor technologies. Electron amplification is then discussed in relation to the microchannel plate. Finally, image intensifiers and their applications are reviewed.

Chapter 4 covers the experimental methods used throughout the course of the thesis, with more detail being given on topics used more extensively within it. Particular emphasis was placed on introducing the seeding of nanodiamond (ND) onto substrates and the subsequent growth of diamond films, as these techniques form the core processes investigated herein.

The first chapter detailing the experimental results, Chapter 5: The formation of neuronal cell networks with nanodiamond, is presented. Functional neuronal cell networks are a particularly difficult challenge for bioengineers to seed and maintain,[11] due in large part to the high degree of specialisation exhibited in all neuronal cell types and the separate immune system seen behind the blood brain barrier.[12] This difficulty is further complicated by the current lack of bio materials that provide conditions similar to that seen in the body, resulting in cell behaviour different to the norm, and in

severe cases cell death. This is undesirable for the study of such cell networks as observations of these networks effectively under tremendous strain would fail to translate well to environments within the normal range of physiological conditions. The issue is compounded when such networks are being interacted with *in vivo*, as the use of artificial (or exogenous) materials to aid in aspects such as conduction, adhesion, or nutrition will alter the culture's response away from the response that would have occurred without the intervention of the investigator. Additionally, the ability to pattern neuronal networks that are behaving in a normal manner, would allow for a closer merging of traditional electronic technologies with the neuronal cells, potentially opening several avenues of novel study platforms, brain machine interfaces or neuroprosthetics. Current technologies take either a pin point approach where a small number of individual neurons are interacted with (e.g. patch clamp), or a much more wide ranging level interaction typically facilitated by several micro electrodes spread throughout a grouping of cells. Recent previous work has found ND layers to form a good interfacial layer between glass slides and neurons, allowing for high cell survival rates and physiologically normal behavour.[1] However little information is known about the ND's parameters that provide ideal cell culture conditions. Here, differing ND seed deposition methods are assessed in terms of surface roughness, seeding density, and the seeded particle radius. The deposited ND layers were then evaluated using Raman and Fourier transform infrared spectroscopy before and after a short growth step. The ability for these layers to support murine hippocampal neuron cultures was then investigated, and the relationships between surface morphology and total neurite extension (a proxy metric for the health of the cell culture) presented. It was found that the only statistically significant metric was the size of the ND particle, which allows for the narrowing of the further study into ND-neuron interaction and frees up bioengineers to modify the other variables (ND origin, surface

terminations, seeding method, and substrate roughness) without fear of reduced culture health. Patterned ND layers were then fabricated with graduated line widths and their ability to produce patterned neuronal networks was assessed and it was found for the first time the neurite outgrowth was present up until the 10μm line width. This discovery will allow for the removal of additional extracellular proteins in the study and treatment of neuronal tissues. Please note – Cell seeding and confocal microscopy within this chapter was performed by Dr. Agnes Thalhammer of the Pharmacology department, UCL.

Chapter 6 makes headway into the staggering lack of electrical characterisation of NDs. Due to ND being a relative newcomer to the fields of diamond and nanoparticles in general, this basic science has not yet been performed on monodispersed ND layers. Understanding of the electrical response of ND is vital to providing information into the conduction processes exhibited by ND at various temperatures as well as the furthering of the electronic uses of the nanomaterial in the wide range of potential and current uses outlined above (and more thoroughly discussed in Chapter 2). Building on earlier work on the electrical characteristics of agglomerated ND layers.[13] This chapter describes the first investigation into controlling the electrical characteristics of nanodiamond layers through surface functionalisation. Firstly, treatment procedures were developed to allow for the modification of surface functional groups on the ND and Fourier transform infrared spectroscopy was utilised to verify the efficacy of the treatments. Initially untreated ND was probed using impedance spectroscopy at a range of temperatures in order to assess both the frequency and temperature dependent behaviour of the nanoparticles. This data was then manipulated to obtain Arrhenius plots, and

hence the activation energy of charge carriers. This process was then repeated for oxygen and hydrogen terminated NDs to investigate the effect of surface termination on the impedance data. Measurements were taken both in vacuum and atmospheric conditions in order to probe the effect of ambient oxygen on the system and for the role of hydrogen in facilitating surface conductivity. The key result from this chapter is the surprising resilience of the diamond like electrical qualities of the ND layers, up to 475°C. This sets the upper limit of the operation of electrical devices based on ND without permanent changes to the device characteristics. Another problem addressed by this investigation is the nature of the conduction paths through the ND layers, which seem to be passing through the semi-disordered lattice structures rather than the more highly crystalline centre of the ND.

The next two chapters are focused on the collaboration with Photonis to integrate nanodiamond layers with a microchannel plate (MCP) within Photonis' current night vision devices for the very first time. Whilst the MCP has a total device gain numbering several tens of thousands, each interaction with the MCP sidewall only generates an average of two secondary electrons. This average has a distribution that includes zero and hence results in the loss of the primary electron generated at the photocathode preceding the MCP (see section 3.3.3), contributing to the device's overall signal to noise ratio (a key metric in the marketing of such devices). Here, goal of the sub project was the inclusion of a diamond layer in the first 60μm of the MCP to raise the secondary electron yield (SEY) from 2 to a target SEY of 10, thus drastically reducing the incidence of lost primary electrons. An additional benefit of the inclusion of a diamond layer would also be improved protection against the generation of ions backscattered towards the photocathode, causing its gradual degradation and

setting the working lifespan of the final product. Chapter 7 starts by documenting the evolution of the substrate cooler design, in an attempt to increase the microwave power applied to the growth of the nanodiamond layers. Note the cooler design process was performed in collaboration with Photonis). The seeding conditions of the MCP was then varied to successfully obtain a conformal layer of ND penetrating 60 μm into the channel. The grain size, grain density and area coverage were analysed as a function of distance from the channel opening, and all three parameters showed a negative correlation. The goals of this sub project were met satisfactorily, which is now ready for passing down to the R&D division within Photonis, provided the project outlined in Chapter 8 also meets its goals.

Chapter 8, the final results chapter documents the first investigation into the effect of growth temperature on the secondary electron yield (SEY) of nanocrystalline diamond films. The tight thermal budget presented by the MCP (420˚C) provided the impetus to perform this study. Little is known about the effect of low growth temperature (which in turn affects many other growth characteristics) on the SEY of diamond films. Low temperature growth is critical for incorporating diamond growth into a wider range of existing industrial fabrication processes, whilst retaining the high SEY seen at normal growth temperatures (Photonis specified an ideal target value of 10). Samples were first seeded with ND and then grown at a range of temperatures on silicon substrates. The resultant films were compared in terms of surface morphology, film thickness, Raman spectrum, and secondary electron yield. The final iteration of the cooler (described in Chapter 7) was then deployed to grow nanocrystalline diamond films, and a comparison with the previous sample series is given and it is shown to greatly surpass the SEY of the films grown at

lower applied microwave power. The engineering challenge of producing high SEY diamond surfaces at low temperature was successfully demonstrated, with a peak SEY of 9.2, slightly short of the goal of 10 set by Photonis.

Chapter 9 gives a summary of the results that have been presented throughout this thesis. In addition, future avenues of research are discussed in order to fully utilise the insight borne by this research.

The novel contributions of the work presented in this thesis are:

1. A rigorous investigation into the effect of the ND's size, surface state and origin on neurite extension, indicating ND size to be the only significant parameter in neuronal outgrowth.

2. ND particle patterning was shown to be suitable for the selective adhesion and directed neurite outgrowth, down to ND line widths of 10 μm.

3. A dry, reliable, and scalable oxygen functionalisation route using ozone was developed.

4. The limits of thermally induced electrical breakdown were shown on hydrogen and oxygen treated ND layers for the first time.

5. ND layers were successfully seeded within the channels of an MCP to a controlled depth and subsequently developed into conformal nanocrystalline diamond at temperatures within safe tolerance for the MCP.

6. A unique cooler design was developed and fabricated to enable the homogenous low temperature diamond growth required on the MCP.

7. The first investigation into the effect of growth temperature on SEY was conducted, revealing a complex relationship between non-diamond inclusions and SEY at lower yields. However high quality diamond, grown with the most advanced iteration of the cooler design, showed high yields very close to the required R&D threshold set by Photonis.

The following publications and conference papers have resulted from the work within this thesis (n.b. due to the commercially sensitive nature of much of this work, the majority of publications have been kept on hold at Photonis' discretion):

Publications

RJ Edgington, A Thalhammer, JO Welch, A Bongrain, P Bergonzo, E Scorsone, RB Jackman, R Schoepfer, "Patterned Neuronal Networks Using Nanodiamonds and the Effect of Varying Nanodiamond Properties on Neuronal Adhesion and Outgrowth", Journal of Neural Engineering 10 (5), 056022.

A Chaudhary, JO Welch, RB Jackman, "Electrical Properties of Monodispersed Detonation Nanodiamonds", Applied Physics Letters 96 (24), 242903-242903-3.

Conference papers

JO Welch, A Chanudhary, RB Jackman

Electrical Properties of Monodispersed Nanodiamonds

Diamond 2010, Budapest, Hungary

JO Welch, A Chanudhary, RB Jackman

Surface Electronic Properties of Nanodiamonds

MRS 2010, Boston, USA

JO Welch, A Chanudhary, RB Jackman

Detonation Nanodiamonds: Properties and Selected Applications

MRS 2011, Boston, USA

JO Welch, J Plumb, RB Jackman

Nanocrystalline Diamond Films for High Yield Secondary Electron Emission

IMRC, Cancun, Mexico

[1] A Thalhammer *et al.*, "The Use of Nanodiamond Monolayer Coatings to Promote the Formation of Functional Neuronal Networks," Biomaterials 31(8), 2009, pp. 1–8.
[2] E Chow *et al.*, "Nanodiamond therapeutic delivery agents mediate enhanced chemoresistant tumor treatment." Science Translational Medicine 3(73), 2011, 73ra21.
[3] Q Zang, "Electrochemical properties of nanodiamond powder electrodes" Diamond and Related Materials 16, 2007, pp. 16–20.
[4] R Ahmad, "Nanodiamond-coated silicon cantilever array for chemical sensing", Applied physics letters 97, 2010, 093103.
[5] Q Zhang, "Fluorescent PLLA-nanodiamond composites for bone tissue engineering", Biomaterials (32), 2001, 87-94.
[6] Y Zhu *et al.*, "Surface modification and dispersion of nanodiamond in clean oil." China Particuology 2(3), 2004, pp. 132-134.
[7] A Chaudhary *et al.*, "Electrical Properties of Monodispersed Detonation Nanodiamonds," Applied Physics Letters 96(24), 2010, 242903.
[8] R Ahmad, "Nanodiamond-gated silicon ion-sensitive field effect transistor", Applied physics letters 98, 2011, 153507.

[9] V Mochalin *et al.*, 'The Properties And Applications Of Nanodiamonds'. Nature Nanotechnology 7(1), 2011, pp. 11-23.
[10] O Shenderova & D Gruen, 'Ultrananocrystalline Diamond: Synthesis, Properties, And Applications'. Springer, 2006.
[11] M Sailer *et al.*, "High-Throughput Cellular Screening of Engineered ECM Based on Combinatorial Polyelectrolyte Multilayer Films," Biomaterials 33(24), 2012, pp. 5841–5847.
[12] M Ward *et al.*, "Toward a Comparison of Microelectrodes for Acute and Chronic Recordings," Brain Research 1282, 2009, pp. 183-200.
[13] M Bevilacqua *et al.*, 'Electrical Properties Of Aggregated Detonation Nanodiamonds'. Applied Physics Letters 93(13), 2008, 132115.

Chapter 2: Diamond and Nanodiamond

2.1 Introduction

The use of diamond to perform a wide array of electrical, chemical and physical functions has been well established. [1] Diamond's electrical characteristics can be modified though the incorporation of non-carbon elements or non-diamond carbon, either as a surface termination or within the crystal lattice itself. For the scope of this thesis, the use of diamond's surface properties will be reviewed. This will then be extended to nanodiamond, with focus on the production, purification and functionalisation of single digit (ultra-dispersed) nanodiamond.

2.2 Diamond

2.2.1 Carbon bonding

It is difficult to overstate the importance of carbon as the fundamental building block of life as we know it. It forms the basis of biochemistry due to its ability to bond with a wide array of atoms, enabling the complex range of carbon based chemicals seen in the biosphere. This naturally extends to the currently most popular sources of energy on the planet; coal, oil and natural gas – the fossil fuels. These two examples can be extrapolated to form the basis of the majority of human technology, from cotton to consumer electronics.

Pure carbon itself provides an important class of materials. Within this there are many allotropes due to the high number of valence bonds carbon can form. Figure 2.1 gives a non-exhaustive list of the most important examples. A large amount of research has been conducted on the allotropes of carbon, however, of these diamond (Figure 2.1a) and graphite (Figure 2.1b) remain the most successfully commercially exploited.[2]

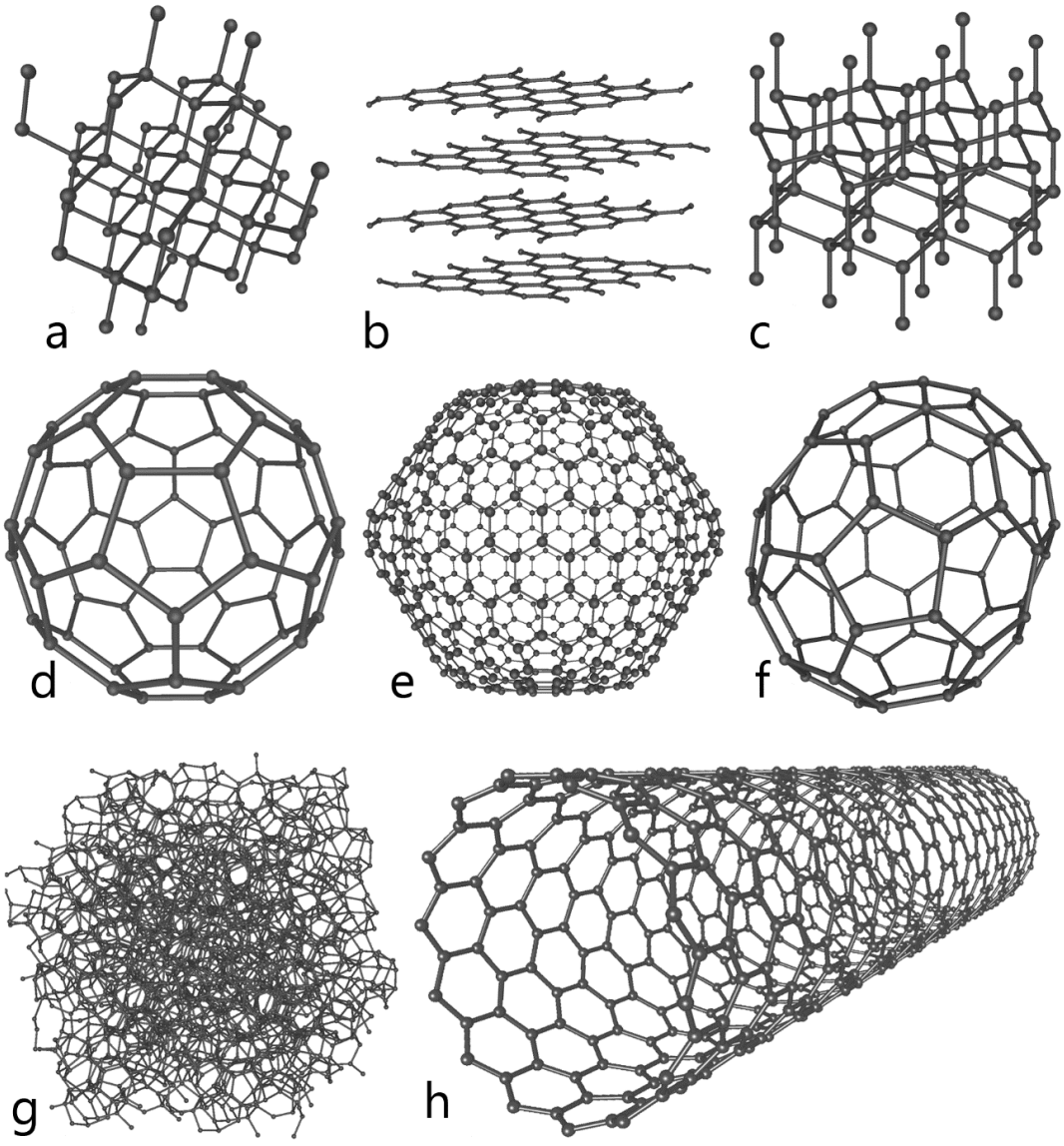

Figure 2.1 Some of the possible allotropes of carbon: (a) Diamond, (b) Graphite, (c) Londsdaleite, (d) C_{60} or buckminsterfullerene (e) C_{540} fullerene (f) C_{70} fullerene (g) Amorphous carbon (h) single walled carbon nanotube. Taken from [3]

Carbon (atomic number 6) has an electron ground state configuration as follows:

$$C \quad \underset{1s^2}{\uparrow\downarrow} \quad \underset{2s^2}{\uparrow\downarrow} \quad \underset{2p_x}{\uparrow} \quad \underset{2p_y}{\uparrow} \quad \underset{2p_z}{}$$

The first two electrons, found in the first (K) shell do not contribute to bonding due to their high stability. Instead, bonding in carbon is achieved through the four electrons in the outer (L) shell through molecular orbital hybridisation. Here, the excitation of the 2s orbital results in hybridisation with the 2p orbitals through mixing of their respective wave functions to form a sp^n hybrid orbital (where n = 1, 2, or 3).[4] sp hybridisation is found in chemical compounds such as the alkynes, giving:

$$C^* \quad \underset{1s^2}{\uparrow\downarrow} \quad \underset{sp}{\uparrow} \quad \underset{sp}{\uparrow} \quad \underset{2p}{\uparrow} \quad \underset{2p}{\uparrow}$$

However, the sp hybrid is not of great importance in the context of this thesis. The next hybrid is the sp^2 configuration, as seen in planar materials such as graphite, graphene and carbon nanotubes:

$$C^* \quad \underset{1s}{\uparrow\downarrow} \quad \underset{sp^2}{\uparrow} \quad \underset{sp^2}{\uparrow} \quad \underset{sp^2}{\uparrow} \quad \underset{2p}{\uparrow}$$

This results in a trigonal arrangement of sp^2 orbitals with an additional unchanged 2p orbital orthogonal to the sp^2 plane this lone 2p electron causes the weak van der Waals attraction between planes in graphite, forming a π bond. When isolated, as in the case for graphene, the accumulation of orbitals overlap to form a highly mobile conduction band.[5]

Finally, the sp^3 hybrid is considered, as seen in diamond:

$$C^* \quad \frac{\uparrow\downarrow}{1s} \quad \frac{\uparrow}{sp^3} \; \frac{\uparrow}{sp^3} \; \frac{\uparrow}{sp^3} \; \frac{\uparrow}{sp^3}$$

This results in a tetrahedral arrangement with bond angle of 109.5° to minimise repulsion between orbitals (Figure 2.2). This tetrahedral arrangement is the root cause for a large number of diamond's extreme properties.

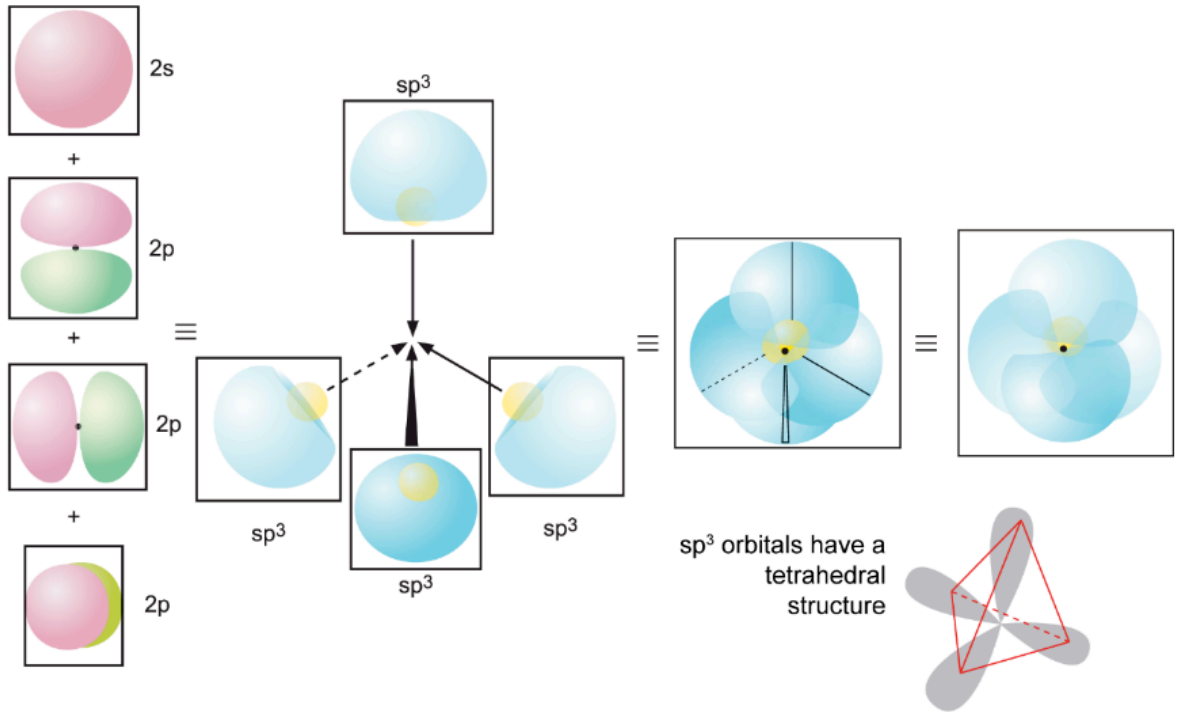

Figure 2.2 Schematic of sp^3 orbital hybridisation. Adapted from [6].

The tetrahedral organisation of the sp^3 bonds manifest in diamond as strong (711 kJ/mol)[7] covalent C-C bonds, with each carbon (except at surfaces) bonded to four neighbours. Each covalent bond is relatively short, at 1.53 Å,[4] and these form a lattice with the highest atomic density seen in solids (1.76×10^{23} atoms/cm^3),[8] resulting in the extreme hardness, stiffness, and incompressibility seen in bulk diamond. The diamond lattice is of the face centred cubic type, with

eight atoms per unit cell. Typically three Miller indices are used to describe diamond surfaces: (100), (110), and (111).

2.2.2 Diamond growth

Terrestrial diamond formed naturally in the earth's crust between 990 million and 4.2 billion years ago, between 140 and 200 km below the surface.[9] Temperatures of 900 – 1400°C and pressures between 4.5 and 6 GPa are required for diamond to form in this way.[10] In order to determine the quality of a natural diamond, visual characteristics are often used. These characteristics are determined by the incorporation of boron-, nitrogen-, and hydrogen-related defects (taken from [4]):

> *Type Ia: Nitrogen is the dominant impurity and is present as aggregates or clustered together within the carbon lattice. It has a pale yellow or brown appearance. 98% of diamonds fall into this category.*

> *Type Ib: Nitrogen is present as single substitutional atoms and is uniformly distributed throughout the carbon lattice. These diamonds can appear deep yellow, orange, brown or greenish depending on the concentration and distribution of nitrogen atoms. They account for 0.1 % of diamond.*

> *Type IIa: These diamonds have a miniscule amount of impurities present. They are colourless unless lattice defect are present, which would render them yellow, brown, pink or red. 1-2 % of diamonds are this type.*

> *Type IIb: This type of diamond contains boron as an impurity and appear, blue, grey or near-colourless and make up approximately 0.1 % of diamonds.*

Diamond can also be synthesised artificially, to overcome many of the limitations of naturally sourced diamond samples (high cost, variable impurity content, and inhomogeneity within the sample). Artificial diamond is usually defined by the size (or absence) of crystals within the bulk. When there are no separate domains, the diamond created is said to be a single crystal. Single crystal diamond (SCD) is transparent and generally exhibits the greatest degree of desired properties such as Young's modulus, hardness, charge carrier mobility etc. These excellent properties are offset by the difficulty in the production of SCD, as a homoepitaxial substrate is required (usually other SCDs or single crystal iridium)[11] to continue the diamond lattice without the inclusion of grain boundaries. When smaller grains of SCD coalesce to form a complete film, the resultant material is referred to as polycrystalline diamond. Within polycrystalline diamond there is further classification, defined by the size of the constituent grains. Microcrystalline diamond grains are in the range of 0.1 to several micrometres, nanocrystalline diamond (NCD) roughly 5-100 nm, and ultrananocrystalline diamond (UNCD) ≤ 5 nm.[12] As a general trend, smaller crystal size corresponds to properties further from those set by SCD, due to greater incorporation of sp^2 bonded carbon.

Another method of categorising artificial diamond is through the method by which it was grown. The first reported route to diamond synthesis was published in 1955 by Tracy Hall *et al.* at General Electric. General Electric developed a process using conditions close to those required for the growth of natural diamond, with pressure exceeding 130 kbar and temperatures *ca.* 3300 K (subsequent addition of transition metal catalysts brought this down to 55 kbar and 1600 K).[13] This technique became known as high pressure high temperature (HPHT), and accounts for the majority of annual production

(approximately 75 tons worldwide).[13] HPHT diamond, whilst incorporating fewer lattice dislocations or stacking faults than natural diamond, still contain high concentrations of impurities – particularly nitrogen.[14] Therefore HPHT diamond has not seen much use in direct electronic or optical applications. Instead, outside of its use in cutting and grinding tools, HPHT is often used as a homoepitaxial substrate for subsequent SCD growth. For more technologically demanding applications chemical vapour deposition (CVD) is usually employed. CVD of diamond can be achieved through a large range of techniques, each with their own strengths and weaknesses (

Table 2.1). The first reported use of CVD for the growth of diamond was in 1962 by William Eversole at Union Carbide Corporation[15] - although there are unpublished reports indicating this work was started before Hall's 1955 HPHT work[16]. It should be noted for balance that separate efforts in the Soviet Union towards both HPHT and CVD diamond yielded successful results shortly after each of the cited examples.[16] However, CVD did not achieve widespread use until both the introduction of atomic hydrogen to etch the graphitic deposits[17] and the NIRIM-type reactor (National institute for research in inorganic materials, Tsukuba, Japan).[18] These developments enabled the growth of high quality films in quantities great enough to garner significant commercial interest. Several detailed reviews of the history of diamond have been published elsewhere.[19,20]

CVD method	Rate (μm/h)	Area (cm^2)	Quality (Raman)	Substrate Material	Pros	Cons
Hot-filament	0.3–40	100–400	+++	Si, Mo, silica, Al_2O_3, etc.	Simple, large area	Contamination, stability
DC discharge (low P)	<0.1	70	+	Si, Mo, silica, Al_2O_3, etc.	Simple, area	Quality, rate
DC discharge (medium P)	20–250	<2	+++	Si, Mo, Al_2O_3,	Rate, quality	Area
DC plasma jet	10–930	2–100	+++	Si, Mo, W, Ta, Cu, Ni, Ti, stainless steel	Highest rate, quality	Stability, homogeneity
RF (low P)	<0.1	1–10	-/+	Si, Mo, silica, BN, Ni	Scale-up	Quality, rate, contamination
RF (thermal, 1 atm)	30–500	3–78	+++	Mo	Rate	Stability, homogeneity
Microwave (0.9-2.45 GHz)	1 (low P), 30 (high P)	40	+++	Si, Mo, silica, WC, etc.	Quality, area, stability	Rate
Microwave (ECR 2.45 GHz)	0.1	<40	-/+	Si	Area, low P	Quality, rate, cost, contamination
Flame (combustion)	30–200	1–100	+++	Si, Mo, Al_2O_3, TiN	Simple, rate	Stability, uniformity

Table 2.1 Comparison of diamond CVD techniques. Taken from [21].

Table 2.1 illustrates the diverse range of techniques for the CVD of diamond, all the methods listed rely on the activation of chemical species into precursor molecules, either by thermal (e.g. hot filament), electric discharge (e.g. DC, radio frequency, or microwave) or combustion flame (e.g. oxyacetylene torch).[1] These ions are then able to either form a carbide layer with the substrate or, more frequently, add to diamond seeds already on the surface[22] - see section 4.4.1 for a more detailed explanation of CVD reactors and their operation.

In order to achieve efficient growth of complete diamond films on non-diamond substrates, a nucleation step is required to achieve an increase in nucleation density beyond that of untreated silicon (10^4-10^5 cm^{-2}).[23] This step can include the inclusion of carbide forming interlayers, such as diamond-like carbon[24] or hydrocarbon oils;[25] bias enhanced nucleation, where a negative DC bias around 100-250 V is applied to the substrate to sub-plant CH_x^+ ions into the surface;[26] substrate abrasion, usually with micro- or nano-sized diamond particles, to embed particles into the substrate and to provide surface defects wherein diamond crystals can form;[27] ultrasonic micro-particle treatment, where stimulation by ultrasonic cavitations abrade and embed particles into the substrate;[28] or the deposition of a monolayer of nanodiamond particles from colloid solutions through electrostatic attraction – this technique will be discussed further in section 2.3.

2.2.3 Doping diamond

Intrinsic diamond is highly insulating,[29] in fact it would take a greater volume than the entire planet to host one mobile charge carrier at room temperature.[30] However, diamond can also incorporate dopants to achieve both *p*- and *n*-type conductivity, [29] as is often required in electronic applications. In this case, the difficulty of finding a shallow dopant in diamond that causes minimal distortion of the tight lattice has resulted in slow progress regarding the use of bipolar devices.[31]

p-type doping with boron has been shown to give the lowest activation energy of any substitutional dopant in diamond where $E_a \approx 0.38$ eV, with little degradation of the intrinsic characteristics[32], although this is not without complications (i.e. deep hole traps).[33] However, room temperature activation results in ionisation of only 0.2% of acceptors. Nevertheless, transistor action has been demonstrated.[34] The most useful aspect of boron incorporation is the appearance of a Mott transition (the transition from non-metal to metal) at around [B] = 2×10^{20} cm^{-3}. This has led to much interest in delta doping of diamond with boron, which will be discussed further in section 2.2.5. Boron can be incorporated into the diamond lattice during HPHT growth, by means of boron-containing metal catalyst, and in CVD growth, through the use of boron based gases such as diborane (B_2H_6). Boron is also seen, very rarely, in natural diamond – causing blue colouring (type IIb).

However, *n*-type conductivity has proven much more difficult to achieve.[35] Through substitutional doping with nitrogen (the same period as carbon and boron) a donor state 1.7 eV from the conduction band edge is observed.[36] Such a high activation energy makes room temperature operation unfeasible. More recently phosphorus, a larger Group 15 element has been used in an attempt to gain a shallower *n*-type dopant, however an activation energy of approximately 0.6 eV, [37] combined with significant lattice distortion [38] has prevented widespread use.

2.2.4 Surface conductivity on diamond

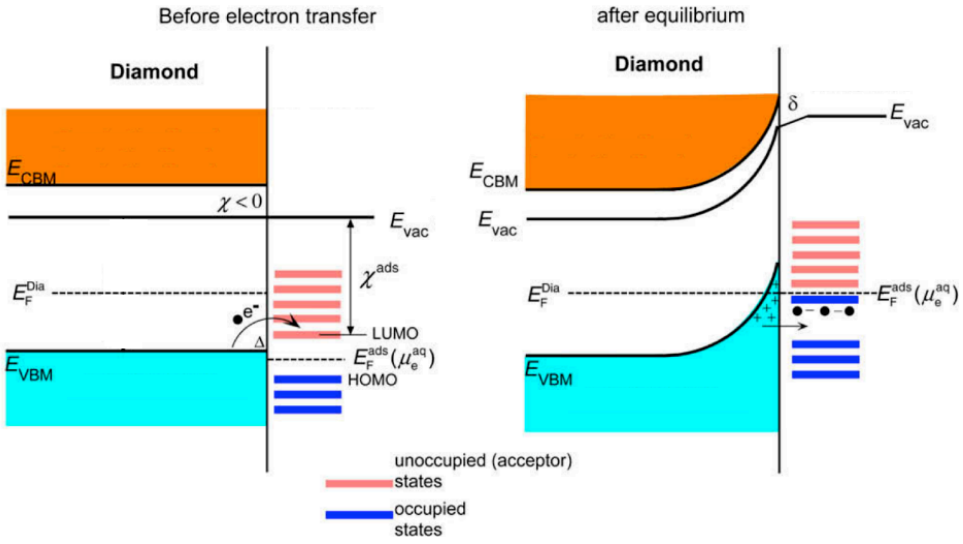

Figure 2.3 Schematic of energy levels during surface transfer doping process (a) before electron transfer and (b) after Fermi level alignment and electron transfer. Adapted from [41].

Due to the significant hurdles to direct doping of the diamond lattice there is also considerable interest in devices based on the surface conductivity of diamond. This is a relatively uncommon phenomenon in semiconductors, first reported in diamond in 1989.[39] Here, hydrogen termination of diamond causes a dipole layer at the surface. When an adsorbed molecule dissociates in a solvent, for example water in normal atmospheric conditions, this causes the reduction of a hydrated proton forming the H_3O^+ ion to provide an electron acceptor for carriers in the valence band of the diamond. The difference in Fermi energy between the diamond and the surface acceptor drives electrons from the top of the diamond valence band to empty acceptor levels in the adsorbates, causing band bending at the diamond surface. The extreme corrosion resistance seen in diamond[40] protects against oxidative dissolution and permits charge transfer to equalise the Fermi levels. This surface charge transfer creates negatively charged adsorbates, which form a compensating

subsurface layer of holes in the diamond valence band.[41] This process is referred to as surface transfer doping[42] (Figure 2.3).

Electronics operating via surface conductivity based on hydrogen terminated diamond has not been widely adopted in industry due to the lack of long term thermal stability of the C-H bond/wetting layer/adsorbates system. Therefore, the search for alternative studies have shown that solids such as fullerene (C_{60})[43] and fluorofullerene ($C_{60}F_{48}$)[44] can act as the surface acceptor, without the need for a solvent layer. Recent progress on hydrogen terminated diamond includes a diamond FET using adsorbed NO_2 to enhance the hole concentration, covered by a protective Al_2O_3 passivation layer in an attempt to offset the aforementioned stability issues. This achieved an f_{max} of 30 GHz with an I_{DSmax} of 1.35A/mm, the highest reported in the literature at the point of writing.[45]

2.2.5 The breadth of diamond attributes and applications

Diamond has only been thought of as an electronic material for the last 25 years, as a result the overwhelming majority (by volume) of commercial applications use diamond in a passive capacity, such as cutting and grinding tools.[22] Other passive roles take advantage of diamond's wide window of optical transparency, from UV (225 nm) to the far infrared.[46] This combined with diamond's strength and resistance to thermal shock make it an ideal material for harsh environments - including UV windows for missile and rocket nose cones[47] and windows for synchrotron radiation.[48]

The stiff sp^3 bonding seen in diamond permits a very high thermal conductivity, at 2200 W m^{-1} K^{-1}(5 times greater than pure copper).[49] CVD layers have been successfully implemented as a heat spreader on high performance electronics, although it remains to be seen if this approach achieves widespread adoption.[50] Micro or Nano Electro-Mechanical Systems (MEMS/NEMS) based on diamond have received a lot attention due to the superlative properties of diamond (e.g. highest Young's modulus: 910-1250 GPa),[4] devices such as whispering gallery mode micro disks,[51] photonic crystal micro cavities,[52] and ring resonator arrays (for radio frequency signal processing)[53] have been produced. Diamond's chemical resilience is also utilised in tritium confinement barriers in fusion reactors.[54] Indeed, the extreme radiation hardness seen in diamond makes it an ideal material for the detection of ionising radiation. Such detectors often rely on the high breakdown field strength of intrinsic diamond (between 4 and 10 MV cm^{-1})[4] to sweep any generated electron hole pairs to appropriately sited electrodes. Deep UV detectors have been reported[55] and are now in commercial production, along with high energy particle detectors (alpha particles, beta particles and neutrons).[56,57] Boron doped diamond is an excellent electrochemical electrode and is already a well established commercial product due to a low background current and the widest potential window in aqueous media.[58] Boron doped diamond can be transparent, enabling the use of diamond electrodes in spectro-electrochemistry[59] and cell growth studies.[60]

Electron emission based on diamond can be induced through photon, electron, or ion bombardment, thermionic emission, or by external electric field. These mechanisms have potential (or realised) applications in large area flat panel displays (field emission),[1] electron amplification (secondary electron

emission – see chapters 7 & 8),[61] and highly efficient plasma ignition systems (ion induced electron emission).[62]

Commercial electronic devices based on diamond have made slow progress, largely due to the difficulties associated with doping. Nonetheless, research into various type of device show great promise, particularly for use in harsh environments such as inside jet engines, inside nuclear reactors, or outside the earth's atmosphere. Schottky diodes haven been successfully demonstrated to operate at 1000°C,[63] whilst field effect transistors (FETs) based on surface conductivity of undoped diamond have reportedly achieved f_{max} of 30 GHz. FETs operating on boron doped diamond are expected to output up to 13 W mm^{-1} in the radio frequency range.[64] Bipolar devices have yielded less impressive results, largely due to the lack of a shallow n-type dopant, still, p-n junctions,[65] and bipolar junction transistors with operating frequencies in the low GHz range have been reported.[66] Another thread of current diamond research focuses on the delta doping model, adapted from the III-V semiconductor process. In diamond, an ultra-thin layer of highly boron doped diamond acts as delocalised charge carrier source (holes in the case of boron delta layers), where the wave function of the delta region extends into the surrounding intrinsic diamond, taking advantage of the high mobility exhibited in this region – *ca.* 1600 cm^2/Vs for holes.[67] Progress in this area has been slow, largely due to the difficulty in creating a 'true' delta layer less than 1 nm thick with high doping concentration, and a sharp interface.[68] The highest reported mobility in such a device was 1-4 cm^2/Vs through Hall effect measurements.[69]

Piezoresistive strain gauges have recently been developed using boron doped NCD, achieving a gauge factor of 7.2. Such a device should provide accurate real time strain data at high temperatures.[70] Quantum information processing is fast becoming one of the main threads of diamond research. Here, colour centres (optically active defects), particularly the nitrogen-vacancy (NV) centre possess long electron spin coherence time after excitation by optical or microwave energy, even at room temperature. Hence, the NV centre can be thought of as a likely fundamental unit of a future quantum computer.[71] The optical emission from the NV centre is also exceptionally sensitive to magnetic and electric fields, making it a promising candidate for a future sensor platform.[72]

The final field where bulk diamond holds great potential lies in biology. The extreme surface stability of surface functionalisation surpasses all other semiconductors[73] and has been used both *in vitro* as a platform for neuronal cell growth[74] and *in vivo* as retinal prostheses (see Chapter 3 for more detail in this area).[75]

2.3 Nanodiamond

2.3.1 Nanodiamond formation and purification

Diamond particles with length scales below 100 nm are classified as nanodiamond (ND). ND can be formed naturally via high power high temperature shockwaves from meteor impacts found at select locations around the world.[76] Indeed, this bottom-up mechanism is the basis of artificially formed

detonation nanodiamond (DND). DND is produced by detonating an explosive containing compound - generally TNT-RDX in a 60/40 ratio[77] - in a cooled, enclosed oxygen-deficient atmosphere - Figure 2.4 (a). The resulting high pressure and temperature shockwave allows carbon from the explosives to take its form liquid nano-droplets *ca.* 1-2 nm, point A on Figure 2.4 (b) and as the pressure and temperature decrease, the droplets coalesce into larger droplets and crystallise.[79] Once the pressure and temperature fall below the graphite-diamond phase equilibrium line, diamond no longer forms, instead NDs are coated with graphite. The resultant detonation soot contains up to 80% aggregated ND in optimal conditions.[7] Although this technique was developed by Russian scientists in the 1960's, the ultra-dispersed material (i.e. individual nanoparticles separated from their aggregates) has only become available in the last few years.[80], and therefore the body of knowledge surrounding this form of diamond is limited when compared to bulk material.

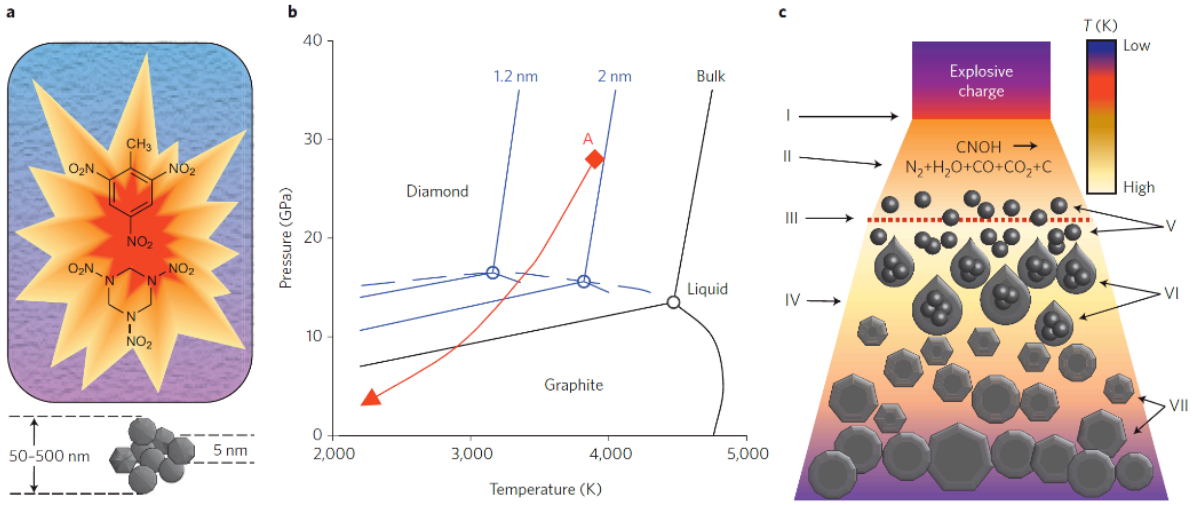

Figure 2.4 Synthesis of detonation nanodiamond (a) a TNT/RDX mixture produces 50-500 nm agglomerates comprised of 5 nm primary particles. (b) Phase diagram of bulk diamond (black) and nanoscale carbon (blue), showing the process isentrope (red). (c) Schematic of detonation wave propagation (I) front of shockwave propagation, (II) explosive molecules decompose, (III) Chapman-Jouguet plane (point A from (b) where energy release and reaction is complete), (IV) detonation products expand, (V) carbon nanoclusters form, (VI) clusters coagulate into liquid nanodroplets, (VII) nanodroplets crystallise, grow, and agglomerate.[79] Adapted from [78].

Ultra dispersed ND is produced by taking the detonation soot and subjecting it to several purification stages, outlined in section 2.3.2. The final, and most recently developed stage is the deagglomeration step. Here, to break up the agglomerated ND particles (Figure 2.4(a)) stirred media milling is performed whereby a slurry of micron sized zirconia beads are rotated at 4000rpm, this breaks the aggregated ND into its primary particles.[81] The ND is then washed through an aggressive acid treatment (heated nitric acid) to remove any newly exposed non-diamond impurities.[82] It is then thoroughly rinsed and is ready for use as a seed for subsequent growth (Chapter 8), or for use as a nanoparticle in its own right (Chapters 5 and 6). An alternative method to stirred media milling is available, known as 'beads assisted sonic disintegration'. Here a sonotrode emits strong ultrasound, causing cavitation assisted breakup of the

agglomerates. However, this method introduces metallic contamination from the sonotrode and is therefore not widely used in applications where high purity is desired.

The other route to ND synthesis is through the top-down approach of crushing and filtering (through centrifugation) of larger diamond particles formed through HPHT into successively smaller grains. However, the major disadvantage with this route is the larger particle median particle size, at approximately 18 nm, which exhibits a wide range of particle distributions ~0-50 nm. [83] The key benefit associated with this approach is the lack of sp^2 impurities on the ND surface, negating any need for further purification steps, as is required of DND.

2.3.2 Nanodiamond surface functionalisation

The ND surface retains all of bulk diamond's functionalisable properties, whilst their nano scale vastly increases the potency of surface functional groups.[84] As a result, there has been considerable interest in NDs and their surface functionalisation as almost all applications require control of the surface functionalisation.

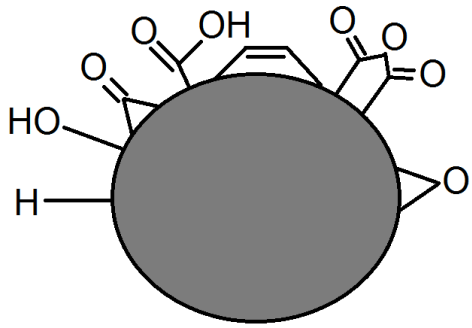

Figure 2.5 The range of surface groups seen on as received ND, note the actual moieties depend on the method of production and purification. Adapted from [84].

The cooling process in detonation synthesis usually uses water or ice as the coolant, therefore reactions with the hydroxyl radical and the ND surface take place. In addition, during the purification process exposure to oxidising agents to remove graphitic deposits and trace metallic impurities (mainly from reaction chamber walls) is required. Both these processes result in a range of oxygen containing functional groups being imparted onto the surface.[85] Hence, when referring to 'untreated' ND, the surface will contain a set of functional groups resembling

Figure 2.5. Further functionalisation of ND is performed using a variety of either wet or dry mechanisms. Wet methods involve immersing the ND in concentrated acid/base solutions. For example a 1:3 mixture of HF and HNO_3, is employed to carboxylate the surface of the ND, this also results in a reduction of graphitic and metallic impurities detected.[86] In the case of dry methods, either a simple high temperature anneal or a plasma treatment in a specific treatment gas will provide the energy to break the bonds of the surface terminations previously in place. As an example, hydrogen termination of ND has been

previously achieved by taking raw ND powder, inserting it in a quartz tube containing a hydrogen ambient and passing 2.45 GHz microwave energy through the tube, igniting a small hydrogen plasma.[87] Any of these methods can then be combined with further (usually wet) processing in order to create more complex surface terminations.

2.3.3 Nanodiamond applications

Due to the relative ease of surface functionalisation, and the wide range of characteristics these surfaces present, there is an assortment of exciting potential applications for surface functionalised ND. Within this field, the uniquely small and stable form of the ND - particularly within the range of environments seen in biological media - can be combined with surface functional groups to anchor useful molecules and transport them into the specific tissues in the body. For example NH_2 termination and the chemotherapy drug doxorubicin, where accurate targeting could significantly reduce the quantity administered.[88] Taking advantage of the ease of depositing NDs across large areas and the high surface curvature surfaces these produce, NDs have been used as a substitute for the traditional extra cellular matrix protein coated substrate used for neuronal cell cultures.[89] This anchor model can be used to employ diamond's extreme hardness by incorporating ND to form composite materials, for example, increasing the hardness and Young's modulus of a biodegradable polymer used in bone scaffolding.[90] As ND monolayers provide a facile means of diamond deposition in 3D on most materials,[91] their promise as porous electrodes has been studied.[92] Diamond can also be used for chemical detection where the nanodiamond surface can be terminated with a molecule that reacts with a specific target molecule or subset

of molecules in order to actuate a sensor. This technique has been utilised by Ahmad *et al.* to form inexpensive chemical sensors by attaching ND to a cantilever structure[93] or by adding ND to the gate of an ISFET.[94] N-V centres have been widely reported in ND, their fluorescence has already been used as a label for ND incubated inside HeLa cells.[95] Commercial uses of ND have been gradually taking hold. For a long time, the only 'commercial' use of ND was in lubricating engine parts in the Soviet Union.[96] ND infused thermal interface paste has found a niche in enthusiast personal computing[97] where the additive yields greater thermal conductivity. As mentioned in section 2.3.1, a very important application of ND to the growth of CVD diamond lies in its ability to uniformly seed large area substrates, enabling uniform growth of thin NCD layers,[81] lowering costs per square centimetre.

2.3.4 Conclusion

Diamond, whilst exhibiting extreme material characteristics, suffers from a high degree of difficulty in the production and manipulation of highly defect free substrates resulting in a slow uptake in engineering applications. This is particularly apparent in the electronic uses of diamond, which have seen the lowest commercial uptake of the fields outlined above. Nanodiamond has seen even fewer successful implementations, although it does have the saving grace that it is a somewhat new form of diamond and as such, has not received the same amount of attention as other forms of diamond. However, much promise remains, with refinements to the processing and applications ongoing resulting in steady (if slow) progress.

[1] P May, "Diamond thin films: a 21st-century material", Philosophical Transactions of the Royal Society of London A (358), 2000, 473-495.
[2] O Williams, 'Nanocrystalline Diamond'. Diamond & Related Materials 20, 2011, pp. 621-640.
[3] Eight allotropes of carbon, Michael Ströck, Wikimedia commons, 2006, accessed 30th July, 2013, http://upload.wikimedia.org/wikipedia/commons/f/f8/Eight_Allotropes_of_Carbon.png
[4] H Pierson, "Handbook of Carbon, Graphite, Diamond and Fullerenes", Noyes, Park Ridge, New Jersey, 1993.
[5] J Morris *et al.*, "Graphene, Carbon Nanotubes, and Nanostructures: Techniques and Applications", CRC press, 2013
[6] S Thompson & J Staley, "Orbitals and Molecular Representation", United States Department of Education, 2011.
[7] A Krueger, 'The Structure And Reactivity Of Nanoscale Diamond'. Journal Of Materials Chemistry 18(13), 2008, pp. 1485-1492.
[8] R Narayan *et al.*, 'Medical Applications Of Diamond Particles & Surfaces'. Materials Today 14(4), 2011, pp 154-163.
[9] M Dundek, "Diamonds", Diamond Industry and Trade, 2009.
[10] G Woods, "Properties *and Growth of Diamond"*, INSPEC, London, UK, 1994.
[11] K Ohtsuka *et al.*, "Epitaxial growth of diamond on iridium", Japanese Journal of Applied Physics Part 2 Letters 35 (8B), 1996, L1072–L1074.
[12] D Reinhard *et al.*, "Fabrication and properties of ultranano, nano, and microcrystalline diamond membranes and sheets", Journal of Vacuum Science & Technology B 22(6), 2004, pp. 2811-2817.
[13] J Angus *et al.*, "Metastable growth of diamond and diamond-like phases", Annual Review of Materials Science 21, 1991, pp. 221–248.
[14] M Naamoun *et al.*, 'Etch-Pit Formation Mechanism Induced On HPHT And CVD Diamond Single Crystals By H_2/O_2Plasma Etching Treatment'. Physica Status Solidi A 209(9), 2012, pp. 1715-1720.
[15] W Eversole, "Synthesis of diamond", U.S. patents 3,030,187 and 3,003,188
[16] J Angus *et al.*, "Chemical vapour deposition of diamond", Philosophical transactions of the royal society A (342), 1993, pp. 195-208.
[17] J Angus *et al.*, "growth of diamond seed crystals by vapour deposition", Journal of applied physics (39), 1968, pp. 2915-2922
[18] S Matsumoto *et al.*, "Growth of diamond particles from methane-hydrogen gas", Journal of Materials Science (17), 1982, pp. 3106–3112.
[19] G Davies, Diamond, Bristol, Adam Hilger Ltd, 1984.
[20] A Badzian & R DeVries, "Crystallization of diamond from the gas phase: part 1", Materials research society bulletin (23), 1988, pp. 131-140.
[21] H Liu and DS Dandy, Diamond Chemical Vapor Deposition: Nucleation and Early Growth Stages, Noyes Publications, 1995.
[22] O Williams, "Nanocrystalline Diamond", Diamond & Related Materials (20), 2011, pp. 621-640.
[23] W Yang & Jung Ho Je, "Effects of secondary pretreatments of substrate on the nucleation of diamond film", Journal of Materials Research 11(7), 1996, pp. 1787-1794.
[24] K Ravi & C Koch, "Nucleation enhancement of diamond synthesized by combustion flame techniques", Applied Physics Letters 57(4), 1990, 348350.
[25] A Morrish & P Pehrsson, "Effects of surface pretreatments on nucleation and growth of diamond films on a variety of substrates", Applied Physics Letters 59(4), 1991, pp. 417–419.
[26] J Robertson, "Mechanism of bias-enhanced nucleation and heteroepitaxy of diamond on Si", Diamond and Related Materials 4(5–6), 1995, pp. 549–552.

[27] B Spitsyn *et al.*, "Vapor growth of diamond on diamond and other surfaces", Journal of Crystal Growth 52, 1981, pp. 219–226.
[28] S Iijima *et al.*, "Early formation of chemical vapor deposition diamond films", Applied Physics Letters 57 (25), 1990, pp. 2646–2648.
[29] R Kalish, "Doping of diamond", Carbon (37), 1999, 781-985
[30] J Ristein, 'Surface Transfer Doping Of Semiconductors'. Science (313), 2006, pp. 1057-1058.
[31] A Aleksov, "Prospects of bipolar diamond devices", Solid State Electron (44), 2000, 369-375.
[32] F Fontaine, "Boron implantation/in situ annealing procedure for optimal *p*-type properties of diamond", Applied Physics Letters 68(16), 1996, pp. 2264-2268.
[33] P Muret, "Deep hole traps in boron-doped diamond", Physical Review B 81(23), 2010, 235205
[34] K Buschow *et al.*, Encyclopedia of Materials - Science and Technology, Volumes 1-11, Elsevier, 2001.
[35] R Kalish, "The search for donors in diamond", Diamond and Related Materials 10, 2001, pp. 1749–1755.
[36] R Farrer, "On the substitutional nitrogen donor in diamond", Solid State Communications 7, 1969, pp. 685–688.
[37] M Nesladek, "Conventional n-type doping in diamond: state of the art and recent progress", Semiconductor Science and Technology 20, 2005, R19– R27.
[38] L Wang & A Zunger, "Phosphorus and sulphur doping of diamond", Physical Review B 66(16), 2002, 161202.
[39] M Landstrass & K Ravi, "Hydrogen passivation of electrically active defects in diamond", Applied Physics Letters 55(14), 1989, pp. 1391-1393.
[40] G Swain, "The susceptibility to surface corrosion in acidic fluoride media: a comparison of diamond, HOPG, and glassy carbon electrodes." Journal of the electrochemical society 141(12), 1994, pp. 3382-3393.
[41] W Chen *et al.*, 'Surface Transfer Doping Of Semiconductors'. Progress In Surface Science 84(9), 2009, pp. 279-321.
[42] R Gi, "Formation mechanism of *p*-type surface conductive later on deposited diamond films", Japanese Journal of Applied Physics 34(10), 1995, pp. 5550-5555.
[43] P Strobel *et al.*, 'Surface Transfer Doping Of Diamond'. Nature 430(6998), 2004, pp. 439-441.
[44] S Paul *et al.*, "Surface transfer doping of diamond by fullerene." Diamond and related materials 14(3), 2005, pp. 451-458.
[45] K Hirama, "Diamond field-effect transistors with 1.3A/mm drain current density by Al_2O_3 passivation layer", Japanese Journal of Applied Physics 51(9), 2012, 0112.
[46] Optical Properties of CVD Diamond, Diamond materials, accessed 6th August, 2013, http://www.diamond-materials.com/EN/cvd_diamond/optical_properties.htm
[47] R Hazen, The Diamond Makers, Cambridge university press, 1999
[48] A Khounsary *et al.*, "On diamond windows for high power synchrotron x-ray beams." Nuclear Instruments and Methods in Physics Research Section A: Accelerators, Spectrometers, Detectors and Associated Equipment 319(1), 1992, pp. 233-239.
[49] E Wörner *et al.*, "Thermal conductivity of CVD diamond films: High-precision, temperature-resolved measurements." Diamond and related materials 5.6, 1996, pp. 688-692.
[50] P Boudreaux, Applications of Diamond Films and Related Materials: 3rd International Conference on the applications of diamond films and related materials, Washington, DC: NIST, 1995.

[51] C Wang *et al.*, "Observation of whispering gallery modes in nanocrystalline diamond microdisks." Applied physics letters 90(8), 2007, pp. 081110-081110.
[52] C Wang, *et al.*, "Fabrication and characterization of two-dimensional photonic crystal microcavities in nanocrystalline diamond." Applied Physics Letters 91(20), 2007, pp. 201112-201112.
[53] J Baldwin *et al.*, "Nanocrystalline diamond resonator array for RF signal processing." Diamond and related materials 15(11), 2006, pp. 2061-2067.
[54] K Takahashi *et al.*, "Chemical vapor deposition diamond window as vacuum and tritium confinement barrier for fusion application." Review of Scientific Instruments 71(11), 2000, pp. 4139-4143.
[55] R McKeag & R Jackman, "Diamond UV photodetectors: sensitivity and speed for visible blind applications." Diamond and related materials 7 (2), 1998, pp. 513-518.
[56] C Wild, Low-pressure synthetic diamond: manufacturing and applications. Springer Verlag, 1998.
[57] A Mainwood *et al.*, "Neutron damage of chemical vapour deposition diamond." Journal of Physics D: Applied Physics 28 (6), 1995, pp. 1279.
[58] Electrically Conductive Diamond Electrodes, CCL Diamond, accessed 7th August, 2013, http://ccl-diamond.com/HTML/Products_Electrodes.html
[59] J Stotter *et al.*, "Optically transparent diamond electrodes for UV/Vis and IR spectroelectrochemistry." Interface 12(1), 2003, pp. 33-38.
[60] M Bonnauron *et al.*, "Transparent diamond-on-glass micro-electrode arrays for ex-vivo neuronal study." physica status solidi A 205(9), 2008, pp. 2126-2129.
[61] J Yater *et al.*, 'Development Of Biased Diamond Current Amplifier'. Vacuum Electron Sources Conference (IVESC), 2012 IEEE Ninth International. 2012, pp. 439-440.
[62] R Kalish, 'Diamond As A Unique High-Tech Electronic Material: Difficulties And Prospects'. Journal of Physics D: Applied Physics 40 (20), 2007, pp. 6467-6478.
[63] A Vescan *et al.*, "High temperature, high voltage operation of diamond Schottky diode." Diamond and related materials 7 (2), 1998, pp. 581-584.
[64] A Aleksov *et al.*, "Diamond power FET concept." High Performance Devices, 2000. Proceedings. 2000 IEEE/Cornell Conference on. IEEE, 2000.
[65] A Aleksov *et al.*, "Diamond diodes and transistors." Semiconductor science and technology 18(3), 2003, S59.
[66] A Aleksov *et al.*, "Prospects of bipolar diamond devices." Solid-State Electronics 44(2), 2000, pp. 369-375.
[67] Harris, "Delta-doping of semiconductors", Journal of Materials Science – Materials in Electronics (4), 1993, pp. 93-105.
[68] G Chicot, "Hole transport in boron delta-doped diamond structures", Applied Physics Letters (101), 2012, 162101.
[69] R Balmer *et al.*, 'Transport Behavior Of Holes In Boron Delta-Doped Diamond Structures'. Journal of Applied Physics 113(3), 2013, 033702.
[70] P Kulha *et al.*, 'Design And Fabrication Of Piezoresistive Strain Gauges Based On Nanocrystalline Diamond Layers'. Vacuum 86(6), 2012, pp. 689-692.
[71] M Dutt *et al.*, "Quantum Register Based on Individual Electronic and Nuclear Spin Qubits in Diamond". Science 316 (5829), 2007, pp. 1312–6.
[72] J Maze *et al.*, "Nanoscale magnetic sensing with an individual electronic spin in diamond". Nature 455 (7213), 2008, pp. 644–647.
[73] W Yang *et al.* "DNA-modified nanocrystalline diamond thin-films as stable, biologically active substrates." Nature materials 1(4), 2002, pp. 253-257.
[74] C Specht *et al.*, 'Ordered Growth Of Neurons On Diamond'. Biomaterials 25(18), 2004, pp. 4073-4078.

[75] P Bergonzo *et al.*, '3D Shaped Mechanically Flexible Diamond Microelectrode Arrays For Eye Implant Applications: The MEDINAS Project'. IRBM 32(2), 2011, pp. 91-94.
[76] D Kennett *et al.*, "Nanodiamonds in the Younger Dryas boundary sediment layer." Science 323(5910), 2009, pp. 94-94.
[77] O Shenderova, "Surface Chemistry and Properties of Ozone-Purified Detonation Nanodiamonds", Journal of Physical Chemistry C (115), 2011, pp. 9827–9837.
[78] V Mochalin *et al.*, 'The Properties And Applications Of Nanodiamonds'. Nature Nanotechnology 7(1), 2011, pp. 11-23.
[79] V Danilenko, "Nanocarbon phase diagram and conditions for detonation nanodiamond formation." Synthesis, Properties and Applications of Ultrananocrystalline Diamond. Springer Netherlands, 2005. pp. 181-198.
[80] E Ōsawa, "Recent progress and perspectives in single digit nanodiamond", Diamond & Related Mater (16), 2007, pp. 2018-2022.
[81] O Williams, "Enhanced diamond nucleation on monodispersed nanocrystalline diamond", Chemical Physics Letters 445(4), 2007, pp. 255-258.
[82] A Krüger, "Unusually tight aggregation in detonation nanodiamond: Identification and disintegration", Carbon (43), 2005, pp. 1722–1730.
[83] Syndia submicron diamond powders, Van Moppes, accessed 9th August, 2013, http://www.vanmoppes.ch/phocadownload/EN-Micron/SubMicron-GAF_EN.pdf
[84] A Krueger & D Lang, 'Functionality Is Key: Recent Progress In The Surface Modification Of Nanodiamond'. Advanced Functional Materials 22(5), 2012, pp. 890-906.
[85] Y Butenko *et al.*, "The Thermal Stability of Nanodiamond Surface Groups and Onset of Nanodiamond Graphitization." Fullerenes, Nanotubes and Carbon Nanostructures 14(2-3), 2006, pp. 557–564.
[86] V Pichot *et al.*, "An efficient purification method for detonation nanodiamonds", Diamond and Related Materials 17(1), 2008, pp. 13-22.
[87] H Girard, "Hydrogenation of nanodiamonds using MPCVD: A new rout toward organic functionalization", Diamond & Related Materials 19(7), 2010, pp. 1117-1123.
[88] E Chow *et al.*, "Nanodiamond therapeutic delivery agents mediate enhanced chemoresistant tumor treatment." Science Translational Medicine 3(73), 2011, 73ra21.
[89] A Thalhammer *et al.*, "The Use of Nanodiamond Monolayer Coatings to Promote the Formation of Functional Neuronal Networks," Biomaterials 31(8), 2009, pp. 1–8.
[90] Q Zhang, "Fluorescent PLLA-nanodiamond composites for bone tissue engineering", Biomaterials (32), 2001, pp. 87-94.
[91] J Hees, "Electrostatic self-assembly of diamond nanoparticles", Chemical Physics Letters 509(1), 2011, pp. 12–15.
[92] Q Zang, "Electrochemical properties of nanodiamond powder electrodes" Diamond and Related Materials 16, 2007, pp. 16–20.
[93] R Ahmad, "Nanodiamond-coated silicon cantilever array for chemical sensing", Applied physics letters 97, 2010, 093103.
[94] R Ahmad, "Nanodiamond-gated silicon ion-sensitive field effect transistor", Applied physics letters 98, 2011, 153507.
[95] F Neugart *et al.*, "Dynamics of diamond nanoparticles in solution and cells." Nano letters 7(12), 2007, pp. 3588-3591.
[96] Y Zhu *et al.*, "Surface modification and dispersion of nanodiamond in clean oil." China Particuology 2(3), 2004, pp. 132-134.
[97] P Kendall & R Sura, "Thermally conductive grease." WIPO Patent Application PCT/US2007/075974, filed August 15th, 2007.

Chapter 3: Neurons and Image Intensifiers

3.1 Introduction

As both topics discussed in this chapter are highly disparate, wide ranging fields, this background chapter aims to collate the relevant information required for a full understanding of the subsequent experimental chapters.

3.2 Neurons

3.2.1 Histology

Neurons are highly specialised class of cells found in most animals (all species within the Eumetazoa group) with the primary function of processing and transmitting electrochemical signals. As the location and function of neuronal cells is highly varied, there is a wide range of observed sizes and electrochemical properties.[1] However a typical neuron can be described as a cell containing a cell body, dendrites, and an axon. The cell body (or soma) contains the cell nucleus, where the majority of protein synthesis occurs. Electrical impulses known as action potentials are received here, carried by dendrites. Dendrites are extensions of the cell that pass (and integrate) the electrochemical information received from 10,000 – 100,000 other neurons into the cell body.[2] Finally, axons are responsible for the conduction of action potentials away from the cell body and on to other neurons or tissues and are typified by a long untapering radius terminated with numerous terminal buttons. At the terminal button synapses transmit action potentials adjacent

dendrites or other structures. Axons are sometimes coated with a myelin sheath (particularly in large animals such as humans), formed by supporting glial cells which create a dielectric layer around the axon, enabling fast transmission of action potentials along the axon and preventing current leakage into the surrounding media. As previously mentioned, the term neuron covers a wide variety of cells found in animals.

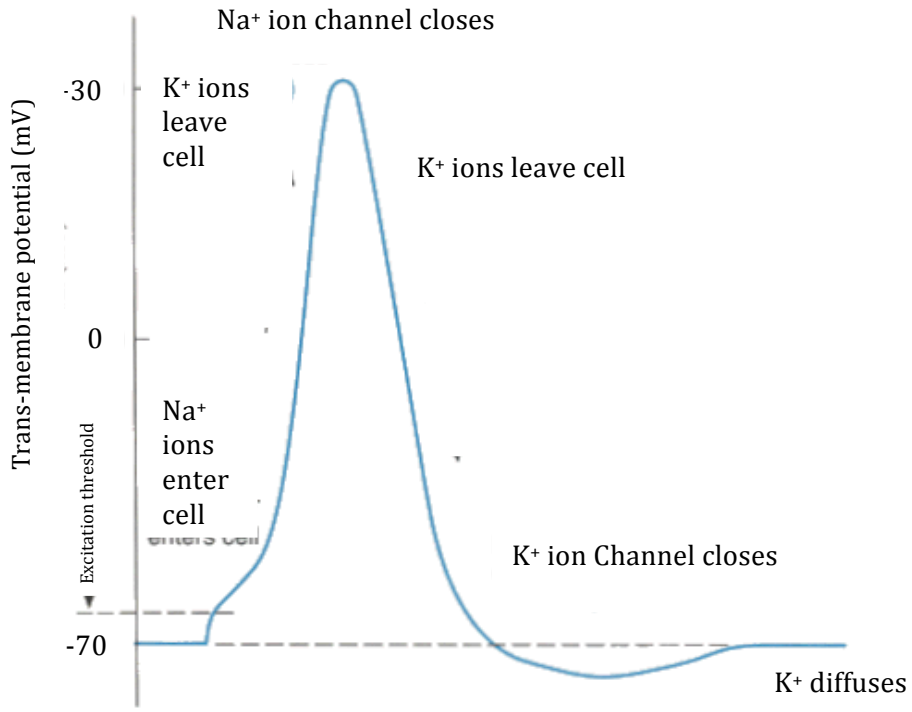

Figure 3.1 Schematic of action potential progression.

Figure 3.1 shows the progression of an action potential, as seen in neurons. Initially sodium ions are outside the cell membrane, whilst potassium ions are inside it, giving a resting polarisation of -70 mV. Upon stimulation, the sodium ions begin to enter the cell through the ion channels, causing a rapid depolarisation across the membrane. Next, potassium ions leave the cell through the potassium ion channels and the sodium ion channels close, causing the sodium ions to remain inside the cell. This has the effect of enacting the

action potential. The cell's membrane then repolarises by pumping the sodium and potassium ions back to their starting positions (outside and inside the membrane, respectively). During this period the cell is said to be in a refractory period where further stimulus will not result in another action potential. The entire timescale of this process (including the refractory period) is around 5 ms.

This thesis is concerned with neurons from a medical perspective; therefore to narrow the field down, only neurons found in the human body will be discussed. The most common type of neuronal cell found in the human body are known as multipolar neurons, these are found throughout the nervous system. Bipolar neurons are found in select areas such as the olfactory epithelium (used in odour detection) and the retina (part of the visual system) and are defined by a single dendrite branch and a single axon. Unipolar neurons (referred to as pseudounipolar neurons when developed from a bipolar neuron form) have one axon, which has split to form an efficient relay of physical stimuli to the spinal cord or brain.[3] Due to this extreme specialisation, neurons have little resilience to environmental stress and hence any foreign bodies detected are subject to an immune response, hampering observation or intervention from external elements.[4] Glial cells, forming support structures around the neural pathways, are instrumental in this immune response, forming glial scar tissue in a process called gliosis. Here, the scar tissue forms around foreign bodies, insulating it from the nervous system. This causes considerable complications for neural biomaterials, particularly those attempting to acquire electrical information, and hence, gliosis is used as a measure of the disruption caused by external damage or the introduction of foreign bodies into neuronal tissue.[6]

The neurons used throughout chapter 5 were embryonic murine hippocampal cells. The hippocampus appears similar between a wide range of mammalian species, and analogous structures are found in other classes of animal, suggesting the hippocampus' role (at least in navigation) was defined early on in Chordata (vertebrate) evolution.[7] The hippocampus is an area of the brain strongly linked to memory,[8] inhibition,[9] and to space (or location)[10] and as such has received a great deal of research interest. Murine (mouse) cells are a commonly used model organism due to their similarity to human genetics, physiology, and anatomy.[11,12] Furthermore, the murine model represents a good trade-off between human similarity and cost of use when compared to other popular model systems such as primates, Danio rerio (zebra fish), and Drosophila melanogaster (fruit fly). [13] Of particular importance is the accelerated lifecycle – approximately 2 years, where one mouse year corresponds roughly 30 human years, allowing for manageable study scales and the observation of processes operating on very long time scales in humans.[14] Embryonic hippocampal cells are used due to their good availability, their high sensitivity to changes in ambient conditions, and the fact they are relatively well characterised making them ideal candidates for the assessment of neuronal biomaterials.

3.2.2 Neuronal biomaterials

Biomaterials are defined by the International Union of Pure and Applied Chemistry (IUPAC) as matter that interfaces with living tissue, organisms or microorganisms.[15] Implanted biomaterials aim to enact the minimal biological response possible, as such a response causes deviation from typical behaviour. Biomaterials destined for use with neuronal cell cultures typically require a

trade-off between being electrically active and biologically active.[16] Put another way, current biomaterials generally act as either electrode-like or tissue-like. All biomaterials must show no cytotoxicity (causing cell death) nor any reactivity within typical biological media.

The ability to control where neurons grow *in vitro* has long been an important goal of bioengineers; such networks could then easily be integrated with electronic systems. In order to pattern neural networks, first the biomaterial used must support cell adhesion. For example silane containing functional groups reduce neural cell adhesion[17] and therefore must be avoided when considering a potential biomaterial or its surface functionalisation. This control has been achieved previously on silicon;[18] however, it was not until measurements of acute brain slices (large number of neurons) within a functional network were also demonstrated on glass coated multi-electrode arrays (MEA)[19] that investigations into their electrical characteristics had been demonstrated. More recently, these two concepts were combined to pattern neurons directly on a MEA, allowing for more complex neuronal network analysis.[20] These studies performed *in vitro* on silicon and silicon dioxide substrates would therefore not be biocompatible for *in vivo* applications.[21] Hence there is great interest in the use of diamond, which can be both conductive and biocompatible. The importance of surface functionalisation on diamond neuronal *in vivo* biomaterials has been investigated by several groups. These groups have shown the crystalline structure of the diamond used seems to greatly alter the influence of the surface functionalisation, for example flat single crystal diamond shows greater cell attachment when oxygen terminated (as opposed to hydrogen terminated).[22] However, nanocrystalline diamond (NCD) shows no difference between hydrogen and oxygen termination.[23,30] This

observation does not hold for neural stem cells as these have been shown to differentiate (become a more specialised cell type) into either neurons (hydrogen termination) or glial cells (oxygen terminated) when cultured on ultrananocrystalline diamond (UNCD). [24] Other investigations into the biomaterial surface state's effect on cellular attachment have revealed positively charged surfaces enable the attachment of neurons through electrostatic bonding with the negatively charged cell membrane,[25] however this effect is only temporary and others have reported the failure of this method in maintaining cell cultures past the first few days *in vitro*.[26]

The first reported use of diamond as an *in vivo* neural electrode was in 2008 from Chan *et al.*, however this resulted in unacceptably high signal to noise ratio.[27] Diamond was first used as a substrate for MEAs by Soh *et al.* in 2004,[28] however it was not until 2011 that Bergonzo *et al.* integrated diamond based MEA technology with living tissue by making flexible polyimide housings for the diamond electrode.[29] In 2004 Specht *et al.* selectively coated single crystal diamond with tracks of laminin using micro contact printing and observed neurons attached solely to the tracks, with clear signs of neurite growth along the track at DIV2 (Figure 3.2).[30] This precoating of laminin, itself an extra cellular protein (ECM) along with fibronectin, forms the molecular support structures and contain, for example the tripeptide sequence RGD (Arginylglycylaspartic acid). RGD is implicated in cellular attachment via receptors known as integrins.[31] These ECM proteins can therefore be applied to biomaterials in order to promote adhesion, and are indeed routinely coated on artificial substrates.[32]

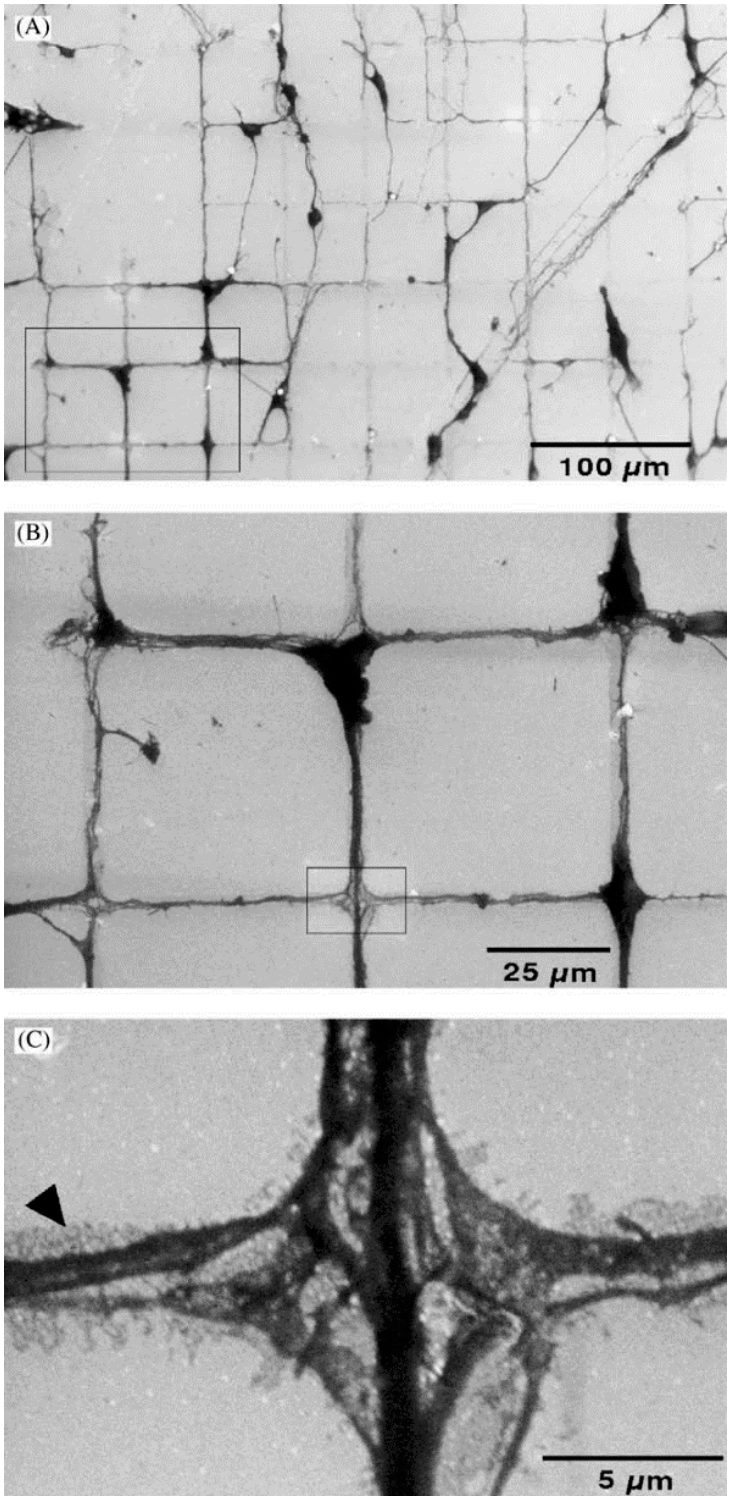

Figure 3.2 Successive detail of ordered neuronal growth on diamond selectively coated with the protein laminin. The arrow on (C) shows the residual signal from the laminin coating. Taken from [30].

3.3 Image intensifiers

3.3.1 Photomultiplication

The ability to amplify photons has created a vast array of novel technologies (see section 3.3.3), however two discoveries were necessary for the principle to gain its wide use today. Firstly, the photoelectric effect, discovered in 1887 by Hertz[33] was fully explained by Einstein in 1905,[34] leading to him being awarded the Nobel Prize in 1921. The effect describes the emission of electrons from matter caused by the absorption of light and led to the discovery that light is comprised of quantised packets of electromagnetic energy, and that it is this quanta of energy rather than the radiative flux that enables the liberation of an electron. The second discovery was that of secondary electron emission by Austin and Starke in 1902,[35] where a primary beam of electrons of sufficient energy incident on a surface results in a larger number of electrons being emitted.

Combining these two phenomena, the first reported use of a photomultiplier was by Iams and Salzberg of the Radio Corporation of America in 1935.[36] This was achieved by combining a photocathode and a single stage secondary electron emitter within a vacuum enclosure. This early model exhibited a gain of 8 and an operating frequency in the kHz range. Modern equivalents, with several secondary emission stages obtain gains as high as 1×10^8 (160 dB) with very low noise.[37]

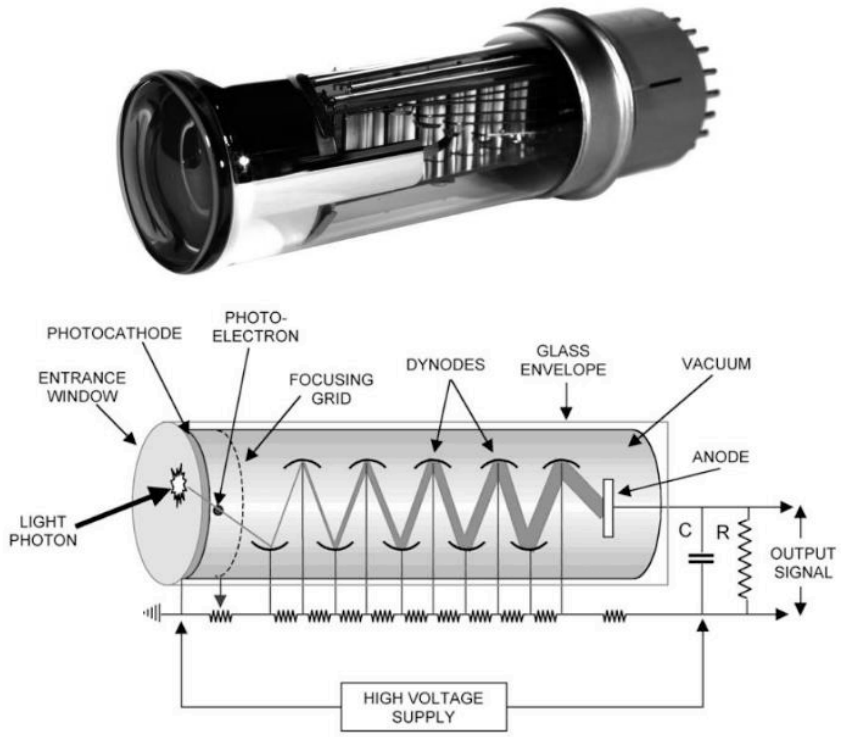

Figure 3.3 Top: Modern photomultiplier tube. Adapted from [38]. Bottom: Schematic of photomultiplier tube. Taken from [39].

In the photomultiplier, light first interacts with a photocathode. Here, light is converted into electrons though the photoelectric effect, provided the quantum energy associated with the photon is sufficient to overcome the work function of the photocathode, and is emitted into vacuum. Care must be taken to minimise electron-electron collisions (which reduce the energy of the excited electron, potentially below that of the work function) by maintaining a thin photocathode layer. This energy requirement can be reduced by the inclusion of semiconductor surfaces exhibiting negative electron affinity (NEA). The electron affinity is defined as the energy gained by taking an electron from vacuum level (outside the surface) to the bottom of the conduction band, conversely, NEA is the energy lost in the unusual scenario of the vacuum level being below the conduction band (see section 4.11 for a more detailed

explanation). Typically photocathodes are based on alkali metals such as Cs-I or Sb-Rb-Cs.[40] After being focused, the photogenerated electrons are attracted to the first dynode with a positive potential. Each electron impacts the surface of the dynode with sufficient energy to emit secondary electrons, these secondaries are then accelerated toward the second dynode by a positive potential greater than the first. A multiplication factor of around ten is seen at each dynode stage, combining these yields the overall multiplication factor of the device (quoted as 1×10^8 above). Typical dynode materials are alkaline earth metal oxides such as BeO or MgO.[41] The amplified electron beam is then directed to the anode, which is of a magnitude that can be detected by conventional electronics.

Commercial photomultiplier tube applications have largely been superseded by lower cost alternatives, such as avalanche photodiodes, charge coupled devices (CCD), and active pixel sensors and are only typically still used in very high performance applications. Avalanche photodiodes are solid state equivalents of photomultiplier tubes, in that the photoelectric effect creates an electron hole pair which then is accelerated through a high internal field, causing gain through avalanche multiplication - free electrons being accelerated to energies sufficient to liberate other electrons through collisions. Avalanche photodiodes are generally used in applications requiring high bandwidth or where preamplifier noise is high, such as fibre optic receivers or laser rangefinders.[42] CCDs are used in less demanding environments where high quality images are still required, such as astrophotography and live cell imaging.

For applications where cost is a determining factor (i.e. consumer electronics), active pixel sensors (also known as CMOS sensors after the fabrication technology – complementary metal-oxide-semiconductor) have gained wide popularity due to the low power consumption (a result of the complementary p- and n-type transistor structure) and ease of scalability. However, continual improvements in CMOS technology are causing a creep into applications previously held by more expensive technologies.

	PMT	CCD	CMOS
Dynamic Range	>1000	>10,000	>5,000
Detection Speed	fastest	slow	fast
Quantum Efficiency	5-20%	25-95%	15-35%
Multi-channel	no	yes	yes
Spectral Sensitivity	300-900nm	300-1100	400-1100
Dark Signal	good	best	best
Read Noise	good	best	best

Table 3.1 Relative merits of differing sensor technologies. Adapted from [43].

3.3.2 The microchannel plate

To discuss the microchannel plate (MCP) it is first useful to introduce the concept of the electron multiplier. Similar in operating principle to the photomultiplier tube, the electron multiplier is instead composed of one continuous amplification stage (as opposed to discrete dynode structures) where the sidewalls act as secondary electron sources. Electron multipliers are typically utilised in the field of mass spectrometry to amplify mass separated ions through ion induced secondary electron emission (Figure 3.5).

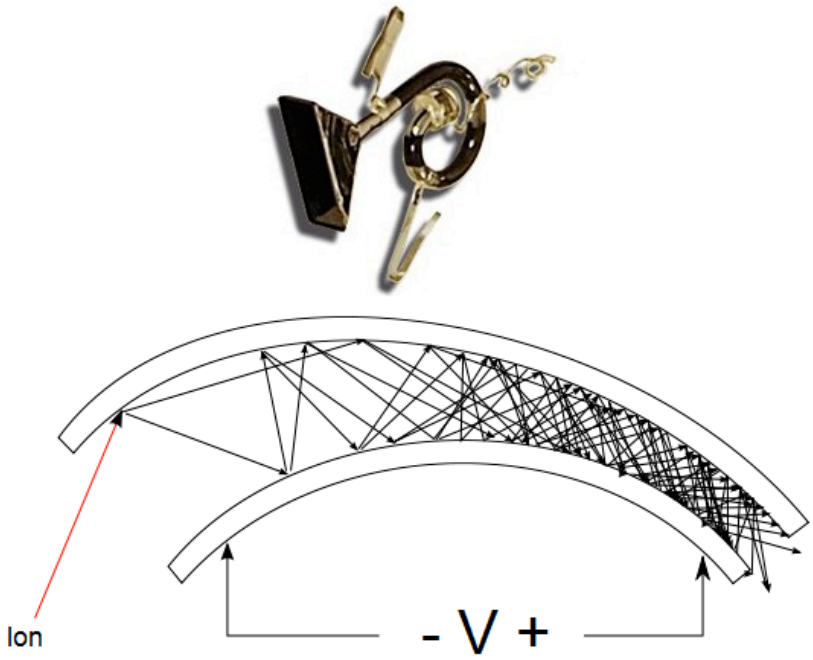

Figure 3.5 Top: Electron multiplier. Taken from [44]. Bottom: Schematic of electron multiplier. Adapted from [45].

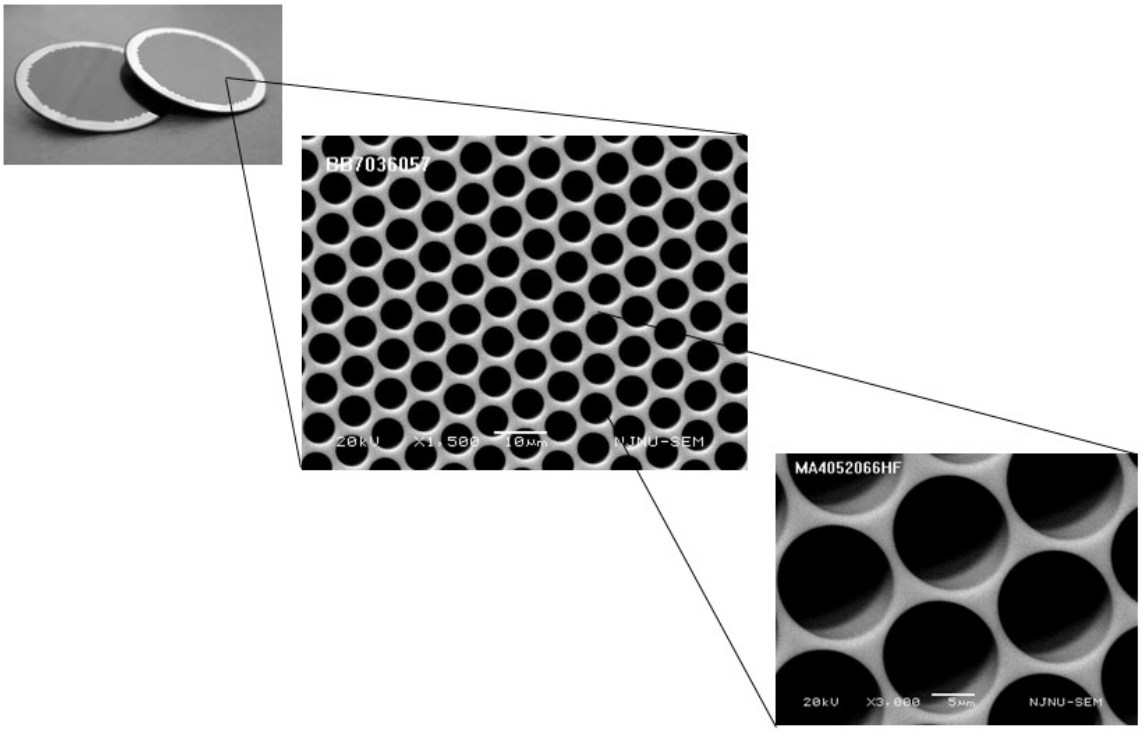

Figure 3.4 MCP microstructure. Note, the channels are continuous and exit on the rear side. Adapted from [47]

The electron multiplier and photomultiplier tube, whilst unsurpassed in detection speed, lack any form of spatial resolution. To overcome this, Goodrich at the Bendix corporation took the concept of the electron multiplier and miniaturised it and placed millions of the channels parallel to each other, forming the MCP structure (Figure 3.4).[46]

The channels of the MCP are set at a small angle (8 - 10°) from the normal and are typically 6 – 20 μm wide and 0.33 – 1.1 mm in length.[47] The front and rear faces are metallised to enable a large voltage, generally 1 kV, across the device to enable the acceleration of secondary electrons to energies capable of generating further secondaries, typically 2 at each impact. The 1 kV voltage on the MCP results in a low current through the device, called the strip current, typically 10 μA. Importantly for the modification of the MCP documented later in this thesis, a resistance of approximately 100 MΩ is required to maintain a low strip current. The strip current allows the 1 kV voltage to be distributed evenly across the channel, preventing the formation of 'dead zones' of low local field. The MCP is made of doped lead oxide glass, the exact proportions of which are an undisclosed commercial secret.

3.3.3 Image intensifiers

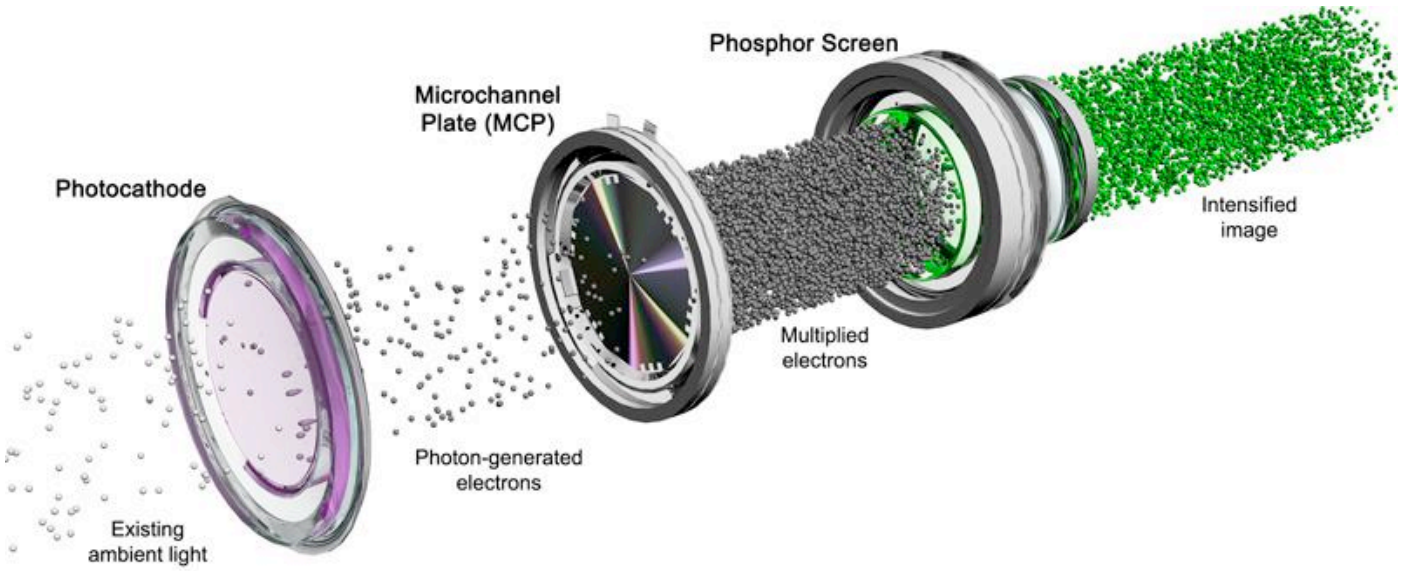

Figure 3.6 Image intensifier tube showing the three main components; Photocathode, MCP and phosphor screen. Taken from [48].

When the MCP is combined with a photocathode and a phosphor screen and arranged as in Figure 3.6, photons are converted to electrons at the photocathode, which are amplified in the MCP. Upon exit of the MCP, electrons interact with the phosphor screen, converting electrons back to photons through fluorescence. At the end of this process, an intensified image is formed. This image can then be detected by the human eye, or further electronics (e.g. CCD) depending on the application. The number of channels in the MCP dictates the resolution of the intensified image (measured in line pairs per millimetre), currently an MCP is produced by Photonis with 11 million channels.[49]

Two types of image artefacts are typically associated with image intensifiers – halos and speckle. A halo is a bright ring around an intense source of light, this

is generally caused by backscattered electrons from the MCP being readsorbed by neighbouring channels. This has since been mitigated with carbon coatings on the walls of the channels. Speckle is caused by the failure of a primary electron to produce secondary electrons, resulting in an effective loss of the original photon and an apparent time dependent variation in point intensity. Speckle can be reduced by increasing the average number of secondary electrons produced upon impact by the primary electron (this issue will be the focus of Chapter 8).

3.3.4 Photomultiplication applications

Early 'electric eye' devices to detect the breaking of beams of light were based on photomultipliers. Photomultipliers are also utilised in many medical applications such as blood analysis in flow cytometers by determining the concentrations of analytes in blood samples. An image intensifier can be combined with other technologies such as scintillators to enable the detection of ionising radiation (e.g. gamma rays in nuclear medicine).

The grade of MCP typically dictates the application it will be used in. Lower quality MCPs are sufficient for Time-of-flight mass spectrometry, residual gas analysis and point detectors. Intermediate quality MCPs can be used in low cost night vision devices, x-ray photoelectron spectroscopy, magnetic sector mass spectrometry and vacuum ultraviolet spectrometry. The highest grade of MCP are designed to operate in applications requiring maximal quality such as night vision in high speed environments (e.g. helicopter pilots), high speed photography, and astrophotography.

3.3.5 Conclusion

Neurons are a critical component within the evolution of complex life, and from an electrical engineering perspective, are arguably the most interesting cells to study and interact with due to their electrical basis of operation. The current state of the art of neuronal biomaterials has made crude interfaces between electronics and the neuron possible. However these surfaces all lack in true long term biocompatibility, which raises worry over future chronic implants. Nano structured diamond therefore holds great promise in improving this interface.

Image intensifiers haven been well studied since their inception due to their inherent usefulness in a wide range of applications. However it is the military applications of night vision that propelled research into image intensifiers. This intensive research has resulted in some spectacular gains in performance over the ~80 years since their first interaction of the design; from a gain factor of 8 to 1×10^{8}.

[1] E Pannese, Neurocytology: Fine Structure of Neurons, Nerve Processes, and Neuroglial Cells, Thieme, 1994.
[2] P Nunez, Electric Fields of the Brain: The Neurophysics of EEG, Oxford University Press, New York, 1981, pp. 484.
[3] A Siegel & H Sapru, Essential Neuroscience, Lippincott Williams & Wilkins, 2010, pp. 66.
[4] K Cheung, "Implantable microscale neural interfaces." Biomedical Microdevices 9(6), 2007, pp. 923–938.
[5] Section 8 - mouse brain, Gene Expression Nervous System Atlas, Nathaniel Heintz, accessed 20th September, 2013, http://www.gensat.org/imagenavigator.jsp?imageID=30018&showAtlas=true
[6] W Streit "Microglial response to brain injury: a brief synopsis." Toxicologic pathology 28(1), 2000, pp. 28-30.
[7] C Broglio *et al.* "Hallmarks of a common forebrain vertebrate plan: Specialized pallial areas for spatial, temporal and emotional memory in actinopterygian fish". Brain Research Bulletin 66(4), 2005, pp. 277–281.
[8] W Scoville & B Milner, "Loss of Recent Memory After Bilateral Hippocampal Lesions", Journal of Neurology, Neurosurgery & Psychiatry, 20(1), 1957, pp. 11–21.
[9] L Nadel *et al.,* "Slam on the brakes: a critique of Altman, Brunner, and Bayer's response-inhibition model of hippocampal function". Behavioural Biololgy, 14(2), 1975, pp. 151–62.
[10] J O'Keefe & J Dostrovsky, "The hippocampus as a spatial map. Preliminary evidence from unit activity in the freely-moving rat", Brain Research, 34(1), 1971, pp. 171–75.
[11] S Hardouin & A Nagy, "Mouse models for human disease." Clinical Genetics 57, 2000, pp. 237-244.
[12] N Rosenthal & S Brown, "The mouse ascending: Perspectives for human-disease models." Nature Cell Biology 9, 2007, pp. 993-999.
[13] D Simmons, "The use of animal models in studying genetic disease: transgenesis and induced mutation." Nature Education 1(1), 2008.
[14] S Schriner & N Linford, "Extension of mouse lifespan by overexpression of catalase." Age 28(2), 2006, pp. 209-218.
[15] D Williams, Definitions in Biomaterials, Proceedings of a Consensus Conference of the European Society for Biomaterials. Amsterdam, Elsevier, 2004.
[16] E Zrenner, "Will retinal implants restore vision?" Science 295(5557), 2002, pp. 1022-1025.
[17] K Patel *et al.*, "Evaluation of polymer and self-assembled monolayer-coated silicone surfaces to reduce neural cell growth." Biomaterials 27(8), 2006, pp. 1519-1526.
[18] C Yeung *et al.,* "Modulation of the Growth and Guidance of Rat Brain Stem Neurons Using Patterned Extracellular Matrix Proteins," Neuroscience Letters 301(2), 2001, pp. 147–150.
[19] M Heuschkel *et al.,* "A Three-Dimensional Multi-Electrode Array for Multi-Site Stimulation and Recording in Acute Brain Slices," Journal of Neuroscience Methods 114(2), 2002, pp. 135–148.
[20] M Suzuki *et al.*, "Neuronal Cell Patterning on a Multi-Electrode Array for a Network Analysis Platform," Biomaterials 34(21), 2013, pp. 5210–5217.
[21] W Streit & C Kincaid-Colton, "The Brain's Immune System", Scientific American 273(5), 1995, P. 54.
[22] P Ariano *et al.*, "On diamond surface properties and interactions with neurons." The European Physical Journal E 30(2), 2009, pp. 149-156.

[23] P Ariano *et al.*, "Cellular adhesion and neuronal excitability on functionalised diamond surfaces." Diamond and related materials 14(3), 2005, pp. 669-674.
[24] YC Chen *et al.*, "The effect of ultra-nanocrystalline diamond films on the proliferation and differentiation of neural stem cells." Biomaterials 30(20), 2009, pp. 3428-3435.
[25] E Yavin & Z Yavin, "Attachment and culture of dissociated cells from rat embryo cerebral hemispheres on polylysine-coated surface." The Journal of cell biology 62(2), 1974, pp. 540-546.
[26] L Bačáková *et al.*, "Cell adhesion on artificial materials for tissue engineering." Physiol Res 53(S1), 2004, pp. S35-S45.
[27] H Chan *et al.,* 2009. A Novel Diamond Microprobe for Neuro-Chemical and -Electrical Recording in Neural Prosthesis. Journal of Microelectromechanical Systems, 18(3), pp.511-521.
[28] K Soh *et al.*, "Diamond-Derived Microelectrodes Array for Electrochemical Analysis," Diamond & Related Materials 13(11), 2004, pp. 2009–2015.
[29] P Bergonzo *et al.*, "3D Shaped Mechanically Flexible Diamond Microelectrode Arrays for Eye Implant Applications: the MEDINAS Project," Irbm 32(2), 2011, pp. 91–94.
[30] C Specht *et al.*, "Ordered Growth of Neurons on Diamond," Biomaterials 25(18), 2004, pp. 4073–4078.
[31] A García, "Interfaces to control cell-biomaterial adhesive interactions." Polymers for Regenerative Medicine. Springer Berlin Heidelberg, 2006, pp. 171-190.
[32] S Rao & J Winter. "Adhesion molecule-modified biomaterials for neural tissue engineering." Frontiers in neuroengineering 2, 2009.
[33] H Hertz, "Üeber einen Einfluss des ultravioletten Lichtes auf die electrische Entladung", Annalen der Physik 267(8), 1887, pp. 983–1000.
[34] A Einstein, "Über einen die Erzeugung und Verwandlung des Lichtes betreffenden heuristischen Gesichtspunkt." Annalen der Physik 322(6), 1905, pp. 132-148.
[35] L Austin & H Starke, "Üeber die Reflexion der Kathodenstrahlen und eine damit verbundene neue Erscheinung secundärer Emission." Annalen der Physik 314(10), 1902, pp. 271-292.
[36] H Iams & B Salzberg, "The secondary emission phototube." Proceedings of the Institute of Radio Engineers 23(1), 1935, pp. 55-64.
[37] Y Hosseini & K Kaler, "Integrated Optics." The Microflow Cytometer, Pan Stanford Publishing, 2010, pp. 147.
[38] RCA 6810A Photomultiplier tube, Hofstra group, accessed 2nd September, 2013, http://www.hofstragroup.com/product/rca-6810a-photomultiplier-tube-2-14-stage-s-11/
[39] PET scanner overview, University of Illinois, Engineering Wiki, accessed 2nd September, 2013, https://wiki.engr.illinois.edu/display/BIOE414/PET+Scanner+Overview
[40] Hamamatsu PMT handbook, Hamamatsu Photonics K.K., accessed 8th September 2013, http://www.coseti.org/www.boseti.org/pdf/hamamatsu%20pmt%20handbook%20ver2.pdf
[41] J McGee & L Marton, "Advances Electronic & Electron Physics", Academic press, 1974, p. 24.
[42] Avalanche photodiode user guide, Perkin Elmer, accessed 6th September, 2013, http://www.perkinelmer.com/CMSResources/Images/44-6538APP_AvalanchePhotodiodesUsersGuide.pdf
[43] What is a CCD?, Spectral instruments Inc., accessed 8th September 2013, http://www.specinst.com/What_Is_A_CCD.html

[44] Channeltron® Electron Multipliers, Photonis, accessed 8th Septemper 2013, http://www.photonis.com/en/ism/55-channeltron-electron-multipliers.html
[45] Electron multiplier, Wikipedia, accessed 8th September 2013, http://en.wikipedia.org/wiki/Electron_multiplier
[46] W Morrow *et al.*, "Development and manufacture of the microchannel plate (MCP)", No. AMSEL-NV-TR-0064. Center For Night Vision And Electro-Optics Fort Belvoir Va, 1988.
[47] Microchannel plates and microchannel plate detectors, Tectra, accessed 8th September 2013, http://www.tectra.de/MCP.htm
[48] How an Image Intensifier Tube Works, Photonis, accessed 8th September 2013, http://www.photonis.com/en/content/102-nightvision-how-it-works
[49] Technology glossary, Photonis, accessed 8th September 2013, http://www.photonis.com/en/content/97-nightvision-technology-glossary

Chapter 4: Experimental methods

4.1 Introduction

This chapter provides an overview of the experimental methods used through the course of this thesis. A more detailed explanation is given when a characterisation technique was used extensively, or where a greater understanding of the technique provides greater insight into the results presented.

4.2 Nanodiamond seeding

4.2.1 On flat surfaces

Nanodiamond (ND) can be deposited on flat surfaces using a number of different routes, all with differing strengths and weaknesses. These include electrostatic adhesion via modified ND with high zeta potential,[1] electrospray,[2] spin coating,[3] and electrophoresis.[4] However this thesis will focus on ultrasonic deposition, within which there are a few alternative techniques relating to the choice of the liquid in which the ND is dispersed. ND in polyvinyl alcohol,[5] ND in ethanol,[6] and ND in de-ionised (D.I.) water.[7,8] For the vast majority of this thesis ND-water colloid solution was used due to the simplicity in preparation, storage and deposition. Therefore, unless otherwise stated, ND seeding throughout is performed using ND dispersed in D.I. water.

All the aforementioned techniques rely on the electrostatic attraction of the particles to the surface, forming complete layers across the entirety of the substrate exposed to the colloid solution. The seeding density depends on the initial concentration of ND solution, the disparity in surface charges of the particles and the substrate, and the pH of the solution.[9]

Ultrasonic agitation increases the rate of collision between particles and the substrate and provides the ND with more energy to help overcome any repulsive forces present. This results in good coverage of substrates in most cases with a high seeding density, ideal for subsequent growth of nanocrystalline diamond (NCD)[10,11] although a large surface charge on the substrate (or from the solution) can still prevent the majority of particles from adhering, particularly with smaller ND varietes.[9]

The way in which substrates are treated after ultrasonification greatly affects the thickness of the deposited layer. For the thinnest layers (i.e. monolayers), a rinse in deionised (D.I) water with mild agitation (either manually or further ultrasonification) followed by drying in N_2 results in the removal of particles not firmly adsorbed to the substrate through Van der Waals forces.[7] For thicker layers, removal of the rinse step and removal of the N_2 dry step (instead allowed to evaporate) results in progressively thicker coatings, up to several hundred nanometres.[12]

4.2.2 On microchannel plates

Complex 3D structures such as microchannel plates (MCP, sometimes referred to as multichannel plate) can be coated using the techniques mentioned in section 4.2.2, however extra care is required due to their fragility (e.g. plastic tweezers instead of metal, lower flow rate of N_2 during drying). Additionally, the effect of the surface tension of water must be considered as the lateral dimensions of the channels (6μm) bring water's behaviour into the realm of microfluidics, affecting the penetration of ND colloid into the channel.

4.3 Photolithography

Photolithography has long been the pre-eminent method of producing patterns on flat substrates. Briefly, this involves the spin-coating of a photoresist layer on a substrate, which is then placed under a mask bearing the desired pattern. UV light is then shone through the mask, curing the exposed photoresist. The substrate is then immersed in developer solution which washes away any soluble resist, leaving a patterned hard layer of photoresist. Depending on the type of photoresist used, positive or negative, the cured resist is soluble or insoluble respectively to the photoresist developer (in the case of this thesis a negative resist, AZ nLOF 2020, was used – see section 5.2: *Patterning*). The remaining patterned photoresist then acts as a mask for subsequent processing steps such as etches, metallisation, and doping. Once the processing step is complete, the photoresist mask is removed and typically the process is repeated with a different mask in order to build up complex planar structures.

4.4 Plasma processing

4.4.1 CVD Diamond growth

Chemical vapour deposition (CVD) diamond has been grown since the 1950's[13] through a number of methods; Combustion flame CVD, direct current glow discharge, direct current arc plasma jet, hot filament CVD (HFCVD), microwave plasma enhanced CVD (MPECVD). Of these, HFCVD and MPECVD are by far the most prevalent[13] and therefore the most scientifically relevant.

HFCVD: The principle was first published in 1982 by Matsumoto *et al.* and practically all subsequent reactor processes are based on the principle they put forward.[14] In essence, a metal filament (typically tungsten or tantalum) is heated to around 2000˚C and the substrate is maintained between 700-1000˚C in vacuum. The filament thermally activates the precursor gas mixture to provide carbon radicals for diamond growth and atomic hydrogen for the etching of non-diamond carbon and the removal of surface bonds (see figure 4.3). A gas mixture of ~1% methane in an excess of hydrogen is then admitted - 1% in the case of Matsumoto, though later iterations would use 0.5-10% methane in order to stimulate lower or higher growth rates respectively. Growth rates around 1-10 μm/h are commonly achieved,[15] although several factors affect growth rates and film quality:[16]

1. As high as possible nucleation density yields continuous films, practically not more than 10^{12} cm^{-2}, best achieved through

ultrasonic scratching of the surface with diamond grit to create surface defects.

2. A temperature of 850˚C provides the greatest growth rate.
3. Higher filament temperature results in higher growth rates.
4. Reduced distance between filament and substrate results in higher growth rate.
5. Increasing methane concentration increases the growth rate, but also increases the inclusion of non-diamond carbon.
6. Increasing gas pressure increases the growth rate, with a maximum at 100 mbar.

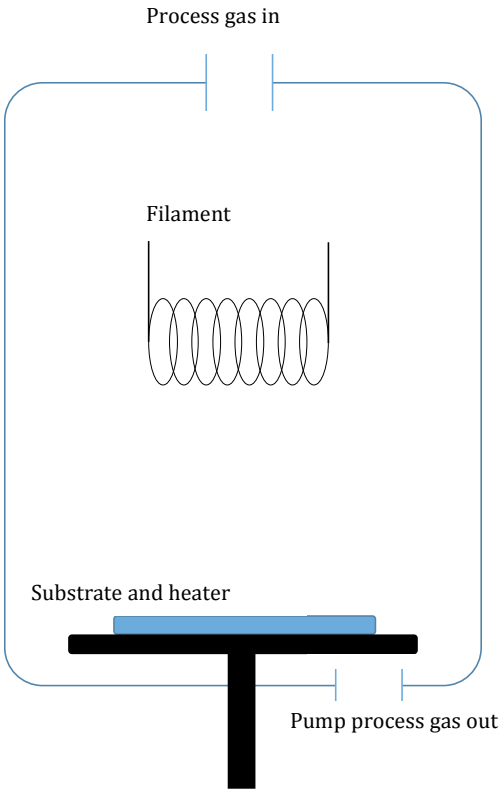

Figure 4.1 Schematic of HFCVD reactor. Adapted from [15].

Although HFCVD provides a simple and scalable method of growing diamond films over a large area[17] and on complex structures,[18] a major drawback is seen in the contamination of the film by metal from the filament, hence limiting the use of HFCVD diamond in electrical and optical applications. This can be offset somewhat by lower filament temperatures and higher

methane concentrations,[13] however, this sacrifices growth rates and phase purity respectively.

MWPECVD: First demonstrated by Kamo *et al.* in 1983,[19] MWPECVD provides a much cleaner, yet more costly route to CVD diamond growth. Although there are a few variants in the basic design – bell jar, ellipsoid, or NIRIM type – the mechanism of action is similar between them. MWPECVD relies on the coupling of microwave power to the reactor chamber through careful design of the electromagnetic cavity. The microwave energy is directed along a waveguide and transmitted into the cavity via a quartz window by an antenna. The diameter of the cavity results in only one microwave radial mode being supported inside the chamber at the microwave frequency used - typically 2.45 GHz, chosen due to the availability of components (the same frequency of operation as domestic magnetrons is used) and availability of spectrum at this frequency. Gases are fed into the cavity and the microwave energy couples energy to the electrons in the gas, which then collide with the gas molecules causing a transfer of energy. The energy directed at the gas molecules cause heating and dissociation, and the ignition of a plasma in the centre of the cavity at the point of highest electrical field strength, leads to the creation of diamond precursor species.[20] The pressure inside the cavity, along with the microwave power applied determines the size of the plasma ball and the energy density it contains. In a similar manner to the HFCVD reactor, the substrate temperature is controlled between 700-1000˚C. It has been reported that the diamond growth rate slows to approximately zero as the substrate temperature approaches 1200˚C.[21] Advances in the generation of 2.45 GHz microwave power have resulted in power input going from ~1.5 kW in the

1990's up to 8 kW today.[22] Such high power systems can yield growth rates greater than 10 μm/h, depending on methane concentrations.[15]

The advantages associated with MWPECVD include the ability to use a wide mix of input gases, allowing for a diverse range of growth chemistries (although CH_4/H_2 is still the most widely used and is the chemistry used in all growth within this thesis). However the main advantage associated with MWPECVD, especially in comparison to HFCVD, is the purity of diamond the technique can produce, and hence has become the preferred method of growth for electronic applications where defects play a major role in the performance of the material. Currently, the most significant drawback of MWPECVD lies in the wafer uniformity. Whilst the azimuthal uniformity is very good, radial uniformity of a wafer grown by MWPECVD is usually poor. However, improvements have been made where uniformity of ±5% was achieved with careful substrate cooling[23], alternatively post-growth chemical-mechanical polishing can flatten the wafer whilst reducing average roughness.[24]

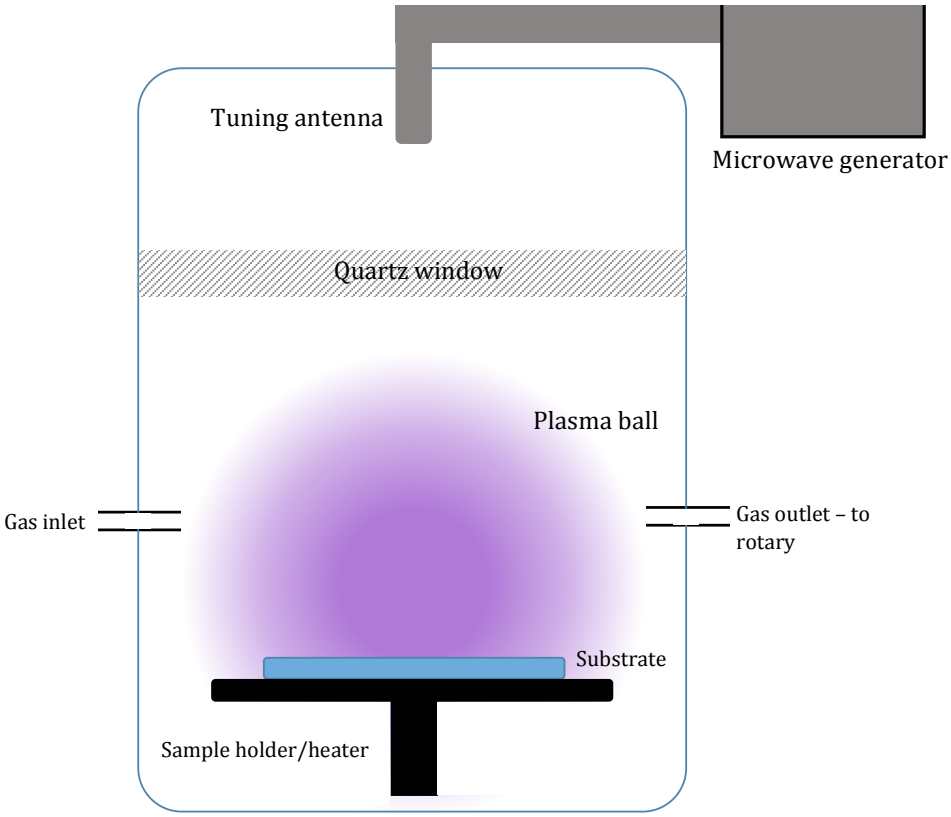

Figure 4.2 Schematic of MWPECVD reactor. Adapted from [15].

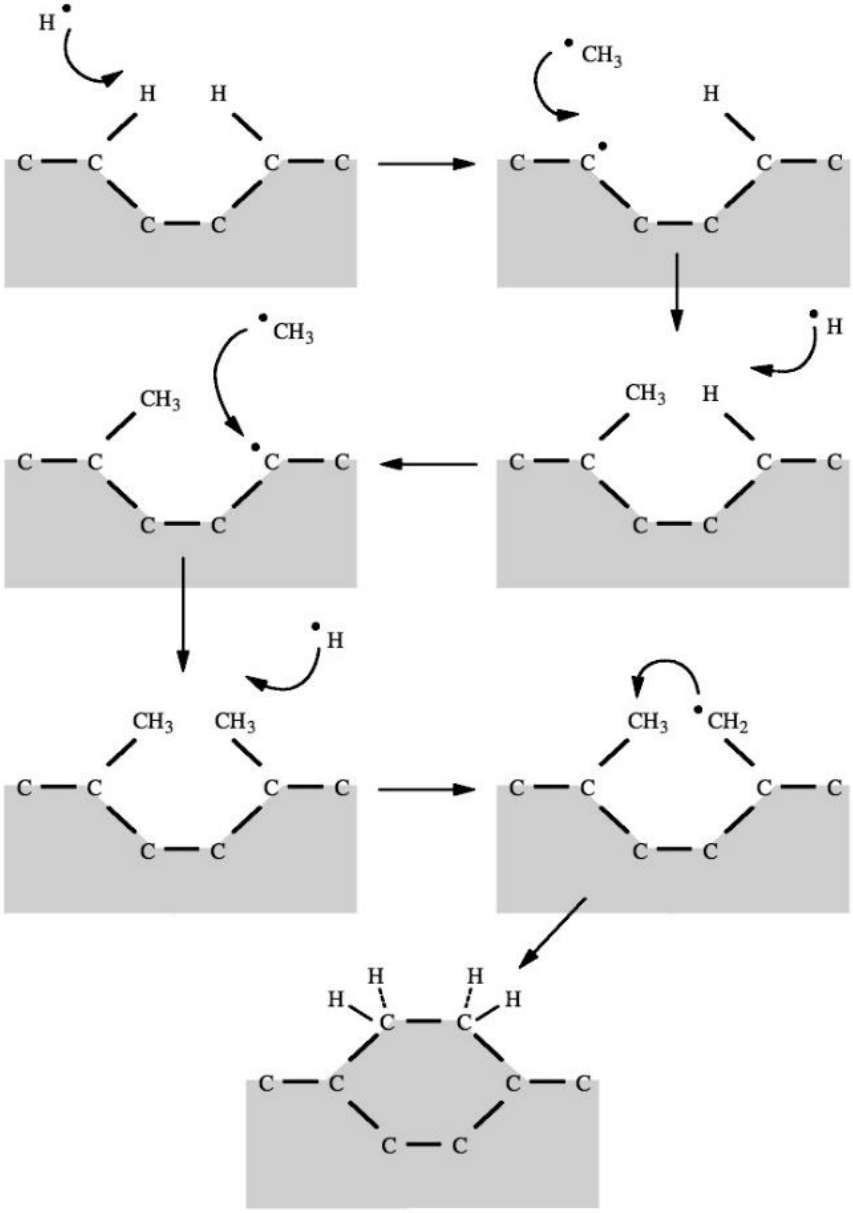

Figure 4.3 Schematic of the reactions occurring at the diamond surface during growth. Adapted from [15].

Both HFCVD and MWPECVD build up diamond in a stepwise fashion. Figure 4.3 shows a highly simplified schematic of the growth process in a CH_4/H_2 environment. Initially, atomic hydrogen causes the removal of surface groups that are replaced with methyl radicals. This process happens again on the adjacent site, then, one final interaction of atomic hydrogen with a CH_3 surface group creates a radical which then reacts with the remaining CH_3 surface group, completing the addition of carbon into the lattice.

4.4.2 Hydrogen termination

MWPECVD reactors, when operated with a pure hydrogen plasma, have three useful effects:[25]

1. Non-diamond carbon is etched at a far greater rate than diamond (by factors of up to 7700).[26]
2. The removal of oxygenated functional groups at the surface.
3. A sp^3 electron configuration at the surface is re-established.

Of particular interest here is the fact that at substrate temperatures over 700˚C, oxygen is removed from the surface and replaced with hydrogen.[27] This occurs due to the high reactivity of the atomic hydrogen present in the plasma breaking the energetic (at 700˚C+) C-O bond. This results in an efficient hydrogen termination of the diamond surface.

Other, less efficient routes to hydrogen terminated diamond include cleaving in a hydrogen atmosphere, mechanical polishing in olive oil followed

by solvent degreasing and annealing in a hydrogen atmosphere.[28] Room temperature exposure to atomic hydrogen is also known to be an efficient route to hydrogen terminated diamond.[29]

Throughout this thesis, both hydrogen termination and MPECVD growth were performed in a Seki Technotron AX5010 reactor, supplied by a 1.5 kW magnetron (at 2.45 GHz).

4.5 Ozone processing

Ozone, the highly reactive allotrope of oxygen, is a powerful oxidant, making it useful in the functionalisation of surfaces. Ozone processing has been previously shown to be a less damaging dry process on diamond substrates than radio frequency reactive ion etching[12] and hence was the natural choice for the modification of diamond films. An additional benefit was reported by Shenderova *et al.* in 2011, ozone processing removes a large proportion of the sp^2 content of ND whilst leaving the diamond surface intact.[30]

For the purposes of this thesis, a custom made ozone chamber was constructed and attached to a commercially available ozone generation unit – the Ozonia TOGC2-100201. The TOGC2 uses corona discharge to create up to 4 g/hr with dry air, or up to 10 g/hr using oxygen.[31]

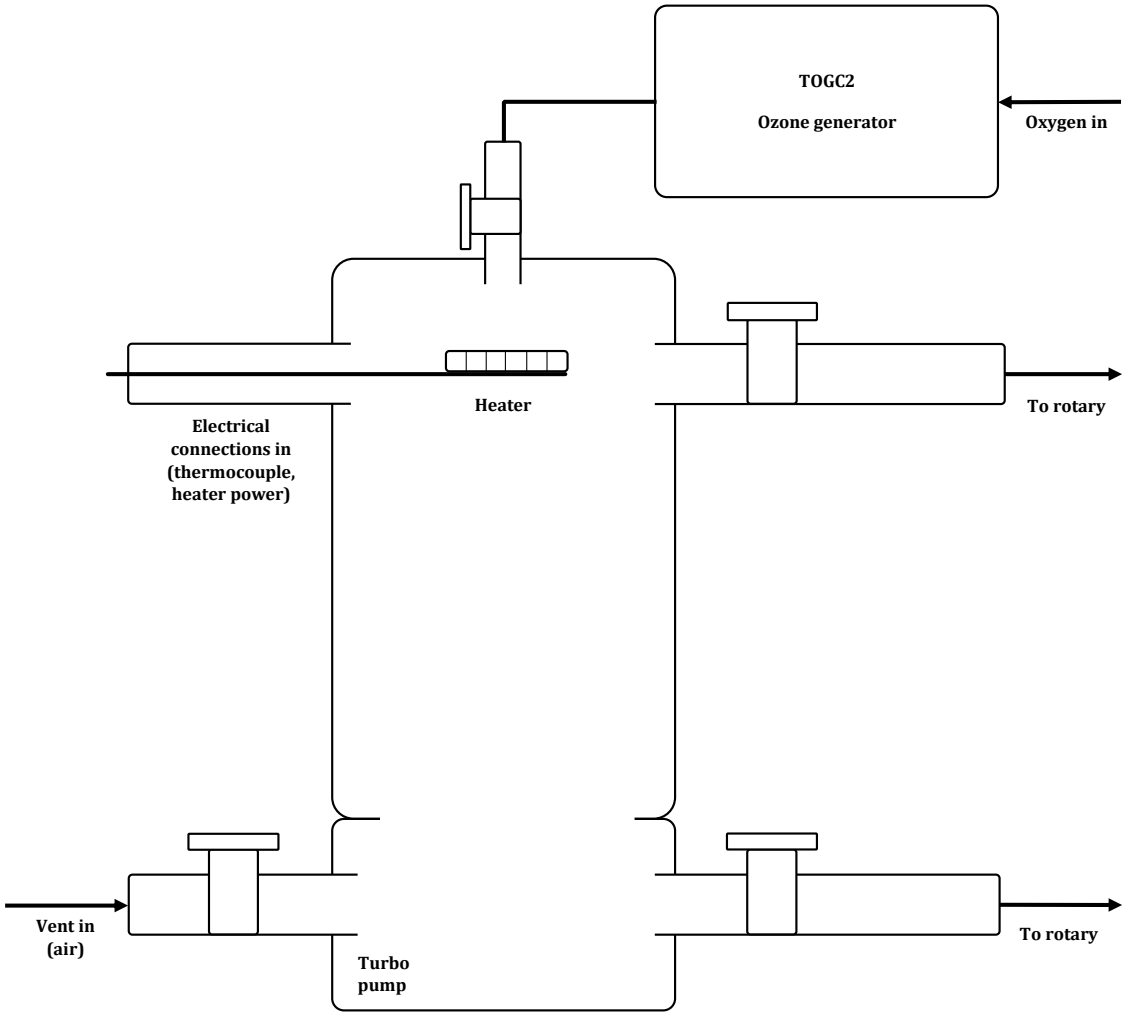

Figure 4. 4 Schematic of Ozone treatment equipment (Ozzie)

4.6 Fourier transform infrared spectroscopy

Fourier transform infrared spectroscopy (FTIR) is a form of infrared spectroscopy that uses the characteristic absorption spectrum from a broadband infrared source to determine the chemical bonds present (as opposed to the use of successive monochromatic light source for each wavelength of interest). Simply put, molecular bonds can be considered as simple harmonic oscillators, where the vibrational resonant frequency is determined by the strength of the bond and the mass of their formative atoms. The bonds of interest to this thesis (essentially organic bonds or molecules) lie in what is termed the 'fingerprint range' - 400-4000 cm^{-1} or mid infrared range[32] - and hence, the broadband light source contains the entirety of this range. If the energy of the incident light equals that of the bond then it will be absorbed, putting the molecule in an excited state. Usefully, diamond's symmetrical and rigid bonding structure results in most incident infrared light not interacting with the bulk material. Instead, only surface terminations interact, making FTIR a useful tool for probing the surface functionalisation of diamond and nanodiamond.

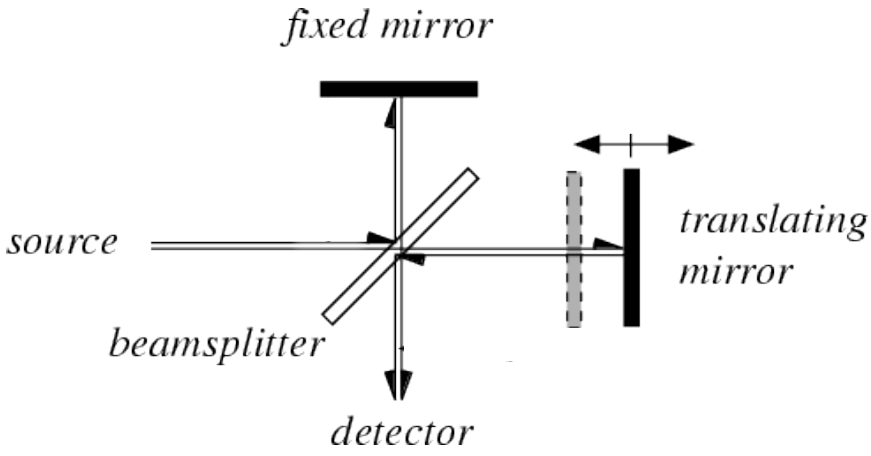

Figure 4.5 Schematic of a Michelson interferometer. Adapted from [33].

The FTIR itself uses a Michelson interferometer to obtain combinations of wavelengths by moving a mirror to change the effective cavity length. Here, the reflected and original beams constructively and destructively interfere, changing the spectrum of the beam (Figure 4.5). The beam then interacts with the material being investigated, with some wavelengths being absorbed and this interacts with the detector, creating a data set of light intensity as a function of mirror position. This data presented graphically is called an interferogram (Figure 4.6).

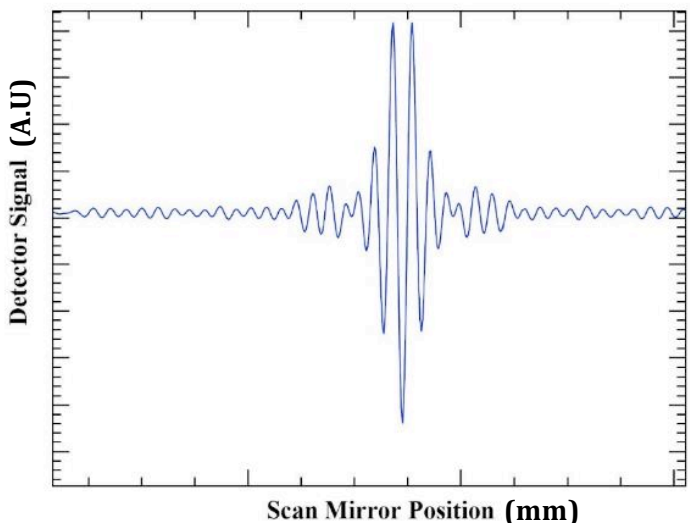

Figure 4.6 Example of an interferogram. Adapted from [34]

The interferogram data is then put through the Fourier transform (specifically the *fast* Fourier transform algorithm) on a computer, converting the space domain information into the frequency domain – usually presented in units of wavenumber, via the equation $\tilde{\nu} = \frac{1}{\lambda}$ (where $\tilde{\nu}$ represents the wavenumber of the light and λ represents the wavelength of the light).

This technique has become the dominant form of infrared spectroscopy due the large reduction in time needed to acquire a scan. This increase in speed also allows for repeated scans, building up an average and increasing the signal to noise ratio.

When FTIR is performed in a lab environment, a scan is first taken of the ambient conditions in order to subtract any absorbance not due to the sample being investigated. In this case, a CaF_2 window (water insoluble material, transparent in the infrared frequency region above 1000 cm^{-1})[35] was first scanned without any analyte in a nitrogen purged atmosphere. Scans were performed in the transmission mode, where the magnitude of absorption observed at each peak Is proportional to the number of associated bonds in the beam's path. KBr pellets, a popular mount for powdered or crushed samples was not used in this series of experiments due to its water solubility. One drawback in the use of FTIR on ND lies in the similarity in size of agglomerated ND particles and the infrared wavelengths used. Therefore some scattering occurs, causing a slope in the baseline, erroneously indicating higher absorbance with wavenumber progression. Unfortunately, the refractivity of carbon causes an opposite baseline slope. Therefore there is a requirement for non-linear baseline correction from an experienced user.

For the work contained in this thesis, a Perkin Elmer Spectrum One FTIR was used with a N_2 purge line fitted. Measurements were taken after a 10 minute N_2 purge to remove adsorbed H_2O. Measurements were taken and averaged for 10 minutes with a resolution of 4 cm^{-1}.

4.7 Atomic force microscopy

Atomic force microscopy (AFM) was a technique developed to overcome the limitation of the scanning tunnelling microscope – namely the requirement that the investigated object must be of conducting or semiconducting material. The first commercially available AFM system (along with the first published account of its operation) came in 1986, out of research at IBM and Stanford University by Binning, Quate and Gerber.[36]

The principle of operation relies on an atomically sharp tip (typically made from silicon or silicon nitride) formed on the underside of a cantilever. Piezoelectric motors drag the tip over (or just above, see below) the surface in a raster pattern. Feedback circuits then maintain a constant height or force depending on what data is required - force or height respectively. The top side of the cantilever reflects a laser towards the centre of four photodiodes where an increase in the detected light in any of the four photodiodes is translated into positional data through the control software.

There exist two main modes of AFM operation, static (or contact) mode and dynamic (or tapping) mode. Within contact mode, there are two varieties. Variable force imaging where the tip's height above the surface is maintained and the deflection of the cantilever is translated into the topography, however, this is only suitable for very flat surfaces as larger features are likely to snap the tip. Constant force imaging varies the height of the tip so as to maintain a

constant force on the cantilever. This data can then be translated into topography. This mode is more suitable to probe medium to low roughness substrates. Dynamic mode operation sees the tip oscillate at or near its resonant frequency, where the dampening of the oscillation (by electrostatic or Van der Waals forces) is translated into topographical information. Dynamic mode is the preferred method for both high roughness and high hardness substrates (in our case, diamond and ND), the latter being due to rapid tip wear through contact between the relatively soft silicon tip and diamond particles, resulting in reduced image quality. Additionally, dynamic mode reduces the occurrence of loose particles from the scanned surface (e.g. nanodiamond) attaching to the tip, causing tip artefacts (erroneous reoccurring shapes in the AFM image), or simply being pushed around by the tip. When imaging nanoparticles with lateral dimensions significantly smaller than the tip radius, their lateral dimensions are overestimated due to tip convolution, however the vertical dimension is unaffected and is therefore used for estimating particle size (Figure 4.7).[37]

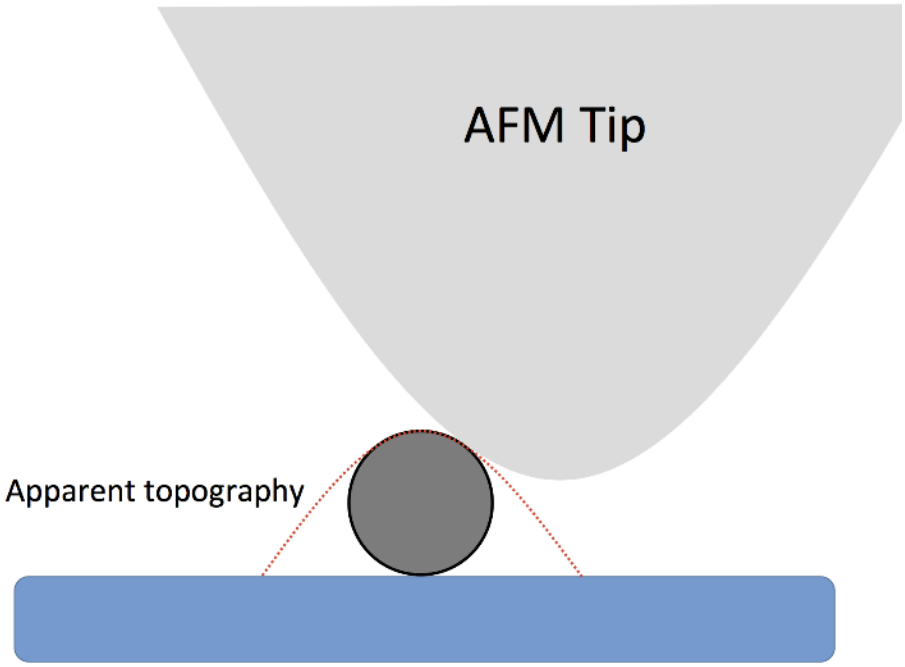

Figure 4.7 Schematic of AFM tip convolution causing lateral dimension overestimation. Adapted from [37].

The AFM used throughout the course of this thesis was a NanoScope V (7.0) controlled Dimension V Scanning Probe Microscope, equipped with an XYZ Hybrid scanner, using aluminium coated silicon AFM probes (resonant frequency ~190 kHz). The system was operated exclusively in tapping mode with a VT-103-3K Acoustic/Vibration Isolation system and the VT-102 Vibration Isolation table. All measurements were performed in lab air at room temperature.

4.8 Raman spectroscopy

Raman spectroscopy is based on the phenomena of Raman scattering. Here, when a photon interacts with the electron cloud or bonds of a molecule, it

generally undergoes Rayleigh (or elastic) scattering. However, a small fraction of the light – around 1 in each 10 million interactions – is scattered with the resultant photon being of a different frequency.[38] The incoming light excites the molecule from its ground state to a virtual energy state. The shift in frequency is caused by the relaxation of the molecule back to a second differing vibrational energy state, emitting a photon of energy equal to the difference between the virtual and second vibrational energy states. In a standard experimental setup, laser light is directed at the substrate (via an optical microscope to aid positioning and focusing) and the scattered light is filtered from the original laser wavelength, leaving only the scattered wavelengths of light. The remaining light is then analysed with a spectrometer (or alternatively a monochromator used in conjunction with a photodiode array), yielding information presented as signal intensity as a function of wavenumber.

Raman spectroscopy was used on diamond films grown in the course of this thesis due to the inherent compatibility of the technique with diamond films supported by opaque substrates. It has been noted in section 4.6 that FTIR is a very useful technique, yielding similar but complementary information to Raman spectroscopy. However, the Raman system available for use is required to function in transmission mode (attenuated total reflectance FTIR was not available) which is not compatible with diamond on silicon. The decisive advantage of Raman spectroscopy over FTIR is seen in its ability to distinguish between sp^2 and sp^3 phases of carbon, thus quantifying their relative abundance in a sample, and hence the quality of a grown diamond film.

Raman spectroscopy was performed on a Renishaw Invia Raman spectrometer with a Modu-Laster argon ion laser of wavelength of 514.5 nm. Data acquisition was performed by WiRE (v 2.0) software.

4.9 Scanning electron microscope

The scanning electron microscope was developed to overcome the fundamental limitation of the optical microscope – resolution finer than that of the wavelength of light used. Over time, improvements to the resolution limit have seen a drop to 0.4 nm at 30 kV.[39] Additionally, the depth of field resolution was improved dramatically by a factor of roughly 300 over traditional optical microscopes.[40] Finally, the very large range of magnification and varieties of electron detection allow for the observation of external morphology, crystalline structure, and chemical composition for the material investigated.

The electron beam was originally generated via field enhanced thermionic emission (the Schottky effect) at the electron gun, however more modern systems make use of cold-cathode field emission which have the advantage of high brightness (up to 1000 times higher) and stability.[41] The electron beam is accelerated into the column (in the z-axis, at energies ranging from 0.2-40 kV), after which its diameter is narrowed by spray apertures. The narrowed beam is then focused using condenser lenses and given x- or y-axis direction by scanning coils (or by deflector plates). The electron beam then interacts with the surface of the sample causing either high energy electrons to be backscattered, Auger electrons of intermediate

energy, lower energy secondary electron emission or the emission of electromagnetic radiation (both visible light and x-ray). The most common mode of imaging is through the secondary electron detector, where a positive bias (*circa* +400 V) attracts low energy secondary electrons (5-50 eV) that largely emerge from the first few nanometres of the sample's surface and can be used to analyse surface morphology and in the determination of particle size (aided by the characteristic large depth of field). The backscattered electron detector is the next most common. Placed in line with the electron beam encompassing it in a toroidal shape, it captures electrons of energy range 50eV up to slightly lower than the beam energy that have interacted with the top micron of material in the sample. Heavier elements backscatter electrons more effectively and can therefore be used to distinguish areas with different chemical compositions, however, the resolution of such images is generally lower. The raster of the primary beam allows the system to correlate flux of electrons with beam position and hence the system displays an image (or video) in real-time of the surface.

The Scanning Electron Microscope used in the course of this thesis was a JOEL JSM 7401F Field Emission Scanning Electron Microscope of cold cathode type – rated to achieve resolution of 1 nm at 15 kV and 2.2 nm at 1 kV with electron acceleration of 0.1 to 30 kV.[42] The system was generally operated in secondary electron imaging mode (SEI) although for samples that exhibited higher degrees of charging, The lower electron image (LEI) mode was used. Samples were adhered to the stage with SEM compatible

conductive tape. Samples proving particularly prone to charging were coated in an ultrathin layer of sputtered carbon.

4.10 Impedance spectroscopy

Impedance spectroscopy (IS) is a technique well suited to the characterisation of mobile or immobile charges in bulk or interfacial areas of polycrystalline materials,[43] Indeed it has the highly useful property of being able to discern the individual contributions of each conduction mechanism.

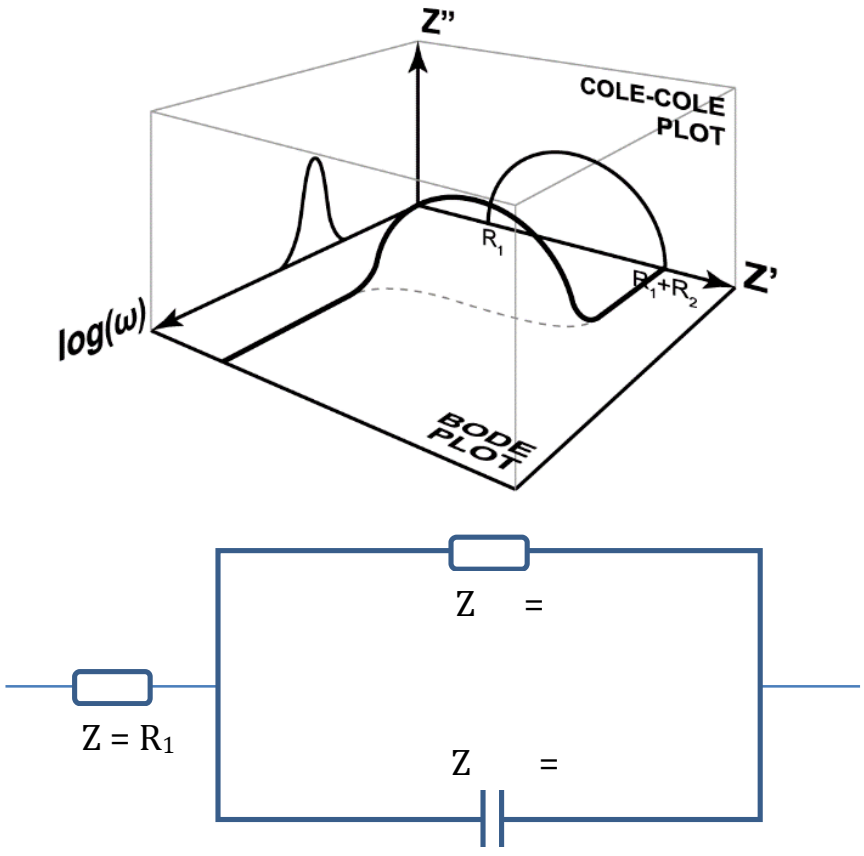

Figure 4.8 Top: Idealised IS data plotted as a single perspective plot of the impedance response showing associations between Bode, Cole-Cole and Z" vs. log(ω). Adapted from [37]. Bottom: Modelled RC equivalent circuit.

Therefore IS forms a sizable part of the experimental results contained in this thesis. IS is also widely used in the study of liquids, semiconductors, ionic solids and mixtures thereof.[44]

Here, a sinusoidal AC input voltage is applied at a range of frequencies and the magnitude and phase of the resultant current is measured. An equally valid approach would be applying an AC current input and measuring the output voltage, however this introduces significantly more difficult instrument design and therefore does not see major use commercially. Modelling can be performed on the impedance data to produce an equivalent circuit. This can be achieved by first considering the complex impedance of the equivalent circuit shown in Figure 4.8:

$$Z(\omega) = R_1 + \left(\frac{1}{R_2} + j\omega C\right)^{-1} \quad \textbf{(4.1)}$$

where ω is the angular frequency $(\omega = 2\pi f)$.

Rearranging equation (4.1) gives:

$$Z(\omega) = R_1 + \left(\frac{R_2}{1+j\omega C R_2}\right) \quad \textbf{(4.2)}$$

Finally, splitting of the real and imaginary part gives:

$$Z(\omega) = R_1 + \frac{R_2}{1+\omega^2 C^2 {R_2}^2} - \frac{j\omega C R_2^2}{1+\omega^2 C^2 {R_2}^2} \quad \textbf{(4.3)}$$

Calculating for the limits of ω where:

For $\omega = 0 \qquad Z(\omega) = R_1 + R_2$

When $\omega \to \infty \qquad Z(\omega) = R_1$

Simply put, at low frequency, current is blocked by the capacitor and flows through R_1 and R_2, whereas at high frequency, the capacitor acts as a short circuit and current flows only through R_1. At intermediate frequency, the impedance is some combination of the two. The semi-circle taken from the Cole-Cole (Figure 4.8) plot takes the form of the following equation:

$$\left[Z' - \left(R_1 + \frac{R_2}{2}\right)\right]^2 + Z''^2 = \left(\frac{R_2}{2}\right)^2 \qquad \textbf{(4.4)}$$

Equation 4.4 is of the form of a complex circle of $\frac{R_2}{2}$ radius and its centre at $\left(R_1 + \frac{R_2}{2}, 0\right)$ All real world measurements use values greater than zero for ω, R_1, and R_2, therefore the plot of real vs. imaginary impedances (Cole-Cole plot - Figure 4.8) yields a semi-circle when both capacitive and resistant components are present. Hence, by fitting semicircles to the Cole-Cole plot, values of the equivalent circuit components R_1, R_2 can be found (assuming the frequency range used is sufficient). To calculate the value of the final component, the capacitor C, the condition at the peak of the plot of Z" vs. log(ω) is taken:[45]

$$\omega_{max} R_2 C = 1 \qquad \textbf{(4.5)}$$

Rearranging to give:

$$C = \frac{1}{\omega_{max} R_2} = \frac{1}{2\pi f_{max} R_2} \quad \textbf{(4.6)}$$

Hence, knowing f_{max} and R_2 the value of C can be found. Similarly, when a Cole-Cole plot contains more than one semi-circular response, which corresponds to more than one conduction path through the material being investigated, each conduction path's R and C values can be calculated.

To relate the R and C values to actual structures within the polycrystalline material being investigated, a physical model of the grain interior, grain boundary and electrodes is required. The most widely used (and successful) model treats the structure as an array of cubic shaped grains of volume d^3, with flat boundaries between the grains of thickness δ.[46] Assuming a one dimensional current flow (ignoring grain corner contributions), two current paths are available; through the grain interior and across the grain boundary, or purely along grain boundaries. The relative magnitudes of the grain and grain boundary conductivity will dictate which conduction path will dominate. It should be noted that this model has been successfully applied to a wide range of materials, showing the bulk resistivity and the grain boundary resistivity may have differing responses.[47]

The capacitance of the grain interior and the grain boundary can be calculated using the standard formula for a parallel plate capacitor:

$$C = \frac{A\varepsilon_r\varepsilon_0}{L} \quad \textbf{(4.7)}$$

ε_0

Where A is the cross sectional area, L is the distance between plates, ε_0 is the permittivity of free space (8.854×10^{-12} F/m), and ε_r is the relative static permittivity of the dielectric. Hence the capacitance of the grain interior becomes:

$$C_{gi} = \frac{A\varepsilon_{gi}\varepsilon_0}{L} \tag{4.8}$$

The capacitance of the grain boundaries then becomes:

$$C_{gb} = \frac{A\varepsilon_{gb}\varepsilon_0}{L}\frac{d}{\delta} \tag{4.9}$$

By taking representative values of A (~10 mm^2), L (~1 mm), and ε_{gi} (5.7 for pure diamond) C_{gi} is found to be approximately 0.5 pF. Assuming the ε_{gb} is the same order of magnitude as ε_{gi}[48] (although it is likely to be slightly higher) and the same values of A and L, and setting δ (~1nm) and d (1 μm), C_{gb} is estimated to be approximately 0.5 nF.

The activation energy (E_a) of conduction paths can be calculated if IS is repeated at a range of temperatures, where R is the extracted value of R_2, T is the temperature of measurement, k_B is the Boltzmann constant in units of J K^{-1}, and q is the elementary electron charge:

$$E_a = \frac{\partial \ln(R)}{\partial\left(\frac{1}{T}\right)} \cdot \frac{k_B}{q} \tag{4.10}$$

The system used throughout this thesis was a Solartron 1260 Impedance/Gain-phase Analyser connected in series with a Solartron 1296A Dielectric interface system for high impedance measurements. Probes were set up on top of a ceramic heater, inside a stainless steel vacuum chamber in order to provide control of the atmospheric and electromagnetic environment inside the chamber (Figure 4.9). It is important to note however, that the vacuum chamber can only achieve low (or rough) vacuum, *ca.* 10^{-2} -10^{-3} mbar. Measurements were taken between 0.1 and 10^{7} Hz (the full range of the system) using as low an applied voltage as possible to prevent electrical breakdown of the sample, in order to yield a reasonable signal to noise ratio.

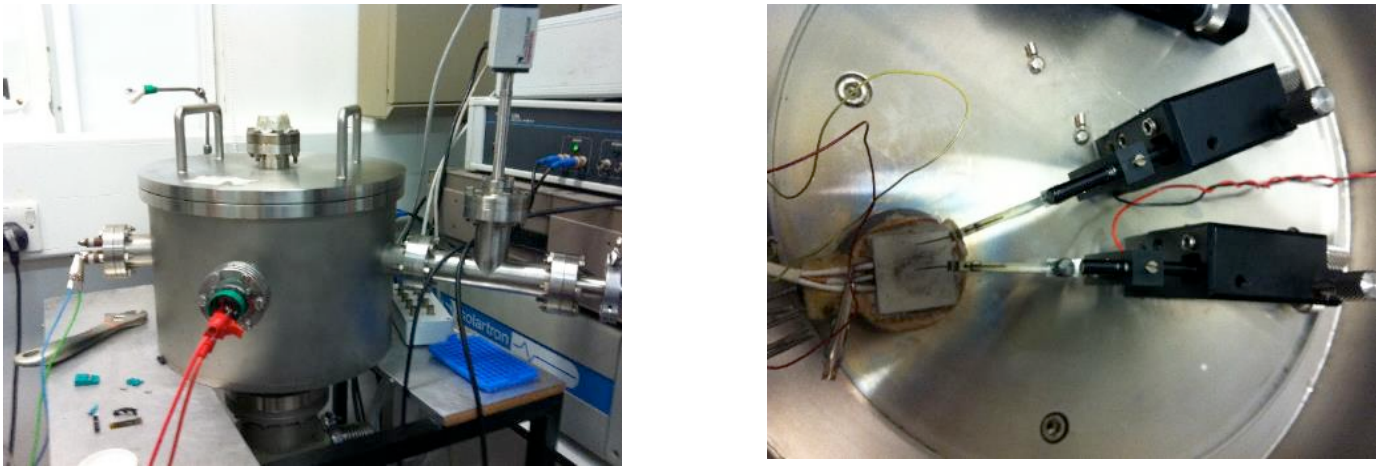

Figure 4.9 Left: Impedance spectroscopy chamber showing electrical connections. Right: Probes and ceramic heater assembly inside chamber.

4.11 Secondary electron emission

Secondary electron emission (SEE) is a phenomena observed when energetic particles, usually charged particles (electrons or ions), strike the surface of a material with sufficient energy to induce the emission of one or more secondary electrons, this is known as impact ionisation. For the purpose of this thesis only electron induced SEE will be considered. Figure 4.10 depicts

the process of generation and emission: (1) The incident electron will excite a valence electron into the conduction band, losing some energy in the process. (2) The generated secondary electron will then travel through the material until it reaches an obstacle - another electron, a phonon, an impurity, a defect or the surface. (3) Upon reaching the surface the electron will be emitted or inelastically scattered, depending on the energy of the electron and the magnitude of the vacuum barrier it encounters. If the energy is sufficient (or the barrier is low or negative – see below) then the electron will be emitted from the surface.

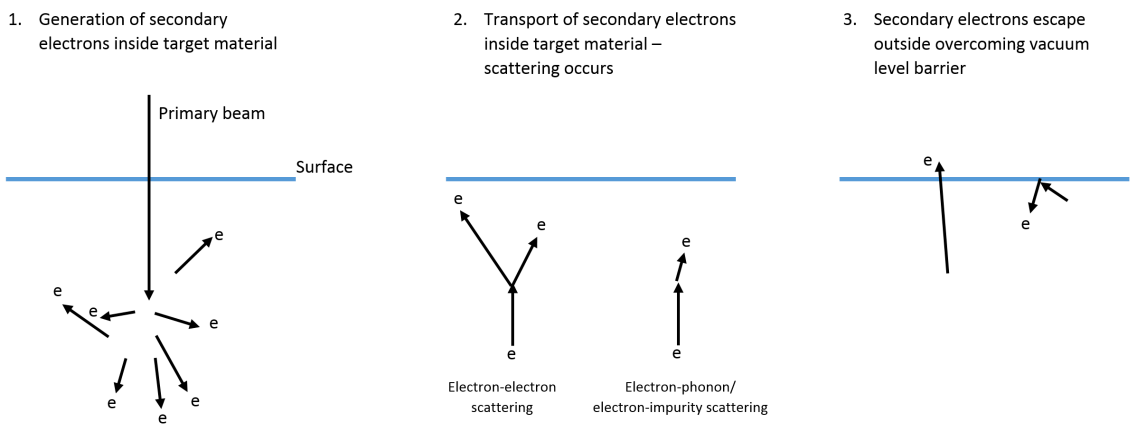

Figure 4.10 Model of secondary electron generation and emission. Adapted from [49]

The electronic state of the surface is of great importance to the emission of electrons to vacuum. The electronic state is set by a combination of the origin of atomic energy levels and more importantly the surface dipole - set by the physical state of the surface (i.e. defects) and by surface terminations. This surface state is known as the electron affinity. Electron affinity (χ) is defined as the energy needed to take an electron from the conduction band minimum (E_c)

to the vacuum level (E_{vac}). Within this there are essentially three distinct schemes (Figure 4.11).

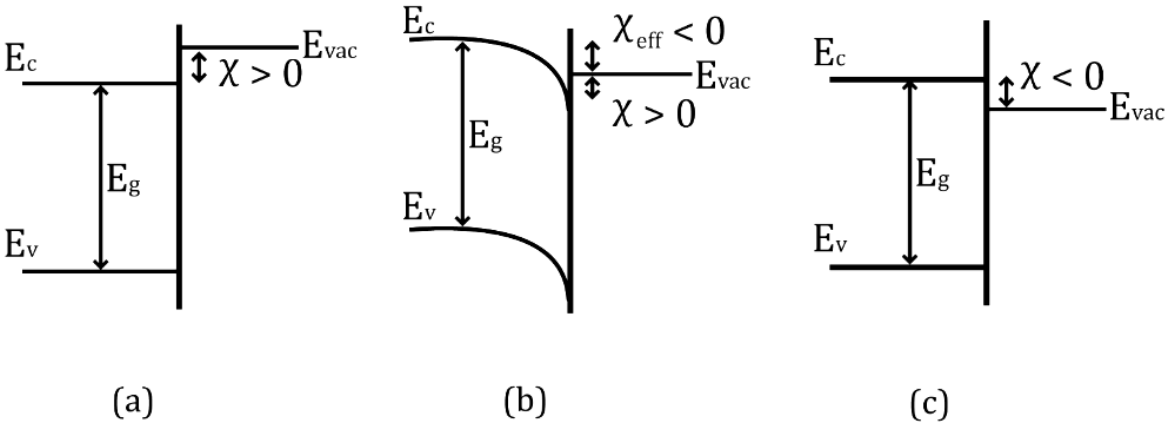

Figure 4.11 Band diagram of three modes of electron affinity. (a) Positive electron affinity (b) Effective negative electron affinity (c) True negative electron affinity. Adapted from [12]

Figure 4.11(a) shows the typical scenario for a semiconductor - including oxygen terminated and bare (111) diamond surfaces.[50] Here, there is a positive electron affinity (PEA), thus presenting a potential barrier to electron emission. PEA combined with band bending at the surface is depicted in Figure 4.11(b). This is caused by a positive dipole at the surface, resulting in an effective negative electron affinity (χ_{eff}). As long as the band bending region is thin enough, electrons can arrive at the surface with energy higher than E_{vac} and thus be emitted.[51] This is the scenario created by partial hydrogen termination of the diamond surface,[52] where a greater degree of hydrogen termination results in stronger band bending.[53] The final example, Figure 4.11(c) shows true negative electron affinity (NEA), here, E_c is above E_{vac}, therefore there is no potential barrier for an electron at the bottom of E_c. It has been suggested that fully hydrogen terminated diamond surfaces are true NEA,[28,52] Cesium oxide terminated diamond has also been shown to give sufficient band bending to

force E_{vac} below E_c, creating a metal-like surface and lowering the workfunction.[54]

Where there is more than one secondary electron emitted, the ratio of secondary electrons per incident electron (known as the primary electron) is described as the secondary electron yield (SEY). The SEY of any material is largely a function of the primary electron energy, labeled E_b. Here, as the beam energy is increased, the number of impact ionisation events increases as the beam gains enough energy to penetrate further into the material, interacting with more possible ionisation sites, generating electrons at greater depths (D_g). The quantity of generated electrons reaching the surface is moderated by the electron escape depth (D_{esc}). D_{esc} is an intrinsic property of a material defined as the mean depth than an electron can reach the surface without first either losing its energy to inelastic scattering, recombining with a hole, or falling into a trap state (D_{esc} is closely related to the inelastic mean free path of an electron) and hence, limits the depth at which generated electrons can usefully add to the SEY. SEY curves have a characteristic shape, defined by D_g, D_{esc} and E_b (Figure 4.12):

(1) The first region with low values of E_b where $D_g < D_{esc}$.

(2) At higher E_b, where $D_g \sim D_{esc}$ resulting in a maximal SEY.

(3) The final region at the highest values of E_b, where $D_g > D_{esc}$, where increasing numbers of secondary electrons are reabsorbed causing the tapering off of the SEY.

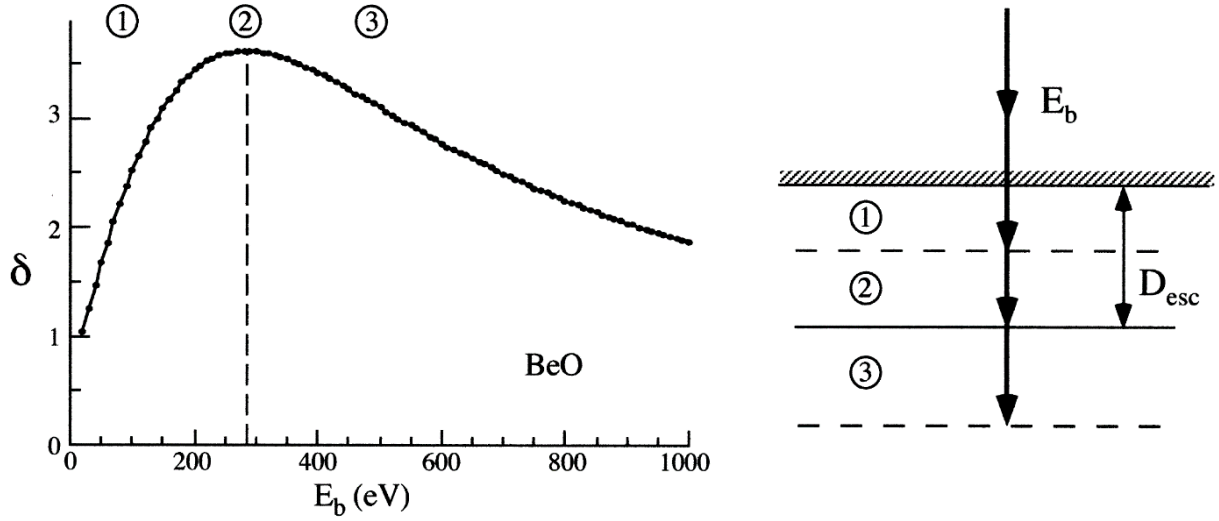

Figure 4.12 Left: Typical SEY curve taken from BeO with three distinct emission regimes. Right: Schematic of the three emission regimes' penetration depth. Adapted from [55].

SEE experiments were performed in a custom built vacuum chamber, utilising a Kimball Physics EGG-301 electron gun as the electron source, a Keithley 487 voltage source, and a Keithley 6485 picoammeter (Figure 4.13).

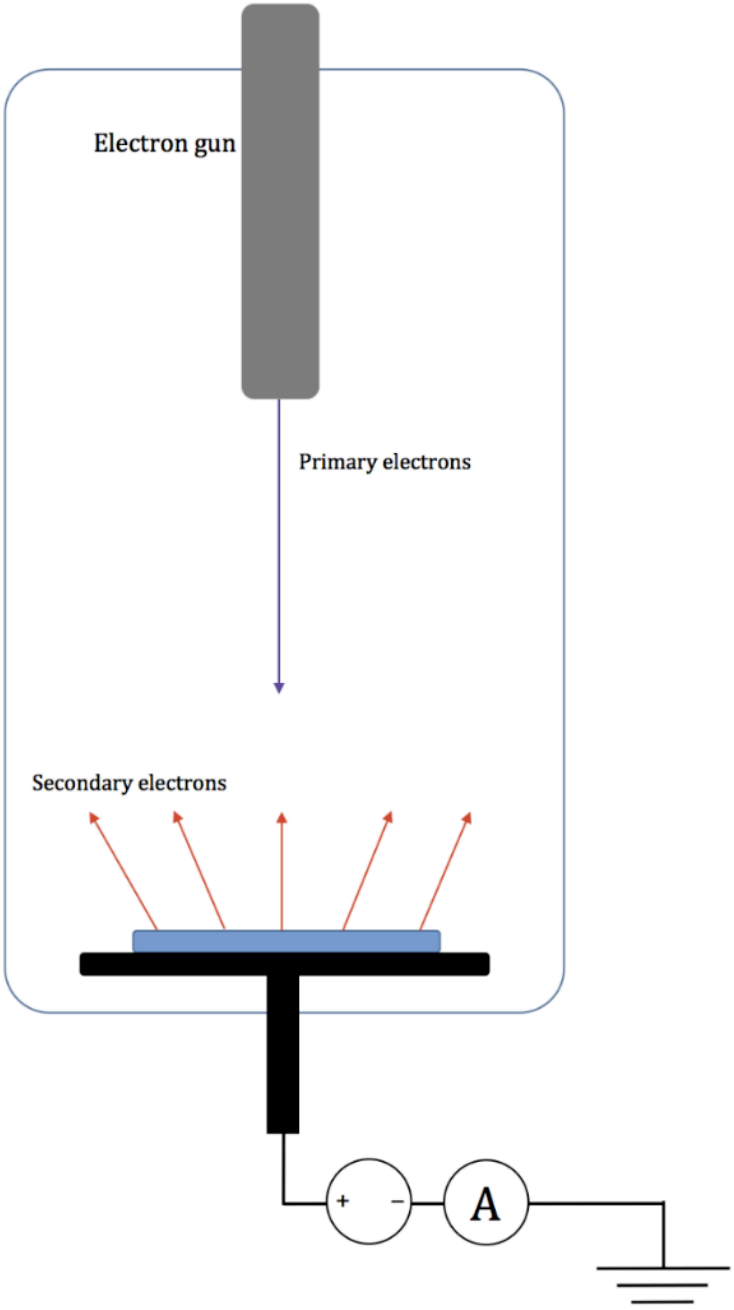

Figure 4.13 Schematic of secondary electron emission, showing arrangement of electron gun, bias source, and ammeter.

4.12 Conclusion

This chapter has reviewed the theoretical background and state of the art of the various experimental methods used throughout this thesis, with particular emphasis on impedance spectroscopy, diamond growth and secondary electron emission due to their central importance to the coming experimental chapters. Additionally, the equipment used in each instance was detailed, to provide insight into the limits of the equipment when making measurements later in the thesis. This chapter also highlights the range of origins of the equipment used – from off the shelf pre-built systems (e.g. AFM) to bespoke home built systems (e.g. SEE), and combinations thereof (e.g. MVPECVD).

[1] Seung-Koo Lee *et al.*, "Direct Deposition of Patterned Nanocrystalline CVD Diamond Using an Electrostatic Self-Assembly Method with Nanodiamond Particles," Nanotechnology 21(50), 2010, 505302.
[2] O Fox *et al.*, "Electrospray Deposition of Diamond Nanoparticle Nucleation Layers for Subsequent CVD Diamond Growth," Diamond Electronics and Bioelectronics–Fundamentals to Applications III, Edited by P Bergonzo, J Butler, R Jackman, K Loh, and M Nesladek, Materials Research Society Symposium Proceedings 1203, Warrendale, PA, 2010.
[3] K Hanada *et al.*, "Nanocrystalline Diamond Films Fabricated by Sol–Gel Technique," Surface Science 601(18), 2007.
[4] D Kalyanasundaram & P Molian, "Electrodeposition of Nanodiamond Particles on Aluminium Alloy A319 for Improved Tribological Properties," Micro & Nano Letters, IET 3(4), 2008, pp. 110–116.
[5] E Scorsone *et al.*, "Enhanced Control of Diamond Nanoparticle Seeding Using a Polymer Matrix," Journal of Applied Physics 106(1), 2009.
[6] Y Li & A Hirose, "Direct Coating of Nanocrystalline Diamond on Steel," Chemical physics letters 433(1), 2006, pp. 150-153.
[7] O Williams *et al.*, "Enhanced Diamond Nucleation on Monodispersed Nanocrystalline Diamond," Chemical Physics Letters 445(4), 2007, pp. 255–258.
[8] G Cicala *et al.*, "Nucleation, Growth and Characterization of Nanocrystalline Diamond Films," Diamond & Related Materials 14(3), 2005, pp. 421–425.
[9] J Hees *et al.*, "Electrostatic Self-Assembly of Diamond Nanoparticles," Chemical Physics Letters 509(1), 2011, pp.12–15.
[10] G Cicala *et al.,* "Smoothness Improvement of Micrometer- and Submicrometer-Thick Nanocrystalline Diamond Films Produced by MWPECVD," Journal of Nanoparticle Research 15(4), 2013, pp. 1549.
[11] M Varga *et al.*, "Study of Diamond Film Nucleation by Ultrasonic Seeding in Different Solutions," Central European Journal of Physics 10(1), 2011, pp. 218–224.
[12] A Chaudhary, "Electronic properties and applications of Nanodiamond" PhD thesis, UCL, 2012.
[13] M Werner & R Locher, "Growth and Application of Undoped and Doped Diamond Films," Reports on Progress in Physics 61(12), 1998, pp.1665–1710.
[14] Matsumoto S *et al*., "Vapor Deposition of Diamond Particles from Methane", Japanese Journal of Applied Physics 21(4), 1982, L183-L185.
[15] P May, "Diamond Thin Films: a 21st-Century Material," Philosophical Transactions of the Royal Society of London. Series a: Mathematical, Physical and Engineering Sciences *3*58(1766), 2000, pp. 473–495.
[16] S Zhou *et al.*, "Study of the Growth Rate of Diamond Film by Hot-Filament CVD," Materials Science and Engineering: B 25(1), 1994, pp. 47-52.
[17] L Schäfer *et al.,* Applications of Diamond Films and Related Materials, ed. Y Tzeng *et al,* Amsterdam, Elsevier, P. 197.
[18] B Lux and R Haubner, "Diamond as a Wear-Resistant Coating," Philosophical Transactions of the Royal Society of London. Series A: Physical and Engineering Sciences 342.1664, 1993, pp. 297-311.
[19] M Kamo *et al.*, "Diamond Synthesis From Gas Phase in Microwave Plasma," Journal of Crystal Growth 62(3), 1983, pp. 642–644.
[20] E Hyman *et al.* "One-point numerical modeling of microwave plasma chemical vapor deposition diamond deposition reactors." Journal of Vacuum Science & Technology A: Vacuum, Surfaces, and Films 12.4, 1994, pp. 1474-1479.
[21] J Angus *et al*., "Metastable Growth of Diamond and Diamond-Like Phases", Review of Materials Science 21, 1991, pp. 221-248.

[22] "Specifications of Microwave Plasma Reactor Models", Seki diamond systems, accessed 14th July, 2013, http://sekidiamond.com/microwave-plasma/reactors.html

[23] S Zuo *et al.*, "Investigation of Diamond Deposition Uniformity and Quality for Freestanding Film and Substrate Applications," Diamond & Related Materials 17(3), 2008, pp. 300–305.

[24] O Williams, "Nanocrystalline Diamond," Diamond & Related Materials 20, 2011, pp. 621–640.

[25] P John & M Stoikou, "Hydrogen Plasma Interaction with (100) Diamond Surfaces," Physical Chemistry Chemical Physics 13(24), 2011, pp. 11503.

[26] C Donnelly *et al.*, "Etching of Graphite and Diamond by Thermal Energy Hydrogen Atoms," Diamond & Related Materials 6(50, 1997, pp. 787–790.

[27] JC Arnault *et al.*, "Surface Chemical Modifications and Surface Reactivity of Nanodiamonds Hydrogenated by CVD Plasma," Physical Chemistry Chemical Physics 13(24), 2011, pp. 11481.

[28] L Pan & D Kania, Diamond: Electronic properties and applications, Springer, 1994, p. 47

[29] S Michaelson *et al.*, 'High Resolution Electron Energy Loss Spectroscopy Surface Studies Of Hydrogenated Detonation Nano-Diamond Spray-Deposited Films'. Surface Science 604(15), 2010, pp. 1326-1330.

[30] O Shenderova *el al.* 'Surface Chemistry And Properties Of Ozone-Purified Detonation Nanodiamonds'. The Journal Of Physical Chemistry C 115(20), 2011, pp.9827-9837.

[31] Ozonia TOGC2, Ozonia, 2011, accessed 3rd June, 2013, http://ozonia.com/media/pdf/ozone/TOGC2-screen.pdf

[32] D Williams & I Fleming, Spectroscopic Methods in Organic Chemistry, McGraw-Hill, 1973.

[33] Fourier transform infrared spectrometer, Science world, accessed 16th July, 2013, http://scienceworld.wolfram.com/physics/FourierTransformSpectrometer.html

[34] Interferogram data, European Space Agency, accessed 16th July, 2013, http://herschel.esac.esa.int/Images/2009/Blog_First_SPIRE_SMEC_interferogram.jpg

[35] P Ts'o, "Infrared and Raman Spectroscopy", in Basic Principles in Nucleic Acid Chemistry", 1974, P. 435.

[36] G Binnig *et al.* "Atomic force microscope", Physical Review Letters 56(9), 1986, pp. 930-933.

[37] R Edgington, "Diamond at the brain-machine interface" PhD thesis, UCL, 2012.

[38] D Harris & M Bertolucci, Symmetry and Spectroscopy, Dover Publications, 1989.

[39] Ultra-high Resolution Scanning Electron Microscope SU9"00, Hitachi hitech, 2013, accessed 21st July, 2013, http://www.hitachi-hitec.com/global/em/fe/su9000.html

[40] J Borch *et al,,* Handbook of physical testing of paper, Marcel Dekker, 2002, P.163

[41] J Pawley, "The Development of Field-Emission Scanning Electron Microscopy for Imaging Biological Surfaces", Scanning 19, 1997, pp. 324-336.

[42] Equipments: Field Emission Scanning Electron Microscopy, DSI materials science laboratory, accessed 21st July, 2013, https://fas.dsi.a-star.edu.sg/equipments/fesem.aspx

[43] E Barsoukov & J Macdonald, Impedance Spectroscopy: Theory, Experiment, and Applications, John Wiley & Sons, 2005.

[44] J Macdonald, 'Impedance Spectroscopy'. Annals Of Biomedical Engineering (20), 1992, pp. 1-17.

[45] P Vanýsek, "Introduction to electrochemical impedance", DTIC Report, Order No. AD-A277081, 1994, P. 78.
[46] J Maier, "Ionic conduction in space charge regions", Progress in solid state chemistry (23), 1995, pp. 171-263.
[47] H Tuller, Solid State Ionics, North Holland, 2000, P. 143
[48] V Daniel, Dielectric relaxation, Academic press, London, 1967.
[49] A Neves & M Nazare, Properties, growth and applications of diamond, INSPEC, EMIS Group, Institution of Electrical Engineers, 2001.
[50] C Bandis, & B Pate, 'Photoelectric Emission From Negative-Electron-Affinity Diamond (111) Surfaces: Exciton Breakup Versus Conduction-Band Emission'. Physical Review B 52(16), 1995, pp. 12056-12071.
[51] C Wu & A Kahn. 'Electronic States And Effective Negative Electron Affinity At Cesiated p-GaN Surfaces'. Journal Of Applied Physics 86(6), 1999, pp. 3209-3212.
[52] I Krainsky, & V Asnin, 'Negative Electron Affinity Mechanism For Diamond Surfaces', Applied Physics Letters 72(20), 1998, pp. 2574-2576.
[53] L Diederich *et al.*, 'Electron Affinity And Work Function Of Differently Oriented And Doped Diamond Surfaces Determined By Photoelectron Spectroscopy'. Surface Science 418(1), 1998, pp. 219-239.
[54] M Niigaki *et al.*, 'Electron Diffusion Length And Escape Probabilities For Cesiated And Hydrogenated Polycrystalline Diamond Photocathodes'. Applied Physics Letters 75(22), 1999, pp. 3533-3535.
[55] J Yater *et al*., 'Electronic Properties Of Diamond For High-Power Device Applications'. Solid-State Electronics 42(12), 1998, pp. 2225-2232.

Chapter 5: The Formation of Neuronal Cell Networks with Nanodiamond

5.1. Introduction

One of the most difficult cell types to support, both *in vitro* and *in vivo*, are neurons.[1] This is due to the high degree of specialisation and the largely separate immune system seen behind the blood-brain barrier which sees glial cells indiscriminately invoking the foreign body response,[2] resulting in gliosis (the appearance of glial scarring – an indication of damaged neuronal tissue, which prevents axonal extensions).[3] Currently, biomaterials for *in vitro* and *in vivo* studies of neuronal cells have differing, if converging, figures of merit. *In vitro* is slightly less demanding in that it only requires conditions amenable for protein adsorption in the first instance, then subsequent facilitation of cell attachment. Protein adsorption is strongly affected by the nanoscale topological structure[4] and the surface chemistry it is in contact with.[5] Here, cell survival rate, neurite extension, and fasciculation (arrangement in bundles) are of key importance as the focus of *in vitro* studies is usually on promoting and retaining cell networks. *In vivo* studies, in addition to the aforementioned factors determining a biomaterial's utility, are also concerned with gliosis (where the scarring electrically insulates the device from the neuronal tissue, rendering any implant useless)[6,7] and healing reactions to the implanted biomaterial.[8] This long list of requirements for biocompatibility with neurons restricts the materials that are suitable considerably and therefore research into new biocompatible substrates is required to push the field of neuronal biomaterials from its early stages to greater development.

This work builds on previous studies showing continuous diamond thin films being able to support neural cells for up to 8 days *in vitro* (DIV8,

approximately the point at which a cell culture is defined as being mature)[9] on single crystal, [10] polycrystalline, and nanocrystalline diamond (NCD). [11] Detonation nanodiamond (DND) monolayers have also been previously shown to be a highly biocompatible substrate for the promotion of functional neuronal networks without the use of the traditionally essential pre cell seeding of artificial extracellular matrix (ECM) proteins (e.g. laminin plus ornithine) to provide an adhesive layer.[11] These materials differ most greatly with respect to their chemical functionalisation; DND has a much wider array of surface groups[12] due to the deagglomeration process (see chapter 2), whereas bulk diamond is hydrogen terminated after growth[13] and can then be treated in a number of different ways to obtain much more homogenous surface groups (see chapter 6). Despite the apparent similarities between NCD and DNDs, DNDs layers have been shown to be a far superior substrate to NCD in sustaining functional neuronal cell cultures in artificial ECM-free conditions. This is particularly interesting in terms of surface roughness. Typically both materials display a RMS (route mean squared) thin film roughness less than 10nm, which in turn is lower than the previously described window of 10-70nm for silicon wafers wherein neuronal cell cultures had maximum adhesion[14]. In general the biocompatibility of surfaces is closely related to the response of cells put into contact with a given material, and particularly their adhesion.[15]

Bulk diamond coated biosensors have been previously shown to be chemically inert in such environments[16], As DND is also highly inert in biological media[17,18] suggesting it may be the surface's organic functional groups alongside its nanoscale dimensions (on the order of individual proteins), causing an effect at the subcellular level.[8] This therefore, is the rationale for the variation of nanodiamond (ND) size, ND source, ND surface functional groups,

and ND coating deposition methods that have been explored in this study. These variations were developed into the following parameters: surface roughness, equivalent disk radius (particle size), and seeding density. These parameters were then analysed for their effect on the process of neuronal adhesion, and ability to support the cell culture until DIV8 – with the aim of gaining greater understanding of the ND-neuron interaction and the optimal parameters needed for healthy neuronal cell cultures supported by NDs.

The *in vitro* studies mentioned previously used an artificial pre-seeded layer of ECM. Such use of additional layers would preferably be avoided, as foreign biomolecules used *in vivo* add significant hurdles to a device's overall biocompatibility. Therefore, as an additional avenue of investigation, and taking advantage of the ease of depositing ND on most 3D structures[19] (such as implanted electrodes), micropatterned DND coated tracks with line widths ranging from 5 to 70 μm were deposited on borosilicate glass slides in order to selectively grow neurons in a desired pattern. Although the focus of the work presented here will be *in vitro*, one important goal for this line of research is the improvement of devices capable of being implanted *in vivo* for long periods of time.

5.2. Experimental methods

Note: Neuronal cultures, immunochemistry and confocal imaging were performed by Agnes Thalhammer of the Laboratory for Molecular Pharmacology, UCL

Chemicals: All chemicals were purchased from Sigma (St Louis, MO), Tocris (Tocris Cookson Ltd, Avonmouth, UK) or Invitrogen (Carlsbad, CA), unless stated otherwise. For all experiments, substrates of borosilicate cover slip glass were used (13 mm Ø cover glass, VWR, UK). Samples were first sterilized by an autoclave following ND deposition. Various ND types and deposition methods were then used as follows:

ND types: Monodispersed DNDs (6–10 nm) were purchased from New Metals & Chemicals Corporation, Japan, and high pressure high temperature NDs (HPHT Syndia SYP 0-0.02 GAF, Van Moppes, ca. 20 nm) were provided by Dr Oliver A Williams (Fraunhofer Institute for Applied Solid State Physics, Freiburg, Germany).

Deposition methods: Ultrasonication (US): Samples were submerged in DND hydrocolloid of concentration 0.5 g/l DND in deionised water (≥20MΩ.cm) and subjected to 10 minutes ultrasonication, then dried by a N_2 gun, which has previously been shown to give 10-30nm thick ND layers.[11] Spin coating (SC): ND hydrocolloids (0.5 g/l, DND and HPHT used) were coated on whole substrates and spin coated (2000 rpm for 20 seconds), then dried by N_2 gun. PVA/PDDAC electrostatic coating: NDs (HPHT used) were deposited using electrostatic attraction. This process is described in detail elsewhere.[20] Essentially, NDs of negative zeta potential diluted in polyvinyl alcohol (PVA) electrostatically bind to the positively charged Poly-diallyldimethylammonium chloride polymer (PDDAC). Remaining solvent and polymers were removed by a short (20–40s) hydrogen microwave plasma using a Seki AsteX AX6550 reactor and the

following parameters: microwave power, 600 W; H_2, 200 sccm; pressure, 20 mbar in order to keep the measured temperature to 500˚C (as probed using an optical pyrometer Ircon Modline 3 series 3L). Dip: Samples were coated in PDDAC and dipped in HPHT NDs diluted in water (3 g /l). PDDAC was removed using the same hydrogen plasma as above.

Fixing: Following coating, some samples were treated to a short microwave plasma enhanced chemical vapour deposition (MWPECVD) process that served to fix the NDs on the surface, also resulting in a hydrogenated diamond surface. The parameters used were as above for the PVA/PDDAC removal, except with a 1% methane addition and a run time of 11 minutes.

Fourier transform infrared spectroscopy (FTIR): Untreated DND and HPHT powders were characterised using a Perkin Elmer Spectrum 100 FTIR with an Attenuated Total Internal Reflection (ATR) accessory. Scans were taken with N_2 purging for at least 30 minutes prior to and throughout the measurement and scans were averaged over 30 scans with 4 cm^{-1} resolution. Samples were compressed onto the ATR crystal using the pressure arm to maximise signal intensity. Fixed samples were prepared on silicon wafers and then mechanically removed for measurement. Spectra were subjected to ATR correction (0 contact factor) and baseline corrected (automatic mode) using PerkinElmer software.

Patterning: Patterning of NDs was achieved using a photolithography mask comprised of a filled surface (control) and a grid of constant pitch (200 µm) with graduated line widths of 5, 10, 15, 20, 25, 30, 35, 40, 50, 60 and 70 µm

(Figure 5.8.a) increase from left to right every 4^{th} to 5^{th} grid unit. Briefly, following the HPHT SC ND coating an Al hard mask was deposited and patterned using AZ NLOF 2020 photoresist and AZ351B developer, which simultaneously developed the resist and etched the Al hard mask. A more detailed description is available elsewhere.[21] The exposed NDs were then etched away using an O_2/Ar reactive ion etch and the remaining resist and Al removed, followed by multiple deionized water rinses.

AFM: AFM measurements were carried out using a NanoScope V (7.0) controlled Dimension V Scanning Probe Microscope equipped with an XYZ Hybrid Scanner (Veeco Instruments Inc., Mannheim, Germany), using aluminium-coated silicon AFM probes with a resonant frequency of 190 kHz (Nanoscience Instruments, Inc., Phoenix, USA). The AFM was operated in tapping mode with a VT-103-3K Acoustic / Vibration Isolation System and the VT-102 Vibration Isolation Table at room temperature in air. Statistical analysis and image processing on AFM images was carried out using Gwyddion software. Firstly topographical data was tilt corrected using a first order plane fit subtraction followed by scar removal and median line correction where necessary. Average roughness, R_a, was calculated as the mean value of the z-height. Particle analysis was then performed on all images. Firstly a low band pass 1D FFT filter was applied to all images to filter out high frequency noise (Fourier modulus density of > 0.2 k nm^{-1} removed). Particle masking was performed using a semi-automatic process of either a watershed or threshold detection method followed by manual editing of the particle masks. Falsely marked particles of insufficient size were subsequently removed using a threshold area filter. Particle statistics of seeding density (N) and equivalent disc radius (EDR - the radius of a disc of the same area as the marked grain)

were then calculated. The standard error of the mean EDR was calculated to represent the breadth of each EDR distribution for each layer. Note: AFM Tip convolution effects resulted in consistent overestimates of EDR for all samples by *ca.* 10 nm, as estimated from the x-axis intercept of the z-axis height of grains vs. their EDR.

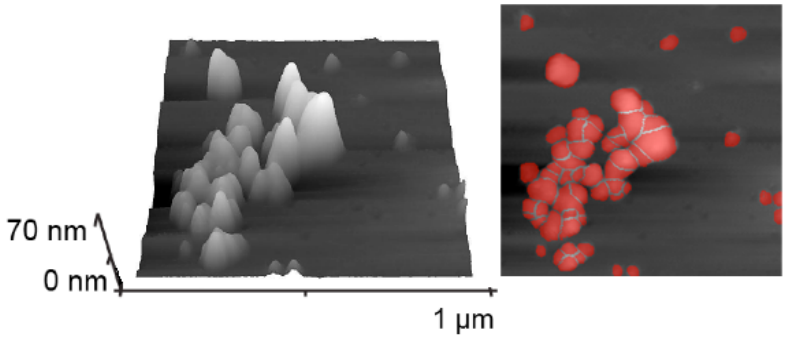

Figure 5.1 Example of ND counting procedure: 3D AFM data (left) is passed through Gwyddion image processing software resulting in particle mask in red (right)

Raman: Raman spectroscopy was carried out with a Renishaw Invia Raman Spectrometer using a laser wavelength of 514.5 nm. Thicker ND coatings were used for characterisation (in order to gain a reasonable signal to noise ratio, i.e greater than 3:1), prepared by evaporating ND hydrocolloid drops on Si wafers in order to be visible to the Raman Spectrometer. In order to prevent damage to the ND layers, laser intensity was set at 10% of the maximum value.

Primary neuronal cultures: Murine hippocampal neurons were obtained at embryonic day 18, essentially as described in earlier work.[22] For cells cultured on ECM proteins (control samples), glass coverslips were incubated overnight (in 100 µL of a 3 µg/ml poly-ornithine (p-ORN) plus 2 µg/ml laminin (LN) solution in phosphate buffered solution; PBS). Cells were seeded in

attachment medium (AM; MEM (medium essential medium) with Earl's salts and glutamine, 10% foetal bovine serum (FBS), 33 mM glucose, 1 mM pyruvate) at 100,000 cells cm^{-2}. After 3–4 h the AM was replaced with maintenance medium (MM; Neurobasal medium, 2% B27 supplement, 2 mM GlutaMAX-I, 100 U/ml penicillin, 0.1 mg/ml streptomycin, 33 mM glucose). Cultures were kept for up to DIV7. All animal work was undertaken under the auspices of the UK Home Office Project and Personal Licenses held by the authors in their designated laboratories.

Immunochemistry and imaging: Samples were fixed with 4% paraformaldehyde/4% sucrose in phosphate buffered saline (PBS; 137 mM NaCl, 2.7 mM KCl, 10 mM Na_2HPO_4, 2 mM KH_2PO_4) for 10 min, then washed with PBS before permeabilisation of cells (0.2% TritonX-100 in PBS for 10 min). After 1–2 h in blocking solution (BS; 5% horse serum in PBS) samples were incubated for 1–2 h with primary antibodies (mouse anti-MAP2, Chemicon, MAB364, 1:500 in BS; rabbit anti-GFAP, DakoCytomation, Z0334, 1:500 in BS). F-actin was stained for 10 min at room temperature (RT) with rhodamine-phalloidin (2 U/ml, Molecular Probes R415) and nuclei for 5 min at RT with Hoechst 33258 (Molecular Probes, 1 mg/ml in PBS). Samples were washed repeatedly and incubated with secondary antibody (Cy2- and Cy5-conjugated goat anti-mouse IgG, Jackson; 1:300 in BS, 115-095-003 and 115-175-003, respectively) for 1 h. Samples were washed with PBS, and stored at 4 ˚C in sterile-filtered PBS until imaging or mounted after wash in Gelmount (Sigma). Confocal microscopy was performed on a Bio-Rad Radiance 2100MP Confocal Microscope with a 20x (Nikon, Plan Flour, 0.75) water-immersion objective using Bio-Rad Lasersharp 2000 software. Alternatively a Leica TCS SPE confocal microscope equipped with a 40x oil-immersion objective (Zeiss, ACS APO, 1.15)

was used in combination with LAS AF software, V1.7.0. Areas for imaging were randomly chosen. Two independent sets of experiments were performed for unpatterned cultures, and one independent set for patterned cultures.

Image processing: Total neurite length (TNL) measurements were performed using a modified version of the NeuriteTracer ImageJ plugin that does not require nuclei markers.[23] TNL was calculated on one set of confocal images of unpatterned DIV2 neuronal cultures. Image processing was performed on the neuronal marker confocal image channel, which had been recorded using the same confocal microscope settings for each image. Processing thresholds were chosen individually for each image to most faithfully trace the neurites. TNL was measured as an average of 4 quadrants of each confocal image in order to reflect the heterogeneity of neuronal cultures, and its associated error is presented as the standard error of the mean. Each quadrant has a surface area of 98,775 μm^2. Pearson product-moment correlation coefficients of TNL with respect to ND coating morphology parameters were calculated using OriginPro 8.6 software, where p-values were calculated using an unpaired Student's 2-tailed t-test (significant for $p<0.05$).

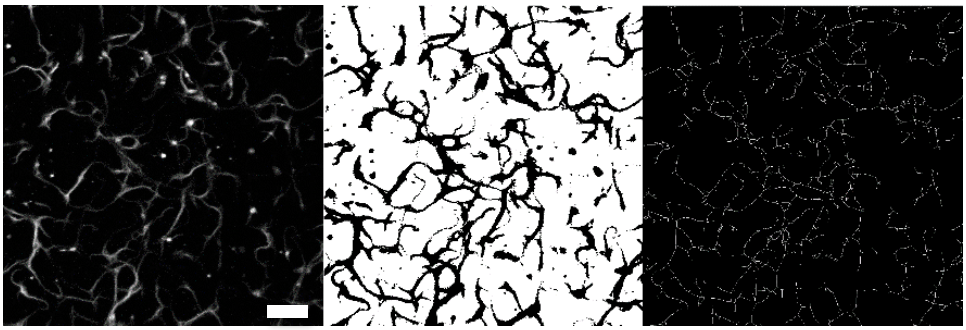

Figure 5.2 Example of TNL calculation procedure: Confocal image (left) was greyscale thresholded to produce a neurite mask (centre), the ImageJ plugin then traces and measures the resultant paths. Scale bar 50µm.

5.3. Results and discussion

5.3.1 Nanodiamond coating and characterisation

Ten types of ND coating were prepared on glass slides, varying ND deposition method, ND source, and with or without the use of a fixing step (to hydrogen terminate the surface whist improving the adhesion of the ND to the substrate) to extensively explore the effect of ND coating type on neuronal adhesion. Monodispersed DNDs were first deposited using US (Figure 5.3a first column) and then SC (Figure 5.3.a second column). SC coated slides showed a sparser, more aggregated coverage, whereas the US coating provided more uniform coverage. Next, ND source was varied in order to investigate the effect of ND particle size and morphology on neuronal adhesion. HPHT NDs were deposited using SC (Figure 5.3.a third column), PVA/PDDAC (Figure 5.3.a fourth column), and dip coating (Figure 5.3.a fifth column).

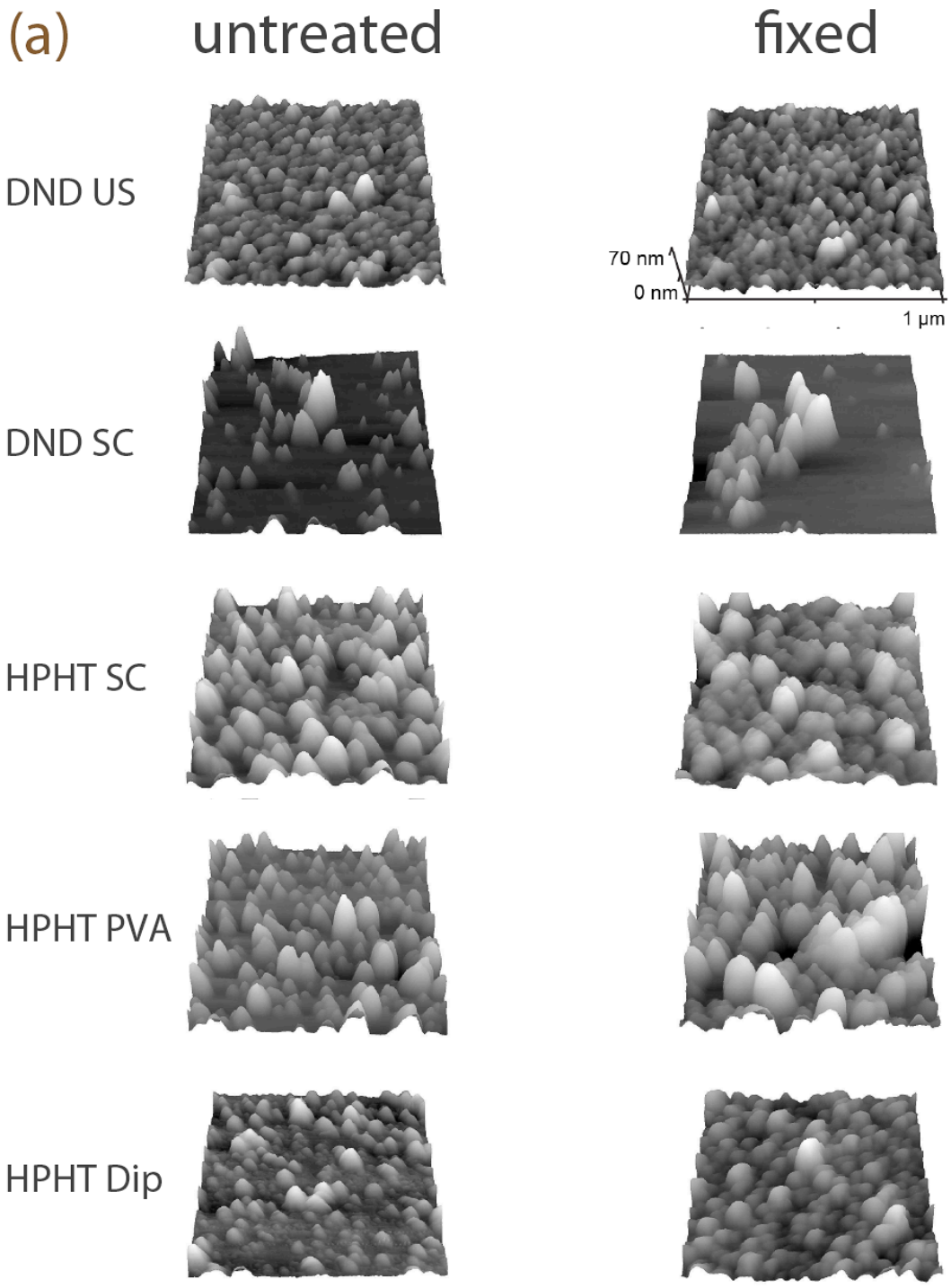
(a)
untreated
fixed
DND US
DND SC
HPHT SC
HPHT PVA
HPHT Dip
70 nm
0 nm
1 µm
(b)
R_a (nm)
EDR (nm)
N (10^10 cm^-2)
DND US
DND USf
DND SC
DND SCf
HPHT SC
HPHT SCf
HPHT PVA
HPHT PVAf
HPHT DIP
HPHT DIPf

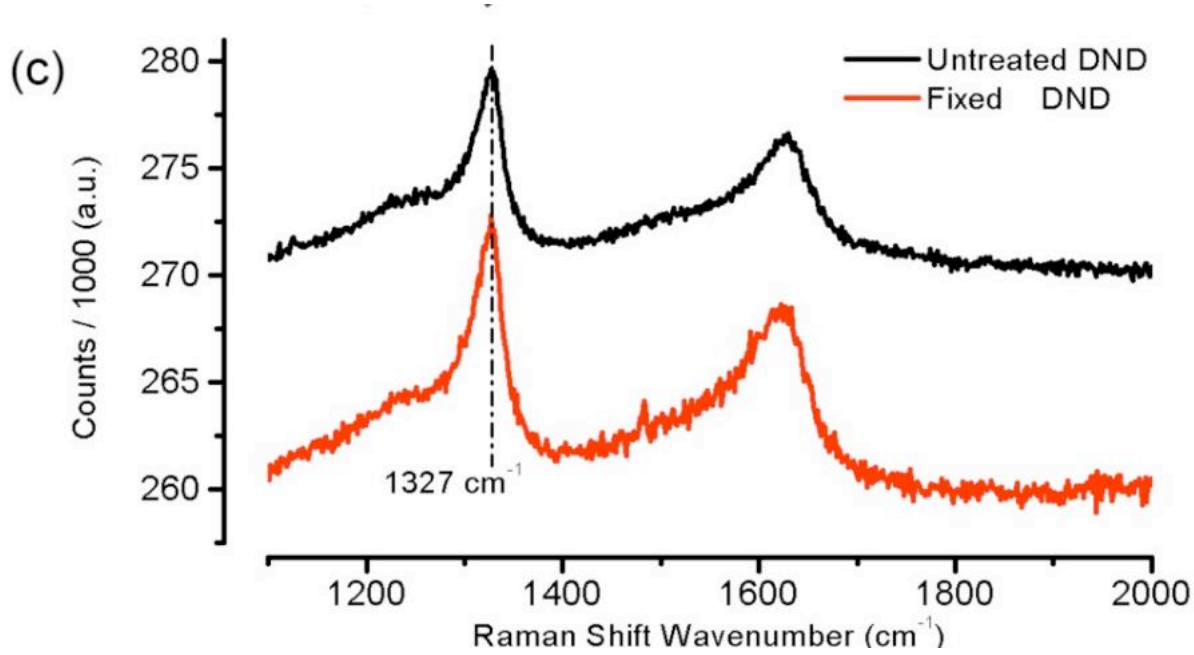

Figure 5.3 (a) 1 µm square AFM images of ND-coated substrates coated using a variety of ND types and deposition methods. Row 1 shows untreated coatings and Row 2 shows MWPECVD fixed coatings, resulting in a hydrogenated surface (see section 5.2 *Deposition methods*). (b) Corresponding average roughness, R_a (nm); equivalent disc radius, EDR (nm); and seeding density, N ($\times 10^{10}$ cm^{-2}) of AFM images. Fixed samples are denoted with an appended 'f'. (c) Raman spectra of untreated and fixated DNDs to show no significant differences in spectra.

The entire sample set was then replicated with an additional MWPECVD fixing step in order to homogenise the surface functional groups to hydrogen termination (see below). No differences in coating were apparent before and after fixing. Scans taken were representative of the whole sample surface and were selected at random over the entire substrate surface.

Following the fixing treatment NDs were seen to have increased adhesion to the glass surface, observed by the prevention of AFM artefacts associated with the imaging of loose powders (i.e. inconsistent alignment of line scans caused by

particles being moved by the AFM tip or erroneous recurring shapes included in the AFM scan caused by particles becoming stuck to the tip) and by the increased resistance to mechanical abrasion. As MWPECVD is very commonly used to grow ND seeded layers into NCD thin films[24] (see chapters 7 & 8), often using methane in an excess of hydrogen (as used in the fixing step), fixing time was kept to a minimum (11 minutes) and at low microwave power in order to maintain as low a growth rate as possible. This resulted in no observable change to the AFM derived data (Figure 5.3.a,b) for the coatings' average roughness (R_a), nor their EDR. The sample 'fixed HPHT PVA' was an exception to this trend, which showed an increase in R_a after fixing. This could be explained by an unusually high heterogeneity of the coating across the sample surface for this deposition method. However, to support this generally positive finding, Raman spectroscopy was performed on the smallest DND particles before and after the fixing step (Figure 5.3.c), as the smallest particles are most sensitive to increasing particle size causing a corresponding change in Raman spectra. The spectra in Figure 5.3.c show no change of the sp^3 and sp^2 associated peaks after fixing, and these peaks are certainly dissimilar from those seen on traditional NCD films.[25] Of highest importance is the lack of Raman shift of the sp^3 peak on both of the spectra remain unchanged at 1327 cm^{-1} - shifted from the value ascribed to pure bulk diamond (1333 cm^{-1}) due to phonon confinement effects regularly seen on ND and in direct correlation to their particle size[26], indicating no change occurred in core particulate size from the fixing treatment.

FTIR was used to characterise the surfaces of both the DND and HPHT particles before and after fixing treatment. The two differing sources of NDs showed quite different chemical groups on their surfaces; DNDs were largely

hydroxyl and carboxylic acid terminated (broad peak around 3400 cm^{-1}, and a narrower peak at 1750 cm^{-1} respectively), whereas HPHT NDs were largely of anhydride terminations (peaks around 1800 cm^{-1}), although the large hydroxyl peak was also present, if slightly different when compared to the DND. Fixing resulted in a reduction in the oxygen containing groups mentioned previously and, importantly, an increase in C-H bonds (2900-3000 cm^{-1}) on both DND and HPHT.

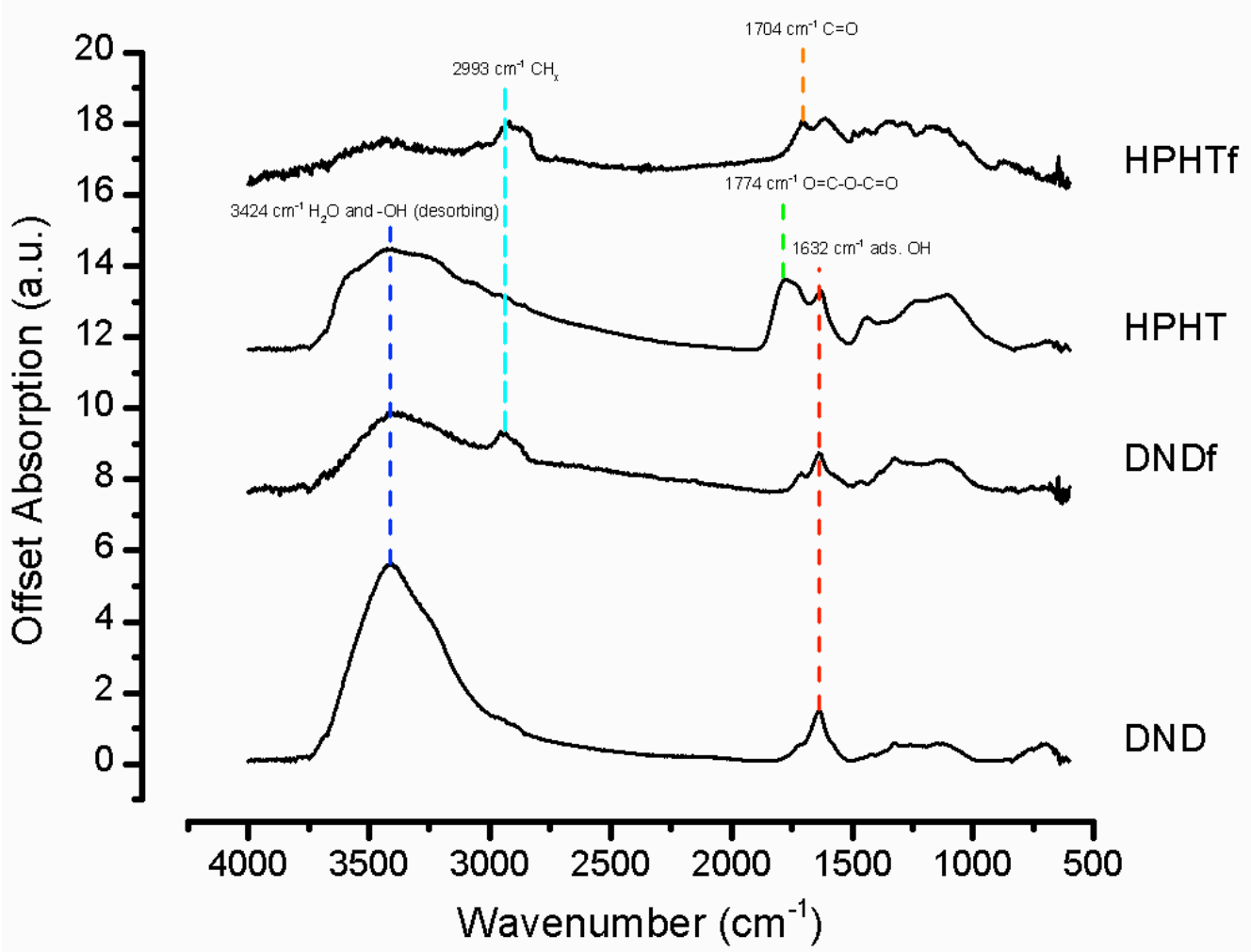

Figure 5.4 FTIR scans of DND and HPHT samples and their corresponding fixed sample spectra, DNDf and HPHTf. DND and HPHT show predominantly oxygen moiety functionalisation prior to MWPECVD fixation, after which increased hydrogenation is measured for both ND types. Intensity magnitude is arbitrary between samples.

5.3.2 Neuron attachment on nanodiamond coatings

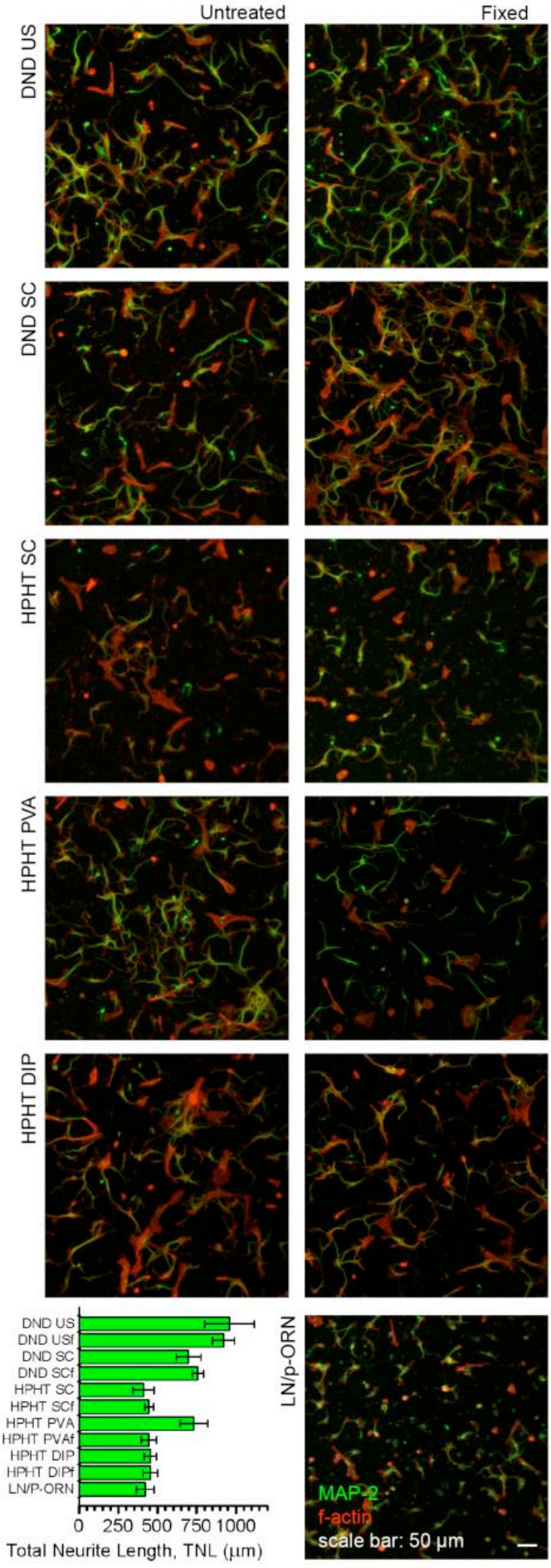

Figure 5.5 Confocal microscopy images of immunostained neuronal cell cultures after DIV2 on ND-coated and LN/p-ORN coated glass substrates. Immunostaining reveals neurons via the dendrite-specific marker MAP2 (shown in green) and cytoskeletal filaments of actin (f-actin) are stained using rhodamine-phalloidin (red), which highlights structures rich in f-actin, such as growth cones at the tips of neurites. Scale bar 50 µm. The quadrant-averaged Total Neurite Length (TNL) of each sample (measured using the NeuriteTracer ImageJ plugin) is shown in the bottom left panel, with error bars corresponding to the standard error of the mean (s.e.m.).

Primary neuronal cell cultures were seeded on the ten different ND-coated samples (Figure 5.3.a), plus a control sample consisting of a glass cover slip coated with traditional ECM proteins (LN/p-ORN). Images obtained at DIV2 using a confocal microscope (Figure 5.5) show the attachment of neurons and outgrowth of neurites on every sample tested. TNL was then measured on each image to quantify the outgrowth observed, as described in section 5.2, with the average displayed in the bottom left panel of Figure 5.5. All samples showed an equal or greater TNL than the control LN/p-ORN sample. Interestingly, there was no discernable difference between the untreated and fixed ND coatings, excluding the HPHT PVA, which showed a reduction of ~40% after fixing (Figure 5.5 4th row). Pearson product-moment correlation coefficients (r) and their significance (s) were calculated to evaluate whether there was any significant linear correlation between TNL and the ND coating parameters in Figure 5.3.b (R_a, EDR, and N), shown in Figure 5.6, with their corresponding r and p values in each panel. The only statistically significant correlation was between EDR and TNL (r=-0.77 p=0.01), suggesting the size of the NDs could have an influence on neuronal adhesion and subsequent neurite outgrowth in this range of particle sizes. Additionally, R_a showed a negative but insignificant correlation coefficient against TNL at this range (r=-0.48 p=0.16), whilst N displayed a positive (which was expected as TNL tends to zero as N tends to zero) yet insignificant correlation (r=0.4 p=0.25).

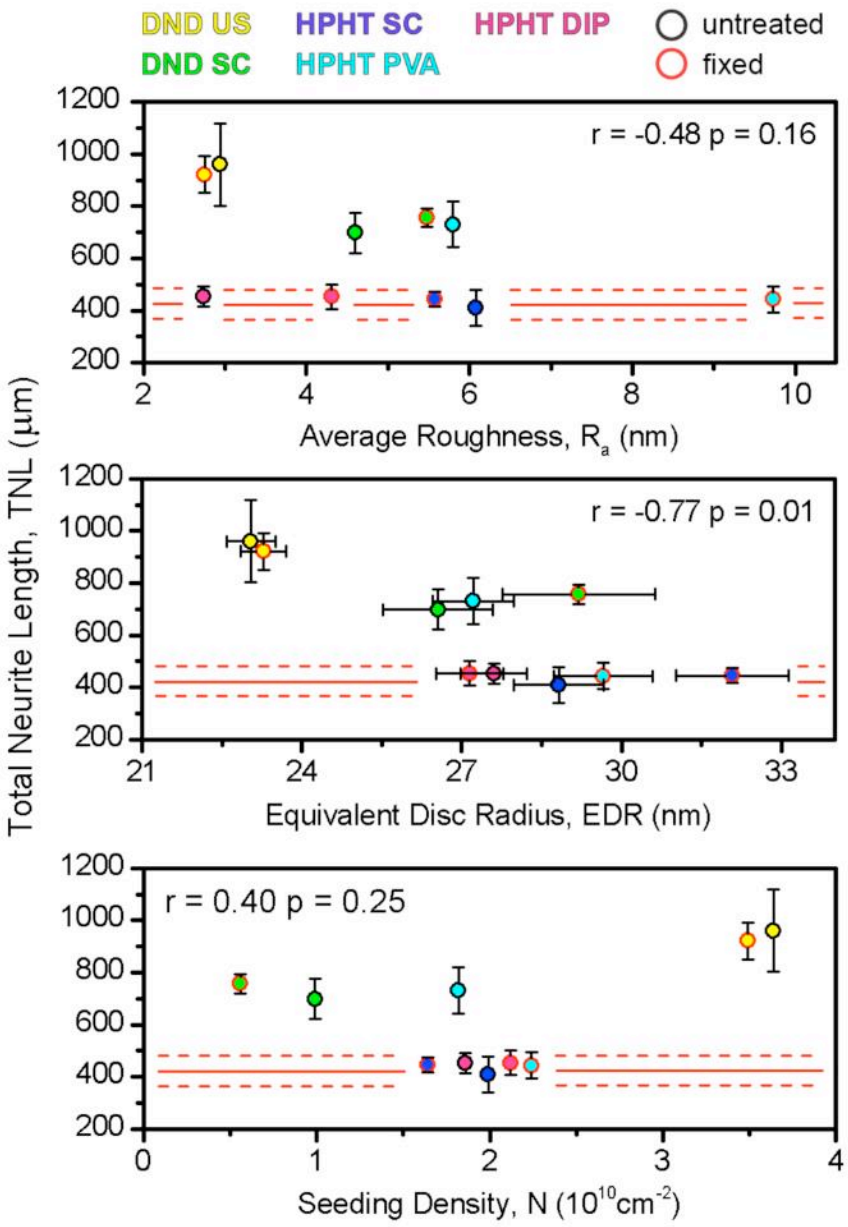

Figure 5.6 Scatter plots showing the relationships between the AFM-determined morphological properties (Figure 5.3.b) of the ND-coated samples against the total neurite extension measured from confocal microscopy images (shown in Figure 5.5). Data point fill colour corresponds to ND coating type, line border colour to untreated/fixed ND. TNL and EDR error bars are both s.e.m.. The solid horizontal line across each panel indicates the LN/p-ORN control sample TNL with the flanking dashed lines indicating ± s.e.m. Inset r and p-values report the Pearson correlation coefficient and 2-tailed significance for each data set.

The neuronal cell cultures were maintained until DIV7, and then imaged using confocal microscopy (Figure 5.7). All substrates imaged showed apparent neuronal networks.

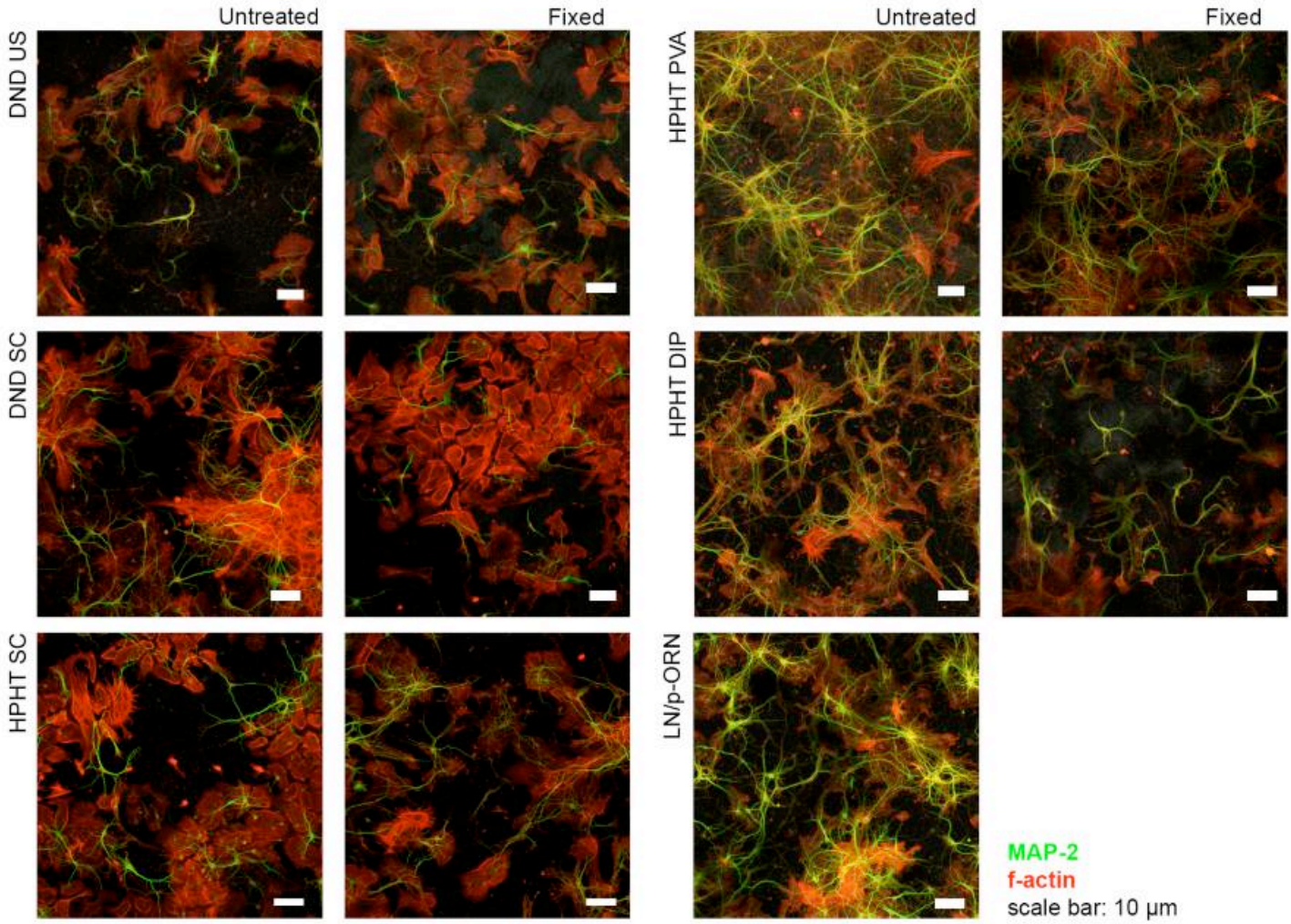

Figure 5.7 Confocal microscopy images of immunostained neuronal cell cultures after DIV7 on ND-coated and LN/p-ORN coated (control sample) glass substrates. Immunostaining reveals neurons via the dendrite-specific marker MAP2 (shown in green) and cytoskeletal filaments of actin (f-actin) are stained for using rhodamine-phalloidin (red), which highlights structures rich in f-actin, such as growth cones at the tips of neurites and glia cells. Scale bar 10 µm.

5.3.3 Mechanism of neuronal adhesion with respect to nanodiamond surface properties

It is relatively common for cellular adhesion to occur on artificial substrates through biomolecule and peptide lamination, however some artificial substrates have been shown to enable some degree of cellular adhesion without the additional lamination. In the simplest case, electrostatic binding of negatively charged cell membranes bind to a positively charged surface – such as polylysine.[27] As NDs also have polar surfaces, it would be reasonable to suggest a similar effect would be seen on such layers. However, when cells adhere through electrostatic binding, they are unable to secrete their own ECM proteins and will die through apoptosis within 24-48 hours.[28] Instead, the surface terminations could be mimicking the functional properties of ECM proteins, directly interacting with cells and initiating cell adhesion. This could be likely when their size, shape, surface charge and organic based functional groups are considered which could lead them to mimic attachment peptide motifs in ECM proteins, such as the RGD motif,[29] as they resemble the characteristics seen in globular proteins. Moreover, other nanoparticles such as gold and nickel-palladium have been previously shown to mimic other biological processes.[30] However, the observation that neuronal adhesion was apparent on both fixed and untreated surfaces (hydrogen and oxygen dominated surfaces respectively) refutes such a direct cell-ND interaction. An alternative explanation is therefore put forward – that the NDs are providing an optimal, or near optimal substrate for the adsorption of ECM proteins found in the cell AMs (vitronectin and fibronectin found in FBS, see section 5.2: Primary neuronal cultures) and subsequently produced by the cells themselves.[31] This is due to the NDs' previously reported high affinity for protein adsorption[32] and their small radii of curvature, which aids the functionally intact adsorption of

fragile globular proteins such as vitronectin and fibronectin.[33] It should be noted that during the course of these experiments it was found that cells fail to attach to NDs in the absence of serum – FBS contains non-adhesive growth factors essential for cell attachment, in addition to the adhesive proteins vitronectin and fibronectin. Furthermore, the slight fasciculation of neurons presented in Figure 5.8.c.v (see below) could suggest that at DIV7 the neurons are attaching to their own endogenous adhesion protein matrix. Fasciculation has been observed on ECM coated substrates previously and could also be ascribed to varying culture conditions.[11]

The correlation coefficient analysis of TNL against EDR (which is inversely proportional to radius of curvature) presented in Figure 5.6 showed significant negative correlation, compared to the more commonly studied biomaterial parameter – average roughness, which was only weakly correlated. Hence, this negative correlation is in agreement with the hypothesis that cell adhesion is improved through increased functional protein adsorption with decreasing ND particle size, creating a more biocompatible surface as shown by enhanced neurite extension.

5.3.4 Patterned nanodiamond neuronal growth

ND coatings were patterned as described in section 5.2: Patterning, using the mask pictured in Figure 5.8a. Note HPHT SC coatings were used for patterning due to the ease of incorporating spin coating into the photolithography process and the resultant high seed density to aid the identification of features with subsequent AFM imaging. The subsequent

etching process provided efficient removal of NDs, resulting in highly contrasted surfaces (Figure 5.8b showing an intersection of two 15 µm thick tracks). Neuronal cell cultures were created on the patterned ND as described in the Experimental methods. Confocal microscopy was performed at DIV2 and showed cell attachment on tracks as narrow as 10 µm (Figure 5.9.i) sitting generally on the intersection of two tracks. For larger line widths, the neurons were found to be tightly conformal along the tracks, with no particular preference displayed for individual tracks or their intersections (Figure 5.9.ii/iii. Figure 5.9.iv shows an unpatterned area taken in the centre of the mask (see Figure 5.8a), the neurons there take a more circular morphology and there is a reduced amount of neurite branching present, in a similar manner to the cell morphology seen on HPHT SC substrates in Figure 5.5. After imaging at DIV2, cell cultures were re-incubated until DIV7 (Figure 5.10.v/vi) where lots of connections between neurons are apparent. Furthermore, in the specific case of Figure 5.10.v, neurons and their neurites have closely conformed to the ND grid pattern and show no sign of the fasciculation observed in Figure 5.10.vi.

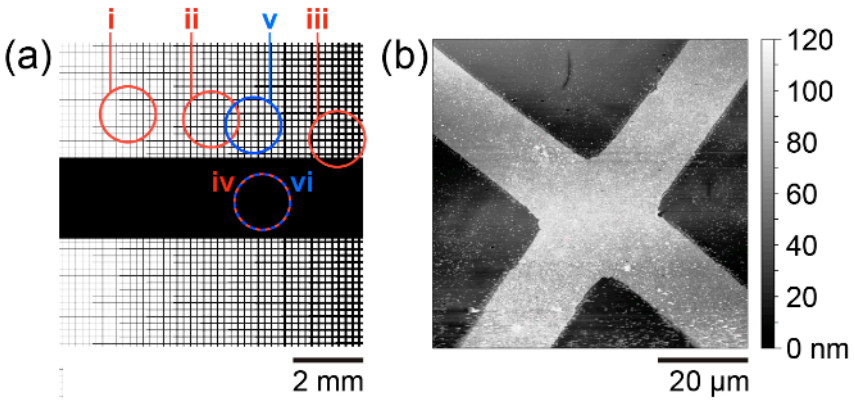

Figure 5.8 (a) Diagram of photolithography mask used for ND patterning (9x9 mm). Black areas are ND filled. The central unpatterned region is used as an ND control surface for each sample. The indicated circular regions correspond to the confocal images in Figure 5.9 and Figure 5.10. (b) 70 µm square AFM image of patterned HPHT SC tracks on glass substrate. Width: 15 µm. Height: *ca.* 35 nm. Note: Roman numerals used to signify position of confocal images used in figures 5.9 and 5.10

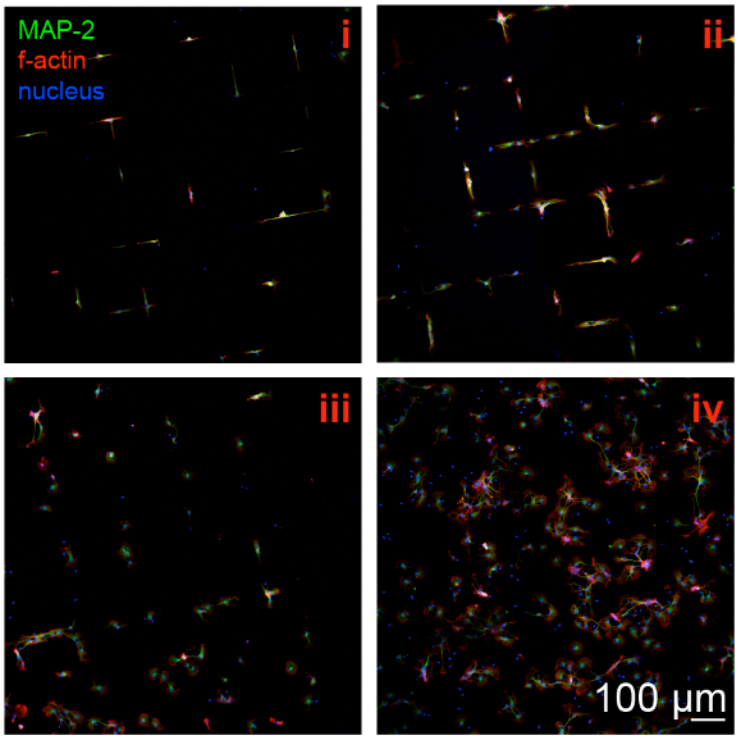

Figure 5.9 Confocal microscopy images of immunostained neuronal cultures at DIV 2 on untreated HPHT SC patterned glass substrates. Cells have MAP2 and f-actin staining as in Figure 5.5. Scale bar 100 µm. Roman numerals correspond to regions on Figure 5.8(a) where confocal images were taken.

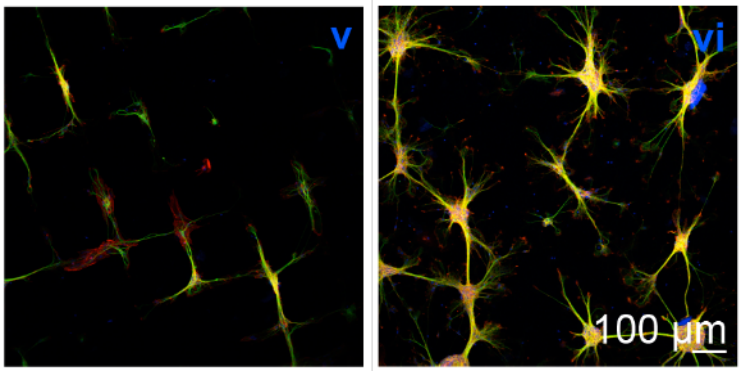

Figure 5.10 Confocal microscopy images of immunostained neuronal cultures at DIV 7 on untreated HPHT SC patterned glass substrates. Cells have MAP2 and f-actin staining as in Figure 5.5. Scale bar 100 µm. Roman numerals correspond to regions on Figure 5.8(a) where confocal images were taken.

5.4. Concluding remarks

The primary aim of this work was to investigate the effect of variation of ND parameters (size, source, surface functional groups, and deposition method) on the adhesion and neurite extension of embryonic murine hippocampal neurons. This was done in order to better understand the adhesion mechanisms that had been observed in earlier studies, and to elucidate whether differing combinations of the aforementioned ND parameters provided preferable surfaces for neuronal adhesion. A wide range of ND coatings were successfully prepared with differing size, origin, deposition method and surface chemistry. These coatings were analysed using AFM and this data was parameterised into average roughness, equivalent disk radius and seeding density. The surface chemistry was also analysed using FTIR, and showed fixing resulted in a reduction of oxygen containing groups and an increase in C-H bonds. These coatings were investigated for their ability to support neuronal adhesion by a combination of confocal microscopy with neurite tracing software, and indeed it was found all the ND coatings were successful in supporting the adhesion of murine hippocampal neurons, with only small variation in total neurite extension. No ND surface was found to prevent ND attachment, indicating a wide variety of NDs are suitable for this use. Of great interest, was the observation that predominantly oxygenated (untreated) and hydrogenated (fixed) surfaces provided similarly hospitable environments for neurons, with no apparent difference in the viability of cell cultures. The possible mechanisms for neuronal adhesion were discussed and parametric coefficient correlation analysis was performed and a significant correlation was found between total neurite extension and ND size (or curvature) where a smaller ND (with higher curvature) promoted a greater degree of neurite extension, with a maximum

recorded value of ~900 μm in the 400 μm^2 confocal images used. Functional adsorption of proteins was suggested as the most likely mechanism for the excellent cell adhesion properties of ND coatings. Further work into this attachment mechanism remains a subject of study for future work in this area. Planned variables would include the influence of other surface terminations, where the variation in zeta potential would likely have an interesting influence on both the inter-particulate binding forces and the hydrophilicity/hydrophobicity of the ND surface. Variation of the cell types seeded upon the ND layers would also provide useful information as to whether cells with differing adhesion and regrowth strategies (e.g. with and without the use of pioneer neurites), and hence whether the technique outlined in this chapter can be rolled out across a wide range of cell types.

Secondly, ND mediated micropatterning of the neuron cultures was attempted through the combined use of photolithography and reactive ion etching. This enabled a graduated grid pattern of NDs to be created, which in turn allowed direct patterning of neuronal adhesion on the ND grid. This was confirmed using confocal microscopy analysis of the immunostained cell cultures. As a result, this work shows ND patterning to be a highly promising platform for the *in vitro* study of ordered neuronal networks. Furthermore, such coatings could provide a possible future coating for *in vivo* chronic implants, for example as an artificial retinal or cochlear microelectrode array. Such devices would certainly benefit from the aforementioned further study into the attachments mechanisms, as the longer term stability of the cell attachment would prove a critical design consideration. Evaluation of this stability under the full range of conditions seen in biological media (i.e. temperature, pH, and pressure) would also be a prerequisite for successful device design.

[1] M Sailer *et al.*, "High-Throughput Cellular Screening of Engineered ECM Based on Combinatorial Polyelectrolyte Multilayer Films," Biomaterials 33(24), 2012, pp. 5841–5847.
[2] M Ward *et al.*, "Toward a Comparison of Microelectrodes for Acute and Chronic Recordings," Brain Research 1282, 2009, pp. 183-200.
[3] C Stichel & H Werner, "The CNS lesion scar: new vistas on an old regeneration barrier," cell and tissue research 294(1), 1998, pp. 1–9.
[4] Y Fan *et al.*, "Adhesion of Neural Cells on Silicon Wafer with Nano-Topographic Surface," Applied Surface Science 187(3), 2002, pp. 313–318.
[5] T collier & J Anderson, "protein and surface effects on monocyte and macrophage adhesion, maturation, and survival," Journal of biomedical materials research 60(3), 2002, pp. 487–496.
[6] W J Streit, "Microglial Response to Brain Injury: a Brief Synopsis," Toxicologic Pathology 28(1), 2000, pp. 28–30.
[7] K Cheung, "Implantable Microscale Neural Interfaces," Biomedical Microdevices 9(6), 2007, pp. 923–938.
[8] H. A. Currie *et al.*, ''Natural and artificial hybrid biomaterials.'' In: Hybrid Materials—Synthesis, Char- acterisation and Applications, edited by G. KICKELBICK (Wiley-VCH, Weinheim, 2007), Chapter 7, pp. 255–300
[9] T Yabe, "nfkappa B Activation Is Required for the Neuroprotective Effects of Pigment Epithelium-Derived Factor (PEDF) on Cerebellar Granule Neurons," Journal of Biological Chemistry 276(46), 2001, pp. 43313–43319.
[10] C Specht *et al.*, "Ordered Growth of Neurons on Diamond," Biomaterials 25(18), 2004, pp. 4073–4078.
[11] A Thalhammer *et al.*, "The Use of Nanodiamond Monolayer Coatings to Promote the Formation of Functional Neuronal Networks," Biomaterials 31(8), 2009, pp. 1–8.
[12] O Williams *et al.*, "Size-Dependent Reactivity of Diamond Nanoparticles," ACS Nano 4(8), 2010, pp. 4824–4830.
[13] A Gaisinskaya *et al.*, "In-Situ Oxidation and Annealing of Hydrogenated Diamond (100) Surfaces Studied by High Resolution Electron Energy Loss Spectroscopy," Diamond & Related Materials, 2010, pp. 1–5.
[14] Y Fan *et al.*, "Adhesion of Neural Cells on Silicon Wafer with Nano-Topographic Surface." Applied surface science 187(3), 2002, pp. 313-318.
[15] JP Kaiser & A Bruinink, "Investigating cell-material interactions by monitoring and analysing cell migration", Journal of materials science: Materials in medicine 15, 2004, pp. 429-435
[16] S Mitura, A. Mitura, P. Niedzielski, and P. Couvrat, in: Nanotechnology in Materials Science, edited by S. Mitura, Pergamon Press, Elsevier, 2000.
[17] A Schrand *et al.*, "Are Diamond Nanoparticles Cytotoxic?," The Journal of Physical Chemistry B 111(1), 2007, pp. 2–7.
[18] A Schrand *et al.*, "Differential Biocompatibility of Carbon Nanotubes and Nanodiamonds," Diamond & Related Materials 16(12), 2007, pp. 2118–2123.
[19] H Girard *et al.*, "Electrostatic Grafting of Diamond Nanoparticles Towards 3D Diamond Nanostructures," Diamond and Related Materials 23, 2012, pp. 83-87.
[20] H Girard *et al.*, "Electrostatic Grafting of Diamond Nanoparticles: a Versatile Route to Nanocrystalline Diamond Thin Films," ACS Applied Materials & Interfaces 1(12), 2009, pp. 2738–2746.
[21] P Bergonzo *et al.*, "3D shaped mechanically flexible diamond microelectrode arrays for eye implant applications: the MEDINAS project", IRBM 32, 2011, pp. 91–94.
[22] C Specht *et al.*, "Subcellular Localisation of Recombinant A- and Γ-Synuclein," Molecular and Cellular Neuroscience 28(2), 2005, pp. 326–334.

[23] M Pool *et al.*, "neuritetracer: a Novel imagej Plugin for Automated Quantification of Neurite Outgrowth," Journal of Neuroscience Methods 168(1), 2008, pp. 134–139.
[24] O Williams, "Nanocrystalline Diamond," Diamond & Related Materials 20, 2011, pp. 621–640.
[25] O Williams *et al.*, "High Young'S Modulus in Ultra Thin Nanocrystalline Diamond," Chemical Physics Letters 495(1), 2010, pp. 84–89.
[26] K Sun *et al.*, "Raman Spectroscopy of Single Nanodiamond: Phonon-Confinement Effects," Applied Physics Letters 92(15), 2008, 153115.
[27] G Rainaldi *et al.*, "Positively Charged Polymer Polylysine-Induced Cell Adhesion Molecule Redistribution in K562 Cells," Journal of Materials Science-Materials in Medicine 9(12), 1998, pp. 755–760.
[28] L Bacakova *et al.*, "Cell Adhesion on Artificial Materials for Tissue Engineering," Physiological Research 53, 2004, pp. S35–S45.
[29] S Rao, "Adhesion Molecule-Modified Biomaterials for Neural Tissue Engineering," Frontiers in Neuroengineering 2, 2009.
[30] N Kotov, "Inorganic Nanoparticles as Protein Mimics," Science 330(6001), 2010, pp. 188–189.
[31] A García, "Get a grip: integrins in cell–biomaterial interactions." Biomaterials 26(36), 2005, pp. 7525-7529.
[32] S Wasdo *et al.*, "Differential binding of serum proteins to nanoparticles." International Journal of Nanotechnology 5(1), 2008, pp. 92-115.
[33] P Roach *et al.*, "Surface Tailoring for Controlled Protein Adsorption: Effect of Topography at the Nanometer Scale and Chemistry," Journal of the American Chemical Society 128(12), 2006, pp. 3939–3945.

Chapter 6: Controlling the Electrical Properties of Nanodiamonds through Surface Functionalisation

6.1. Introduction

Diamond provides a usefully manipulatable material from which to derive a wide range of functional surfaces. These include, but are not limited to hydrogen, hydroxide, oxygen, esters, carboxyl, amines, silane, and halogens.[1] The ultra-low dimensions of the nanodiamond (ND) result in the constituent atoms being largely at the surface, therefore functionalisation of the surface has a large effect on the characteristics of single and aggregated ND. The electrical properties of ND layers in particular form a basic design variable that is currently not well understood. Such understanding is vital to enable the coming plethora of ND incorporated devices likely on the horizon. The range of potential and current uses of functionalised nanodiamonds stretches from most conceivable materials applications: electrochemical, biological, mechanical, and importantly for this chapter, electrical.

From the perspective of electrochemistry, ND based electrodes have been thoroughly investigated. A study from 2007 showed the ND powder electrode is a very stable platform in KCl electrolytes over a wide potential range (-1.2/+2.0 V) where the reaction is quasi reversible when used in a 0.1 M KCl solution with the ferricyanide-ferrocyanide redox couple.[2] Sensors based on ND layers have been proposed; such layers gain two highly conductive pathways upon exposure to ammonia gas (where only one conduction path, several orders of magnitude was seen before exposure), these conduction paths were ascribed to the grain interior and grain boundary processes[3] – opening the possibility of ND based reactive gas sensors. In a similar vein, ion-sensitive field-effect transistor (ISFET) devices have been demonstrated on (as received) ND coated

commercially available silicon ISFETs. This improved a device for the detection of small changes in pH (55 mV/pH, very close to the Nernst limit).[4] Following the previous example, off the shelf silicon cantilevers have been modified with ND layers to produce sensitivity of the resonant frequency to dinitrotoluene (a chemical analogue of trinitrotoluene, commonly referred to as TNT).[5]

NDs functionalised via the Fenton process (leaving the surface largely OH terminated) have been shown to enable the support and transport of noble metal nanoparticles in order to act as a quencher of free radicals such as reactive oxygen species inside human cells.[6] The fluorescence and long spin coherence times of the nitrogen vacancy centre seen in diamond, combined with the minimal disruption to biological systems upon ND incorporation, extends the possibility of real time detection and monitoring of a wide range previously inaccessible processes – as was demonstrated in human HeLa cells recently.[7] As extensively discussed in Chapter 5, NDs small radii of curvature can be used as an interface between solid state objects (such as glass coverslips or microelectrode arrays) and murine hippocampal neurons.[8] NDs functionalised to give positive zeta potentials (hydrogen and hydroxyl in this case) were found to exhibit a significant improvement over traditional methods of adsorption of mycotoxins (toxic secondary metabolites produced by organisms from the fungi kingdom) in solution.[9] Later work from the same group showed ozone treated ND to be an efficient absorber of propidium iodide dye (used due it being a well characterised dye that is commonly used in microbiology to detect dead cells).[10] ND has also been shown to improve the mechanical characteristics of biomaterials such as cortical bone scaffold, where a 10%wt addition of octadecylamine functionalised ND (ND-ODA) resulted in an increase in Young's modulus of 200% and hardness by 800%.[11] ND-ODA, in

addition to the mechanical advantages, also provides bright fluorescence and a platform for further options for drug loading and delivery through subsequent chemical modification. Shenderova *et al.* also reported on the fluorescence generated by ND composites. Here, they found ND-polymer (ND-Polydimethylsiloxane) composites fluoresced under a flux of MeV protons, suggesting such a material could function as proton dosimeters for spacecraft.[12]

ND as a drug delivery system has received a lot of research interest recently, due in part to the wide range of possible chemical combinations to choose from, the prospect of drastically reducing the quantity of drug administered (reducing side effects and costs), the ability to target specific areas or tissues of the body (further reducing side effects), and the ease in scalability of such a vector. Examples of ND mediated drug delivery include ND-Dexamethasone (an anti-inflamatory and immunosuppressant steroid) [13], ND-doxorubicin (an anthracycline antibiotic, used in chemotherapy) [14], and ND-polyethylenimine-siRNA (small interfering ribonucleic acid) - siRNA is not a drug but provides therapeutic benefits such as the enhancing of GFP (green fluorescence protein) plasmid transfection efficacy.[15]

Nickel-ND composites have been deposited on aluminium alloy (A319), resulting in increased hardness and resistance to wear.[16] This leads directly to the possibility of improving the durability of lightweight engine components. Other mechanical uses of ND include engine lubrication – here, ND dispersed in lubricant (oil or water based, depending on the surface functionalisation)

allows for ~5% reduction in fuel consumption, although the mechanism for this improvement is still unclear.[17]

Zhirnov *et al*. studied electron field emission from nanodiamonds extensively in 2004. Here, as received and hydrogen plasma treated particles were contrasted, resulting in lower emission thresholds after hydrogen treatment.[18] Hydrogen functionalised nanodiamonds are also being investigated as a material for applications in molecular nano-electronics. It was found hydrogen terminated ND has a high concentration of free radicals (up to 10^{21} spin/g) due to structural defects (dangling C-C bonds), perhaps indicating a viable electrode material.[19] Recently a patent was granted indicating the successful production of conductive nanodiamond by a dynamic synthesis approach. Within this patent the author suggested conductive ND could find use as storage materials for batteries or as electrode material in double-layer capacitors.[20] For the uptake of functionalised ND applications to accelerate, reliable and low cost functionalisation routes are needed, along with the ability to significantly scale up the production of such particles.

Whilst the current and future range of applications of ND is vast, only a small amount of work has focused on the study of their electrical properties. This work aims to improve understanding of the electrical properties of ND with differing surface functional groups. In order to change the NDs surface, suitable equipment for ozone treatments was designed and custom built by the author, whilst an existing system was repurposed as a hydrogen anneal chamber. Treatment protocols were then developed (described in section 5.2) in order to reliably functionalise the ND layers. In order to assess the efficacy of

the functionalisation Fourier transform infrared spectroscopy (FTIR) was utilised during the protocol development period and throughout the experimental procedure described in this chapter. FTIR is a useful technique for the study of surface terminations on ND as it is able to detect species of low atomic weight, particularly as hydrogen is an important functional group within this series of experiments, and in the wider field of ND applications.

Due to the novelty involved in electrical characterisation of ND, sample preparation and measurement protocols were also developed to the point described in section 5.2. Impedance spectroscopy (IS) was then performed on ND layers in both sandwich and planar configurations at the maximum range of temperatures possible in the equipment used. This was done in order to study thermal stability and the progression of temperature dependent characteristics. Please note the late addition of a more powerful power supply unit enabled the temperature range to be extended to 530°C (from a previous maximum of 475°C). Additional experiments were performed in vacuum in order to provide a comparison against the effect of oxygen on the decomposition of the NDs constituent components, and to prevent adsorbates from the air providing the electron sink needed for surface conductivity (see section 2.2.4).

Oxygen and hydrogen functionalisations were chosen due to the previously reported large observed changes in surface conductivity,[21,22] electron affinity[23], hydrophobicity/hydrophilicity,[24] and thermal stability[25,26] seen in various forms of diamond.

IS was employed for this study due to its previously demonstrated suitability of electrically investigating nano- and microcrystalline materials - including diamond.[27,28] IS is of particular use in this instance, as its use in the deconvolution of the conduction paths seen in complex arrangements of diamond and carbon materials which has been previously well established.[29,30] Data has been presented as Bode, Cole-Cole and Arrhenius plots.

Control of the diamond surface sp^2/sp^3 ratio has been widely investigated, due to the initially high fraction of sp^2 material in untreated material, and the superior properties seen after sp^2 removal. Routes to achieve this purification are generally mechanical, chemical or thermal. Mechanical purification through wet milling with zirconia beads was the first method reported and this enabled the deagglomeration of ND into single (monodisperse) particles.[34] Chemical routes to ND purification include ozone, [31] acid treatment,[17] and hydrogenation.[22] Thermally induced purification has been achieved in ambient conditions at temperatures between 350-450°C,[32] this range is of particular interest as this lies within the range of impedance spectroscopy measurements presented below.

6.2. Experimental methods

Sample preparation: Monodispersed DND colloid was bought from NanoAmando (New Metals & Chemicals Corporation, Japan) and used throughout this experiment series. The NanoAmando colloid (hereafter referred to as DND) has been subjected to a deagglomeration process utilising wet milling with zirconia[33,34] (see section 2.3.1). In order to perform IS through (rather than across) the ND layer a sandwich arrangement was produced by coating one side polished (at the ND-silicon interface), highly conductive silicon (arsenic doped, ρ = 0.001 Ω.cm) seeded with ND as described in section 5.2. Note this results in a ~10 nm thick layer across the surface.[35] The plate separation caused by bowing of the silicon plate is estimated to be less than 2μm (using a Young's modulus value of 170 GPa for (100) silicon bending in the (100) plane and an upper estimate of 100 N force exerted by the probe).[36] The effect of particle seeding uniformity was also considered. Here, AFM data (Figure 6.2) showed the point of maximal variation to be 30 nm, or 3-6 ND layers. Assuming no particle repositioning after arranging the coated silicon wafers into a sandwich arrangement, the ND thickness variation would introduce a plate separation of 60 nm. In reality there may be some repositioning and this value would drop, however an accurate estimation of this drop has not been performed. This gap suggests none of the *ca.* 5nm NDs are in contact with both the top and bottom plates, therefore this investigation is into the combined ND layer response.

Preliminary experiments using silicon plates in the sandwich configuration, without the addition of nanodiamonds showed the uncoated plates to have an

extracted R and C value of 420 Ω and 9.8×10^{-11} F in air and 160 Ω and 1.1×10^{-10} F in vacuum.

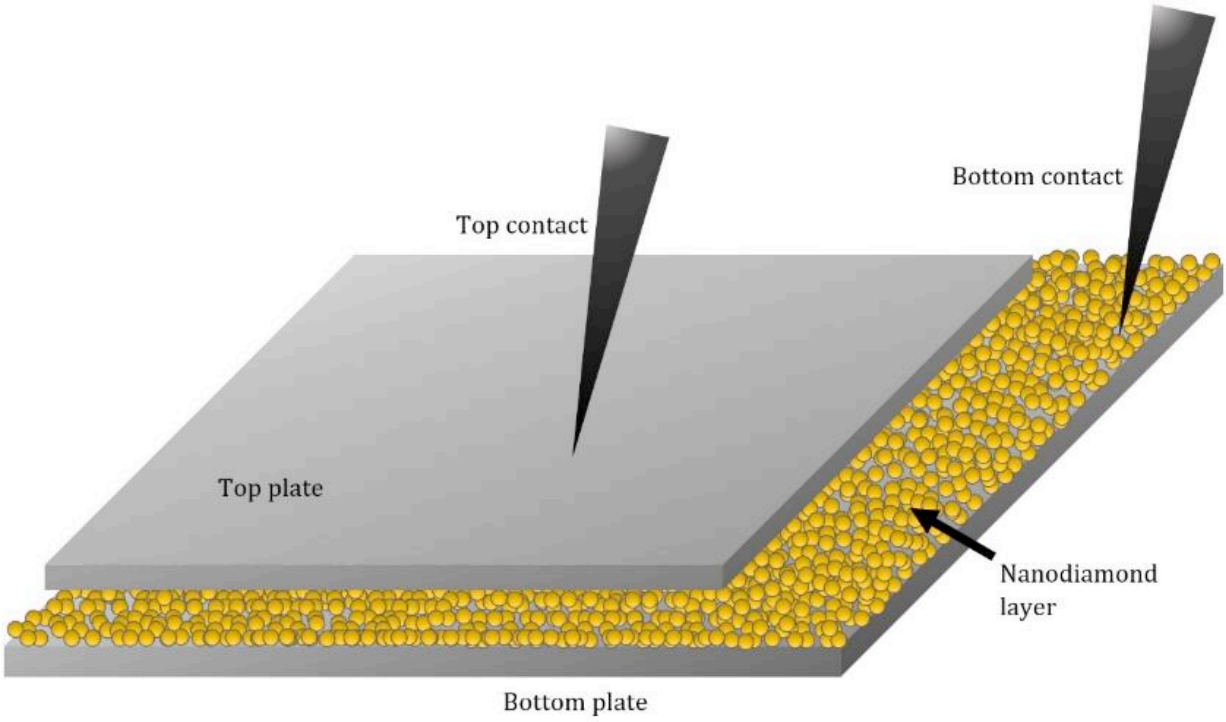

Figure 6.1 Illustration describing the ND sandwich arrangement for IS readings. Top and bottom plates were made from highly doped silicon coated with DND, top and bottom contacts are probes from IS kit.

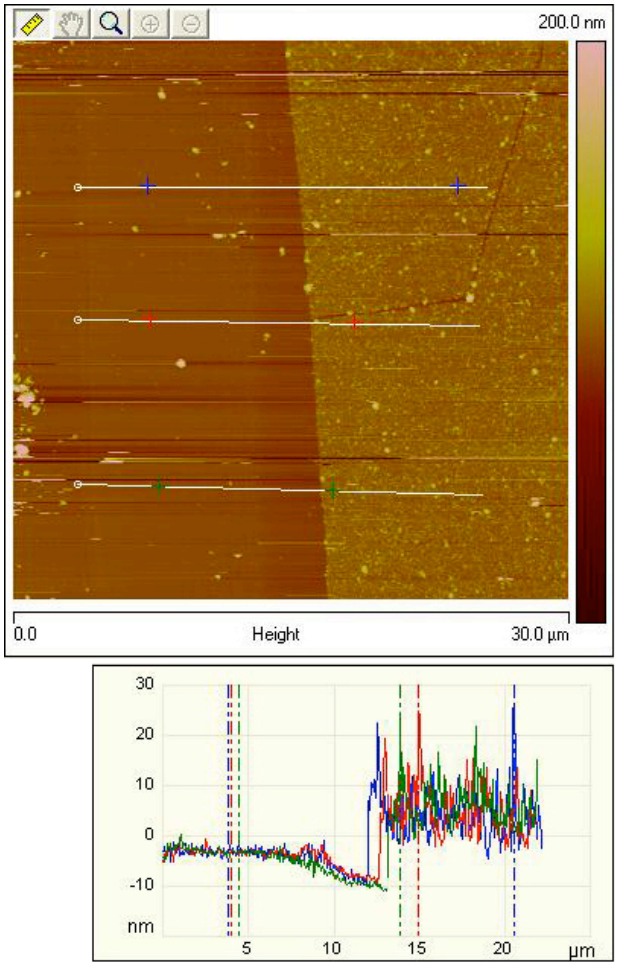

Figure 6.2 Top: AFM scratched area of ND ultrasonically coated on silicon. Bottom: line scans of scratched areas showing a coverage ~10 nm thick. Taken from [37]

For thicker coatings of ND, the method known as drop coating was employed. Here, a silicon substrate was placed on a hot plate set to ~100˚C and a couple of drops (enough to form a droplet on the substrate's surface held by surface tension) of 0.5g/l ND solution in water was dropped from a micropipette onto the hot surface where the water was allowed to evaporate. This process is repeated until l50µl of solution has been consumed (Figure 6.3), resulting in ND layers several micrometres thick, although this figure varies widely (on the order of hundreds of micrometers) due to the random nature of the water evaporation. This was a large factor behind the decision not to

calculate resistivity of each layer, as the variation in sample thickness (both within the sample, and between samples) made such deductions somewhat meaningless. All sample preparation procedures were performed in a class 100 cleanroom to prevent airborne contamination. As with the thin ND layers, there was expected to be a maximal silicon bowing of 2 μm. Again it is assumed that no individual ND particle spans both silicon plates.

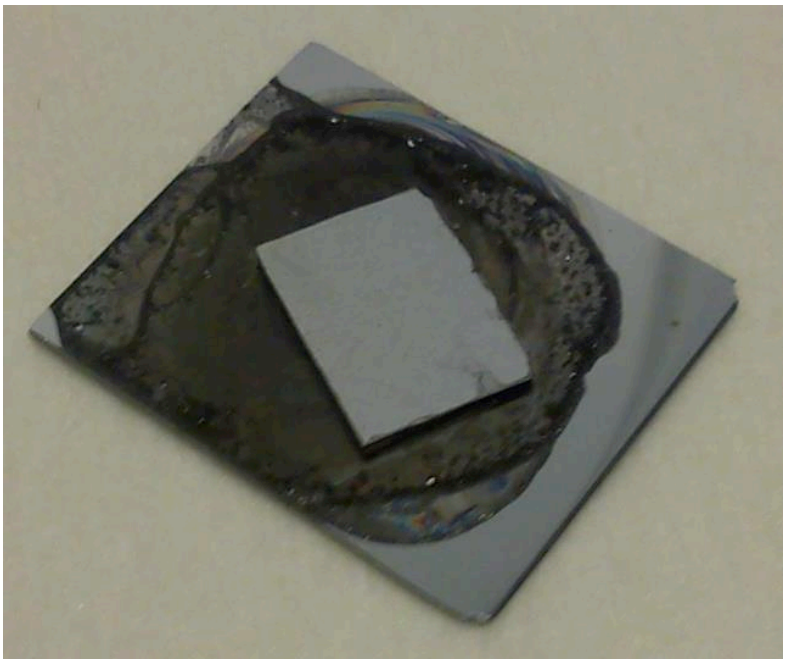

Figure 6.3 Drop coated thick ND layers in 'sandwich' configuration. The larger bottom silicon electrode has uncoated areas so as to allow the IS probes unfettered access to the highly conductive silicon electrode.

Hydrogen anneal treatment: A custom made chamber (known as "Plasma king" due to its ability to produce a DC plasma) was used to heat samples in an atmosphere of hydrogen for 5 hours at 500 ˚C.

Treatment steps

1. The chamber was pumped down to 10^{-5} torr using the turbo pump. Once this pressure was reached the turbo pump was turned off.
2. Hydrogen gas was admitted to the chamber and the flow was adjusted until the pressure in the chamber reached 10 torr. To maintain this pressure, the valve on the rotary pump was adjusted as necessary.
3. The temperature controller for the heating plate was set to 500 °C and the sample heated. The sample was left in these conditions (10 torr of H_2 at 500 °C) for 5 hours.
4. After 5 hours had elapsed, the heating plate was cooled, whilst still maintaining the 10 torr of H_2 pressure. When the heating plate had reached room temperature, the hydrogen flow to the chamber was stopped and all the gas line valves were closed.
5. The chamber was pumped down to rough vacuum to remove the hydrogen before bringing it up to atmospheric pressure to open. The sample was then immediately transferred to the FTIR for analysis or to the ozone equipment for oxidation.

Ozone treatment: A chamber custom built by the author (see section 4.5) was used in conjunction with a commercially available ozone generation unit (Ozonia TOGC2-100201). The TOGC2 uses corona discharge to create up to 4 g/hr with dry air, or up to 10 g/hr usin

Treatment steps:

1. The sample was placed on a heater inside the custom built chamber.
2. The chamber was pumped to low 10^{-2} torr, using the rotary pump but through the turbo pump connection. Whilst pumping, oxygen was admitted into the chamber via a valve fitted connection and through the TOGC2. The flow duration was 30 seconds, achieving a chamber pressure of 1-5 torr. The valve was then closed and the chamber again pumped to low 10^{-2} torr. The purpose of this step was to flush the lines with pure oxygen gas prior to treating the sample, ensuring a minimum of non-oxygen species. The turbo pump was then started and the chamber was pumped down to 10^{-5} torr. The sample was then heated to 200°C for 30 minutes.
3. The oxygen gas line is connected to the chamber via the TOGC2. Oxygen was introduced into the chamber by opening the required valves, allowing the pressure to rise slowly, the turbo pump was turned off and the pumping lines were switched in order to protect the turbo pump from ozone damage. Using a combination of the oxygen variable area flow meter and the rotary pump valve, a chamber pressure of 50 mbar was established and maintained.
4. The ozone production was initiated by turning on the TOGC2 unit and continued for 30 minutes. After 30 minutes, the sample was cooled to room temperature in ozone. Once the sample had reached room temperature, the TOGC2 ozone production was stopped, the oxygen flow to the chamber was shut off and the chamber was pumped down to remove gases before venting. The sample was immediately transferred to the nitrogen purged FTIR if analysis was required.

Impedance spectroscopy: Measurements were made by taking the coated DND substrates and placing them inside the Solartron 1260 Impedance system. This system was also integrated with a Solartron 1296 Dielectric Interface in order to measure the high impedance anticipated (the 1296 in conjunction with the 1260 is specified to the range of 100 - 10^{14} Ω and 0.1 – 10^{7} Hz).[38] The sample was placed on a ceramic heater inside the steel vacuum chamber (to provide electrical and environmental isolation), connected to the impedance equipment. Two metal probes were then placed on the top and bottom plates (see

Figure 6.1) in order to probe through the ND layer. Measurements were then taken either at atmospheric pressure or medium vacuum (10^{-2} - 10^{-3} mbar), through a temperature range from room temperature to a maximum of 475°C (later 580˚C), where the temperature was maintained for 10 minutes unless otherwise specified. The use of vacuum and air measurements allows for the separation of the influence of air on the measurement, which is likely a major component. The full range of frequencies was always used. If during the course of taking a heated measurement there was significant change in the magnitude of the impedance, the sample was then cooled to room temperature and retested, these cases are explicitly stated on the graphs' legend. Control measurements were taken using uncoated silicon plates to ensure the effects observed were due to the ND layers. Samples were tested until destruction or the limits of the measurement equipment (e.g. loss of resistivity or gain in noise) or heater assembly were reached.

Model fitting: Data obtained by the Solartron Impedance software was then fitted to an equivalent circuit model using ZView (Scribner Associates). Here the simplified Randles circuit was taken as the model's starting point, with additional parallel RC circuits added if necessary to correctly model the

observed data (i.e. overlaying semicircles).[39] The raw data for the fitting calculations are included in Appendix A with their respective errors. The modelled data from the fit (R_1 and R_2 if applicable) was then used to draw Arrhenius plots of activation energy against inverse temperature.

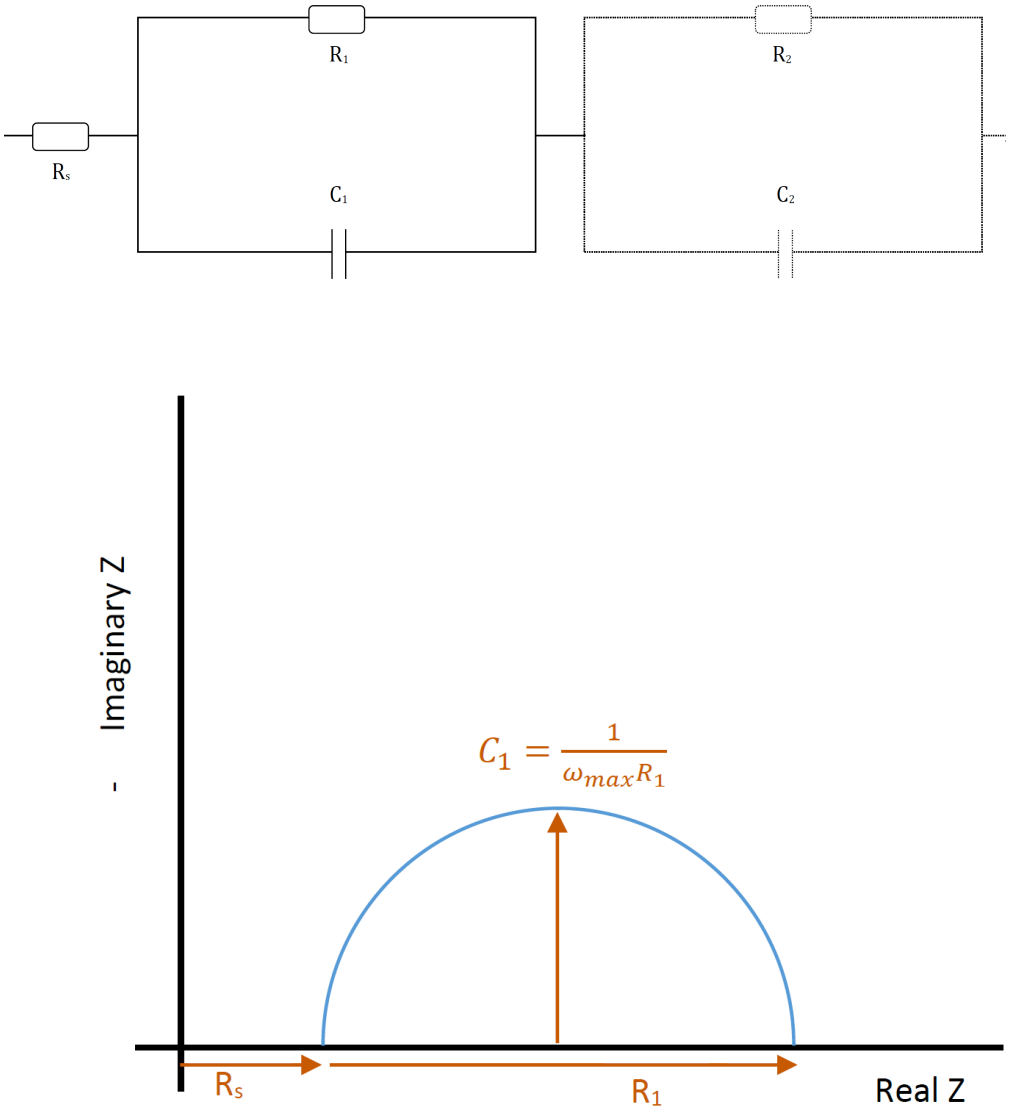

Figure 6.4 Top: Simplified Randles equivalent circuit showing default components R_s (series resistance, where applicable), R_1 and C_1 (1st conduction path resistance and capacitance respectively) in solid lines. The dotted components R_2 and C_2 were added to the model if required to fit the observed data in the case of a second conduction path). Bottom: Idealised Cole-Cole plot showing relationship between circuit components and semicircle fitted data.

FTIR: FTIR spectroscopy was performed using a Perkin Elemer Spectrum One FTIR Spectrometer. Samples were either directly drop coated onto (when in solution), or scraped from the treatment substrate onto CaF_2 windows for analysis. Drop coating was performed in a clean room environment by pipetting one drop at a time of concentrated solution onto CaF_2 windows placed a bench top heater set to ~100 ˚C. Scrape coated windows had a similar volume of ND to the drop coating method deposited on it, then another CaF_2 window was placed on top to secure the loose ND powder between the windows. Note monolayers of ND (as used in the electrical measurements) were not used due to their low IR absorption, resulting in unacceptable signal to noise ratio, therefore the drop coated ND layers were *ca.* 300 nm thick. Both styles of coated CaF_2 window were then mounted in the FTIR with a corresponding (single or double) uncoated reference window from which to compare spectra in order to remove any influence of the CaF_2 window. Mounted samples were then allowed to sit in the N_2 environment to desorb water, measurements were taken after a 10 minute N_2 purge (FTIR is kept under nitrogen at all times to avoid introducing contaminants. Samples were scanned and an average was calculated over 10 minutes between 800 and 4000 cm-1.

6.3. Results and discussion

6.3.1 Nanodiamond surface modification

Figure 6.5a shows the FTIR spectrum of untreated ND. Here, the most striking feature is the wide peak between 3000-3600 cm^{-1} which can be attributed to the covalent hydroxl bond from adsorbed water.[40] The narrow peak at 1726 cm^{-1} can be ascribed to the C=O stretch seen in carboxylic acid groups and anhydride functionalities.[41] Between 1000 and 1500 cm^{-1} there is a convoluted set of peaks typical for ND (as seen in figure 2.11), including COO^-, C-O-C, C-OH and C-H.[42] The surface state after hydrogen treatment is shown in Figure 6.5b. Of high importance is the strong CH_x stretch centred at 2923 cm^{-1}, coupled with the peaks at 1461 cm^{-1} and 1377 cm^{-1} (CH_2 and CH_3 respectively) which strongly indicate hydrogenation of the diamond surface.[43] Also of note is the reduced occurrence of the C=O stretch at 1726 cm^{-1} in comparison to the untreated surface. The complete absence of the wide peak between 3000-3600 cm^{-1} seen in Figure 6.5a can be explained by the hydrophobicity of hydrogen terminated diamond preventing readsorption of water.[44] The remaining oxygen containing groups were likely inaccessible to the hydrogen gas during treatment. Figure 6.5c shows the FTIR spectrum obtained after the ozone treatment. There is a peak at 1755 cm^{-1}, the C=O stretch, emerging from the anhydride peak. C-O-C and C-O peaks are seen at 1249 cm^{-1} and 1141 cm^{-1} respectively, indicating oxidation of some bonds. However, the CH_x stretch is still apparent, so a full oxidation of the surface has not taken place.

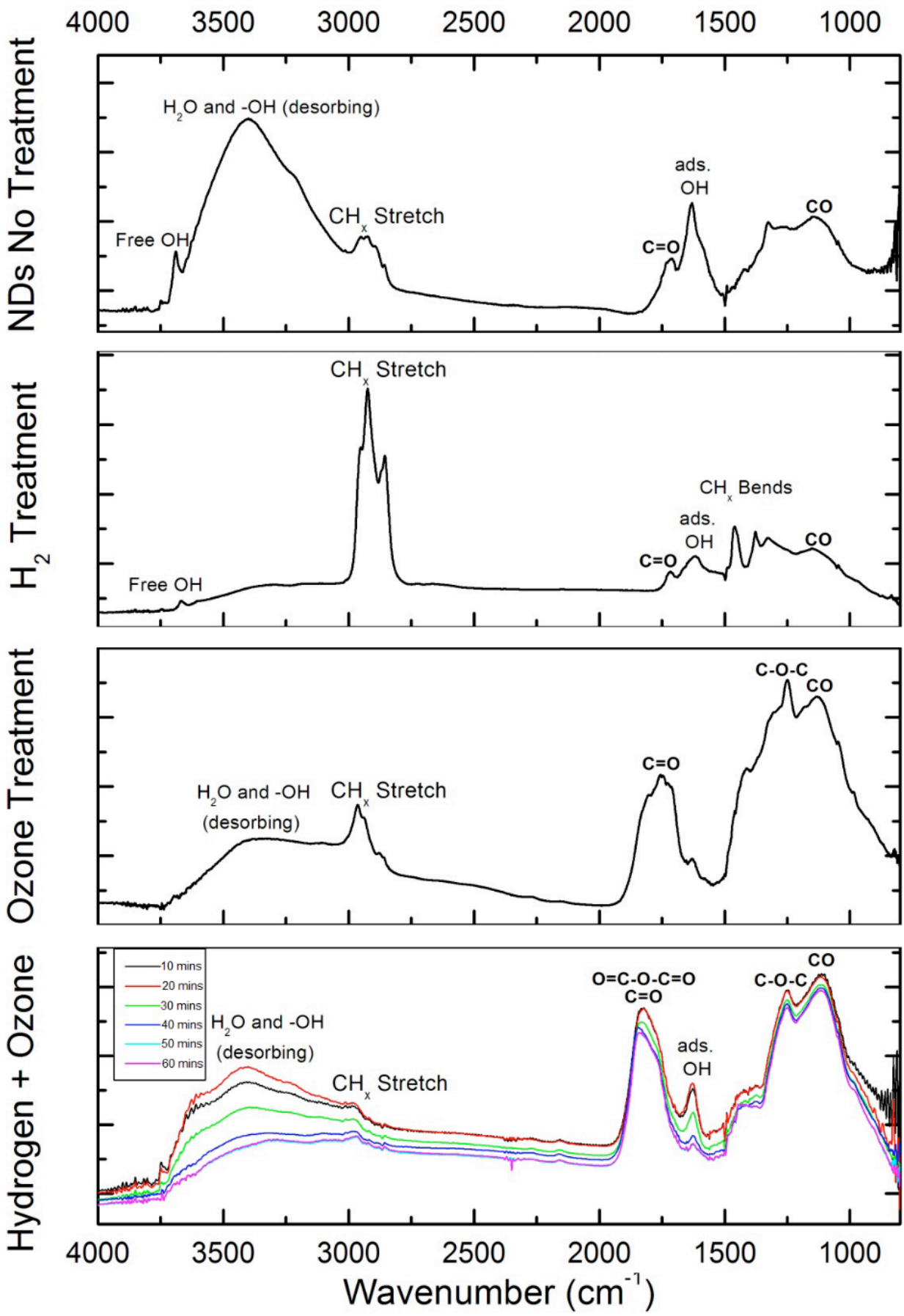

Figure 6.5 FTIR spectra taken on (a) as received ND, (b) hydrogen treated ND, (c) ozone treated ND, (d) hydrogen then ozone treated ND with increasing N_2 purge durations.

Figure 6.5d shows the spectra taken after hydrogen and subsequent ozone treatment. Of high importance here is the very weak CH_x stretch – when compared to the ozone only treatment, there is a greater efficacy of CH_x removal. The band centred around 1800 cm^{-1} (associated with cyclic acid anhydride) is also distinct from that seen on the ozone only treatment. Strong peaks can also be seen at 1256 cm^{-1} and 1123 cm^{-1} corresponding to C-O-C and C-O peaks respectively. The desorption of water from the surface can be seen across 3000-3750 cm^{-1} with increasing duration of N_2 purges, suggesting a hydrophilic surface – corresponding to oxygen terminated diamond.[44] Shenderova *et al.* have previously reported on the use of ozone to oxidise ND. In their experiments 80 nm aggregated ND was exposed to ozone for 72 hours at temperatures ranging between 150 and 200°C.[45] Hence, the combination of hydrogen and ozone treatments provides well-defined oxygen containing peaks and is preferable to ozone treatment alone. As all samples are dried before or during processing therefore the adsorbed water (or hydrophilicity) seen on the untreated and oxygenated NDs should not be a contributing factor. Instead, the homogenous surface left by the hydrogen treatment seems to provide an easier target for ozone to oxygenate ND, resulting in short treatment durations.

6.3.2 Electrical properties of thin nanodiamond layers

Here, thin ND layers refers to substrates ultrasonically coated with ND to a thickness of approximately 10 nm, as described in section 5.2. A note on symbols used: Hollow symbols depict measurements made in vacuum, and solid symbols for measurements performed in air. □ is used to depict untreated ND, △ depicts hydrogen terminated ND, and ○ depicts oxygen terminated ND.

6.3.2.1 *Untreated nanodiamond*

Air

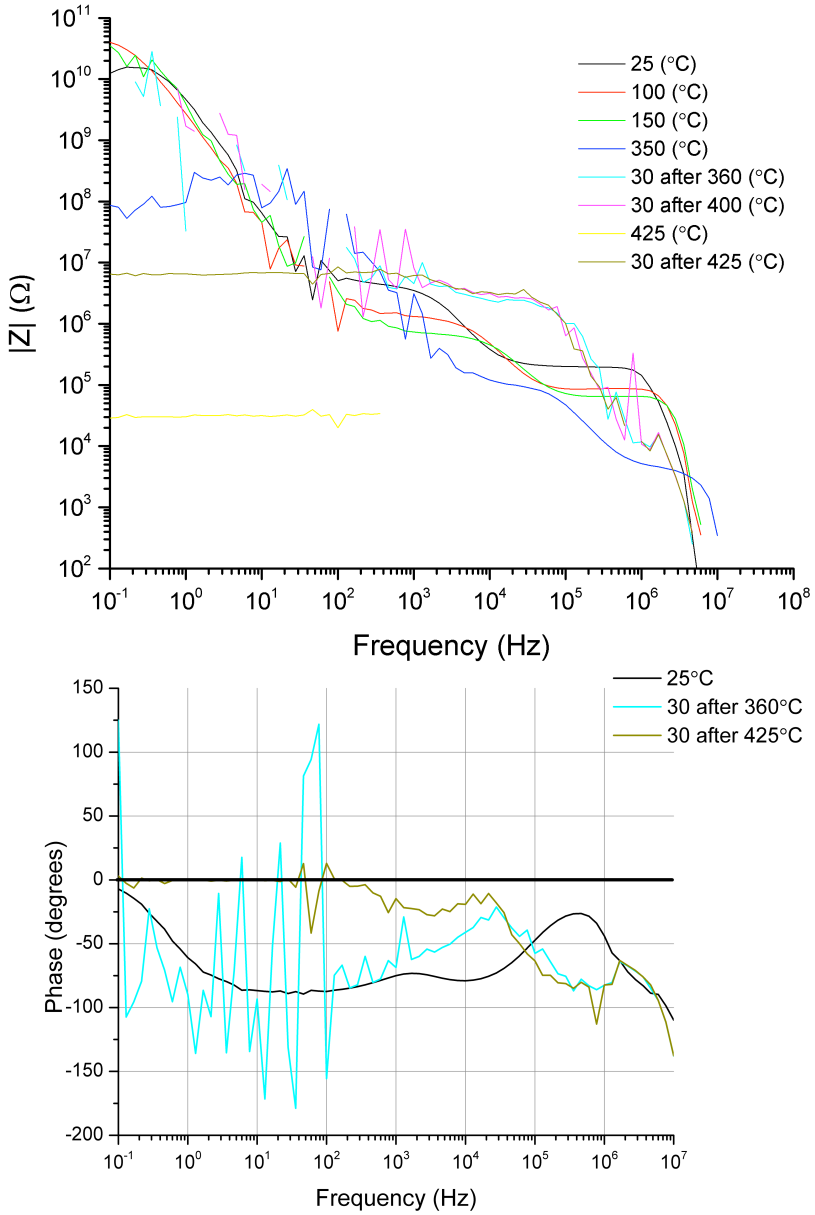

Figure 6.6 Top: Bode plot of untreated ND, measured in air at a range of temperatures. A subset of the data series is presented in chronological order of measurement temperatures performed throughout the experiment. Note: Due to the close proximity of many of the data points in this figure, a line graph is presented to aid the reader. Bottom: Phase plot of untreated ND measured in air.

Figure 6.6 shows the ND layer to have a surprisingly high impedance at 10^{10} - 10^{11} Ω, similar to both bulk diamond and aggregated nanodiamond.[46] The behaviour with measurement frequency also mimics a high quality dielectric, where effective resistance falls with rising measurement frequency. Low frequency impedance is reduced with rising measurement temperature, although upon returning the ND layer to room temperature, the low frequency impedance fully recovers indicating typical semiconductive behaviour. However, once the sample was heated to 425°C the full range of frequencies could not be acquired, due to excessive noise in the measurement. At this point the dielectric properties have been lost and the observed low impedance is retained after a return to room temperature, indicating a structural change to the ND layer. This onset temperature is slightly lower than that reported by Lee *et al.* for 150-600 nm CVD diamond spheres heated in dry oxygen (450°C),[47] although the large change in dimensions from the CVD diamond spheres to ND could adequately account for this. It should be noted that due to the production method, the surface of CVD diamond spheres are hydrogen terminated.

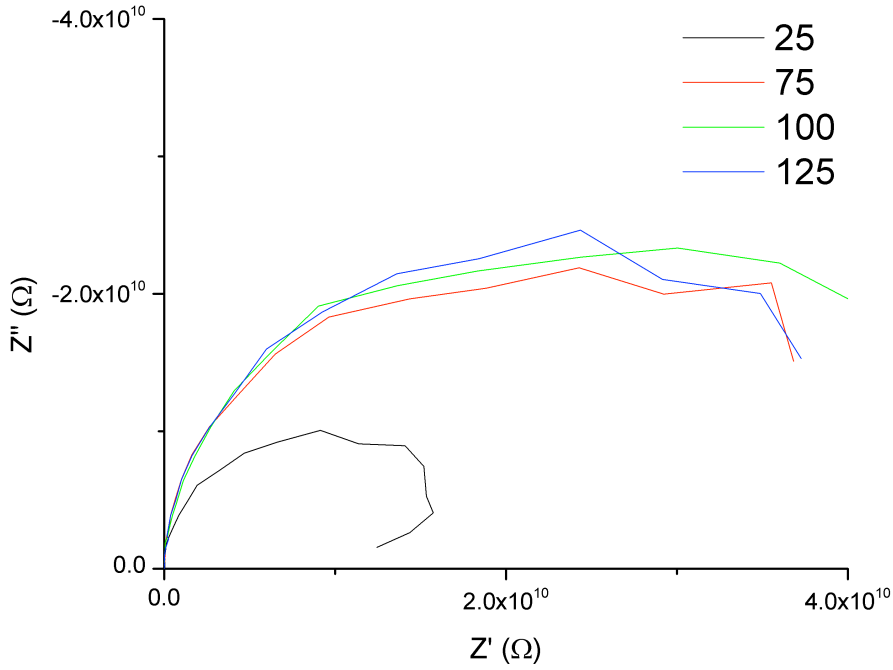

Figure 6.7 selection of Cole-Cole plots (real versus imaginary components of impedance as a function of measurement frequency) of untreated ND layers in air between 25 and 150°C. As the Cole-Cole plot uses linear axes to represent the semicircular response, and these responses often vary by several orders of magnitude, only measurements of interest that fit on one graph will be presented in order to prevent this data from overwhelming this chapter. Frequency values have been added to graph to aid recognition of differing applied AC voltage frequency.

The Cole-Cole plot in Figure 6.7 indicates only one semicircle can be fitted per measurement temperature and hence only one observed conduction mechanism.[48] This conduction path exhibited a capacitance in the picofarad range at all measurement temperatures. Picofarad capacitance has been reported previously to indicate grain interior conduction in polycrystalline film (whereas nanofarad capacitance is associated with grain exterior conduction).[49]

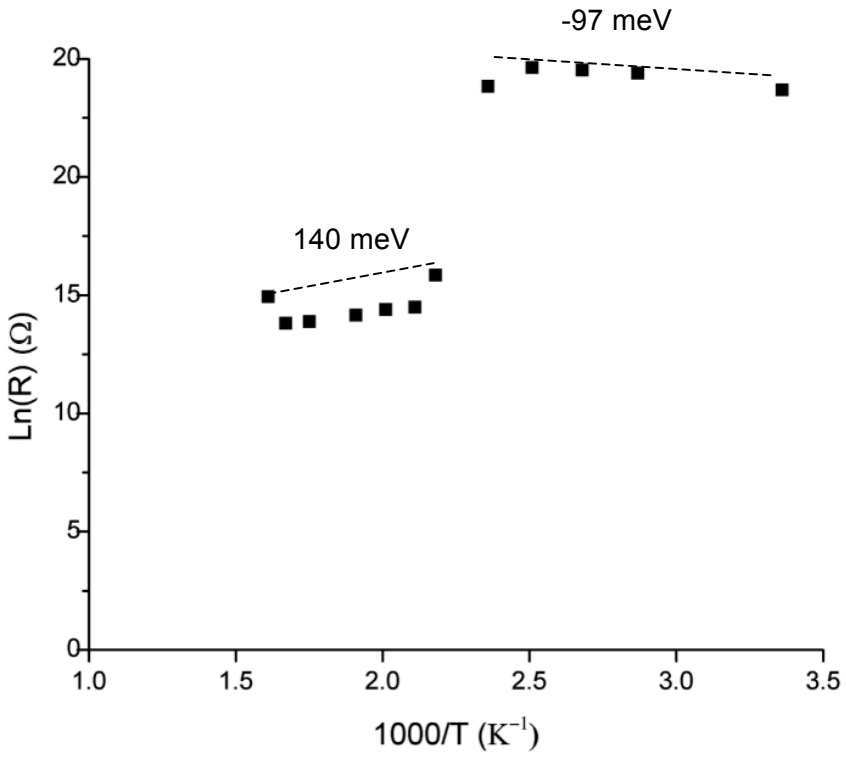

Figure 6.8 Arrhenius plot showing activation energy for semicircular responses from untreated ND layers in air. Fitted activation energies are plotted in a dotted line to aid recognition.

Figure 6.8 shows the Arrhenius plot (natural logarithm of the R value calculated from the fitted semicircles from the Cole-Cole plots, plotted as a function of reciprocal temperature) of the untreated ND layers. The slopes of the Arrhenius plot can then be equated to activation energy for the given temperature range using the Arrhenius equation:

$$\ln R = \frac{-E_a}{k}\frac{1}{T} + \ln A \tag{6.1}$$

where R is the resistance of the fitted semicircle, E_a is the activation energy, k is the Boltzman constant expressed in eV K^{-1}, T is the temperature, and A is a

$$\ln R = \frac{-E_a}{k}\frac{1}{T} + \ln A$$

constant (the pre-exponential factor).

(6.1 is of the form $y = mx + c$. Therefore the activation energy can be taken as:

$$E_a = -k\left[\frac{\partial \ln R}{\partial\left(\frac{1}{T}\right)}\right] \tag{6.2}$$

Hence, Figure 6.8 shows two distinct regimes with a rapid transition phase. The activation energy of the untreated ND between 25-125°C was found to be -97 meV (with a standard error (S.E.) of 12 meV). For the transitional phase between 150 and 185°C E_a = 3.3 eV (S.E = 0.47 eV), and between 185 and 350°C E_a = 140 meV (S.E = 110 meV). The *ca.* -100 meV activation energy seen between 25-125°C is likely to have arisen from the evaporation of water adsorbed on the surface[50] (see Figure 6.5(a)), which is readsorbed upon cooling to room temperature. The activation energy seen at higher temperatures (185 and 350°C), whilst of a similar magnitude to the lower temperature trend (higher on the reciprocal temperature scale) is likely due to the thermal activation of trap states originating from defects and impurities within the ND.

6.3.2.2 Hydrogen terminated nanodiamond

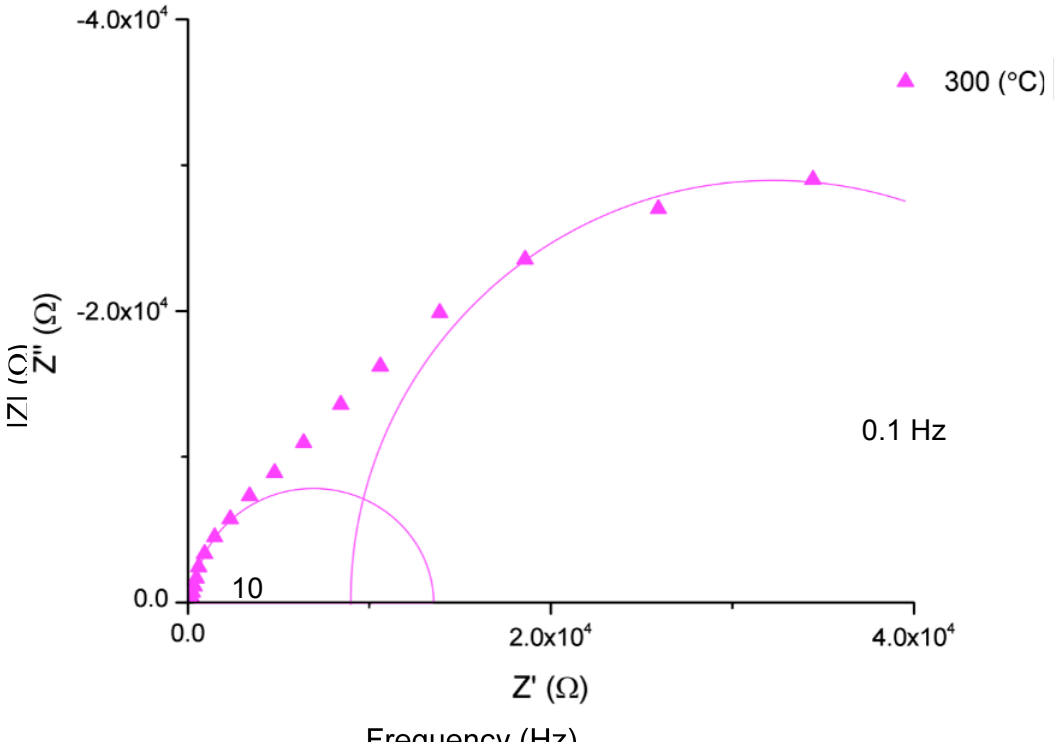

Figure 6.10 Cole-Cole plot of hydrogen terminated ND layer measured at 300°C. Two semicircular responses are observed and have been fitted to the plot to aid recognition.

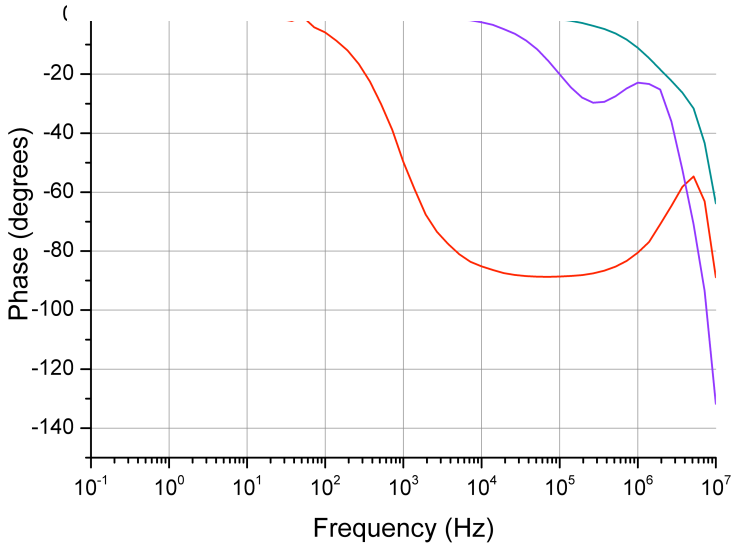

Figure 6.9 Top: Bode plot of hydrogen terminated ND in air. Successive cycling between temperatures near the permanent deformation point of untreated ND (seen in Figure 6.6) and room temperature were performed to compare temperature stability. Bottom: Phase plot of hydrogen terminated ND in air.

Air

The primary observation from Figure 6.9 is the low frequency impedance response is three orders of magnitude lower than that seen in Figure 6.6, at 10^6 - $10^7\Omega$. This observed drop is likely due to surface transfer doping, as has been reported on ND by other groups very recently.[22, 26] The recovery of the original room temperature impedance occurs at higher temperatures than the untreated ND layers, a full 24 hours after heating to 475°C for 10 minutes, no significant permanent change is detected at room temperature. This suggests hydrogen termination provides greater protection against the permanent damage inflicted at higher temperatures. Indeed, hydrogen termination of bulk diamond has long been known to stabilise the surface during and after CVD growth, preventing the transition to other phases, such as graphite.[51] However after one hour of heating to 475°C it is apparent that upon return to room temperature (RT after 1 hr 475 (°C)) the impedance does not begin to revert to the initially observed impedance levels. Subsequent measurements at room temperature showed no change. Instead the layer remains much like that seen at 475°C, indicating a permanent structural change has occurred.

Whilst only one semicircular response could be determined between 30 and 250°C from the Cole-Cole plots, a second semicircle emerges between 300-400°C (Figure 6.10) and is still apparent upon cooling to room temperature. The second conduction path only becomes apparent at temperatures beyond the boiling point of water, which is required for surface conductivity. Therefore this second conduction path cannot be ascribed to hydrogen induced surface conductivity. However this second conduction path is maintained once the sample is returned to room temperature. Therefore this trend could be present at lower temperatures, but masked by the larger, lower frequency semicircle. Figure 6.10 shows the first emergence of the second semicircle at 300°C and

highlights the limit in resolving closely positioned conduction paths. The semicircles fitted to the data presented in Figure 6.10 were determined to show capacitance magnitude in the tens of picofarads, only one order of magnitude greater than the untreated ND layers, indicating a similar, if slightly less ordered, material through which the conduction mechanism passes.

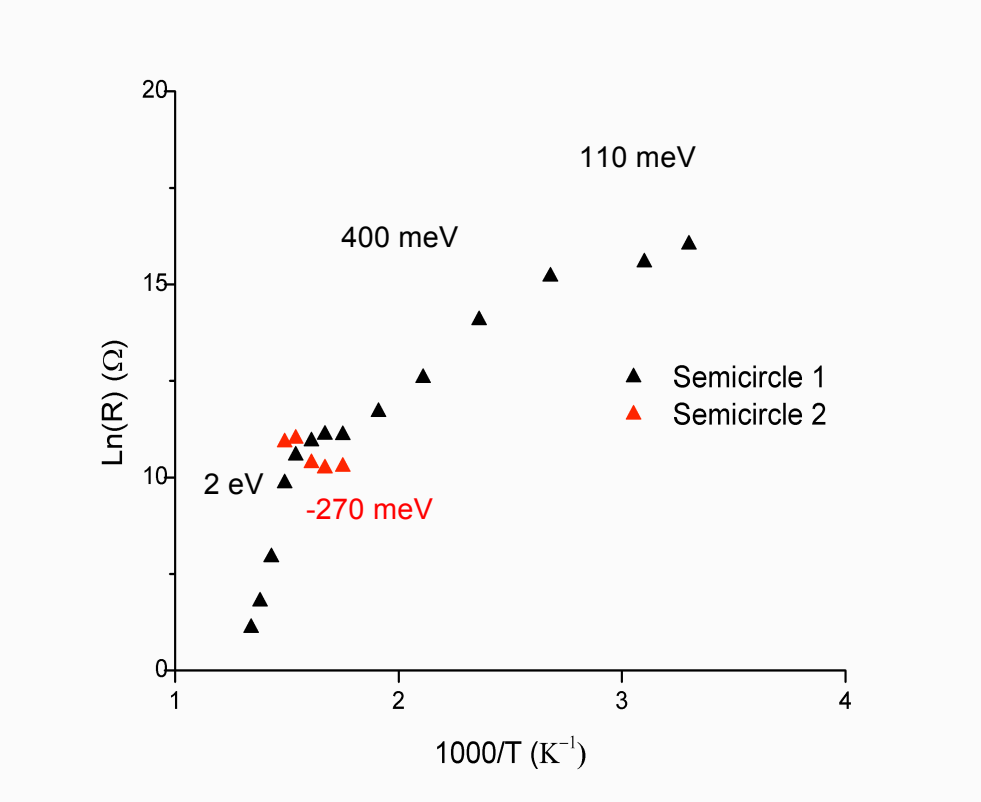

Figure 6.11 Arrhenius plot of two conduction paths observed on hydrogen terminated ND layer.

Figure 6.11 shows an Arrhenius plot of the extracted semicircular responses seen on a hydrogen terminated ND layer. For the first semicircle, two or three regimes are apparent. Assuming the temperature range of 30-300°C is two distinct processes then between 30-100°C E_a = 110 meV (S.E = 30 meV), and for 100-300°C E_a = 400 meV (S.E = 20 meV). Taking 30-300°C to be one continuous trend then between 30-300°C E_a = 260 meV (S.E = 30 meV). For 375- 475°C E_a = 2 eV (S.E = 130 meV). The second semicircle has a negative activation energy of -270 meV (S.E = 85 meV) between 300-400°C. The low temperature range

activation energy is again likely due to the removal of the adsorbed wetting layer. The mid-level activation energy (100-300°C) is due either to the removal of adsorbed gas (ND has a very high sorption capacity between 150-450 $m^2 g^{-1}$),[52] or just through previously reported, unspecified defects shown to have an activation energy at 400 meV.[53] The activation energy seen above 375°C is far greater than those previously seen. At 2 eV this activation energy is substantially lower than reported in the literature. A value of ~80 kcal mol^{-1} (corresponding to 3.47 eV) was found by Su *et al.* through temperature programmed desorption, however this was performed on {100} orientated bulk diamond at UHV pressures (2×10^{-10} Torr) [54] and hence cannot be directly compared to the present case. Studies on the thermal decomposition of ND (at 10^{-5} Torr) show the onset of CH_x groups' desorption to be *ca.* 750°C, [55] far below the temperature reached in this experiment. Additionally, the fact the impedance values recover upon return to room temperature (at least below 475°C) indicates the hydrogen termination, and hence the surface conductivity, is not lost.

Zhao *et al.* calculated the size dependence of the onset of nanodiamond-graphite transition.[56] Their calculations suggest 5 nm ND would undergo graphitisation as low as 425°C. Indeed this theoretical prediction was later confirmed by the work of Osswald *et al.* who showed that below 375°C, oxidation in air was not detected, however above 450°C both sp^2 and sp^3 carbon are oxidised. Therefore, the activation energy seen in Figure 6.11 between 375-475°C is likely the oxidation of graphite with a possible contribution from the early stages of diamond oxidation. Finally, the onset of the second semicircle results in an observed negative activation energy suggesting a barrierless reaction where increasing the temperature decreases the probability of the

excitation of a charge carrier. In isolation, this may be due to detrapping at defect sites, however as previously discussed the close proximity of a larger semicircle (e.g. Figure 6.10) may be preventing the identification of this trend at lower measurement temperatures.

Vacuum

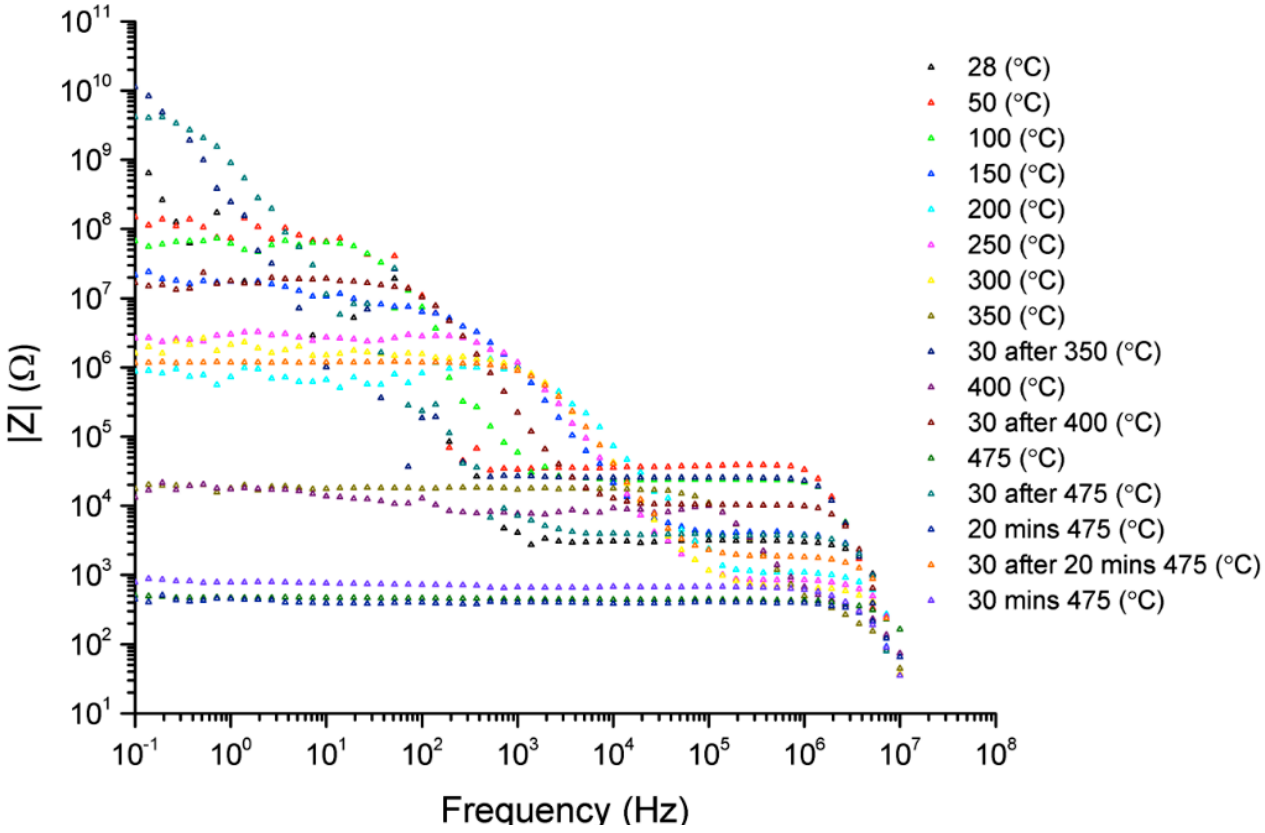

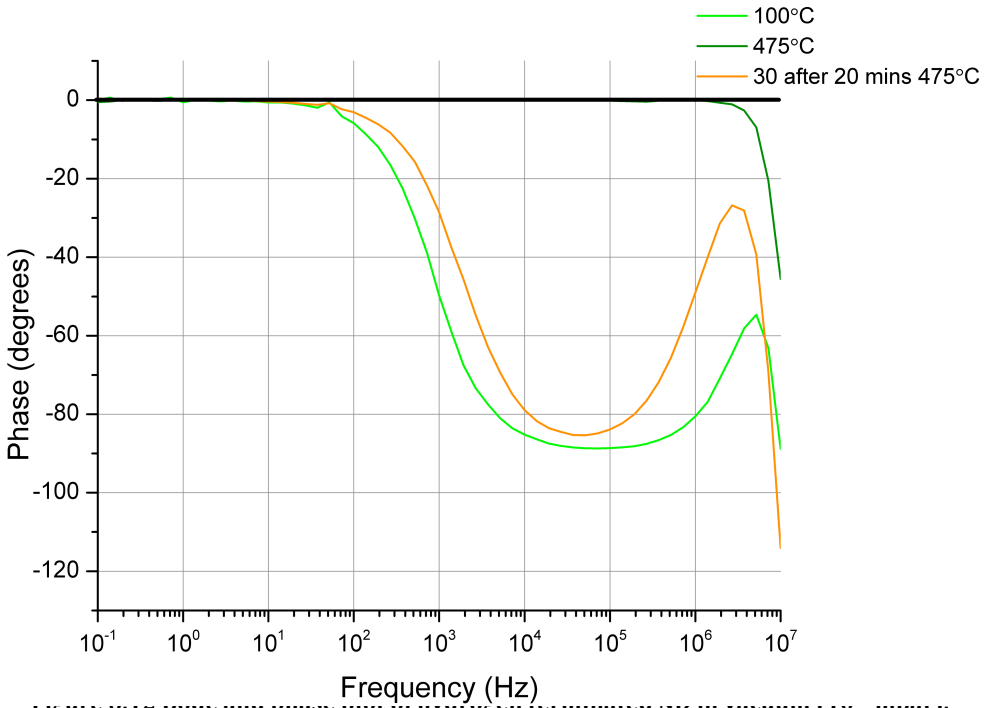

Figure 6.12 Bode and phase plot of hydrogen terminated ND in vacuum (10^{-6} mbar).

Figure 6.12 shows the stark difference when measuring hydrogen treated ND in vacuum, as the room temperature impedance is three orders of magnitude greater than that seen in air. As such, the layer more closely resembles the response seen in untreated or oxygen terminated ND layers (Figure 6.6 and Figure 6.15 respectively). This corroborates the evidence presented in Figure 6.9 of the hydrogen treatment inducing surface transfer doping as this effect is not seen in vacuum due to the removal of necessary surface adsorbates (see section 2.2.4). Above 150°C the behaviours of the layers are largely identical, as would be expected of a conduction mechanism that relies on the presence of a wetting layer and adsorbates.

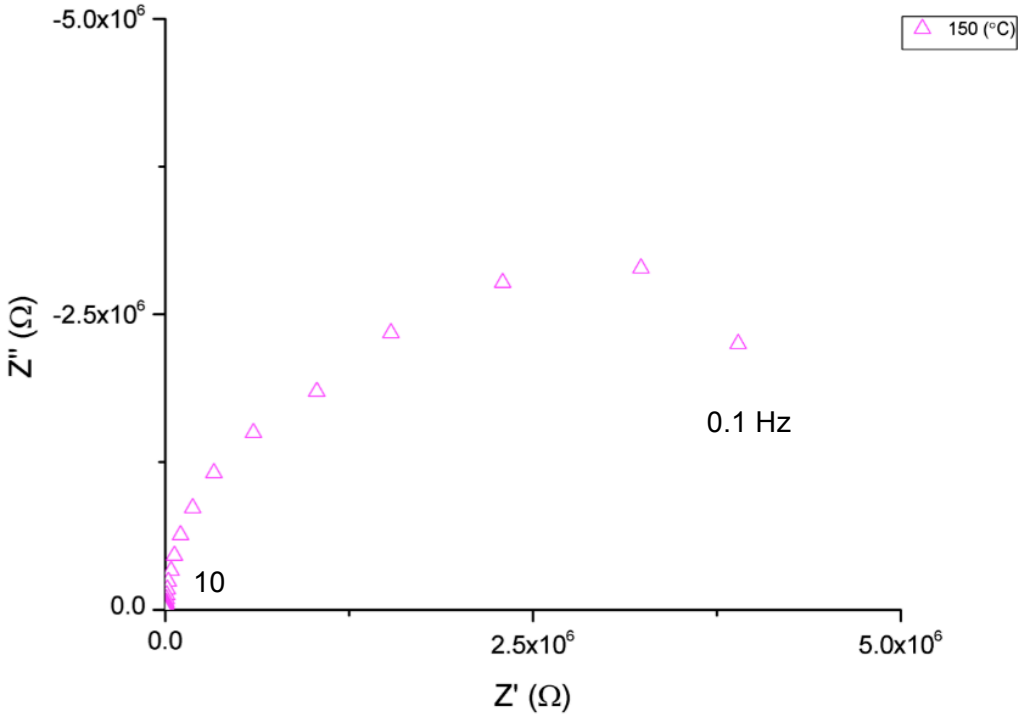

Figure 6.13 Cole-Cole plot of Hydrogen terminated ND layer measured in vacuum. For the data presented at 150°C. Two semicircular responses are apparent.

In contrast to the data acquired in air, hydrogen terminated ND in vacuum show two conduction paths below 150°C. The primary conduction path does not show as great a disparity between vacuum and air measurements in the magnitudes of room temperature impedance (10^{10} and 10^{6} Ω respectively). Instead, the gap is narrowed to 10^{7} and 10^{6} Ω, so whilst the bode plots indicate similar room temperature behaviour between untreated ND in air and hydrogen terminated ND in vacuum, closer analysis of the data reveals this relationship only holds for the absolute magnitude of impedance. Interestingly, the second conduction path in vacuum is of the same order of magnitude as that seen above 300°C in air, lending some weight to the earlier proposition that a second conduction path does exist below 300°C in air, buried by a closely situated semicircle. Both vacuum and air measurements show the second semicircle to remain upon return to room temperature.

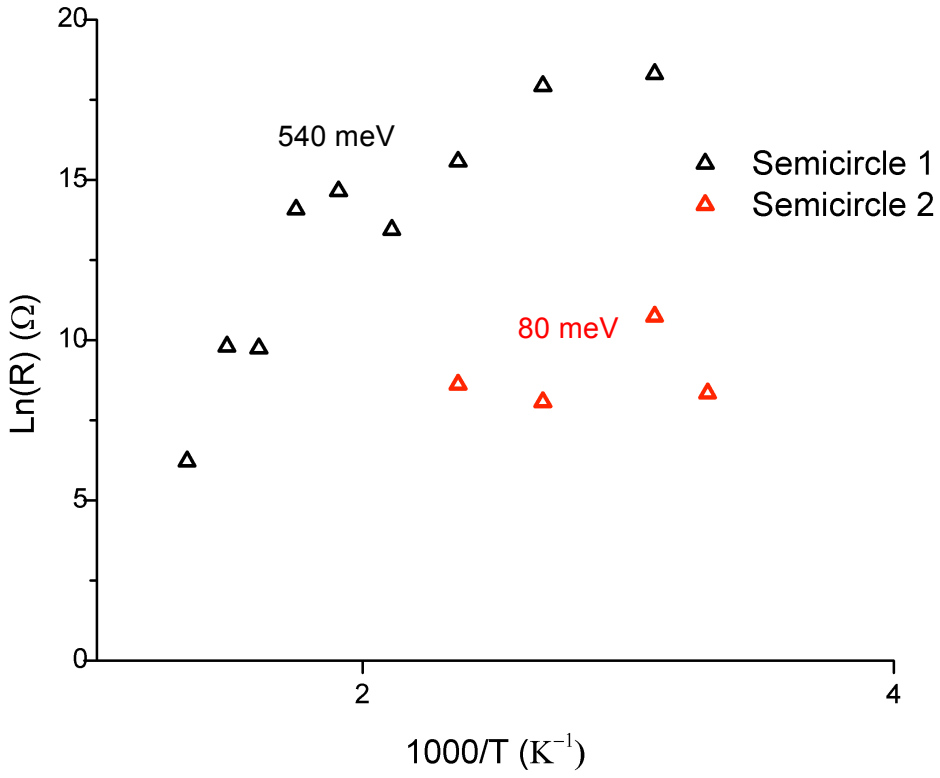

Figure 6.14 Arrhenius plot of primary and secondary conduction paths seen on hydrogen terminated ND measured in vacuum.

Figure 6.14 shows an Arrhenius plot of the extracted semicircular responses seen on a hydrogen terminated ND layer measured in vacuum. Due to the noise observed, it is difficult to ascertain whether the primary semicircle is one regime or more. Fitting the entire range yields E_a = 540 meV (S.E = 94 meV) between 30 and 475°C. There is a greater incidence of noise around the second semicircle where between 30-150°C E_a = 80 meV with a rather high standard error (S.E = 170 meV). As a result of this somewhat unreliable data it is difficult to draw firm conclusions from the Arrhenius plots.

6.3.2.3 *Oxygen terminated nanodiamond*

Air

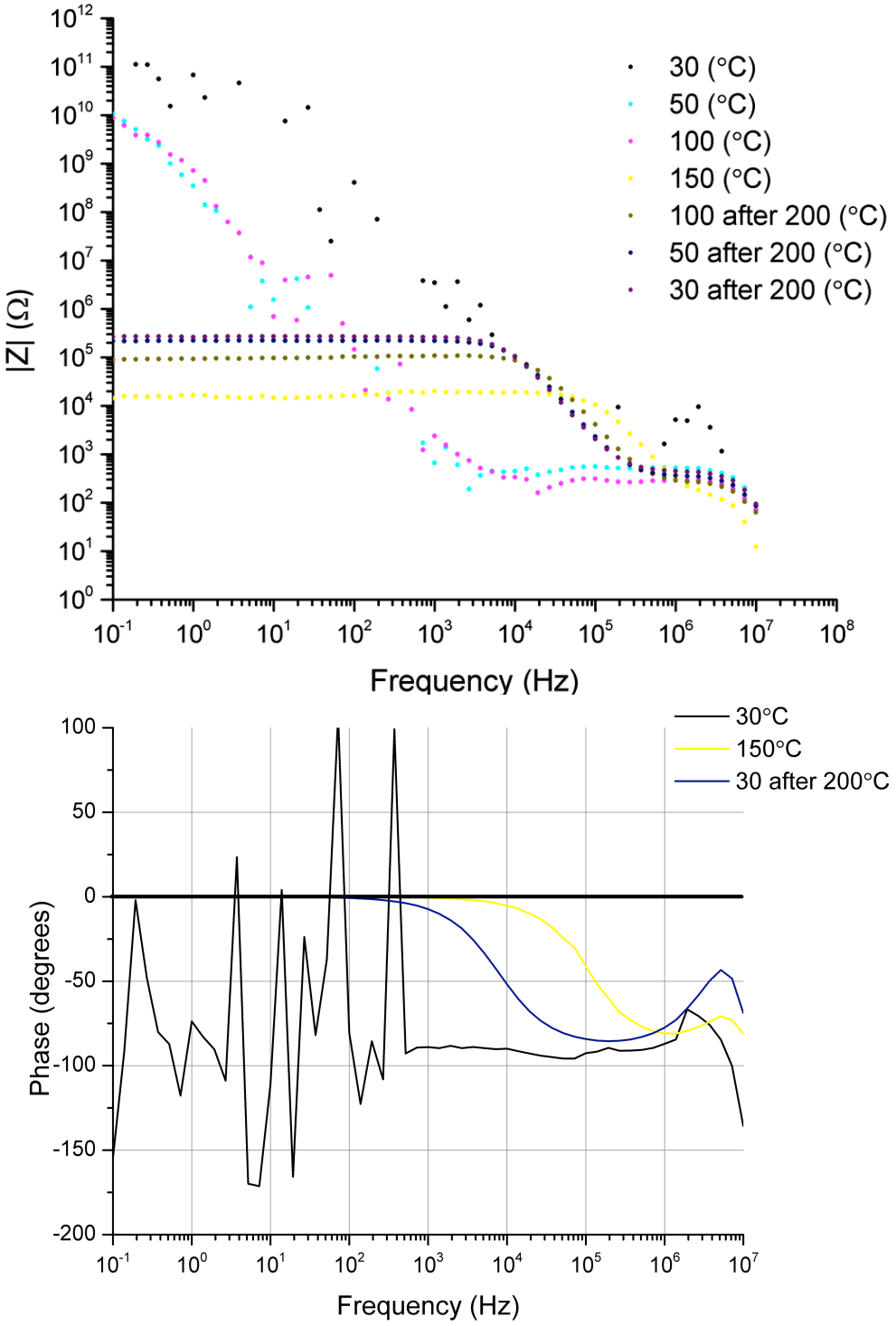

Figure 6.15 Bode and corresponding phase plot of oxygen terminated ND, measured in air.

Figure 6.15 goes some way to indicate the difficulty in taking a suitable measurement on oxygen terminated ND in air. The data is initially highly noisy at room temperature, however beyond a temperature of 150°C measurements were not possible due to the sample becoming too conductive. Therefore it was ascertained that permanent damage had occurred through the ND layer at a far lower temperature (200°C) than that seen on either the untreated or hydrogen terminated samples. The sample was subsequently slowly cooled and measurements taken at regular temperature intervals to investigate at what point the sample became measureable again. It was found the oxygen terminated ND had a far lower impedance, approximately 10^5 Ω, and this was only weakly temperature dependent. This difficulty is likely due to the oxygen termination hastening the onset of graphitisation, possibly accelerated through the increased presence of adsorbed water (see Figure 6.5(d)) due to the hydrophilic nature of oxygen terminated ND. Previous studies have shown water to act as a catalyst for the graphitisation of 40-60 nm ND particles in high pressure high temperature conditions (2 GPa, 1060-1760 K),[57] therefore it is likely that this mechanism is amplified for smaller particles and hence this effect could be observed at ambient pressure and a temperature of 200°C. The oxygen in the air also has an effect. Danilenko reported that the exclusion of oxygen caused a three orders of magnitude shift in rates of graphitisation over a 22 year period at room temperature.[58] This work found the shells of NDs were first graphitised, then oxidised leaving a smaller core size of ND. This process would continue until the ND reached a core size around 4 nm where a dramatic graphitisation of the entire particle would take place. This process reportedly occurred at 800 K, far above the temperatures used in the current study, however it is likely that this process is occurring, albeit at a greatly reduced rate. This might provide insight into why at high temperature the ND layer is too

conductive to measure - the thermal activation of carriers as seen in the untreated and hydrogen terminated ND, combined with the graphitisation of the ND shell, causes effective conduction routes through the ND layer, causing a collapse in measured impedance. Upon return to sub-critical temperatures (i.e. 100°C) the removal of the thermally activated carriers leaves the ND layer with an impedance response between that of pure ND (or bulk diamond) and graphite, where the isolated graphitic regions do not yet form a continuous conduction path.

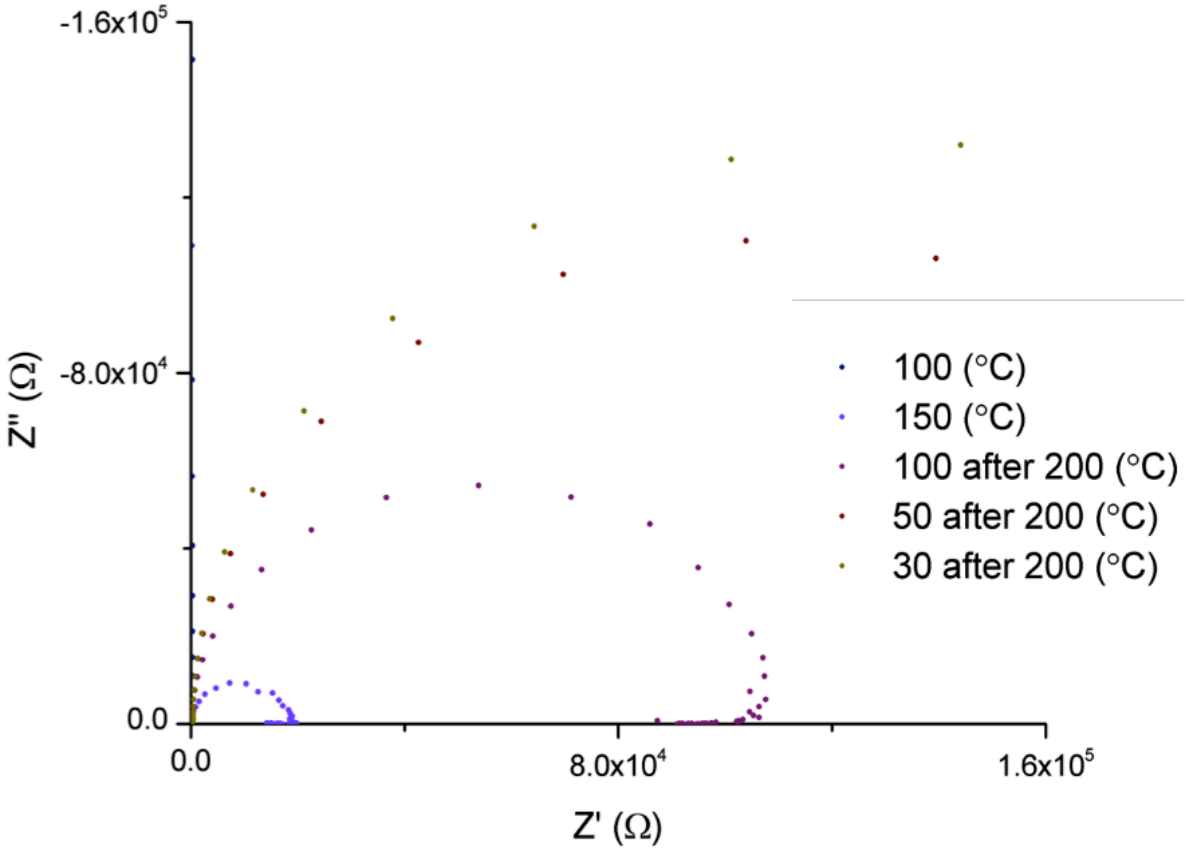

Figure 6.16 Cole-Cole plot of oxygen terminated ND measured in air.

Figure 6.16 shows the single conduction path seen in oxygen terminated ND layers. The measurements that were achieved showed a wide range of resistance values associated with the fitted semicircles in a very narrow temperature window - $10^{10}\,\Omega$ for 50°C, and $10^{3}\,\Omega$ for 150°C. The data points extracted from this experiment are insufficient to draw conclusions from, and therefore will not be presented.

Vacuum

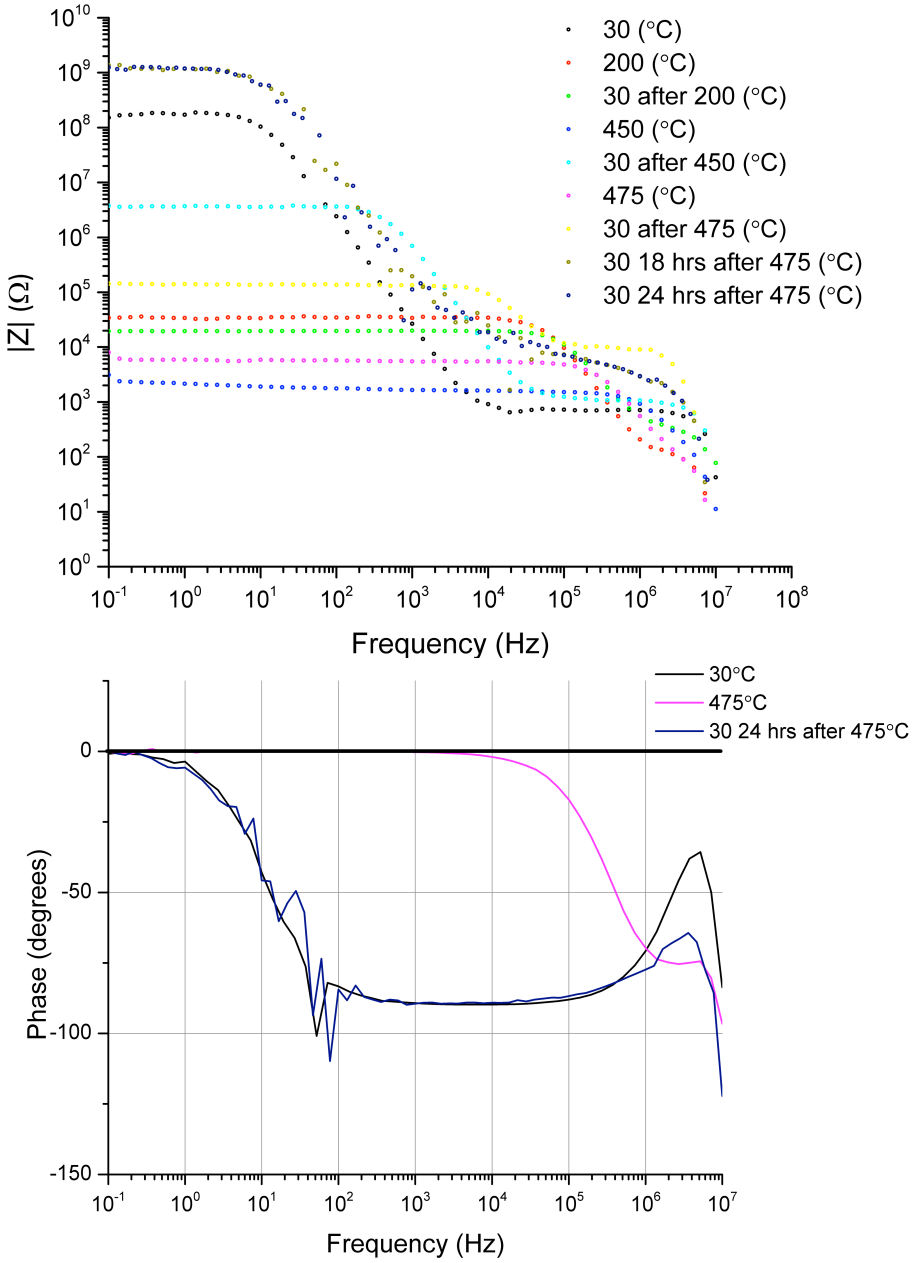

Figure 6.17 Top: Bode and phase plot of oxygen terminated ND in vacuum. Successive cooling stages were performed in an attempt to find the temperature where permanent reduction of the impedance occurs. Additionally, a large cooling period was performed to investigate the recovery of impedance at room temperature.

Figure 6.17 shows an initial impedance of 10^8 Ω, 2-3 decades lower than that observed at atmospheric pressure. This lies close to the initial impedance seen on hydrogen terminated diamond when measured in vacuum and may be due to the removal of surface adsorbates that aid conduction through the wetting layer, as after heating and once the ND layer has had 18-24 hours to recover, the impedance is a full order of magnitude higher than the initial value. This recovery behaviour is distinct to the previous experiments, where permanent change to the impedance was observed. In this case, the overall increase in impedance suggests the heating and cooling stages are removing graphitic deposits.

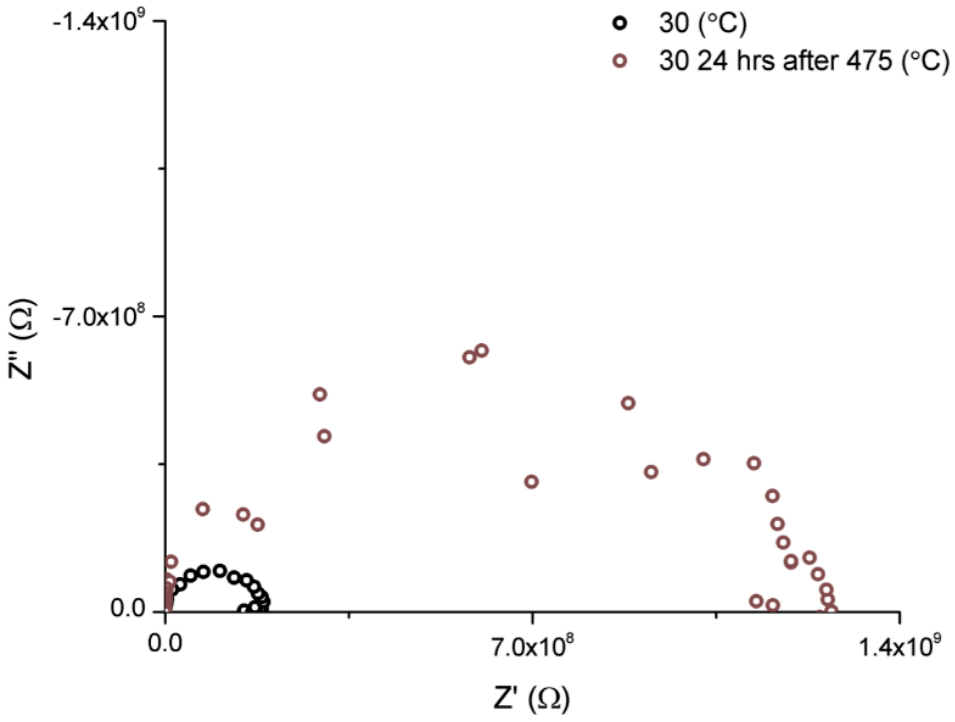

Figure 6.18 Cole-Cole plots of original and recovered impedance values from oxygen terminated ND layers in vacuum.

Figure 6.18 depicts the recovery of impedance after several heating and cooling cycles. Both sets of data exhibit a high degree of noise, however semicircle fits before and after exposure to 475°C yield extracted resistance values only one order of magnitude apart. All extracted capacitance values are of the 10 pF order of magnitude, indicating crystalline material remains. At the peak temperature, the only conduction path seen was *ca.* 5 kΩ (C = 95 pF), however when measured immediately after return to room temperature (25 minutes later) two conduction paths were visible, with the primary at 3×10^8 Ω (C = 88 pF) and the secondary at 10 kΩ (C = 5 pF). The observed shift in capacitance was the only observed occurrence. This effect was not seen after further time at room temperature. Therefore considering the noise on the data, and the single occurrence, it is difficult to draw firm conclusions from this observation.

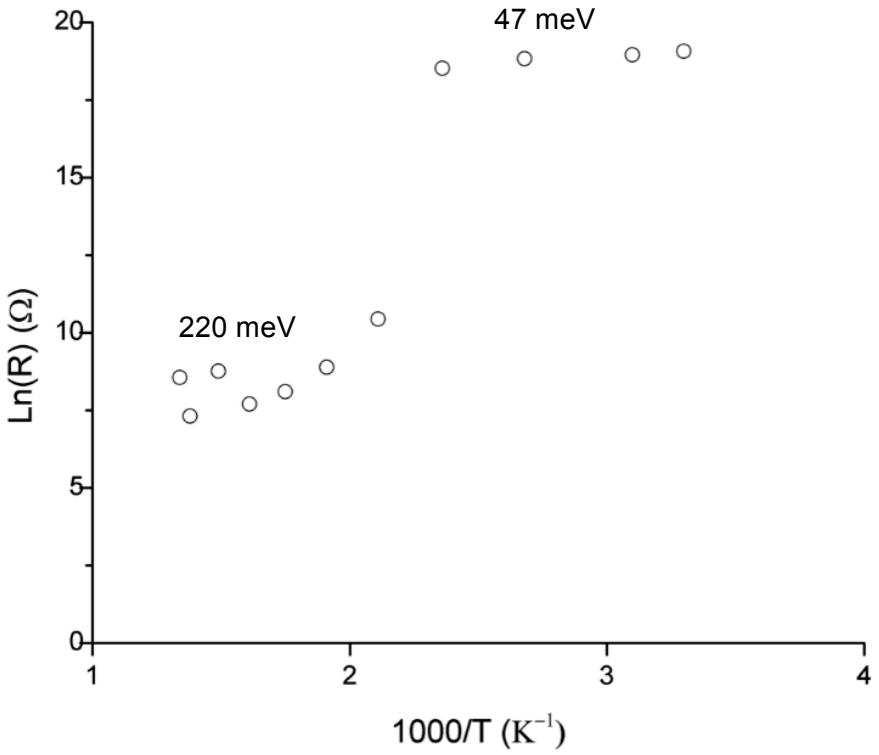

Figure 6.19 Arrhenius plot of the extracted conduction path resistance values, taken on oxygen terminated ND layers in vacuum.

The Arrhenius plot resembles that of untreated ND measured in air, with two distinct regions separated by a sudden shift in extracted resistance at 200°C. For the first region between 30 and 150°C, E_a = 47 meV (S.E = 8.5 meV), whereas for the second high temperature region between 200-475°C, E_a = 220 meV (S.E = 96 meV). Neither value for E_a is of the order expected for ND graphitisation, suggesting only desorption and oxidation processes occurring on the oxygen terminated ND layer.

6.3.3 Electrical properties of thick hydrogen terminated ND layers

Note thick ND layers refers to layers several micrometers thick deposited using the drop coating method described in section 5.2.

Vacuum

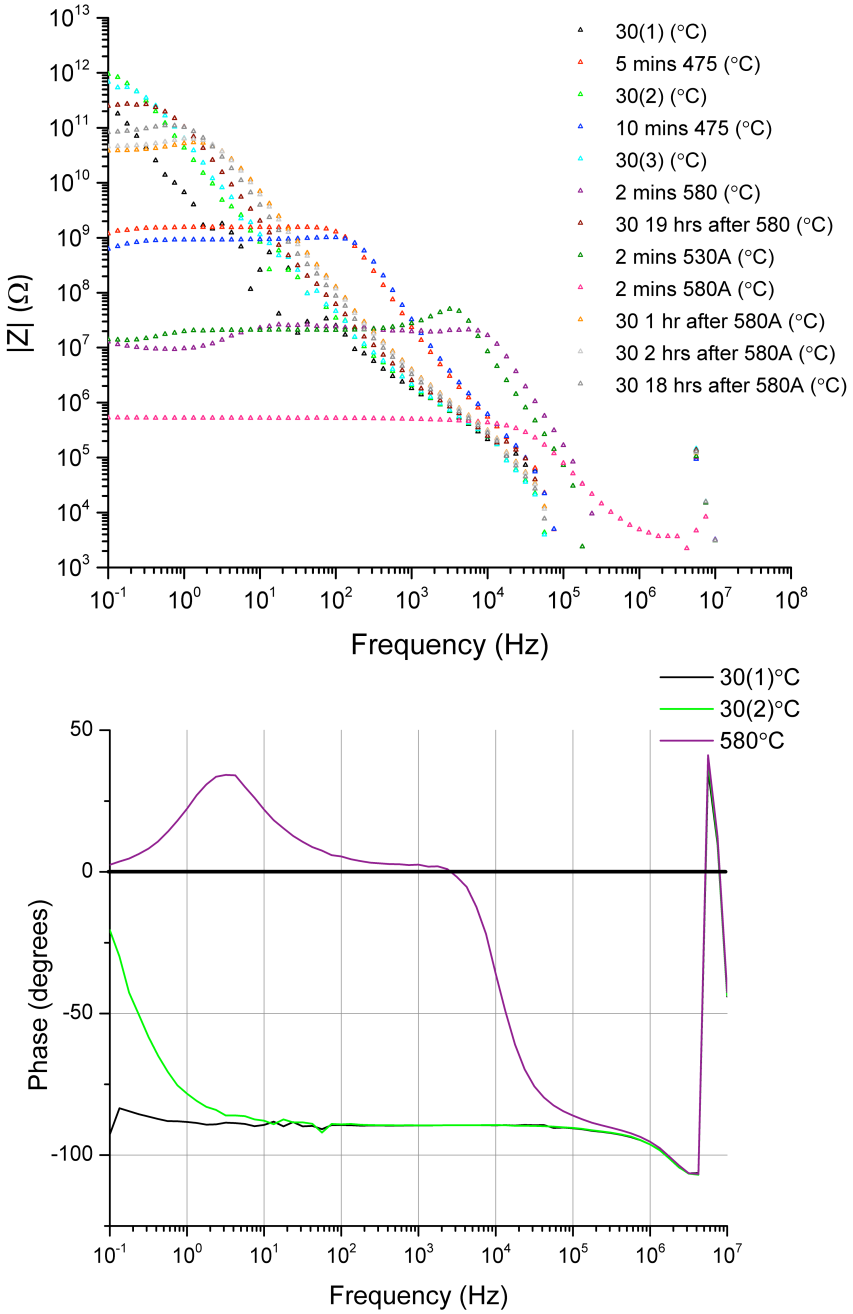

Figure 6.20 Bode and plot of hydrogen terminated thick ND layer measured in vacuum. Improvements to the heating assembly allowed for higher recording temperatures. Data series ending in 'A' denotes second round of heating after 19 hours at room temperature.

In an attempt to overcome the extremely noisy data seen on hydrogen terminated thick ND layers, measurements in vacuum were performed with a greater amplitude of applied AC voltage, 5 V in the present case (as a comparison, 0.01 V was used for thin hydrogen terminated ND layers). Successive heating and cooling cycles were performed in an attempt to find the temperature beyond which the electronic properties have been destroyed. Figure 6.20 shows the thick layer behaves in a similar fashion to oxygen terminated ND (Figure 6.17), where when given sufficient time to recover, the original impedance value returns. The initial impedance value is very high, similar to that seen on bulk diamond.[27]

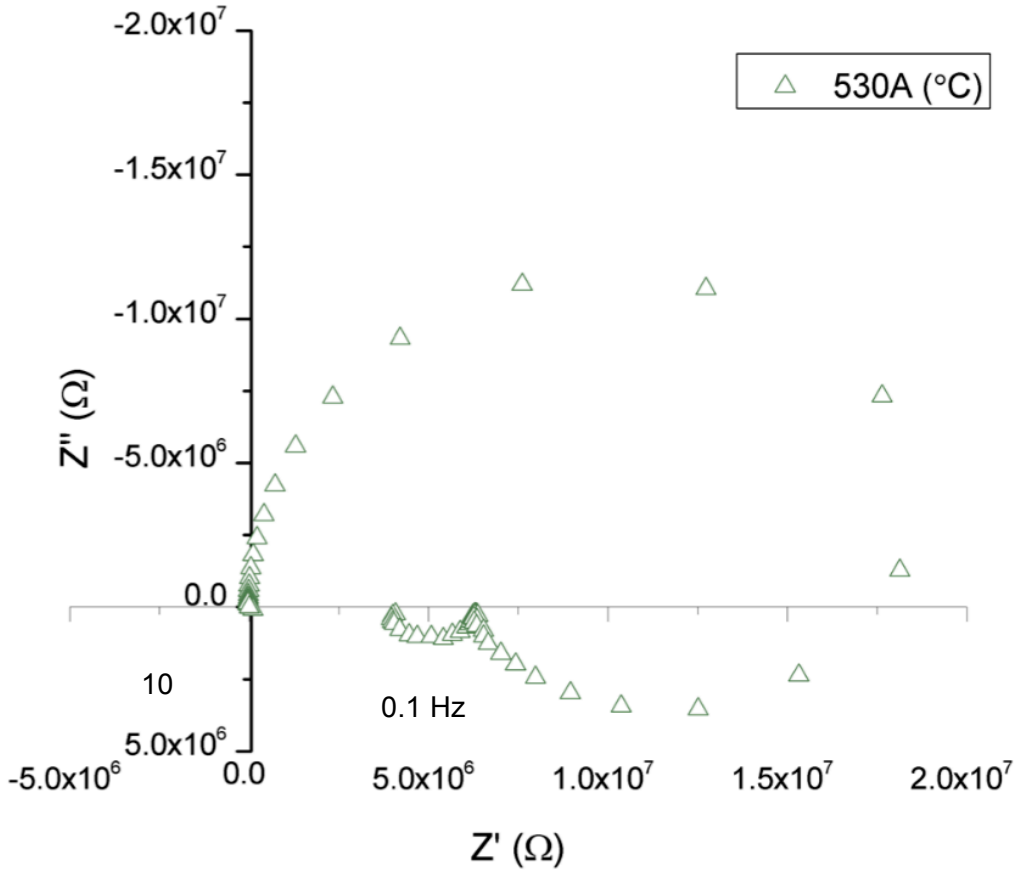

Figure 6.21 Cole-Cole plot of hydrogen terminated thick ND layer measured in vacuum. Data series ending in 'A' denotes second round of heating after 19 hours at room temperature.

The Cole-Cole plot presented in Figure 6.21 presents features not seen in any of the preceding experiments – semicircular responses in the positive plane of the imaginary impedance. Such features normally correspond to a measured inductance, however such an interpretation is unlikely as the degree of diamagnetic permeability seen in diamond is very low, at -2.1 × 10^{-5}.[59] Therefore a more likely explanation lies in use of high excitation voltages across the relatively thin ND layer (on the order of micrometers), leading to field strengths outside diamond's electrochemical window (approximately 3.5 V).[60] Consequently, this drives redox reactions at the diamond surface which are then measured as positive imaginary impedance. When observed on Cole-Cole plots this effect is dubbed pseudocapacitance. Two pseudocapacitive effects are seen in Figure 6.21 at 530°C, and were also observed at 540°C, all other measurements exhibited only one pseudocapacitive semicircle.

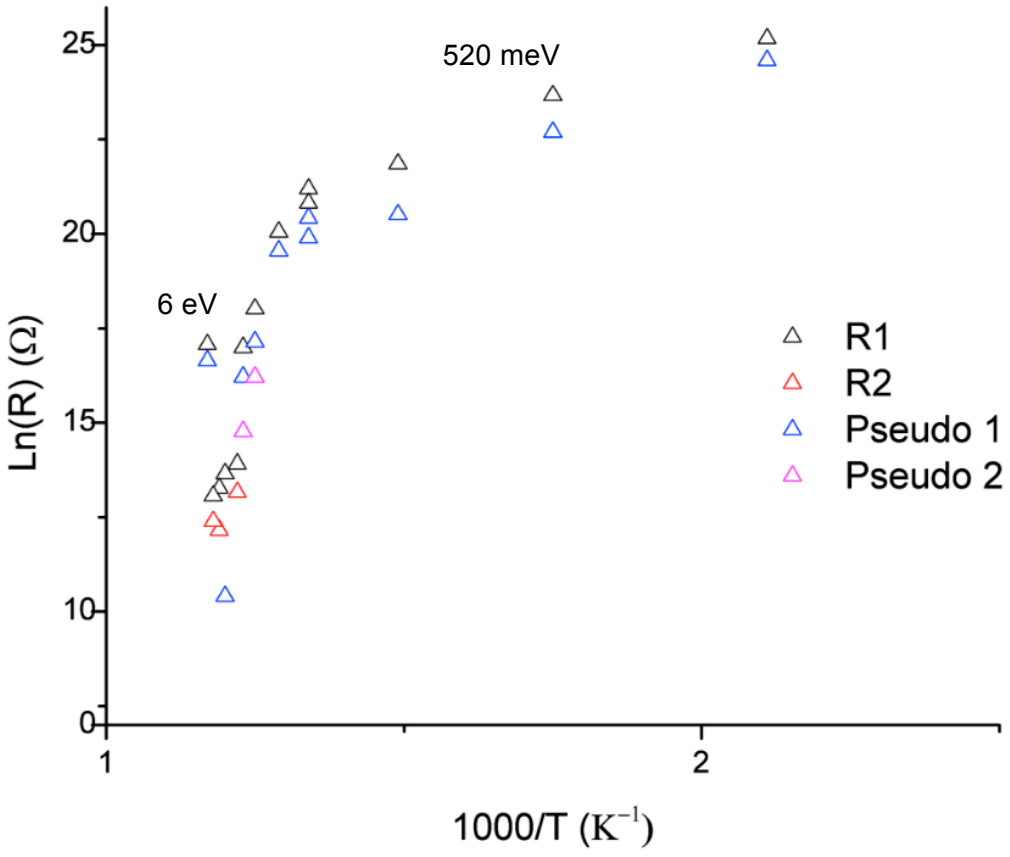

Figure 6.22 Arrhenius pot of hydrogen terminated thick ND layer measured in vacuum.

The activation energies calculated from Figure 6.22 were 520 meV between 200-475°C (S.E = 39 meV) and 6 eV between 500-580°C (S.E = 0.79 eV). The low temperature activation energy can again be attributed to surface desorption. The high temperature activation energy is far greater than any that have been previously observed, likely due to the higher temperatures used in this experiment. Therefore beyond 500°C in vacuum a new mechanism is apparent, this could be attributed to the excitation of carriers across the band gap of diamond (usually given as ~5.5 eV)[61] as, when the standard error is taken into account, the activation energy observed is of a similar magnitude.

Hydrogen terminated ND has been shown recently by Su *et al.* to exhibit properties that correlate to the occurrence of surface transfer doping, however this work required a bespoke measurement setup.[62] Therefore, it is likely that the current measurement setup is not sufficient to provide accurate measurements of thick layers of hydrogen terminated ND without the necessarily high supply voltages causing redox reactions.

6.4. Concluding remarks

The acquisition of FTIR required very thick layers to be treated in order to obtain enough material for the transmission experiments, however this is sub-optimal for static dry processing as some ND material will not be exposed to the reactants and therefore the observed changes to the ND surface may be underestimated, particularly when compared to thin ND films. Therefore it is reasonable to suggest the spectra shown in Figure 6.5 are comparable to the

thick ND layers presented in section 6.3.3, whereas the thin layers used throughout section 6.3.2 are likely functionalised to a greater degree due the reduced volume of ND treated. Mechanical agitation of the powders may be able to provide a greater homogeneity of functionalisation when dealing with larger volumes of ND, therefore this will be taken into account in future chamber designs.

During the temperature cycling, the electronic properties of hydrogen terminated ND particles recover after short exposures to high temperature (475°C). However, the observation that this is lost with greater durations of heating (1 hour), leading to behaviour similar to that seen on oxygen terminated ND, suggests hydrogen terminations are gradually replaced by oxygen containing groups from the atmosphere (in the case of air measurements). This process is not observed in vacuum, reinforcing the notion that the ambient air - likely the oxygen and moisture content – plays a vital role in the degradation of the electronic properties, as these highly reactive species are able to degrade the surface. Oxygen terminated ND is seen to degrade at a far lower temperature threshold (200°C) in air. This is likely mediated through its hydrophilicity,[42] where OH ions are free to attack oxygen containing surface groups, occasionally resulting in the formation of dangling bonds, which are thought to be required for the graphitisation of the surface, resulting in a catastrophic breakdown of the initially observed impedance.[63] This then excludes oxygen terminated ND from operating without degradation in ambient atmosphere above 200°C – which covers a large swathe of potential applications.

Perhaps the most surprising result was the extremely resilient behaviour of the NDs, particularly in vacuum. Potentially leading to protective coatings in a range of hostile environments (e.g. within combustion engines, or tokomak reactors). However, this behaviour seems only to hold under low excitation voltages used in impedance spectroscopy measurements. Accelerated degradation of the ND surface was eventually observed due to high (5 V) electric fields used in section 6.3.3 driving reactions at the surface. At this level of AC bias, the electrical properties were still recovered, suggesting only a small fraction of the ND surface is damaged through the hypothesised redox reactions, although longer duration experiments would be needed to confirm this. Therefore this result highlights the importance of the thickness of ND layers within this context; too great a thickness results in extremely noisy data, which is ameliorated by higher excitation voltages, which result in pseudocapacitive effects being observed for the first time. Conversely, too thin a coating also results in unstable measurements due to the instability of the experimental setup. Further improvements to the setup are under development to alleviate this limitation.

Fitting the impedance spectroscopy data to equivalent circuit models, several different configurations of modelled resistor and capacitors were found. When a second semicircle was observed on a Cole-Cole plot, this was found to be most accurately fitted to 2 parallel RC networks in series with each other. This arrangement has long been ascribed to two competing conduction paths through the material being probed.[48] In the present case, only the hydrogen treated layers behaved in this way, hinting at hydrogen mediated surface conductivity. This conduction mechanism typically requires surface acceptors from the ambient air dissociated in an adsorbed wetting layer. Therefore

measurements made in medium vacuum and at temperatures above the boiling point of water would not be expected to exhibit this behaviour. Although surface conductivity based on systems other than the wetting layer/atmospheric acceptors (see Chapter 3), the likely reason for the persistent surface conductivity is the combination of insufficient vacuum conditions and the increased difficulty in fully drying the nanoparticles.

The ubiquitous occurrence of picofarad magnitude capacitance throughout the sample series suggests the conduction paths observed are associated with grain interiors.[49] This is unexpected as the disordered (and conductive) sp^2 shell of the ND is supposed to dominate conduction through the ND, however these findings indicate this is not the case. Whilst surface treatments certainly modulate the number of charge carriers present, this study indicates the bulk of charge transfer occurs within the ordered sp^3 interior of the ND, not the mixed phase surface. One possible explanation lies in the fact that the depth of hydrogen mediated subsurface acceptor sites in bulk diamond has been shown to be approximately 15nm.[64] This length scale is greater than the ND particle, therefore it is possible that acceptor sites are located throughout the ND, within the highly crystalline centre. When surface transfer doping is not present (i.e. oxygen terminated ND) capacitance values of the order of tens of picofarads are observed, suggesting conduction through the outer sp^3 regions where higher concentrations of defects are present at the interface between the core and shell of the ND,[65] but not through the grain boundary where nanofarad magnitude capacitance is expected.[49] This observation suggests the conduction mechanism of ND layers in this arrangement do not easily compare to traditional NCD when looked at carefully, although the macro scale effect of the combined ND layers is somewhat similar to bulk diamond in terms of its magnitude of impedance. This

suggests that whilst the cores of the particles are indeed fully sp^3 bonded, the interaction between the particles is less well defined, and certainly distinct from NCD. What is certain is that there lies a small window for the selective oxidation of sp^2 over sp^3, between 400 and 430°C.[66] Therefore within the results presented here there are likely displaying competing regimes of sp^2 and sp^3 oxidation, further complicating the evolution of the conduction paths at elevated temperatures. This may be further studied through the use of inert atmospheres (i.e. helium) in lieu of sufficient vacuum pressures - borrowing from the field of thermogravimetric analysis, where the change in the physical structure of materials is contrasted both in ambient air and an inert atmosphere.

[1] S Szunerits & R Boukherroub, "Different Strategies for Functionalization of Diamond Surfaces," Journal of Solid State Electrochemistry 12(10), 2008, pp. 1205–1218.
[2] J B Zang *et al.*, "Electrochemical Properties of Nanodiamond Powder Electrodes," Diamond and Related Materials 16(1), 2007, pp. 16–20.
[3] M Bevilacqua *et al.*, "The Influence of Ammonia on the Electrical Properties of Detonation Nanodiamond," Journal of Applied Physics 106(12), 2009, 123704.
[4] R Ahmad *et al.*, "Nanodiamond-Gated Diamond Field-Effect Transistor for Chemical Sensing Using Hydrogen-Induced Transfer Doping for Channel Formation," Applied Physics Letters 97(20), 2010, 203503.
[5] R Ahmad *et al.*, "Nanodiamond-Coated Silicon Cantilever Array for Chemical Sensing," Applied Physics Letters 97(9), 2010, 093103.
[6] R Martin et al., "Nano-Jewels in Biology. Gold and Platinum on Diamond Nanoparticles as Antioxidant Systems Against Cellular Oxidative Stress," ACS Nano 4(11), 2010, pp. 6957–6965.
[7] L McGuinness *et al.,* "Quantum Measurement and Orientation Tracking of Fluorescent Nanodiamonds Inside Living Cells," Nature Nanotechnology 6(6), 2011, pp. 358–363.
[8] A Thalhammer *et al.*, "The Use of Nanodiamond Monolayer Coatings to Promote the Formation of Functional Neuronal Networks," Biomaterials 31(8), 2009, pp. 1–8.
[9] N Gibson *et al*., "Immobilization of Mycotoxins on Modified Nanodiamond Substrates," Biointerphases 6(4), 2011, pp. 210–217.
[10] N Gibson *et al.*, "Electrostatically Mediated Adsorption by Nanodiamond and Nanocarbon Particles," Journal of Nanoparticle research, 14(3), 2012, pp. 1-12.
[11] Q Zhang *et al*., "Fluorescent PLLA-Nanodiamond Composites for Bone Tissue Engineering," Biomaterials 32(1), 2011, pp. 87–94.
[12] O Shenderova *et al*., "Detonation Nanodiamond and Onion-Like Carbon: Applications in Composites," Physica Status Solidi *(a)* 205(9), 2008, pp. 2245–2251.
[13] R Lam & D Ho, "Nanodiamonds as Vehicles for Systemic and Localized Drug Delivery," Expert Opinion on Drug Delivery 6(9), 2009, pp. 883–895.
[14] E Chow *et al*., "Nanodiamond Therapeutic Delivery Agents Mediate Enhanced Chemoresistant Tumor Treatment," Science Translational Medicine 3(73), 2011, 73ra21.
[15] M Chen *et al*., "Nanodiamond Vectors Functionalized with Polyethylenimine for siRNA Delivery," The Journal of Physical Chemistry Letters 1(21), 2010, pp. 3167–3171.
[16] D Kalyanasundaram & P Molian, "Electrodeposition of Nanodiamond Particles on Aluminium Alloy A319 for Improved Tribological Properties," Micro & Nano Letters, IET 3(4), 2008, pp. 110–116.
[17] V Dolmatov, "Detonation Synthesis Ultradispersed Diamonds: Properties and Applications," Russian Chemical Reviews 70(7), 2007, pp. 607–626.
[18] V Zhirnov *et al*., "Electron Emission Properties of Detonation Nanodiamonds," Physics of the Solid State 46(4), 2004, pp. 657–661.
[19] V Osipov *et al.,* "Magnetic Properties of Hydrogen-Terminated Surface Layer of Diamond Nanoparticles," Fullerenes, Nanotubes and Carbon Nanostructures 14(2), 2006, pp. 565–572.
[20] O Shenderova, "Production of Conductive Nanodiamond by Dynamic Synthesis Approaches," U.S. Patent Application 12/820,230.

[21] D Malta *et al*., "Secondary Electron Emission Enhancement and Defect Contrast From Diamond Following Exposure to Atomic Hydrogen," Applied Physics Letters 64(15), 1994, pp. 1929–1931.
[22] T Kondo *et al*., "Electrical Conductivity of Thermally Hydrogenated Nanodiamond Powders," Journal of Applied Physics 113(21), 2013, pp. 214307.
[23] J Cui *et al*., "Electron Affinity of the Bare and Hydrogen Covered Single Crystal Diamond (111) Surface," Physical Review Letters 81(2), 1998, pp. 429–432.
[24] M Karlsson *et al*., "From Hydrophilic to Superhydrophobic: Fabrication of Micrometer-Sized Nail-Head-Shaped Pillars in Diamond," Langmuir 26(2), 2010, pp. 889–893.
[25] S Zeppilli *et al*., "Thermal Stability and Surface Modifications of Detonation Diamond Nanoparticles Studied with X-Ray Photoelectron Spectroscopy," Diamond and Related Materials 19(7), 2010, pp. 846–853.
[26] S Su *et al.*, "Hydrogen-Terminated Detonation Nanodiamond: Impedance Spectroscopy and Thermal Stability Studies," Journal of Applied Physics 113(2), 2013, 023707.
[27] S Nath & J Wilson, "Impedance Measurements on CVD Diamond," Diamond and Related Materials 5(1), 1996, pp. 65–75.
[28] S Curat *et al*., "An Impedance Spectroscopic Study of N-Type Phosphorus-Doped Diamond," Journal of Applied Physics 98(7), 2005, 073701.
[29] N Tumilty *et al*., "Multiple Conduction Paths in Boron δ-Doped Diamond Structures," Applied Physics Letters 94(5), 2009, 052107.
[30] H El-Hajj *et al*., "Characteristics of Boron δ-Doped Diamond for Electronic Applications," Diamond and Related Materials 17(4), 2008, pp. 409–414.
[31] G Cunningham *et al.*, 'Ozone-Modified Detonation Nanodiamonds'. Diamond & Related Materials 17(4-5), 2008, pp. 650-654.
[32] O Shenderova *et al.*, 'Modification Of Detonation Nanodiamonds By Heat Treatment In Air'. Diamond and Related Materials 15(11-12), 2006, pp. 1799-1803.
[33] D He *et al*., "Electron Transport and Electron Field Emission of Nanodiamond Synthesized by Explosive Detonation," Diamond and Related Materials 9(9), 2000, pp. 1600–1603.
[34] E Osawa, "Monodisperse Single Nanodiamond Particulates," Pure and Applied Chemistry 80(7), 2008, pp. 1365–1379.
[35] A Chaudhary *et al*., "Electrical Properties of Monodispersed Detonation Nanodiamonds," Applied Physics Letters 96(24), 2010, 242903.
[36] J Wortman and R Evans, "Youngs' Modulus, Shear Modulus and Poisson's Ratio in Silicon and Germanium", Journal of Applied Physics 36(1), pp. 153-156.
[37] A Chaudhary, "Electronic properties and applications of Nanodiamond" PhD thesis, UCL, 2012.
[38] Solartron 1296A, Solartron, accessed 13th June 2013, http://www.solartronanalytical.com/material-test-systems/model-1296a-dielectric-interface-system.aspx
[39] N Hirose & A West, "Impedance Spectroscopy of Undoped $BaTiO_3$ Ceramics", Journal of the American Ceramic Society 79, 1996, pp. 1633-1641.
[40] T Jiang & K Xu. "FTIR study of ultradispersed diamond powder synthesized by explosive detonation." Carbon 33(12), 1995, pp. 1663-1671.
[41] P Chung *et al.*, "Spectroscopic study of bio-functionalized nanodiamonds." Diamond and related materials 15(4), 2006, pp. 622-625.
[42] C Chu *et al.*, "Temperature-dependent surface CO stretching frequency investigations of functionalized nanodiamond particles." Diamond and Related Materials 18(1), 2009, pp. 76-81.
[43] C Cheng *et al.*, "The CH stretching features on diamonds of different origins." Diamond and related materials 14(9), 2005, pp. 1455-1462.

[44] L Ostrovskaya *et al.*, "Wettability and surface energy of oxidized and hydrogen plasma-treated diamond films." Diamond and related Materials 11(3), 2002, pp. 845-850.
[45] O Shenderova *et al.,* "Surface chemistry and properties of ozone-purified detonation nanodiamonds." The Journal of Physical Chemistry C 115(20), 2011, pp. 9827-9837.
[46] M Bevilacqua *et al.*, 'Electrical Properties Of Aggregated Detonation Nanodiamonds'. Applied Physics Letters 93(13), 2008, 132115.
[47] J Lee *et al.*, "Oxidation of CVD diamond powders." Diamond and related materials 13(4), 2004, pp. 1070-1074.
[48] P Vanýsek, "Introduction to electrochemical impedance", DTIC Report, Order No. AD-A277081, 1994, pp. 78, CAN 123:352926.
[49] L Hench & J West, Principles of Electronic Ceramics, Wiley, 1990, Chapter 5.
[50] V Pichot *et al.*, 'An Efficient Purification Method For Detonation Nanodiamonds'. Diamond & Related Materials 17(1), 2008, pp. 13-22.
[51] H Kawarada, 'Hydrogen-Terminated Diamond Surfaces And Interfaces'. Surface science reports 26(7), 1996, pp. 205-206.
[52] H Kulakova, 'Surface Chemistry Of Nanodiamonds'. Physics of the Solid State, 2004, pp. 1-8.
[53] V Mortet *et al.*, 'Thin Nanodiamond Membranes And Their Microstructural, Optical And Photoelectrical Properties'. Diamond and Related Materials 14(3-7), 2005, pp. 393-397.
[54] C Su & J Lin, 'Thermal Desorption Of Hydrogen From The Diamond C(100) Surface'. Surface Science 406(1-3), 1998, pp. 149-166.
[55] V Kuznetsov & Yu Butenko, "Nanodiamond graphitization and properties of onion-like carbon", In Synthesis and Applications of Ultrananocrystalline Diamond", D Gruen *et al.* (eds.), Springer: Dordrecht, 2005, pp. 199–216.
[56] D Zhao *et al.*, 'Size And Temperature Dependence Of Nanodiamond–Nanographite Transition Related With Surface Stress'. Diamond and Related Materials 11(2), 2002, pp. 234-236.
[57] C Pantea *et al.*, "Dislocation density and graphitization of diamond crystals." Physical Review B 66(9), 2002, 094106.
[58] V Danilenko, 'Assessment Of The Influence Of Particle Size And Degree Of Cohesion Of Detonation Nanodiamonds On Their Thermal Stability'. Journal of Superhard Materials, 2009, pp. 1-8.
[59] H Young, University Physics, 7th Ed., Addison Wesley, 1992, pp. 29-8
[60] A Kraft. "Doped diamond: a compact review on a new, versatile electrode material." International journal of Electrochemical Science, 2(5), 2007, pp. 355-385.
[61] S Szunerits & R Boukherroub. 'Different Strategies For Functionalization Of Diamond Surfaces'. Journal of Solid State Electrochemistry 12(10), 2008, pp. 1205-1218.
[62] S Su *et al.*, 'Hydrogen-Passivated Detonation Nanodiamond: An Impedance Spectroscopy Study'. Diamond & Related Materials 113(2), 2011, pp. 1-5.
[63] L Li & X Zhao, 'Dangling Bond-Induced Graphitization Process On The (111) Surface Of Diamond Nanoparticles'. The Journal of Chemical Physics, 2011, pp. 1-11.
[64] D Tryk *et al.*, 'Relationships Between Surface Character And Electrochemical Processes On Diamond Electrodes: Dual Roles Of Surface Termination And Near-Surface Hydrogen'. Diamond and Related Materials 10(9-10), 2001, pp. 1804-1809.
[65] V Mochalin *et al.*, 'The Properties And Applications Of Nanodiamonds'. Nature Nanotechnology 7(1), 2011, pp. 11-23.

[66] S Osswald et al., "Control of sp2/sp3 carbon ratio and surface chemistry of nanodiamond powders by selective oxidation in air", Journal of the American Chemical Society 128, 2006, pp. 11635.

Chapter 7: Fabrication of Nanodiamond-Microchannel plate structures

7.1. Introduction

The second half of the experimental chapters within this thesis (Chapters 7 and 8) will take a somewhat different format as they document attempts to solve specific engineering challenges, with the results were reported to the industrial collaborator for this project, Photonis, over the duration of the PhD.

Here, the aim was to achieve thin conformal nanocrystalline diamond (NCD) layers penetrating controlled depths of the microchannel plate (MCP) in order to combine the benefits associated with nanocrystalline diamond without significantly altering the MCP fabrication route. The primary goals of this aspect of the LCN-Photonis collaboration are:

1) Conferring the observed high yield secondary electron emission (SEE) seen on diamond[1]onto the diamond-MCP device. Briefly, the SEE on the channel wall of the MCP averages at 2 per incident electron, therefore statistically speaking this may be any value between 0 and 4, if 0 electrons are emitted then the incident photon that provided the primary electron has been wasted, resulting in decreased signal to noise ratio – for a detailed description, see Chapter 8.

2) An NCD layer is also expected to prevent sputtered ion production in the MCP, where positive ions can be accelerated back to the photocathode (see figure 3.7). Therefore the NCD layer should prevent poisoning of the layer and result in a greatly extended lifetime of the device.

In addition, any addition to the device must maintain or surpass current MCP characteristics for diamond inclusion to be considered successful, leading to inclusion in later Photonis products. Particularly important is the 100 Mohm resistance through the MCP, necessary to maintain a strip current low enough to enable the 1000 V potential difference through the MCP. This potential difference is needed to accelerate electrons to energies sufficient for the liberation of secondary electrons within the channels of the MCP

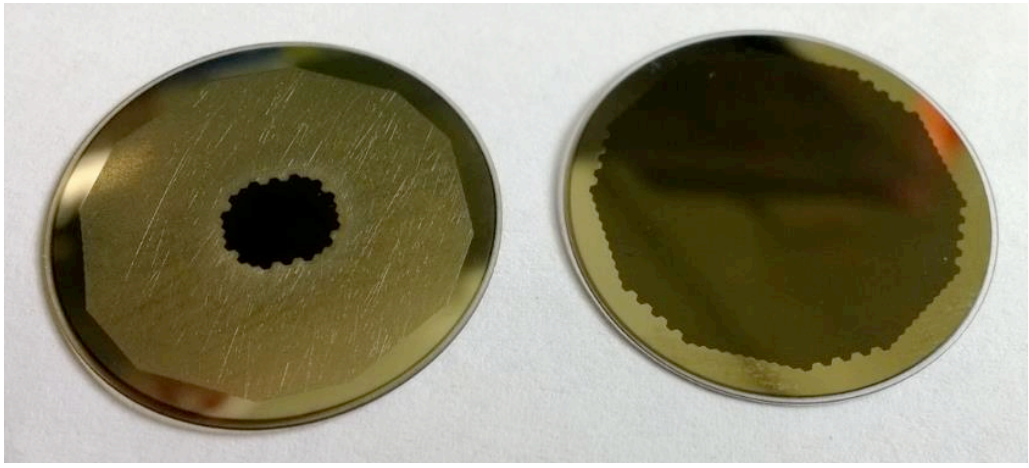

Figure 7.1 Reduced channel (left) and full size MCP supplied by Photonis. Note both MCPs have undergone metallisation of the top and bottom surfaces of the inactive regions.

The MCPs used throughout this chapter were supplied by Photonis, who kindly supported this work. Two varieties of MCP were available, the first a "full-size MCP" 25 mm in diameter with 11 million 6 μm wide channels set 8° from the normal,[2] and the second a "reduced channel MCP" where the active area has been reduced to 6 mm. The reduced channel MCP has greater mechanical stability and thermal conductivity and is generally used by Photonis (and throughout this thesis) as a test structure in research and development.

The MCP has severely limited thermal budget, the structure softens in temperatures beyond 400-420°C (bearing in mind the typical growth temperature of diamond lies in the 800-1000°C region)[3]. Therefore, custom made sample holders for the Seki Technotron AX5010 reactor were required to enable aggressive cooling of the substrates. Three iterative designs were created, allowing increased microwave power to be used, resulting in greater growth rates and reducing the duration of growth required and hence the stress imparted to the MCP during growth. The distance of the sample to the centre of the plasma ball when undergoing diamond growth was also considered, resulting in the final iteration of the sample holder incorporating height adjustment. The key goal of this sub-project was to enable the growth of a conformal NCD layer through 60 μm (or 10 channel diameters, '10D') of the MCP. Thus, when optimal diamond growth conditions were determined on silicon (see Chapter 8), this could be incorporated on an MCP. 10D was chosen by Photonis as an ideal depth into the channel such that incoming electrons will always interact with diamond coated channel first, allowing for higher secondary electron yields (SEY). This higher yield is expected to have a large effect on the device signal to noise ratio as currently, due to the statistical nature of secondary electron emission in the MCP, whilst the average SEY value is quoted as 2, zero yield is a possibility and therefore results in the loss of the incoming electron. Raising the SEY to 10 should alleviate this problem, for more detail please see Chapter 8.

The primary engineering challenge associated with this chapter is the growth of NCD on complex three dimensional structures. Indeed this is the first time diamond has been grown on MCP structures. Previous efforts to fabricate

diamond structures outside the traditional planar configuration were usually constrained to the top-down approach. This approach typically etches (e.g. reactive ion etching, RIE) or mills (e.g. focused ion beam) bulk diamond into the desired shape. Taking this idea further, planar films were grown heteroepitaxially upon silicon and both the diamond and its substrate have been selectively etched to create three dimensional diamond coated pillars. These complex post like structures were intended for use as superhydrophobic/hydrophilic surfaces depending on the surface termination of the diamond surface. Diamond grown on three dimensionally structured substrates have been previously reported by Monteiro *et al.* where attempts were made at depositing chemical vapour deposition (CVD) diamond inside silicon vias coated with a layer of tetragonal amorphous carbon (a form of diamond-like carbon).[4] These structures were narrower than MCP channels but significantly shallower and hence pose a similar challenge to that attempted in this chapter. However, a direct comparison is not possible as the aforementioned example was a proof of concept whereas the current work requires high quality diamond (with high impedance being of major concern) as an electron emitter, grown in severely sub-optimal conditions.

7.2. Experimental methods

Nanodiamond deposition: ND was deposited using a modified version of the ultrasonication technique described in 5.2 where MCPs were inserted in a purpose built water tight jig provided by Photonis. The jig was then submerged in a DND hydrocolloid (concentration 0.5 g/l DND in deionised (D.I) water, ≥20MΩ.cm) and subjected to varying durations of ultrasonication (US), or

simply dipped in nanodiamond (ND) hydrocolloid without additional agitation. MCPs were then carefully dried in N_2 to avoid damaging the MCP. In order to achieve a variable depth of ND penetration, before the insertion of the MCP, the jig is first backfilled with a defined quantity of D.I water (ranging between 1600 - 20 µl) using the following procedure:

ι. Fill jig with D.I water (1600µl, 800µl, 60µl, 40µl and 20µl.)

ιι. Place MCP on jig, forcing water below through channels

ιιι. Tighten jig and add 3ml of ND solution (0.5 g/l) to top surface

ιϖ. Ultrasound for required duration

ϖ. Rinse jig in D.I water 30 seconds with mild agitation

ϖι. Remove MCP from jig and rinse for 30 seconds in D.I water with mild agitation

ϖιι. N_2 dry (from bottom first)

Figure 7.2 MCP jig supplied by Photonis before MCP insertion (left) and after removal from water rinse (right). Note the well can be observed in the left image, where backfilled water is placed. The mirror finish on the seal surrounding the MCP makes the jig water-tight.

Diamond growth: After seeding each MCP would undergo a short growth in a customised microwave plasma enhanced chemical vapour deposition (MWPECVD) chamber (Seki Technotron AX5010) in order to 'fix' them in place for subsequent analysis, as NDs would be too small to image without enlargement. Growth conditions were kept homogenous throughout the series of experiments: 400˚C +/- 10°C, 2 hours duration, and 0.5% methane in hydrogen with 100 sccm flow. Sample temperature was monitored by a Williamson Pro 92-20 dual wavelength fibre optic pyrometer (temperature range: 200-600°C). The samples were heated by the hydrogen plasma until within 10% of their desired growth temperature, at which point methane is slowly added to avoid thermal shock and to reduce the inclusion of non-diamond carbon. The sample stage used for the depth of ND penetration experiment was the 2 pipe sample holder/cooler with an additional of 10mm shim. The sample stage was supplied with high pressure chilled water from a Neslab CFT-300 chiller unit, set to provide 12°C water. To prevent accumulation of non-diamond carbon phases through the MCP channels, the growth chamber was fitted with a vacuum pump connected to the rear of the MCP, preventing a long residence time of reaction products far from the plasma surface.[5] To prevent thermal shock damaging the MCP, a temperature ramp of 2°C/minute between room temperature and 350°C, and a ramp of 1°C/minute between 350-400°C. This ensured minimal distortion to the MCP's shape, and any deviations from this were noted in the samples' experimental log.

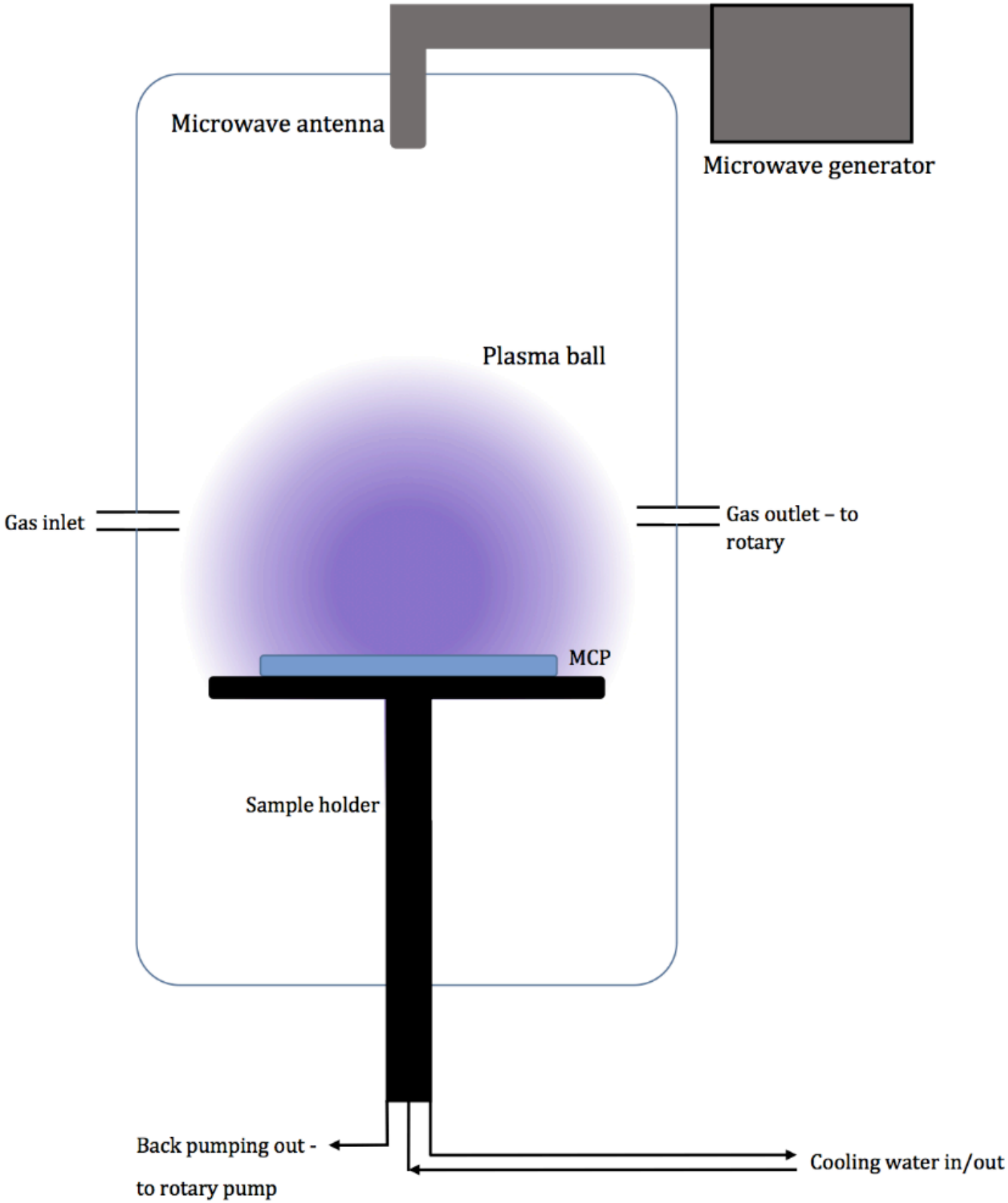

Figure 7.3 Schematic of customised MWPECVD chamber, showing arrangement of back pumping and substrate cooling.

Scanning electron microscope: The scanning electron microscope (SEM) was used extensively to acquire images of diamond seeding/growth through the length of the channel for subsequent image processing (see below). Samples were cleaved to expose the length of the channel and a suitable channel was selected near the centre of the MCP. Images were taken along the length of the channel. The SEM was operated in combined secondary electron/backscatter mode at an 80:20 ratio in order to obtain a satisfactory combination of image contrast and topographical information (secondary mode) and material identification (backscatter mode). All images, unless explicitly stated, are taken at x11,000 magnification with a working distance of 8.6 mm. Images were acquired using the lower detector (LEI) due to the propensity of the samples to charge up during scanning. A low accelerating voltage of 2.0 kV was used to yield detailed topographical information as higher accelerating voltages probe the subsurface structure to a greater extent. When imaging proved difficult due to excessive charging of the surface (essentially throughout Round 1), a <1nm coating of amorphous carbon was applied to one of the cleaved halves of the MCP (noted in the experimental log). This allowed built up charge from the electron beam to be effectively dissipated. All images were acquired with column vacuum conditions greater than 3.6×10^{-4} Pa.

Image processing: Individual SEM images were first combined to give one continuous image of the channel. The image was then divided into 3.0 × 2.5 μm sections taken from the middle of the channel in order to provide images as flat as possible to aid subsequent image processing. Both image manipulation stages were performed with Adobe Photoshop CS5. Next the image was flattened using Gwyddion, the image analysis software detailed in section 5.2. Gwyddion was then used to create a particle mask, as described in 5.2. Average

grain size, grain density, and area coverage were then calculated using the extracted values from the particle mask. Average grain size is calculated by taking the mean number of equivalent square sides (measured in pixels) in each individual grain marked on the mask, and converting this figure to metres. The standard deviation of the mean is used to denote the error on each average grain size measurement. Grain density is taken as the number of individual grains in the area bounded by the cropped image (3.0 × 2.5 μm), the error on the measurement is taken to be 10% across all values due to an estimation of the limitation in resolution of the SEM data causing twinned or overlapping grain phases being counted as more than one grain, or several grains without a distinct grain boundary being counted as a single grain. Area coverage takes the proportion of the total image area covered by the grain mask. As the Gwyddion software includes a non-zero area for grain boundaries, area coverage greater than 75% can be thought of as a complete film. The error included on the area coverage is taken to be 5% due to the limit of resolution on the images enabling misidentification of grain coverage. Thicknesses of the NCD layer at the channel entrance was estimated by focusing on the cleaved cross section, and taking the average of six measurements using the ruler tool within the Gwyddion software.

7.3. Results and discussion

7.3.1 Thermal obstacles

As previously mentioned, the MCP has a thermal limit of 400-420°C beyond which the doped glass structure softens and device characteristics are permanently degraded. Hence substantial efforts were put into the development of cooled sample stages to grow diamond within this temperature

limit. The efficacy of sample stage coolers was continuously evaluated and iterative redesigns were conducted to enhance cooling performance. Cost was a factor in the design process, with increasing complexity considerably increasing the cost of production of the bespoke coolers. Additionally the adequate supply of chilled water was of the highest concern, initial attempts utilised the same chiller unit (Julabo FLW1701, 1.5 kW cooling capacity at 1 bar)[6] as was used for cooling the microwave power supply on the MWPECVD kit. However this was found to be insufficient and hence for all data quoted in table 7.1 the Neslab CFT-300 recirculating chiller is used. The Neslab CFT-300 has a maximal cooling capacity of 9 kW at a pressure of 2 Bar.[7]

The first cooler design used a two pipe arrangement (hence designated the '2 pipe cooler') where one cooling line was welded to the sample mount, which in turn screws into the sample holder. This was simplest design and it was

Figure 7.4 Left: 2 pipe cooler complete view. Note the back pumping line is sealed off in this image. Right: View of sample mount surface, showing carbonaceous deposits.

found the screw-mount arrangement provided a surface sufficiently distant from the plasma to allow the build-up of graphitic deposits, limiting the quality of diamond able to be grown in the chamber.

The second cooler design used four pipes, after it was noted the shaft of the '2 pipe' sample holder remained extremely hot after growth. The first pair cools the sample holder shaft and the second pair cool the sample mount. The screw-mount assembly was dispensed with in favour of a permanent braze between the cooling pipe and the sample mount. The sample mount contained a small void slightly larger than the cooling pipe to spread the cooling fluid, similarly the shaft cooling pipe opened into a small void on the perimeter of the sample mount surface. This arrangement was found to be more effective than the 2-pipe cooler in terms of cooling ability. Table 7.1 shows the increased power and pressure applied whilst maintaining a substrate temperature of 400°C. However, the setup resulted in several MCPs being highly warped or breaking altogether (Figure 7.7(a/c)), possibly due to the two separate cooling zones causing a temperature gradient across the MCP. Hence a further iteration of the cooler design was initiated.

Figure 7.5 Left: 4 pipe cooler complete view, back pumping port is obscured by cooling pipes. Right: Focused view of sample mount surface. Note the recess for the MCP in the centre.

The third and final cooler design presented in this thesis utilised a large, unified reservoir over the previous cooler pipe designs. This resulted in a very large gain in cooling efficacy as shown in table 7.1. It was noted that the previous iterations of cooler design maintained a gap of approximately 10 mm between the bottom of the plasma ball and the sample surface (see Figure 7.3). This raised concerns about the degree of activation of hydrocarbon groups and atomic hydrogen in this arrangement of low power and high substrate-plasma distance, as previous reports suggest this contributes to sub-optimal conditions.[8,9] Therefore the redesigned stage included the ability to raise and lower the substrate by +/- 50 mm, in order to maximise growth efficiency. This movement freedom introduced instability into the microwave resonance

chamber (see section 4.4.1), however after careful calibration a stable plasma, 'hugging' the sample mount was achieved (see Figure 7.3).

Figure 7.6 Left: Complete view of reservoir cooler. Note the largely compressed vacuum bellows present (photograph taken whilst cooler was at almost full extension). Right: Focus view of sample mount. Note the reuse of an inner recess for the MCP, combined with a larger outer recess for a weight to cover the MCP in an attempt to prevent warping – however this was not required in later growths as no warping was observed.

Stage variant	MCP- Typical microwave power (Watts)	MCP - Typical gas pressure (Torr)	Silicon- Typical microwave power (Watts)	Silicon - Typical gas pressure (Torr)
2 pipe cooler	570	12	600	13
4 pipe cooler	620*	12*	680	15
2 pipe reservoir + height adjustment	950	30	1270	40

Table 7.1 Typical growth parameters at 400°C for successive iterations of sample cooler design on MCP and silicon wafer. * Growth using the 4 pipe cooler resulted in the MCP breaking or warping to an unacceptable degree.

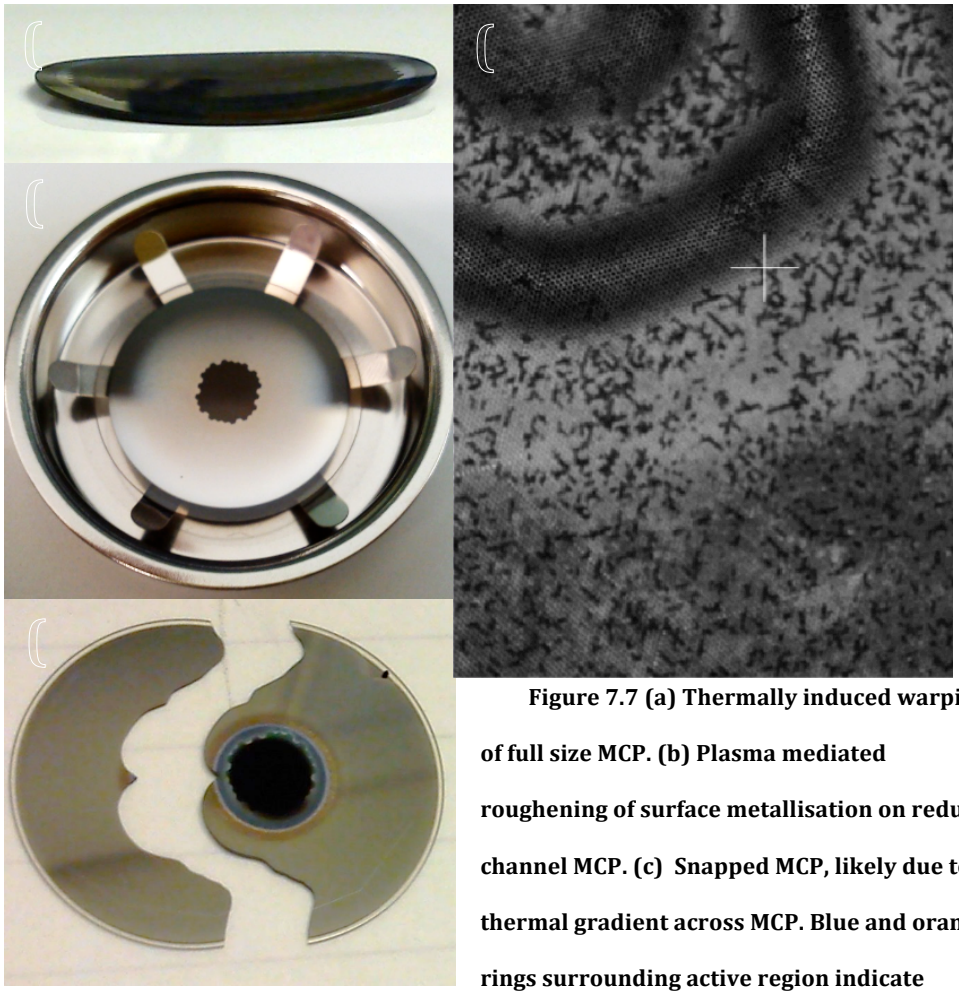

Figure 7.7 (a) Thermally induced warping of full size MCP. (b) Plasma mediated roughening of surface metallisation on reduced channel MCP. (c) Snapped MCP, likely due to thermal gradient across MCP. Blue and orange rings surrounding active region indicate diamond growth. (d) Optical microscope image of damage to active region in sample that exceeded 420°C.

7.3.2 Nanodiamond seeding of microchannel plates

In order to achieve control over the depth of penetration of ND when seeding before NCD growth, reduced channel MCPs were first backfilled with D.I water to reduce NDs adhering to the sidewalls of the MCP channels from the ND solution. Round 1 focused on the backfill volume, whilst Round 2 varied the duration of sonication in an attempt to further improve the resultant NCD layers both in terms of depth of penetration and conformity to the original MCP shape. The depth of penetration was initially determined by eye (via SEM images) as the region where ND coverage had fallen to approximately half its original value. This was performed to help choose which backfill volume to maintain throughout Round 2. Later, once both Round 1 and 2 were complete, a detailed analysis of the SEM data was prepared (see 7.2). Here, the composite SEM image of the entire channel has been cropped to show only the ND coated regions. A discussion of the results and their trends is presented at the end of this section.

Round 1 results

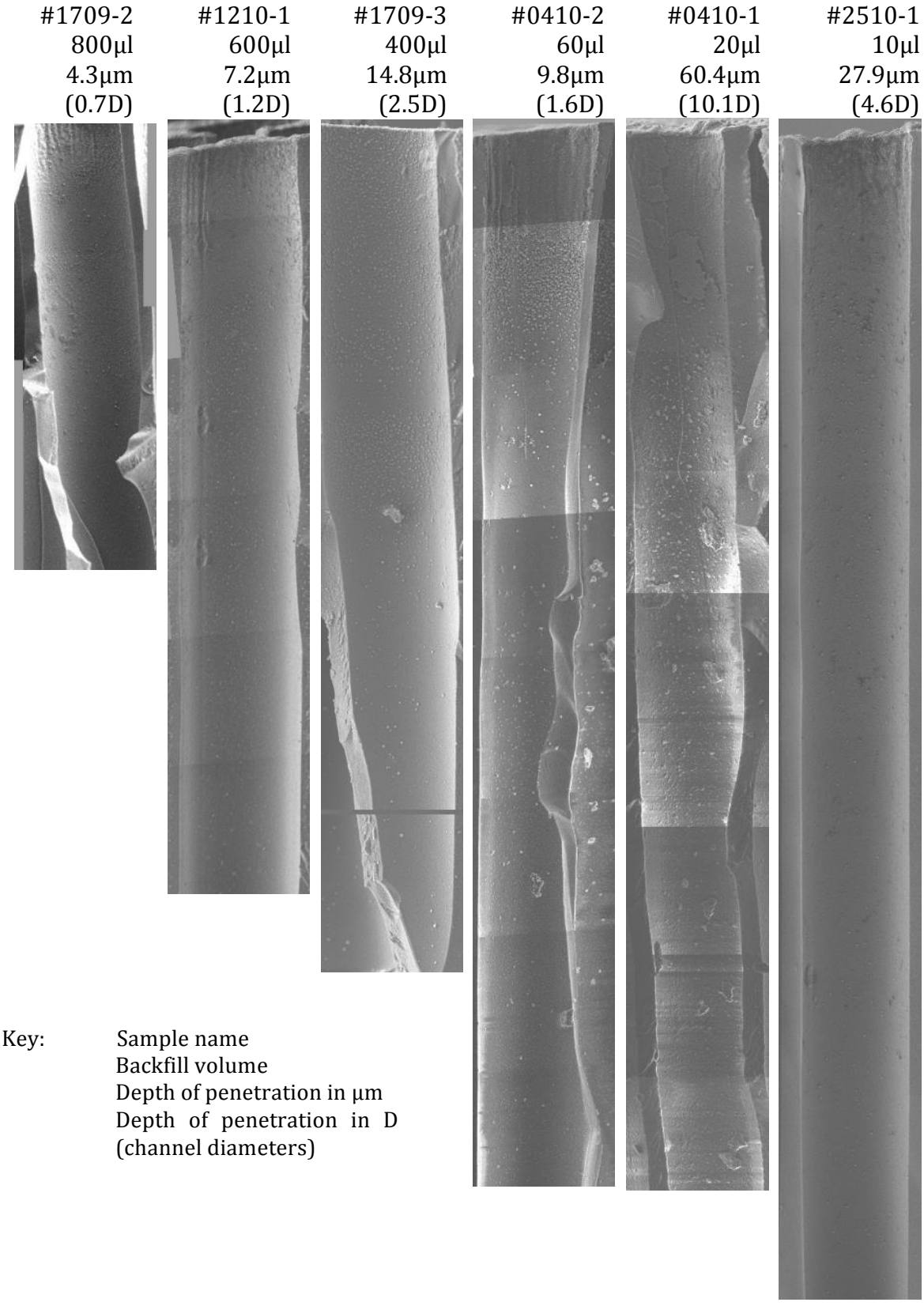

Figure 7.8 Round 1 results. Labelling scheme is as follows: Sample name, D.I water backfill volume, and depth of penetration (both in µm from channel entrance and in multiples of 'D' the channel diameter).

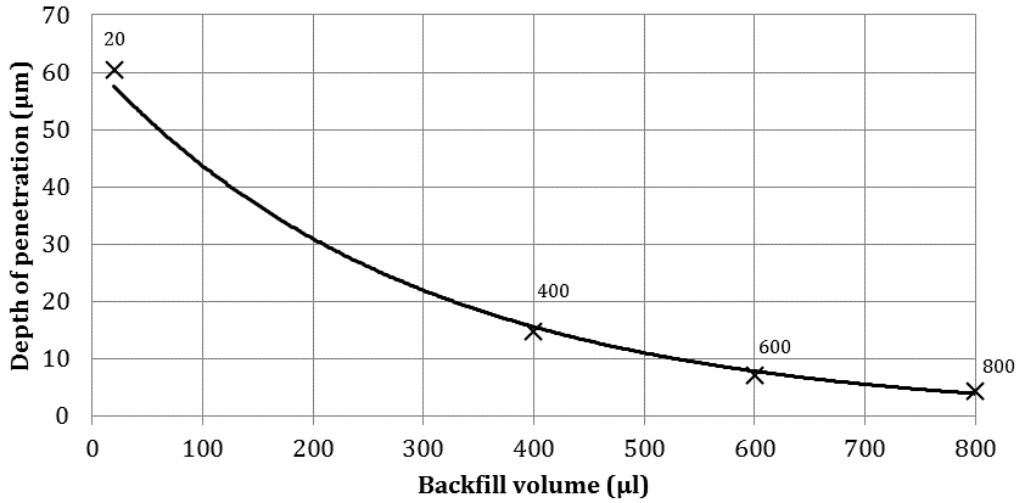

Figure 7.9 Depth of penetration (µm) as a function of backfill volume (µl). The trend line exhibits an approximately exponential response. Note the exclusion of #0410-2 due to erroneous growth conditions.

Sample name	Backfill volume (µl)	Channel penetration (µm)	Penetration diameters	Outlier results
1709-2	800	4.3	0.7	
1210-1	600	7.2	1.2	
1709-3	400	14.8	2.5	
0410-2	60	9.8	1.6	Growth error (2% CH_4)
0410-1	20	60.4	10.1	
2510-1	10	27.9	4.6	Backfill too small, incomplete coverage

Table 7.2 Round 1's raw data of depth of penetration (µm) as a function of backfill volume (µl), with inclusion of outlier results.

Note: Round 1's full sample details are given in Appendix B

Round 2 results

Here, the backfill volume was set at 20µl, and a variation of deposition parameters was performed in order to ascertain the optimal deposition conditions.

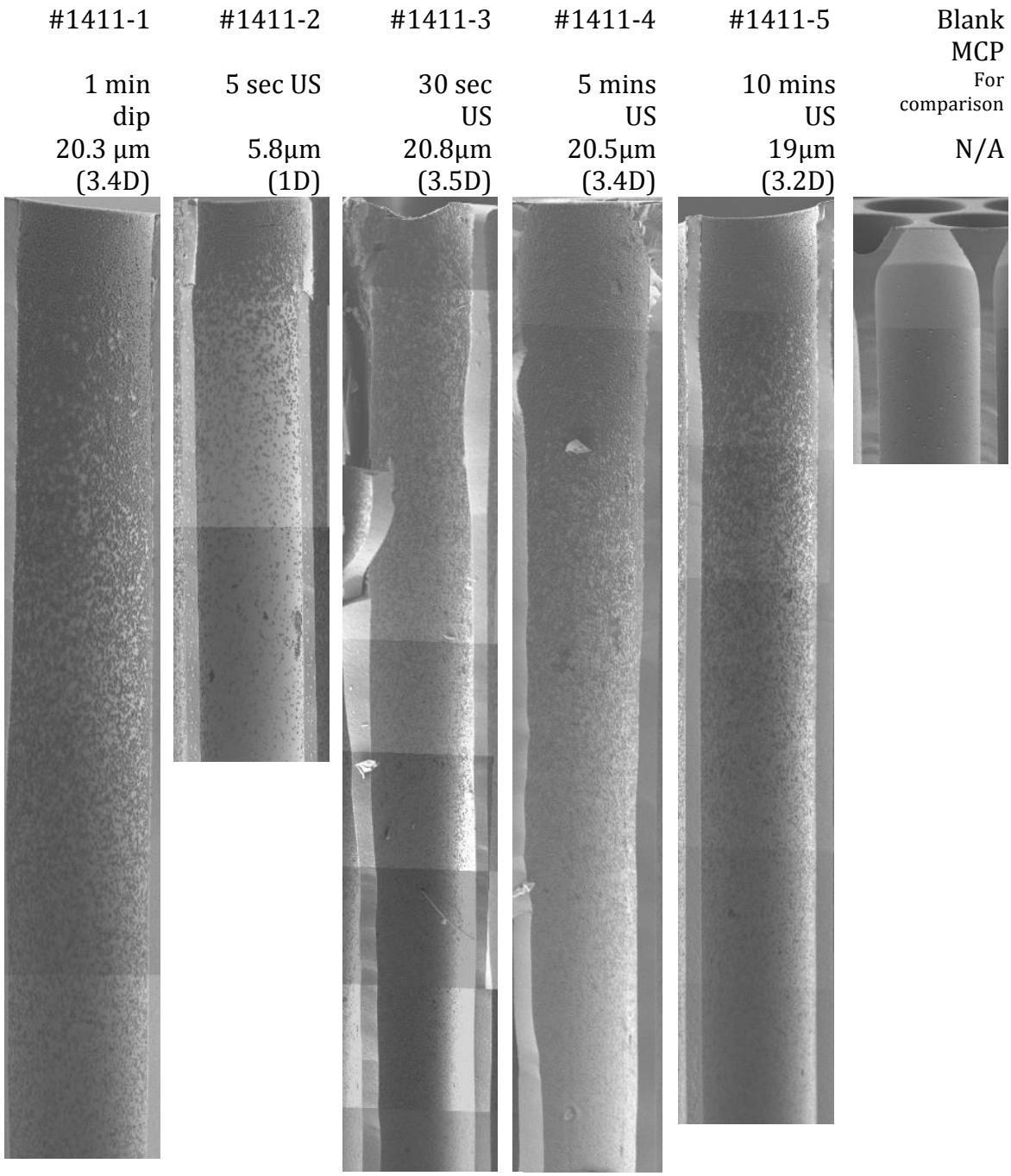

Key: Sample name
Backfill volume
Depth of penetration in µm
Depth of penetration in D (channel

Figure 7.10 Round 2 results. Labelling scheme is as follows: Sample name, deposition conditions, and depth of penetration (both in µm from channel entrance and in multiples of 'D' the channel diameter).

Sample name	Seeding parameters	Channel penetration (μm)	Penetration diamters
1411-1	1 min dip	20.3	3.4
1411-2	5 sec US	5.8	1.0
1411-3	30 sec US	20.8	3.5
1411-4	5 mins US	20.5	3.4
1411-5	10 mins US	19.0	3.2
blank mcp			

Table 7.3 Round 2's raw data of depth of penetration (μm) as a function of backfill volume (μl).

Note: Round 1's full sample details are given in Appendix B

7.4. Discussion of results

Vertically aligned lines are apparent on the channels of Round 1's MCPs, particularly near the entrance where growth is thickest, giving an indication of high stress on the NCD layers in Round 1.[10] The total absence of such lines on the Round 2's MCPs suggests this is not due to ultrasonication of the MCPs but possibly from the natural variance in surface properties seen between batches of MCPs (Round 1 and 2's MCPs were manufactured and supplied by Photonis several months apart). The average particle size data for Round 1 did not show a clear trend with respect to the volume of water used to backfill the jigs. However, for Round 2 there was a more defined negative correlation of particle size with depth in channel (distance on the x-axis). This is in keeping with the observation that the efficacy of the plasma on growth would be restricted as it penetrated deeper into the channel, as has been reported by others.[4] As the initial starting size of the ND is fixed at 5-10 nm, variation in the grown NCD

layers must be ascribed to the local conditions within the plasma. Diamond growth rates have previously been negatively correlated with distance from the carbon activation vector[11] as the gas phase mixture is altered by surface (and gas phase) recombination reactions.[4] Whilst the data does not conclusively prove this hypothesis, the results suggest an effect would be less than a 50% drop over 30μm. The range of average grain size throughout Rounds 1 and 2 did not exceed 34 nm (e.g. #1709-3: maximum – 77 nm, minimim – 34 nm). It is worth noting that sample 1709-3 is the maximum, whereas the average range was calculated to be 23 nm. The absolute values for the average grain size did not fall below 10 nm (#2510-1) nor exceed 77 nm (#1709-3). This reduction in growth rate has implications for future secondary electron emission, as it has been reported that increased distance from the CVD plasma causes a lower incidence of hydrogen incorporation on the diamond surface,[12] which in the present case would translate to lower secondary electron yields.

Atomic force microscopy (AFM) results from Chapter 8 have shown the thickness of the NCD layers grown in similar conditions to be ~500nm when grown on silicon wafers. Therefore although the SEM data cannot determine accurately what the growth thickness is, a reasonable estimation of the thickness was found by examining the cleaved edge of the MCP near or on the top surface (whichever was more apparent) and taking an average of six measurements. Both Round 1 and 2 showed approximately the same thicknesses of growth, between 100 and 145nm. Hence, we can come to a very approximate value for the growth rate of 33-48nm/hour, which contrasts with the value for growth on silicon substrates ~167nm/hr. Noting that the efficiency of cooling on silicon substrates was better presumably due to the higher thermal conductivity seen on silicon wafer than microstructured PbO

glass,[13,14] allowing for a higher plasma power and pressure than on MCPs. However, the increase of growth rates seen cannot be fully explained by the differences in growth conditions, the choice of substrate is a likely cause of the large disparity as PbO glass is an unusual platform for diamond growth – whereas silicon has been shown to be a good substrate for diamond growth.[15]

Particle density has an important effect on average grain size, as at lower densities particles were less constrained and were allowed to achieve maximum diameter. At high particle densities where continuous films are observed, the term grain density/size is more appropriate to describe NDs that have coalesced into larger grains. During Round 2, where the seeding was generally seen to be 'cleaner' or less stacked, the density near the top of the channel was so high that there is an observable drop in average particle size in the majority of the samples for the first few micrometres (this is most apparent in #1411-2). The particle density can be seen to have a general trend of falling off with depth in channel. The changing of the backfill volume in Round 1 results in a predictable exponential change of penetration with continuous coverage in Round 1 (see Figure 7.9). In Round 2 there is much less variation of depth with continuous coverage when only the seeding technique is varied, although there is a slight correlation of duration of ultrasonication with penetration of (non-continuous layers) of particles – however, the goal of this investigation is the penetration of full continuous layers of particles and so this effect is of little importance to the overall aims of this project. The range of densities observed in each Round were similar, with $\sim 10^{10}$ particles per square centimetre near the entrance to the channel, and $\sim 10^{9}$ at the end of the measurement – where the SEM imaging was halted due to the lack of coverage. This high seeding density shows hydrocolloidal ND to be a good candidate for

the seeding of complex 3-D structures, with densities approaching that of the highest reported in the literature.[16]

The data shows the expected trend of decreasing coverage with distance from the channel entrance. Throughout Round 1, there appears a section of full coverage followed by a sharp cut-off, indicating the variation of water backfill is having the desired effect of preventing significant ingress of ND deep into the channel. Round 1 showed a large range of penetration with a range of <1D to 10D (where D corresponds to the channel diameter - 6 μm). However, the SEM images revealed the quality of seeding to be generally of a lower quality than seen in later samples (Round 2). On the top surface, there seems to be an excess of ND deposited, with conglomerations occurring throughout the seeded part of the channel. The 20μl backfill (#0410-1) gave a full coverage coating to a depth of ~60μm – or 10D, achieving the goal of this work.

However, during Round 2, whilst still using 20μl backfill of the MCP seeding jig but whilst examining the variation in seeding deposition technique and time, there was much less variation, all were ~3D. There was also a general decrease in penetration depth, comparable to a backfill of several hundred micro litres. Again, this may be due to the variation between batches of reduced and full channel MCPs, leading to concern for the reliability of ND penetration in an industrial setting. One likely contender for the cause of this variation is the use by Photonis of a hydrogen anneal to fine tune the measured strip current (essentially the resistance between the top and bottom surfaces of the MCP) causing variation in the surface charge between MCP batches, and hence the ease at which ND seeding occurs. This effect was unanticipated in this context,

as adhesion of nanoparticles to the MCP surface had not been attempted before (to the author's knowledge) and hence the tuning hydrogen anneal might require revaluation if the addition of ND layers to the final product is given the go ahead. Before any drastic action would be taken, further work would be necessary to properly elucidate the cause of this variation.

As a side note, the technique of backfilling the jig with full channel MCPs gave a wide variation of seeding density when comparing from edge to centre. This is likely due to the backfill only filling the central channels, the outer ones are left vacant, allowing ND solution to enter. This observation indicates full size MCPs will require a redesigned seeding technique. However, as this project is primarily interested in proving the project concept in reduced channel MCPs, the observed variation is of low importance currently.

7.5. Concluding remarks

The design of the sample cooler, did eventually yield positive results (see Chapter 8), however it can be seen that modification of precision engineered scientific equipment is not a trivial undertaking. Iterative design methods were employed and with persistence, the final design was successful and will be put to use both in the continuation of this project and by later members of the project team. Further characterisation of the final design is still needed to glean the maximal benefit of the cooler. This characterisation would investigate the optimal plasma-substrate distance and the cooling efficacy on multiple growth substrates (varying in both material and dimensions). However, for the purposes of this chapter the advanced cooler design can be said to function

extremely well and will prove a useful tool in further avenues of investigation within the field of low temperature MWPECVD growth.

This chapter has shown that there can be close control of depth of nanodiamond penetration up to and including the desired '10D'. This method of ND seeding can be scaled up to substrates of unlimited size, which will undoubtedly be useful within industrial applications. Additionally the need for backfilling the MCP suggests that extremely deep penetration of 3D objects is possible. This leads to the conclusion that coating conformal diamond layers on increasingly complex structures can be achieved with careful seeding, assuming the subsequent growth mechanism can cope with the complexity presented. Even without subsequent growth into NCD, the ability to form ND layers throughout the MCP for the first time opens several avenues of exploitation of diamond hybrid devices. The results clearly show the backfill volume to be of great importance to the depth of ND penetration, whilst the seeding durations/energies investigated did not provide a great variation in effect. In addition, it has been seen that highly conformal NCD films can be grown in the centre of a reduced channel MCP. However to date, both these desirable characteristics have not yet been performed on a full size MCP. The discovery that NCD grows at a much slower rate (around four times lower) on the MCP has implications for the remainder of the collaboration with Photonis, as complete layers are required to maximise the benefit brought by the addition of diamond to the channel. This effect has been observed more generally before by diamond growers, however the unique composition of the MCP glass means the rates found over the course of this project will usefully add to the current catalogue of diamond growth rates.

[1] K O'Donnell *et al.,* 'Diamond Surfaces With Air-Stable Negative Electron Affinity And Giant Electron Yield Enhancement'. Advanced Functional Materials, 2013.
[2] Technology glossary, Photonis, accessed 8th September 2013, http://www.photonis.com/en/content/97-nightvision-technology-glossary
[3] Y Muranaka *et al.*, 'Worldwide Status Of Low Temperature Growth Of Diamond', Diamond & Related Materials 3(4-6), 1994, pp. 313-318.
[4] O Monteiro *et al.* 'Nucleation And Growth Of CVD Diamond Films On Patterned Substrates'. Diamond and Related Materials 12(8), 2003, pp. 1357-1361.
[5] J-H Jiang *et al.*, 'Effects Of Gas Residence Time On Microwave Plasma Enhanced CVD Of Ultrananocrystalline Diamond In Mixtures Of Methane And Argon Without Hydrogen Or Oxygen Additives', Diamond & Related Materials 24, 2012, pp. 153-157.
[6] FLW1701 Recirculating Cooler , Julabo, accessed 4th October 2013, http://www.julabo.com/en/products/recirculating-coolers/flw1701-recirculating-cooler
[7] NESLAB CFT-300 Product specifications, Thermo electron Corporation, accessed 1st October 2013, http://www.atecorp.com/ATECorp/media/pdfs/data-sheets/ThermoNeslab-CFT-300_Datasheet.pdf
[8] Y Liou *et al.*, 'Low-Temperature Diamond Deposition By Microwave Plasma-Enhanced Chemical Vapor Deposition'. Applied Physics Letters 55(7), 1989, pp. 631-633.
[9] S Zhou *et al.*, 'Study Of The Growth Rate Of Diamond Film By Hot-Filament CVD'. Materials Science and Engineering B25, 1994, pp. 47-52.
[10] F Ahmed *et al.*, "Stress evolution and cracking of crystalline diamond thin films on ductile titanium substrate: Analysis by micro-Raman spectroscopy and analytical modelling." Acta Materialia 59(14), 2011, pp. 5422-5433.
[11] S Matsumoto *et al.*, "Growth of diamond particles from methane-hydrogen gas." Journal of Materials Science 17(11), 1982, pp. 3106-3112.
[12] B Stoner *et al.,* 'Electrical Conductivity And Photoluminescence Of Diamond Films Grown By Downstream Microwave Plasma CVD'. Journal of electronic materials 21(6), 1992, pp. 629-634.
[13] G Slack, 'Thermal Conductivity Of Pure And Impure Silicon, Silicon Carbide, And Diamond'. Journal of Applied Physics 35(12), 1964, 3460.
[14] M Burzo *et al.*, "Thermal Transport Properties of Gold-Covered Thin-Film Silicon Dioxide", Components and Packaging Technologies, IEEE Transactions on 26(1), 2003, pp. 80-88.
[15] O Williams, 'Nanocrystalline Diamond'. Diamond & Related Materials 20, 2011, pp. 621-640.
[16] O Williams *et al.*, "Enhanced diamond nucleation on monodispersed nanocrystalline diamond." Chemical Physics Letters 445(4), 2007, pp. 255-258.

Chapter 8: Low temperature Nanocrystalline Diamond Growth for High Yield Secondary Electron Emission

8.1. Introduction

As part of the project to enhance Photonis' current generation of microchannel plates (MCPs), a study was performed investigating the optimal growth parameters to maximise the secondary electron yield (SEY) of nanocrystalline diamond (NCD) films. Therefore, as mentioned in Chapter 7, combining the higher SEY of diamond with the current capabilities of the MCP. Here, temperature was the primary variable due to the 400-420°C softening point of a MCP. Due to the high cost and complexity of the MCP, silicon was used as a platform for growth. Silicon was used due to its near ideal characteristics as a model growth platform - namely low cost, ease of availability of both conductive (doped) and insulating (intrinsic) substrates, and the ease in growing NCD upon it due to its ability to accept nanodiamond (ND) seeds adsorbed to its surface.[1] However, the great ease with which NCD can be grown upon silicon does contrast with the significantly lower growth rates seen on MCPs (see chapter 7). Therefore, all the results presented in this chapter refer to NCD grown on silicon wafer.

As a result of the growth process, the surface of NCD emerges hydrogen terminated.[2] This leads to a property known as negative electron affinity (NEA), see section 4.11 for a detailed explanation of this effect. This removes the barrier for secondary electron emission and combined with the wide band gap seen in diamond ($E_g \approx 5.5$ eV), prevents the low energy secondaries from colliding with valence electrons,[3] allowing for high SEY. Very high secondary yields have been reported on several diamond systems. However these headline results typically utilise natural single crystal diamond,[4] chemical vapour

deposition (CVD) grown single crystal diamond,[5] and boron or nitrogen doped CVD diamond.[6,7] Unfortunately each of these are unable to be incorporated within a MCP structure as natural diamond would be too costly, single crystal diamond would not grow on three dimensional structures (nor on non-homoepitaxial substrates), and doped diamond would reduce the effective cross-MCP resistance, preventing the 1000 V necessary for normal operation. However, high SEYs on polycrystalline diamond have been reported,[5] and hence the compatibility of NCD on MCPs leads directly to the work presented in this chapter.

Conventionally diamond is grown between 800-1000°C,[8] however as previously mentioned the MCP is limited to 400-420°C. Such low growth temperature of diamond, whilst critically sub-optimal, has been reported quite early in the literature, due to the interest in combining CVD diamond with other material systems that would not withstand such high temperatures. A review by Muranaka and co-workers as early as 1994 reports on several growth chemistries achieving low temperature growth of diamond.[9] Of these, the CH_4/H_2 chemistry that has found widespread popularity (and is in use for this project), was reported to grow diamond at 430°C using low energy microwave plasma without additional substrate cooling.[10] However, DC plasma excitation achieved growth at temperatures as low as 140°C using the same gas system.[11] This diverse range comes at the cost of crystalline quality, as defined by Raman spectroscopy[12] where ~400°C appears to be the cut off temperature for high quality films. This cut off point is likely to correspond to a reduction in SEY, although there is currently no direct evidence for this in the literature.

Whilst electron emission from hydrogen terminated diamond has been well established,[2-7] less well characterised is the use of alkali metals on the diamond surface to create a stable NEA surface. Alkali metals have been utilised for electron emission for quite some time, with Mearini *et al.* using coatings of CsI on diamond in 1995.[13] These coatings, under electron beam irradiation leave the surface Cs terminated and result in SEY ten times that of the as grown surface. Very recently, a group led by Ley reported an enhancement factor of 200 of a lithium treated surface over that of oxygen terminated diamond (which exhibits a positive electron affinity).[14] Such high enhancement factors are no doubt aided by the use of doped single crystal diamond, but the change is nonetheless profound. In other work resulting from the collaboration between UCL and Photonis (which will not be presented here), caesium termination of NCD layers yielded an enhancement of SEY over hydrogen terminated NCD. Therefore, consideration of the potential gains to be made by alternative surface terminations is necessary when evaluating the results contained in this chapter.

8.2. Experimental methods

Seeding: Silicon substrates (highly doped, as used in section 6.2) were first cleaned using the standard RCA SC1 procedure:

i. Mix NH_3OH:H_2O_2:D.I water in a 1:1:5 ratio sufficient to cover samples
ii. Heat mixture to 75°C
iii. Add silicon wafer and allow to react for 10 minutes (at 75°C)

ιϖ. Rinse silicon in D.I water with ultrasonic agitation for 1 minute

ϖ. N_2 dry

Nanodiamond (ND) was then seeded on the silicon substrates using the methods described in section 5.2, with the addition of a piece of low residue tape over one corner to allow for film thickness determination. The tape was removed prior to growth and any residue is of low concern as it would be removed during the first few seconds of exposure to a hydrogen plasma.

Growth: NCD was grown according to the procedure laid out in section 7.2. The microwave power, gas pressure, and applied cooling intensity were varied in order to achieve growth temperatures of 380, 400, 420, 600, and 800°C for a duration of 3 hours (unless explicitly stated otherwise). All samples presented in section 8.3.1 were grown on the 2 pipe cooler depicted in figure 7.8. The samples presented in section 8.3.2 were grown on the latest iteration of cooler design, the 2 pipe reservoir cooler (figure 7.10), resulting in the use of the higher applied microwave power presented in table 7.1. These later samples were also grown shortly after a recalibration of the mass flow controllers (MKS 1159, powered by a MKS 247 four channel mass flow controller power supply/readout), which gives greater reliability to the stated methane ratio of 0.5%. After growth, all samples were allowed to cool in hydrogen to ensure a well hydrogenated surface.

Secondary electron yield: Measurements were taken in a custom built vacuum chamber, with a Kimball Physics EGG-301 electron gun as the source combined with a Keithley 487 voltage source and a Keithley 6485 picoammeter.

All samples were dried within the vacuum chamber on a ceramic heater at 150°C prior to measurment to remove the adsorbed wetting layer, which would quench any electrons escaping the surface. Measurements were taken in vacuum pressures lower than 5×10^{-6} mbar. To measure the SEY of a surface, first the primary electron beam current (I_p) is established by biasing the sample with a large positive voltage (+500 V) to reabsorb any secondary electrons emitted. The current flowing through the sample to ground, designated I_t is equal to I_p (see Figure 4.13). By reversing the polarity of the sample bias, emitted secondary electrons are repelled from the surface (I_S), subtracting from the current measured, giving I_p - I_S. Therefore SEY can be calculated as follows:

$$SEY = \frac{I_s}{I_p}$$

Sample to ground current at positive bias; $I_{t+} = I_p$

Sample to ground current at negative bias; $I_{t-} = I_p - I_s$

substituting gives:

$$SEY = \frac{I_{t-} - I_{t+}}{I_{t+}}$$

By combining the primary beam energy with the influence of the applied bias, the incident electron kinetic energy can be determined using the identity $E_i = E_b + eV_b$. Therfore SEY can be plotted as a function of E_i.

Scanning electron microscopy: The SEM was used as described in section 7.2. However, the addition of a conductive carbon over layer was not required.

Atomic force microscopy: AFM was used to measure the step height difference between the NCD layer and the bare silicon substrate. The microscope was used as described in section 5.2, although only the line scan data was used.

Raman spectroscopy: Raman spectroscopy was performed on the NCD layers using the equipment and procedure detailed in section 5.2. However, one deviation from the aforementioned procedure was in the choice of laser intensity. NCD has excellent thermal conductivity[15] and as a result laser intensity was raised from 10% to 100% to achieve greater signal to noise ratio without risk of damage to the sample.

8.3. Results and discussion

8.3.1 Secondary electron yield of NCD as a function of growth temperature

400˚C

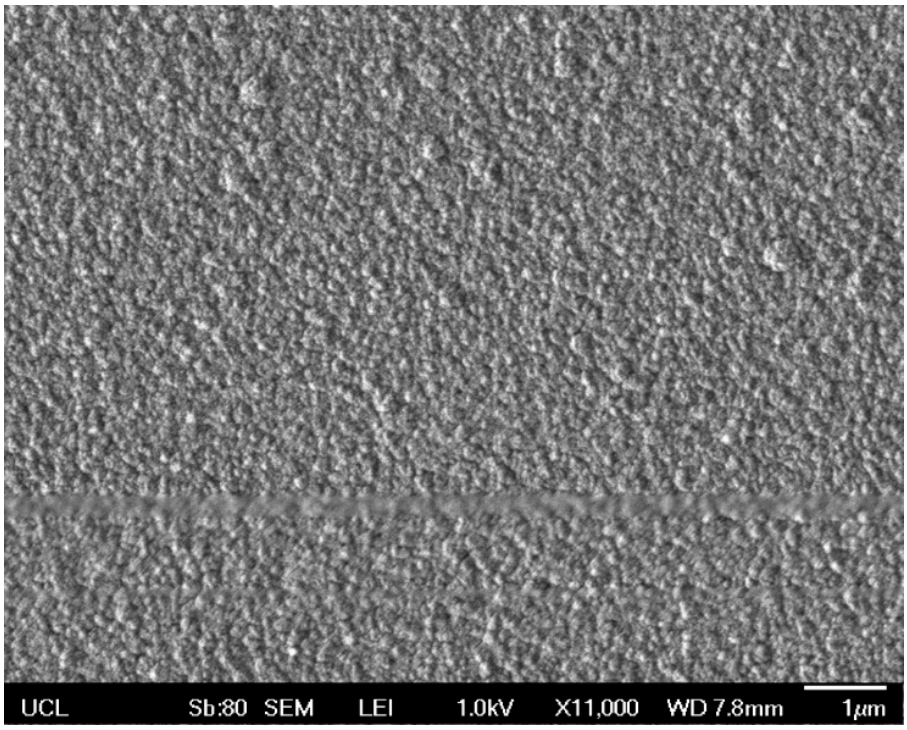

Figure 8.1 Scanning electron micrograph of NCD surface grown at 400°C.

The layer grown at 400°C exhibits a very different surface morphology in comparison to that seen at 380°C (Figure 8.13). The average grain size is markedly smaller, less than 100 nm, suggesting renucleation of the NCD grains is happening at a greater rate than that seen at 380°C. This shift in morphology (which is not seen in the other growth temperatures) indicates the critical growth temperature for this gas system lies between 380 and 400°C, which is in good agreement with that reported by Michler and co-workers.[2] The NCD layer shows complete coverage of the substrate and the measured thickness was 223 nm (Figure 8.2) giving a growth rate around 74 nm/hr.

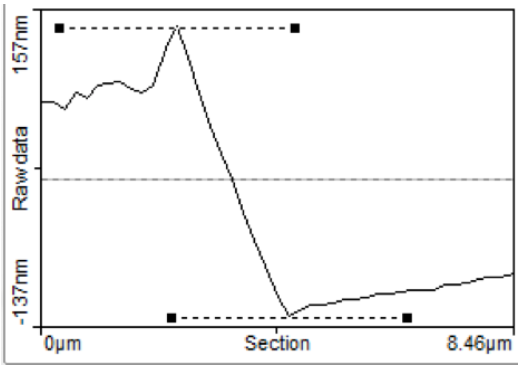

Figure 8.2 AFM line scan of NCD film grown at 400°C.

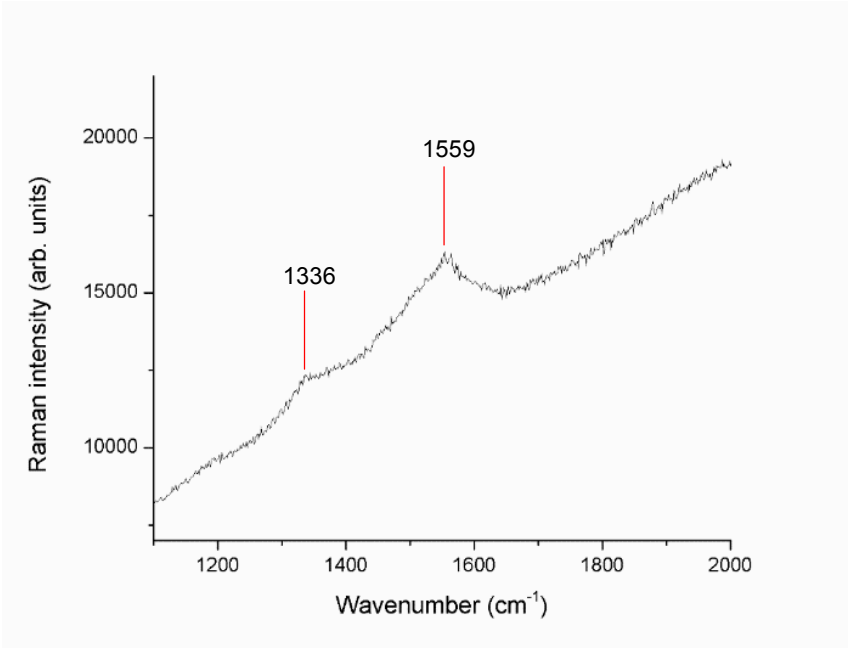

Figure 8.3 Raman spectrum of NCD film grown at 400°C.

The Raman spectrum of the film grown at 400°C (Figure 8.3) shows a very weak sp^3 peak centred at 1336 cm^{-1} (associated with the first order Raman mode of the cubic diamond lattice) [16] and a larger peak at 1559 cm^{-1}, corresponding to poor quality diamond. The peak at 1559 cm^{-1} is associated with the G-band, however the relative intensities are misleading as graphite is known to have a Raman scattering efficiency ratio 50 times that of diamond [17] and 233 times for amorphous carbon,[18] (measured with a 514.5 nm wavelength

laser, as used in this thesis) resulting in a comparatively stronger peak. As with the film grown at 380°C, there is a strong background luminescence. The large background luminescence detected (resulting in a positive slope convoluted with the Raman peaks) is likely a result of defects and impurities in the diamond lattice.[19] Figure 8.4 shows a maximum SEY of 5.7 at 700 eV. The observation that the peak gain occurs at higher incident energy suggests secondaries are being generated and emitted most effectively further from the surface than in the 380°C sample.[20]

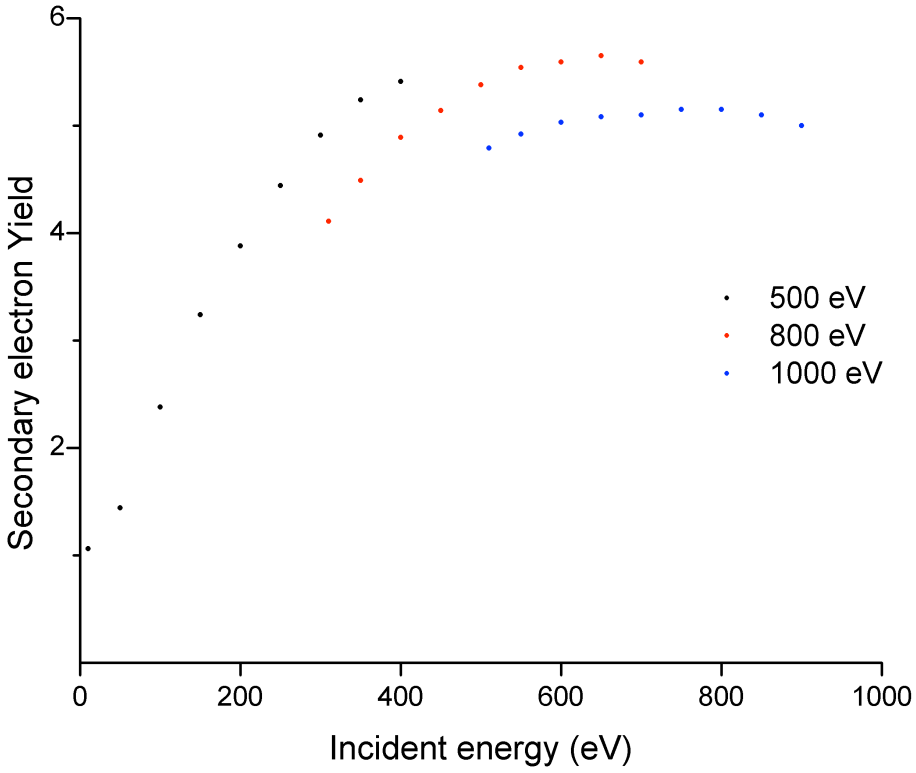

Figure 8.4 SEY of NCD film grown at 400°C as a function of incident electron energy.

800˚C

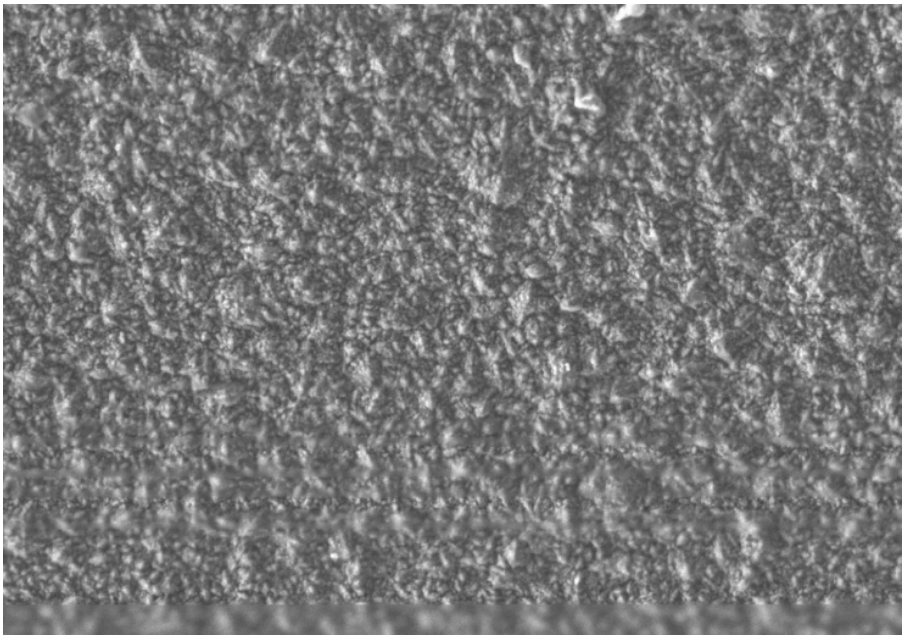

Figure 8.5 SEM of NCD surface grown at 800°C

Figure 8.5 shows the surface grown at 800°C is similar to that seen at 600°C, with slightly more definition of grains – although this may be a SEM artefact from improved micrograph focus. Following the trend throughout this sample set, the thickness of the 800°C growth was measured to be 2.7 µm, giving an average growth rate over the three hour run of 900 nm/hr – 4.5 times the rate seen at 600°C (Figure 8.6).

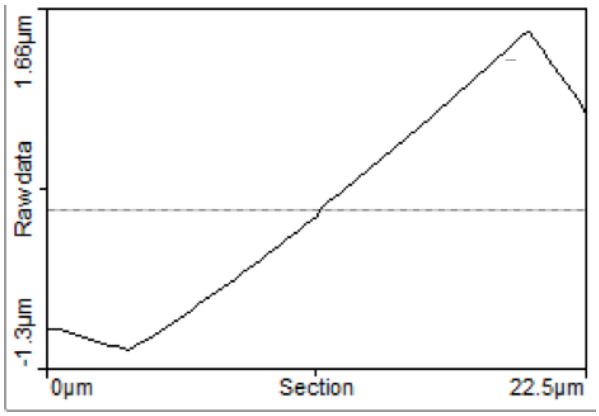

Figure 8.6 AFM line scan of NCD film grown at 800°C.

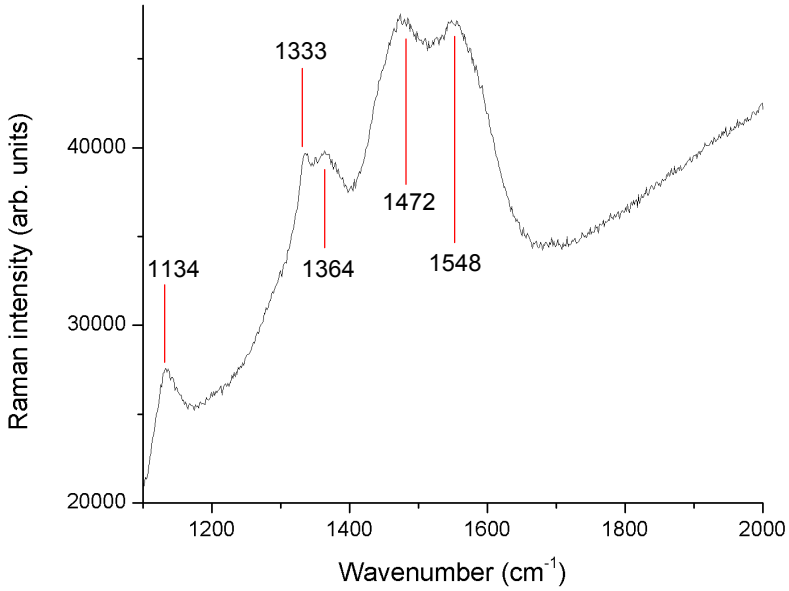

Figure 8.7 Raman spectrum of film grown at 800°C.

Figure 8.7 displays a wide array of peaks from the Raman spectrum. The first at 1134 cm^{-1} can again be ascribed to trans-polyacetelene, 1333 cm^{-1} can also be attributed to sp^3 carbon, whilst the peak at 1364 cm^{-1} has been previously attributed to graphitic deposits.[21] The two slightly overlapping peaks at 1472 and 1548 cm^{-1} are considerably stronger than the other peaks presented. 1472 cm^{-1} has not yet been assigned, although some reports link it to sp^3 carbon based systems,[22] whereas 1548 cm^{-1} has been previously associated with the G peak.[23] This association is somewhat contentious as others have argued this peak may be due to a combination of sp^3 carbon and the D peak.[24] A SEY of 5.5 was measured at an incident electron energy around 700 eV, although the broad peak first seen at 600°C reappears, albeit in a less well defined manner. Again, the increased thickness of the 800 and 600°C layers are the likely cause. This SEY figure is comparable to that seen on NCD grown at 400°C.

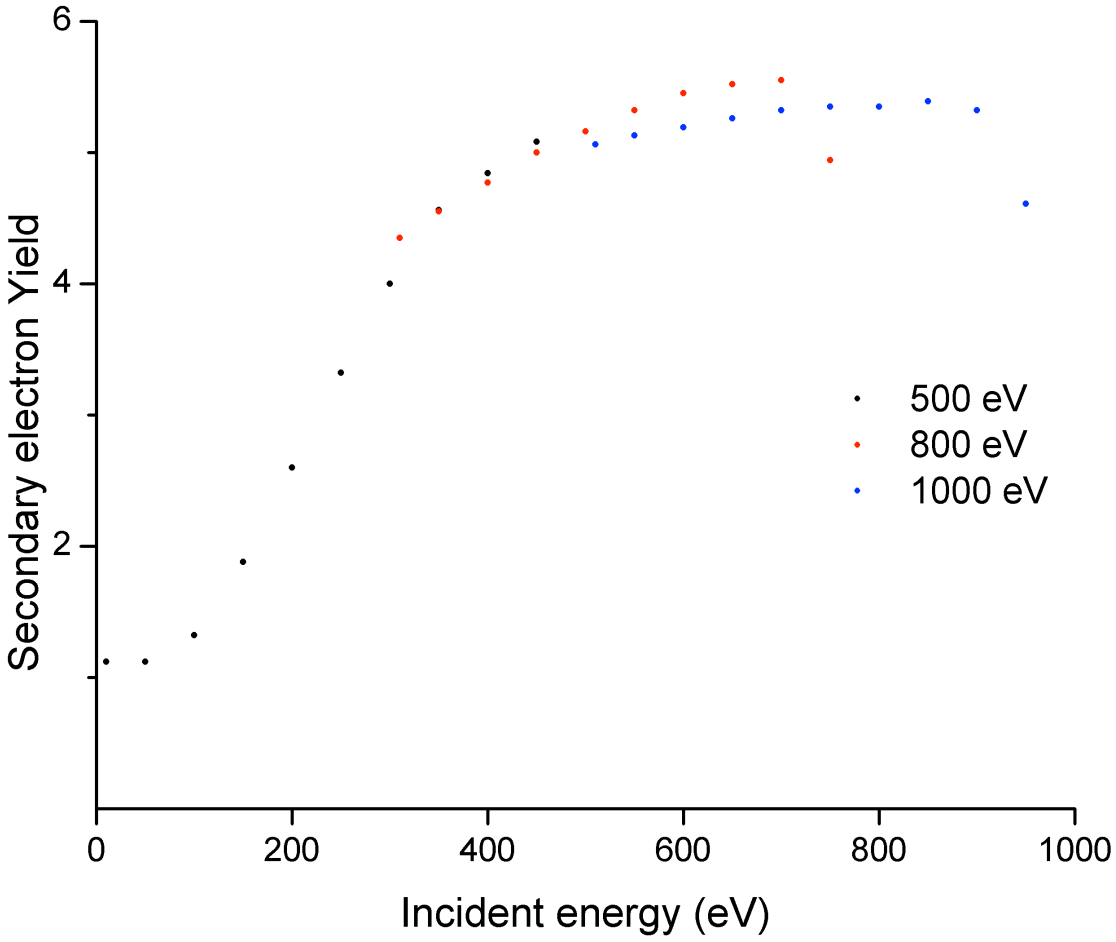

Figure 8.8 Secondary elctron yield of NCD film grown at 800°C

8.3.2 Influence of sample holder on growth and gain

9 hour growth

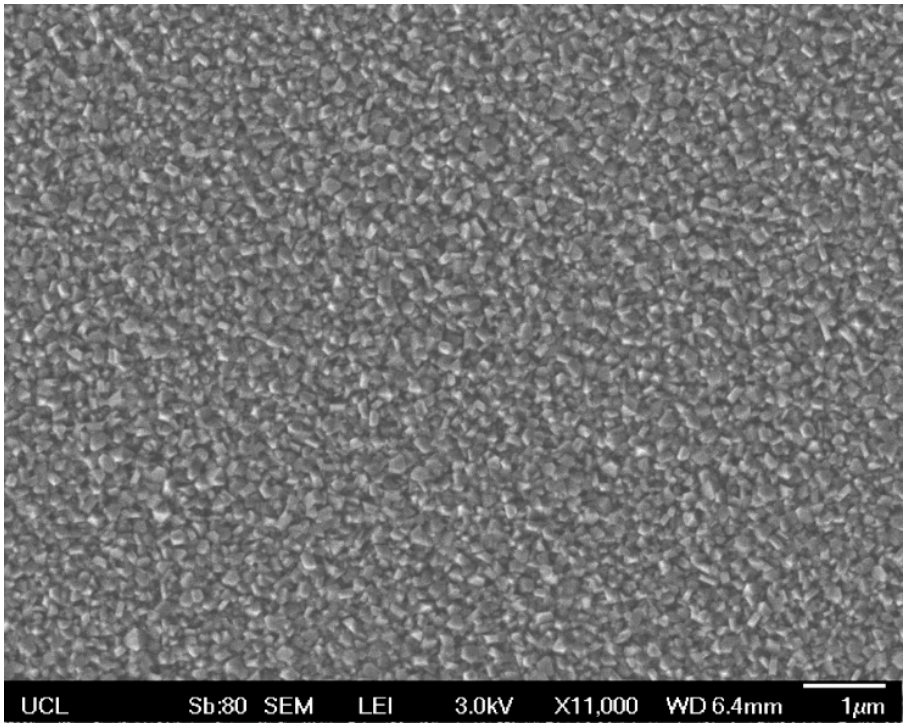

Figure 8.10 Scanning electron micrograph of NCD grown at 400°C using the 2 pipe reservoir cooler, with a total growth duration of 9 hours.

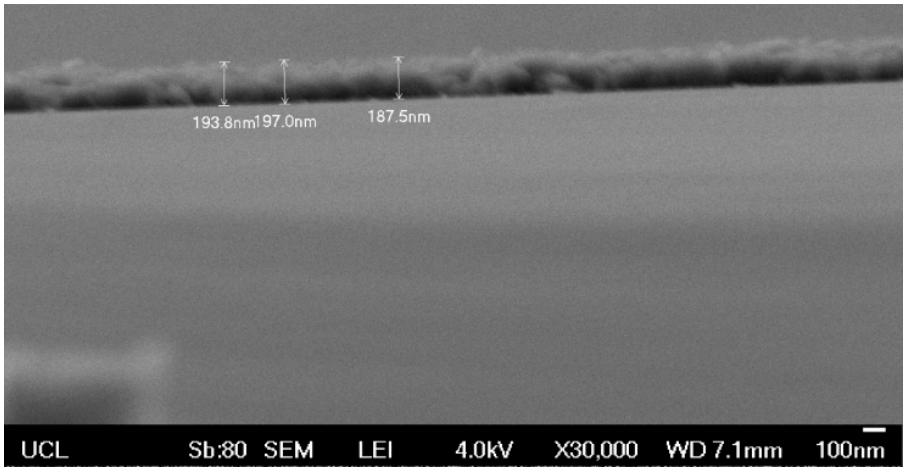

Figure 8.9 Cross sectional view of 9 hour growth at 400°C using the 2 pipe reservoir cooler, Thickness measurements of the NCD layer were made with the mcroscope software package are shown.

As a result of the incomplete film seen in Figure 8.25, the growth duration was significantly increased to 9 hours to ensure a continuous NCD layer. The reduced growth rate in comparison to the results presented in section 8.3.1 is likely due to the enhanced dissociation efficacy of the higher energy plasma causing a greater density of atomic hydrogen (an etchant) and a lower density of graphitic precursor molecules.[25] Figure 8.10 and Figure 8.9 indicate this was successful, as no gaps in the film are visible. Strong facetisation is observed with surface grain sizes of the order of 200-250 nm. The cross section view of the film shows the film to be approximately 193 nm thick, giving a growth rate of the order of 20 nm/hr, 3-4 times slower than that seen in the comparable growth using the earlier cooler iteration. The surface morphology is similar to that seen in NCD grown at more traditional temperatures.[26]

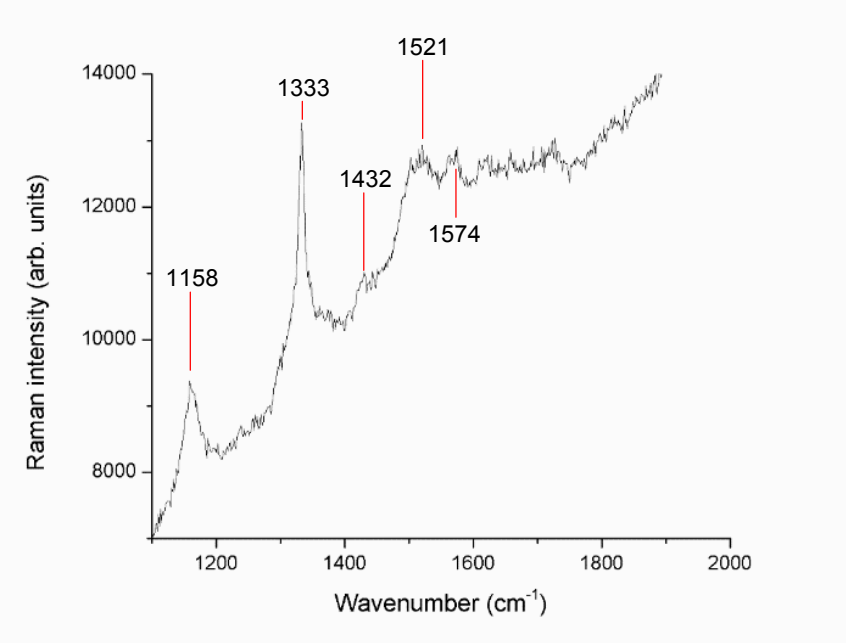

Figure 8.11 Raman spectrum of 9 hour growth with peaks labelled.

The Raman spectrum of the sample showed an extremely strong, sharp peak at 1333 cm^{-1}, indicating the presence of high quality diamond. The peak observed at 1158 cm^{-1} is again attributed to trans-polyacetylene at the grain boundaries,[4] as can the small peak at 1432 cm^{-1}.[27] Figure 8.11 shows a very

broad G peak between 1500-1750 cm^{-1}. Punctuating this broad yet weak feature are peaks at 1521 and 1574 cm^{-1}, the former is associated with disordered graphitic carbon,[28] indicating a small amount of non-diamond carbon present in the film, and the latter is also attributed to the C-C stretching mode of graphitic deposits.[29] In all, Figure 8.11 presents a model spectrum for good quality NCD.

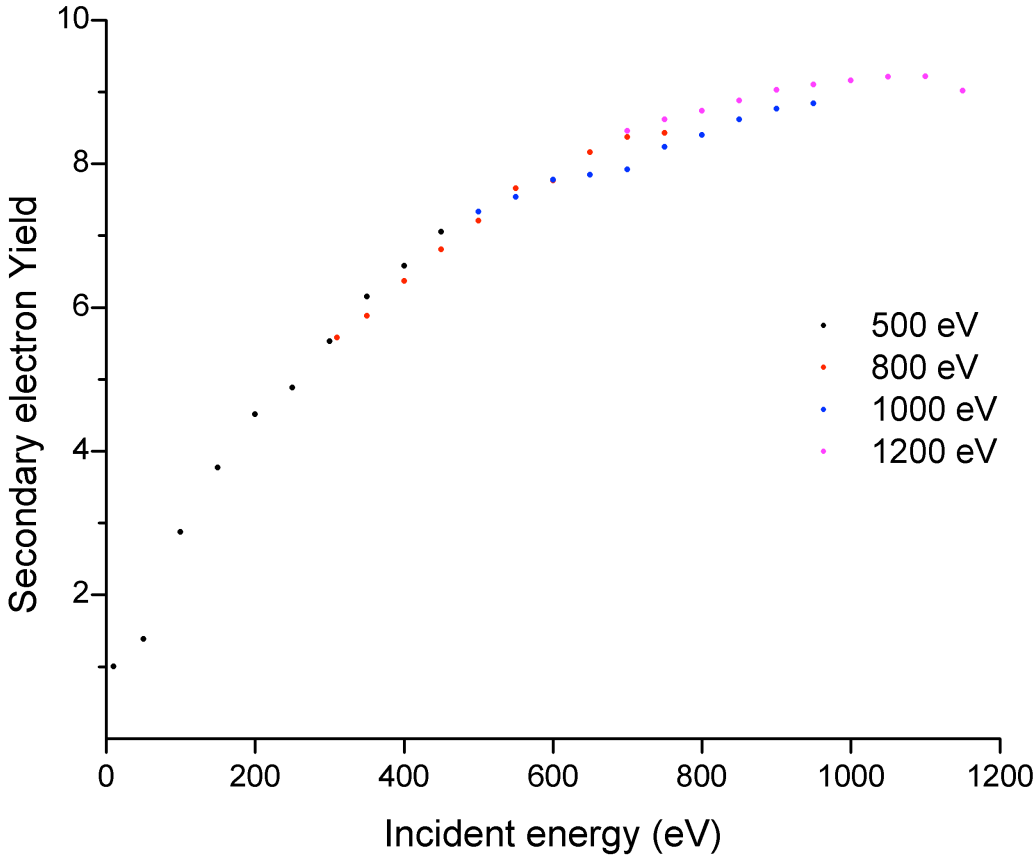

Figure 8.12 SEY of NCD surface grown at 400°C for 9 hours using the final sample cooler, the 2 pipe reservoir.

Figure 8.12 yielded the highest secondary electron emission seen using low temperature growth parameters. The high value of 9.2, coupled with the peak centred on 1100 eV suggests secondaries are able to escape from a greater depth. This increased escape depth in comparison to the previous examples is further (if indirect) evidence for the quality of the diamond film, as escape depth is correlated with carrier scattering probability.[30]

8.4. Concluding remarks

Within section 8.3.1 (using the old cooler) there were peak SEYs on samples grown at both 400 and 800°C. The higher yield seen on the 800°C sample was expected, as this lies within the preferred temperature range for diamond growth. However the high yield on the samples grown at 400°C was unexpected due to the lower quality of the resulting film (as shown by the Raman spectrum in Figure 8.3). One possible explanation is the combination of reduced film thickness and increased sp^2 content allows for reduced charging effects at the NCD surface through local conductive regions. These regions would provide electron sources for the replenishment of the emitted secondary electrons, allowing for the continuous emission from the nearby diamond regions. The complex interplay between high and low quality regions has been hinted at with this work, however to fully understand these mechanisms, further investigations into the effect of methane concentration and plasma-substrate distance are required before an authoritative description of the optimal ratio of sp2 and sp3 seen within an NCD film

The primary observation when comparing the SEY results of sections 8.3.1 and 8.3.2 is that temperature does not have as great an influence on SEY as energy density – greatly improved yields (up to 9.2) are seen on the higher applied microwave power (see table 7.1 for raw values). This was a surprising result as high quality diamond grown at low temperature is difficult, if not without precedent.[31] This result then raises an important question from the perspective of the device engineer: at what point does this relationship breakdown? This will undoubtedly be the focus of future collaborations with Photonis. As a result of the improved energy densities, the surface morphology, as determined by scanning electron micrographs, were not a reliable indicator of SEY. However, smooth or ballas (rounded) type NCD did give smaller SEY then that seen on the well faceted layers. Scanning electron micrographs appear to show highest brightness at upward facing crystal edges, hinting at an optimal morphology incorporating such features in future growths of high SEY layers.

There was some variation in the incident electron energy that provided the peak secondary electron emission. This is closely associated with variations in the scattering probabilities of each material. Hence, when the peak of the secondary electron yield is at higher incident electron energy, it can be deduced that the escaping secondary electrons are originating from deeper within the sample and that the absorption coefficient has decreased. This has the knock on effect of allowing for carriers generated at depths under the electron escape depth to have a higher probability of leaving the surface, adding to the total yield. As scattering probability in a crystalline material is typically dominated by defects, this gives insight into the quality of the nanocrystalline diamond

films produced for this chapter, and supports the data acquired through Raman spectroscopy.

The majority of the Raman spectra suggest poor quality diamond was grown across the temperature range, with appearance closer to that of diamond like carbon. When taken into account with the upgraded sample cooler, this highlights the importance of the substrate's position in relation to the surface of the plasma ball in the CVD chamber, as has been previously reported by Zhou *et al.* in 1994.[32] Other variables would need to be tested fully for a complete understanding of the optimal growth conditions for this application, such as methane concentration and growth duration. Both factors would have a large effect on final film thickness, for which the optimal value required for maximal gain, is not yet known.

Finally, this work was largely successful in fabricating a NCD layer with a SEY near 10, the goal set by Photonis. Whilst this avenue of research is by no means complete, good headway has been made into ultimate goal of the incorporation of NCD layers in night vision devices, and with further refinements, should yield a stable high yield secondary electron emitter.

[1] O Williams *et al.*, 'Enhanced Diamond Nucleation On Monodispersed Nanocrystalline Diamond'. Chemical Physics Letters 445(4-6), 2007, pp. 255-258.
[2] H Hopman *et al.*, 'Secondary Electron Emission Measurements On Synthetic Diamond Films'. Diamond And Related Materials 8, 1999, pp. 1033-1038.
[3] A Shih *et al.*, 'Secondary Electron Emission From Diamond Surfaces'. Journal of Applied Physics 82(4), 1997, pp. 1860-1867.
[4] J Yater *et al.,* 'Cold Emission Characterization Using Secondary Electron Emission Spectroscopy'. Applied Surface Science 146, 1999, pp. 341-346.
[5] J Yater & A Shih, 'Secondary Electron Emission Characteristics Of Single-Crystal And Polycrystalline Diamond'. Journal of Applied Physics 87(11), 2000, pp. 8103-8112.
[6] S Bozeman *et al.*, 'Electron Emission Measurements From CVD Diamond Surfaces'. Diamond & Related Materials 5, 1996, pp. 802-806.
[7] H Yamaguchi *et al.*, 'Electron Emission From Conduction Band Of Diamond With Negative Electron Affinity'. Physical Review B 80(16), 2009, 165321.
[8] S Zhou *et al.*, 'Study Of The Growth Rate Of Diamond Film By Hot-Filament CVD'. Materials Science and Engineering B25, 1994, pp. 47-52.
[9] Y Muranaka *et al.*, 'Worldwide Status Of Low Temperature Growth Of Diamond'. Diamond & Related Materials 3(4-6), 1994, pp. 313-318.
[10] Y Liou *et al.*, "Low-temperature diamond deposition by microwave plasma-enhanced chemical vapor deposition." Applied Physics Letters 55(7), 1989, pp. 631-633.
[11] S Nakao *et al.*, "Deposition of diamond onto an aluminum substrate by DC plasma CVD." Japanese journal of applied physics 29(part 1), 1990, pp. 1511-1514.
[12] Y Muranaka *et al.*, "Characterization of diamond films synthesized in the microwave plasmas of CO/H 2 and CO/O 2/H 2 systems at low temperatures (403–1023 K)." Journal of applied physics 69(12), 1991, pp. 8145-8153.
[13] G Mearini *et al.*, 'Stable Secondary-Electron Emission From Chemical-Vapor-Deposited Diamond Films Coated With Alkali-Halides'. Applied Physics Letters 66(2), 1995, pp. 242-244.
[14] K O'Donnell, 'Diamond Surfaces With Air-Stable Negative Electron Affinity And Giant Electron Yield Enhancement'. Advanced Functional Materials, 2013.
[15] J Philip *et al.*, "Elastic, mechanical, and thermal properties of nanocrystalline diamond films." Journal of Applied Physics 93(4), 2003, pp. 2164-2171.
[16] J Filik, "Raman spectroscopy: a simple, non-destructive way to characterise diamond and diamond-like materials." Spectroscopy Europe 17(5), 2005, pp. 10-17.
[17] N Wada & S Solin, "Raman efficiency measurements of graphite." Physica B+ C 105(1), 1981, pp. 353-356.
[18] S Sails *et al.*, "Monitoring the quality of diamond films using Raman spectra excited at 514.5 nm and 633 nm." Diamond and related materials 5(6), 1996, pp. 589-591.
[19] R Rudder *et al.*, "Thermal CVD of homoepitaxial diamond using CF_4 and F_2." Electronics Letters 25(18), 1989, pp. 1220-1221.
[20] J Yater et al., 'Electronic Properties Of Diamond For High-Power Device Applications'. Solid-State Electronics 42(12), 1998, pp. 2225-2232.
[21] S Mominuzzaman *et al.*, "Camphoric carbon soot: a new target for deposition of diamond-like carbon films by pulsed laser ablation." Thin Solid Films 376(1), 2000, pp. 1-4.

[22] P May *et al.*, "Interactive Raman spectra of adamantane, diamantane and diamond, and their relevance to diamond film deposition." PhysChemComm 1(4), 1998, pp. 35-44.
[23] A Ogwu *et al.*, "Characterisation of thermally annealed diamond like carbon (DLC) and silicon modified DLC films by Raman spectroscopy." Physica B: Condensed Matter 269(3), 1999, pp. 335-344.
[24] J Wagner *et al.*, "Resonant Raman scattering of amorphous carbon and polycrystalline diamond films." Physical Review B 40(3), 1989, pp. 1817-1824.
[25] A Kromka *et al.*, 'Early Stage Of Diamond Growth At Low Temperature'. Diamond & Related Materials 17(7-10), 2008, pp. 1252-1255.
[26] O Williams *et al.*, 'High Young'S Modulus In Ultra Thin Nanocrystalline Diamond'. Chemical Physics Letters 495(1-3), 2010, pp. 84-89.
[27] H Kuzmany *et al.*, "The mystery of the 1140 cm^{-1} Raman line in nanocrystalline diamond films." Carbon 42(5), 2004, pp. 911-917.
[28] Z Ma & B Liu, "Boron-doped diamond-like amorphous carbon as photovoltaic films in solar cell." Solar energy materials and solar cells 69(4), 2001, pp. 339-344.
[29] R Nemanich & S Solin, "First-and second-order Raman scattering from finite-size crystals of graphite." Physical Review B 20(2), 1979, pp. 392-401.
[30] D Malta *et al.*, 'Secondary Electron Emission Enhancement And Defect Contrast From Diamond Following Exposure To Atomic Hydrogen'. Applied Physics Letters 64(15), 1994, pp. 1929-1931.
[31] A Kromka *et al.*, 'Early Stage Of Diamond Growth At Low Temperature'. Diamond & Related Materials 17(7-10), 2008, pp. 1252-1255.
[32] S Zhou et al., 'Study Of The Growth Rate Of Diamond Film By Hot-Filament CVD'. Materials Science and Engineering B25, 1994, pp. 47-52.

Chapter 9: Conclusion

This thesis has highlighted the wide array of potential and current uses of nanodiamond (ND), with a particular emphasis on the novel industrial application of image intensification. In all, ND has shown itself to be a remarkably versatile form of diamond, itself already a material used in a wide array of typically niche applications. The extreme properties seen in diamond often correlate to extreme performance, however this has been shown to be tempered by the significant technological hurdles that yet to be overcome when working with this iconic material, preventing the uptake of ND as an electronic material. Some progress has been made within this thesis, towards narrowing this gulf of understanding of ND, which is detailed below. However, much remains to bring ND research up to the level enjoyed by bulk diamond and even other electronic materials (the preeminent example being silicon). For example, the influence of applied voltage and current on ND would greatly help the progress of ND in high power applications (an area that holds great interest for those looking at uses of bulk diamond).

In chapter 5 the ability of ND based biomaterials to provide a platform for neuronal outgrowth without the use of adhesion proteins was reported. Here, the formation of neuronal cell networks on nanodiamond layers, and the subsequent fabrication of patterned cell networks has been presented. Glass cover slips were coated with two types of ND, using three deposition methods, and two types of surface functionalisation. Analysis of the total neurite length as a function of ND variables (average roughness, equivalent disk radius, and seeing density) found all the ND layers supported the murine hippocampal cells. The only statistically significant correlation was the inverse relationship between equivalent disk radius and total neurite length, suggesting the smaller size (or higher curvature) of the particles to be the major contributing factor to

the adhesion of neurons and their ensuing neurite outgrowth. Interestingly, no significant difference was seen between the treated (hydrogen terminated) and untreated (predominately oxygen containing groups) surfaces. Leading from these two observations it has been proposed that the adsorption of proteins in their primary functional state is the likely mechanism for the cell adhesive properties seen on ND layers. The full determination of the adhesion mechanism remains a goal of this line of work, and future experiments hope to elucidate this. Also reported in this chapter was the patterning of ND to provide a structured platform for neural networks. The patterned ND layers were successful in producing neuronal networks conformal with the ND pattern, down to 10 μm, potentially opening a new avenue for the study of ordered neuronal networks both within *in vitro* environments and for *in vivo* chronic implants. Again, further understanding of the attachment mechanism will aid in conferring these findings to an effective laboratory tool.

Chapter 6 presents the results of the investigation into the effect of surface termination of NDs on their electrical properties. The lack of understanding of the effect of surface termination on ND electrical properties created a significant hurdle for the adoption of ND based electronics. Additionally the issue of reliable and scaleable functionalisation routes was raised. As a result, a protocol for the facile hydrogen and oxygen termination of NDs was devised. The remaining issue in this area is the limited number of chemical groups conferred on the ND and the inhomogeneity seen via Raman spectra. The electrical characteristics were then investigated using impedance spectroscopy. It was found that in air the hydrogen terminated ND was more resilient to thermal decomposition than the oxygen terminated, suggesting at elevated temperatures (475°C onwards) the hydrogen at the surface is being replaced by

oxygen from the atmosphere. This then results in the permanent degradation of the ND and a loss of the high impedance seen initially. This process occurs at much lower temperatures (200°C) on the oxygen terminated ND. This low onset of oxidation precludes the use oxygen terminated ND in environments or modes operation that would exceed 200°C – excluding it from a large swathe of potential application areas (particularly those in the concerned with tribology and heat transfer). When measurements were taken in vacuum, the oxygen terminated ND layers showed a greater tolerance to high temperatures, surviving up to 475°C, giving weight to the argument that atmospheric conditions accelerate the decomposition of the ND. This shows the importance of surface termination on both the basic electrical properties and the thermal resilience of NDs, in both vacuum and ambient conditions. Some evidence was present of surface conductivity on the hydrogen terminated ND when comparing the vacuum and air measurements as the phenomenon is reliant on surface adsorbates from the atmosphere. The investigation into hydrogen and oxygen terminated ND has chipped away at the lack of understanding of the electrical changes that differing surface terminations have on the ND surface, however a large number of further terminations remain. Building from simple fluorine terminations all the way through to complex molecules – an understanding of the interaction of such surface functional groups with nano scale diamond remains outstanding. Additionally, heating under vacuum to higher temperatures would be required to fully resolve the critical temperature of decomposition.

Chapter 7 begins by reporting the increased cooling efficiency of successive cooler designs along with, the evolution of ND seeding within the microchannel plate (MCP). 3 dimensional coatings of ND, and their subsequent growth into

complex shaped NCD films were shown to be an important and ever more demanding use of ND. Here, the industry-led aim of achieving a 60 μm (or 10D) penetration of ND was achieved, and after a short growth step, the MCP-ND structures was then analysed in terms of grain density, area coverage, and grain size. This analysis revealed the water backfill to be of higher importance than the manner in which ND is seeded in achieving a 10D conformal NCD layer within the MCP. However it remains for both 10D layers and fully conformal NCD to be seen in the same sample. In addition, the gradual improvements made to the sample cooler within the growth chamber was also outlined, culminating in a cooler design that allowed for ~85% of the total available microwave power (1270 W of a total of 1500 W) to be applied whilst maintaining a silicon substrate temperature of 400°C. This figure was reduced to 60% (900 W) on the less thermally conductive MCP substrate. These higher energy densities resulted in far higher quality NCD films, as evidenced by Raman spectra in Chapter 8. Therefore the energy density was seen to be a far more important factor than substrate temperature in the growth of high quality NCD.

The final experimental chapter presents the investigation into the optimal growth temperature of NCD from ND seeds for high yield secondary electron emission, stemming from the thermal budget set by the MCP (400-420°C). It was found that the growth temperature has a large effect on the resulting surface morphology; from ballas to faceted crystallites. In addition, the rate of NCD growth is strongly dependant on substrate temperature. However, substrate temperature was not a reliable indicator of film quality, as determined by Raman spectroscopy, although there was a general inverse trend between sp^2 content and growth temperature. With regard to secondary

electron yield, samples grown at 400 and 800°C gave the highest yields, just below 6. However this was contrasted with NCD substrates grown on the most advanced design of the sample cooler, where the substantially higher energy input resulted in well faceted films with maximal secondary electron yield around 10 on films grown at 400°C, meeting the goal set by Photonis. This showed the energy density of the plasma ball used in chemical vapour deposition diamond growth is of higher importance than growth temperature. Many other variables remain unexplored, for example the methane concentration of the growth and the substrate-plasma distance are likely to significantly alter the surface and hence the secondary electron emissive properties.

Finally, this work has resulted in a better understanding of the physical properties of ND, both as received and after surface functionalisation. This will aid the design of ND based systems, particularly those reliant on the electronic properties of ND. Additionally this thesis has reported on the useful progress in both biological and applied physics fields of ND use, bolstering the claim that although still in its infancy, ND has a bright future ahead of it.

Future work

This thesis has documented both the continuation of the work of others (Chapters 5 and 6) and initiated novel lines of enquiry. However the search continues to better understand nanodiamond. Here, a full list of the anticipated future experimental work is given:

Chapter 5 – The attachment mechanism between ND and protein remains poorly understood, therefore by blocking groups of receptors through the use of exogenous chemicals, and seeding neurons upon the ND layers, it is hoped the interaction between ND and cellular proteins can be picked out by the resultant variation in attachment probabilities.

Chapter 6 – The influence of the magnitude of applied voltage was hinted at in this chapter. However a full investigation into this effect would undoubtedly yield useful information with respect to the stability of ND under high field conditions. Furthermore, the range of surface terminations needs to be expanded to give a better understanding of the range of possibilities afforded by surface functionalised ND. Finally, high temperature vacuum measurements presented here do not reach high enough temperatures to fully oxidise the ND. Therefore additional measurements at high temperature (i.e. greater than 530°C) would complement the presented results well, as would the heating being performed in an inert gas atmosphere.

Chapter 7 – Although the goal of the chapter was ostensibly met, further refinement of the developed seeding process is required to translate the findings outlined here to full sized MCPs for use in actual devices. A full characterisation of the final iteration of cooler design is also required to discover the optimal plasma-substrate separation.

Chapter 8 – Whilst the effect of growth temperature was shown to be less significant than the design of the cooler, the other growth variables are still in need of proper investigation. An investigation into methane concentration and growth duration (i.e. growth thickness) with respect to secondary electron emission is needed to find the optimal conditions for hydrogen mediated secondary electron emission. This would then be complimented by the use of alkali metal oxide mediated diamond surfaces, of which early theoretical calculations show promise in greater negative electron affinities and higher long term stability.

The next major challenge facing the introduction of NCD films into Photonis' image intensifier system would be combining the positive results seen in chapters 7 and 8. The results, at this early stage, can be thought of commercially, as proof of the concept of diamond enhanced image intensifier systems.

Appendix A: Equivalent circuit model data

This appendix details the values assigned to the circuit components by modelling the data presented in the Cole-Cole plots throughout Chapter 6. Here, the extracted values are given for a simplified Randles circuit, using the structure described in Figure 6.4 as a starting point. N/A is shown for data sets that were more accurately modelled by the removal of the series resistance. This indicates the material at this temperature showed little (in context with the other modelled circuit components) or no series (or access) resistance. Note values of R_x are in Ω and C_x in F.

Untreated ND layer in air

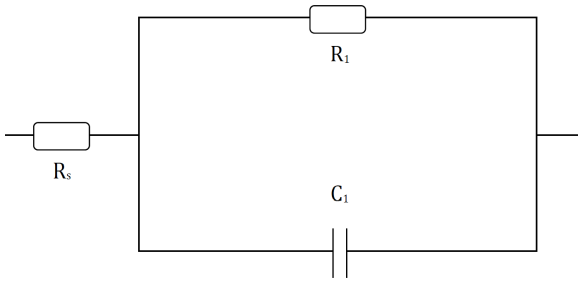

Temperature (°C)	Element	Value	Error	Error %
25	R_s	986240	2.781E05	28.198
	R_1	1.767E+10	1.7623E09	9.9734
	C_1	1.255E-11	5.6801E-13	4.5263
75	R_s	9.3421E05	1.912E05	20.466
	R_1	4.1046E10	4.09E09	9.9644

	C_1	1.3221E-11	4.23E-13	3.1995
100	R_s	7.9167E05	1.2147E05	15.344
	R_1	4.594E10	3.378E09	7.3531
	C_1	1.3613E-11	2.9745E-13	2.185
125	R_s	6.5199E05	78601	12.056
	R_1	4.4742E10	2.2488E09	5.0261
	C_1	5.45E05	1.7713E05	32.501
150	R_s	5.45E05	1.7713E05	32.501
	R_1	1.8958E10	1.7038E09	8.9872
	C_1	1.3607E-11	4.8659E-13	3.576

Hydrogen ND layer in air

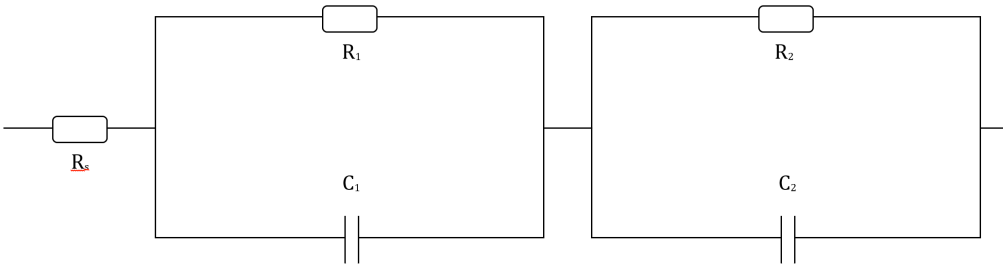

Temperature (°C)	**Element**	**Value**	**Error**	**Error %**
300	R_s	N/A	N/A	N/A
	R_1	62366	1058.1	1.6966

	C_1	5.2271E-11	1.6095E-12	3.0791
	R_2	22522	4078.8	18.11
	C_2	4.7069E-11	1.7109E-12	3.6349

Hydrogen ND layer in vacuum

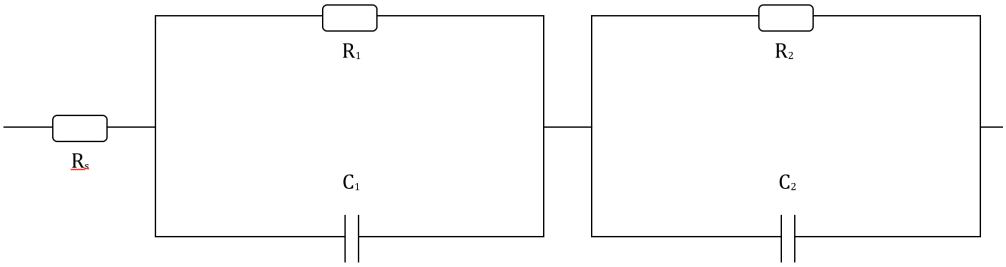

Temperature (°C)	**Element**	**Value**	**Error**	**Error %**
150	R_s	N/A	N/A	N/A
	R_1	1.3604E07	6.3863E05	4.6944
	C_1	7.5123E-11	3.4162E-12	4.5475
	R_2	3088	360.56	11.676
	C_2	1.3792E-11	2.5815E-12	18.717

Oxygen ND layer in air

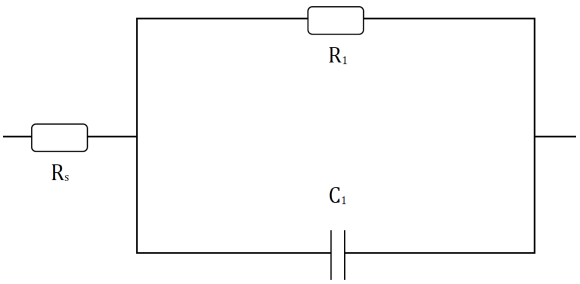

Temperature (°C)	Element	Value	Error	Error %
100	R_s	N/A	N/A	N/A
	R_1	6.684E09	3.6142E08	5.4072
	C_1	7.6282E-11	1.0849E-12	1.4222
150	R_s	N/A	N/A	N/A
	R_1	16835	340.96	2.0253
	C_1	7.6845E-11	5.7264E-12	7.4519
100 after 200	R_s	N/A	N/A	N/A
	R_1	1.0008E05	1207.9	1.2069
	C_1	7.6688E-11	1.937E-12	2.5258
50 after 200	R_s	N/A	N/A	N/A
	R_1	2.2024E05	533.24	0.2421
	C_1	7.638E-11	3.318E-13	0.4344
30 after 200	R_s	N/A	N/A	N/A
	R_1	2.6646E05	682.87	0.2562

	C_1	7.638E-11	3.3927E-13	0.4441

Oxygen ND layer in vacuum

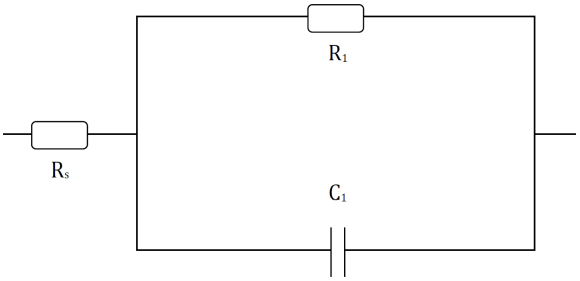

Temperature (°C)	Element	Value	Error	Error %
30	R_s	465.6	35.304	7.5825
	R_1	1.7782E08	5.1998E06	2.9242
	C_1	7.7877E-11	1.4097E-12	1.8102
30 24 hours after 475	R_s	330.9	246.6	74.524
	R_1	1.0489E09	6.3275E07	6.0325
	C_1	1.2656E-11	5.0585E-13	3.9969

Thick hydrogen ND layer in vacuum

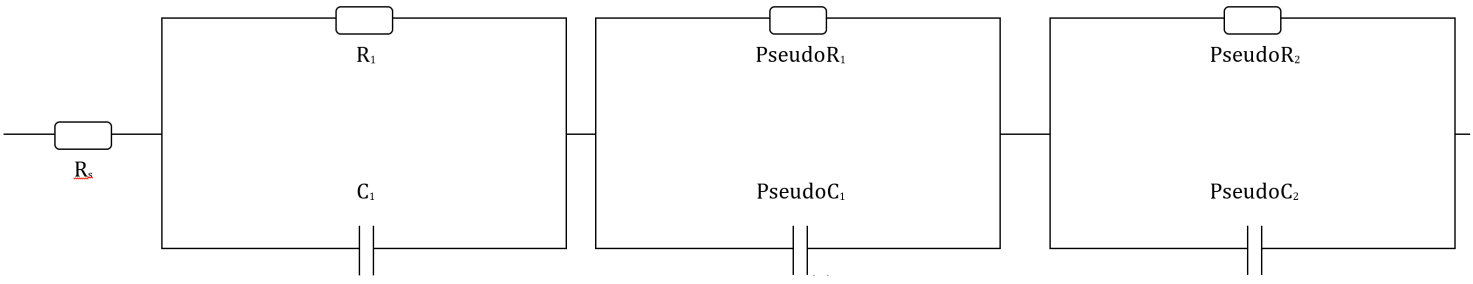

Temperature (°C)	Element	Value	Error	Error %
530	R_s	*80670*	*18793*	*23.296*
	R_1	*6.0404E07*	*3.5647E07*	*59.014*
	C_1	*7.2779E-13*	*6.3915E-14*	8.7821
	$PseudoR_1$	-1.5494E07	8.1135E05	5.2365
	$PseudoC_1$	-8.4548E-12	1.0474E-12	12.388
	$PseudoR_2$	-7.9124E06	3.7093E05	4.688
	$PseudoC_2$	-4.6664E-08	3.0736E-09	6.5867

Appendix B: Chapter 7 data

Round 1 full sample details

Note: Under the SEM, all Round 1 samples showed evidence of stress lines at the top of the channel.

#1709-1 (not shown in SEM Table 7.2) (reduced diameter MCP)

Conditions: 1600µl backfill, 1 minute ultrasonication (US). Base pressure 6×10^{-6} mbar, growth power 583 W, growth pressure 11.5 Torr. Notes: Strong blue colour apparent, quite quick on temperature ramp between 350-375˚C, slow from 380-400˚C and allowed plenty of time to acclimatise. Sent to Photonis for measurement (hence not in SEM table above), resistance found to be approximately 10^5 MΩ (10nA @ 1000V, where 10^3 MΩ is considered normal), secondary electron yield (SEY) = 2.8. Large increase in resistance not thought to be critical problem by Photonis.

#1709-2 (reduced diameter MCP)

Conditions: 800µl backfill, 1 minute US. Base pressure 9×10^{-6} mbar, growth power 580 W, growth pressure 11.5 Torr. ½ carbon coated for reduced charging in later SEM. Notes: SEM shows 750nm diameter 'chocolate drop' structure 12µm down, likely coalesced ND.

NB: Estimated growth thickness at channel entrance (from SEM image) = 103nm

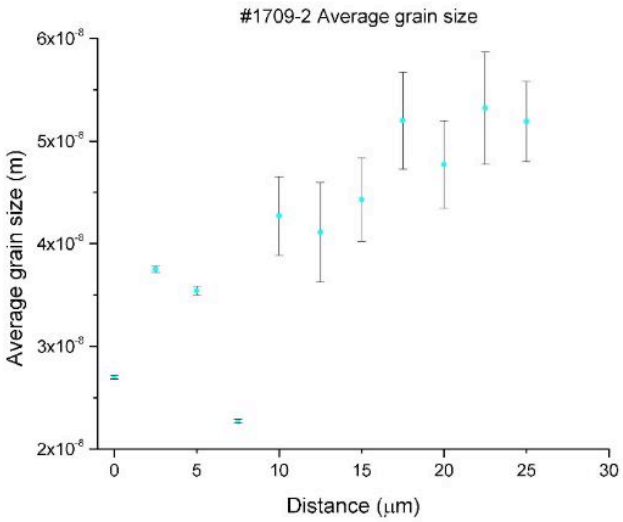

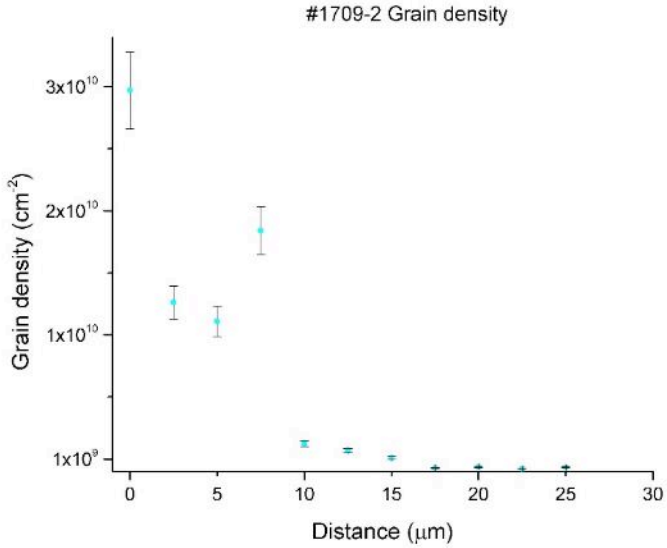

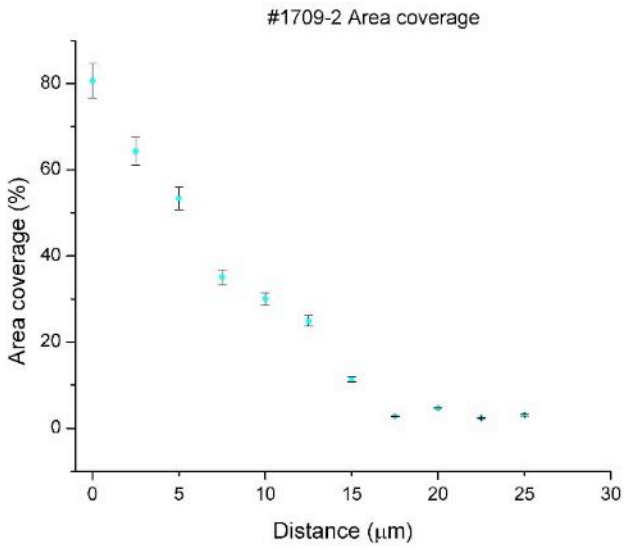

Figure 7.11 Data analysis of sample number 1709-2 (800μl backfill). Distance is measured from the top of the channel opening.

#1210-1 (reduced diameter MCP)

Conditions: 600µl backfill, 1 minute US. Base pressure 5×10^{-5} mbar, growth power 548 W, growth pressure 14 Torr. ½ carbon coated (after taking SEM images on surface). Notes: went to 300˚C in H_2 plasma briefly (H_2 shortage) and back to room temp day before growth. SEM shows lots of ND on cleaved surface, possibly due to poor adhesion of NDs.

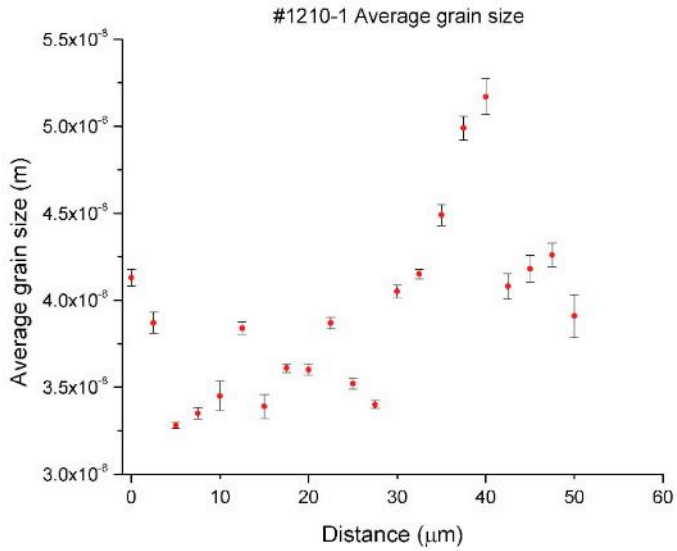

Estimated growth thickness at channel entrance was impossible to distinguish from SEM image.

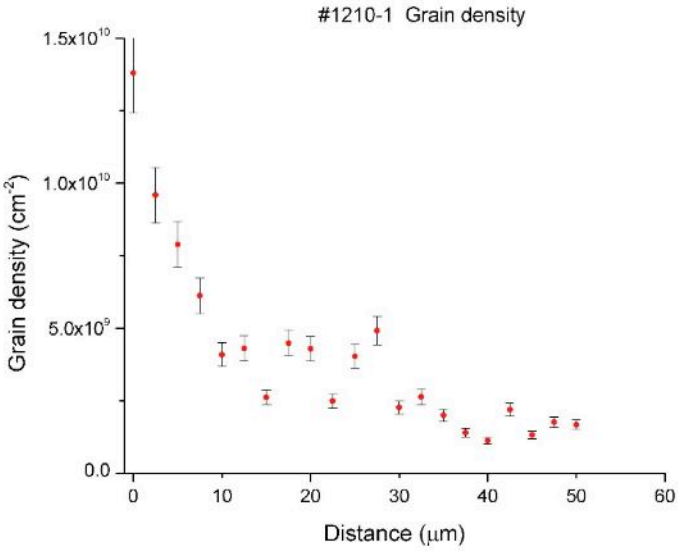

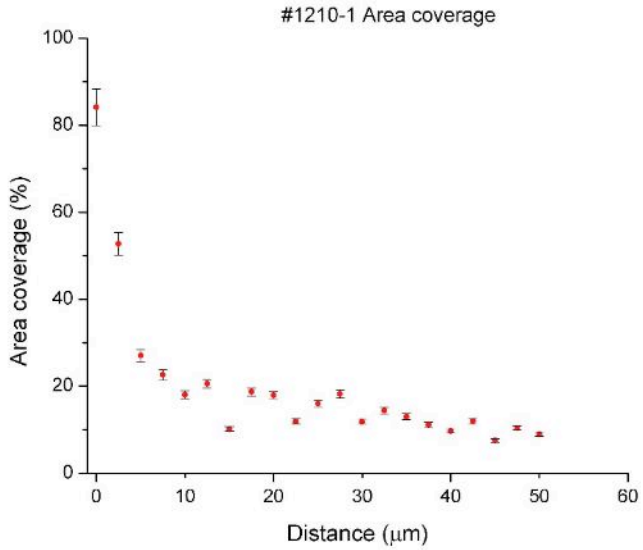

Figure 7.12 Data analysis of sample number 1210-1 (600μl backfill).

#1709-3 (reduced diameter MCP)

Conditions: 400μl backfill, 1 minute US. Base pressure 6.5×10^{-6} mbar, growth power 582 W, growth pressure 12 Torr. ½ carbon coated (after taking SEM images on surface). Notes: Plasma off centre, as evidenced by misaligned damage to metallisation.

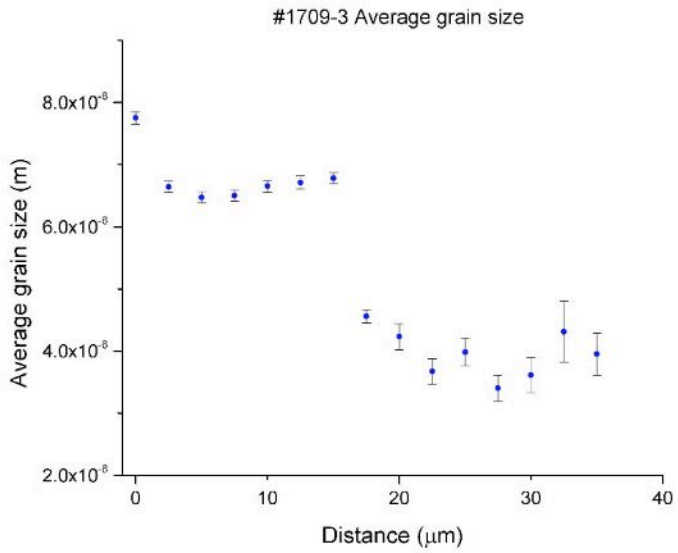

Estimated growth thickness at channel entrance (from SEM image) = 147nm

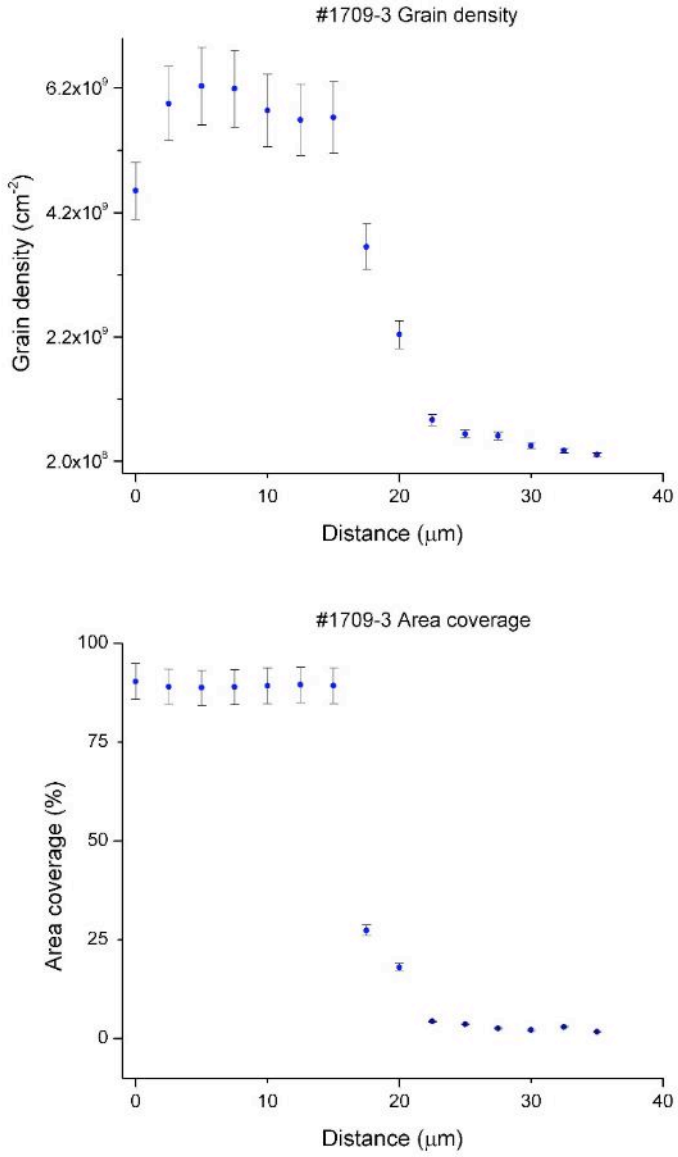

Figure 7.13 Data analysis of sample number 1709-3 (400μl backfill).

#0410-2 (reduced diameter MCP)

Conditions: 60μl backfill, 1 minute US. Base pressure 5×10^{-5} mbar, 0.5% CH_4 at start only, 2% for majority of growth (2 hours ~390˚C), growth power 573 W, growth pressure 13.6 Torr. ½ carbon coated (after taking SEM images on surface). Notes: 1 hour 30 mins into growth CH_4 content accidentally up to 2% due to reduction in hydrogen flow, sample holder very sooty after growth. SEM shows some ND residue on cleaved surface, again, likely due to poor adhesion.

Estimated growth thickness at channel entrance (from SEM image) = 113nm

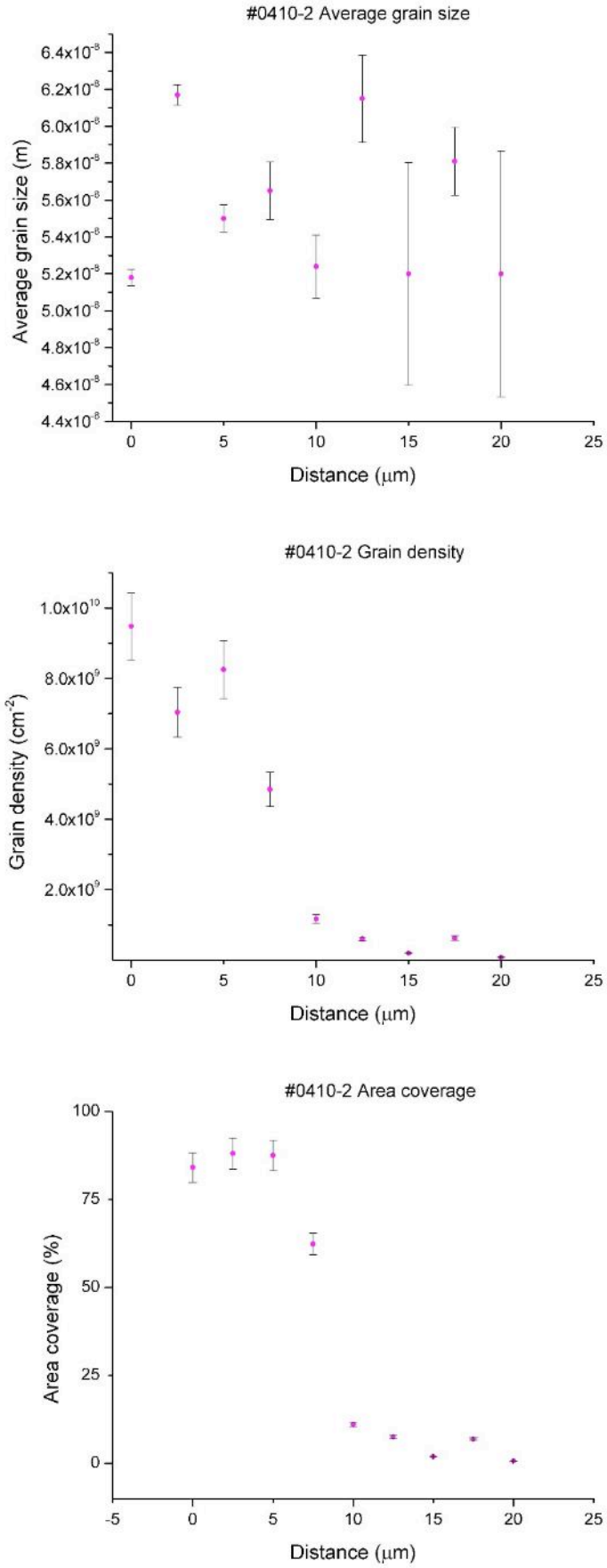

Figure 7.14 Data analysis of sample number 0410-2 (60μl backfill).

#0410-1 (reduced diameter MCP)

Conditions: 20µl backfill, 1 minute US. Base pressure 9×10^{-6} mbar, growth power 573 W, growth pressure 13.6 Torr. ½ carbon coated (after taking SEM images of surface). Notes: SEM shows large agglomerations, with high surface roughness.

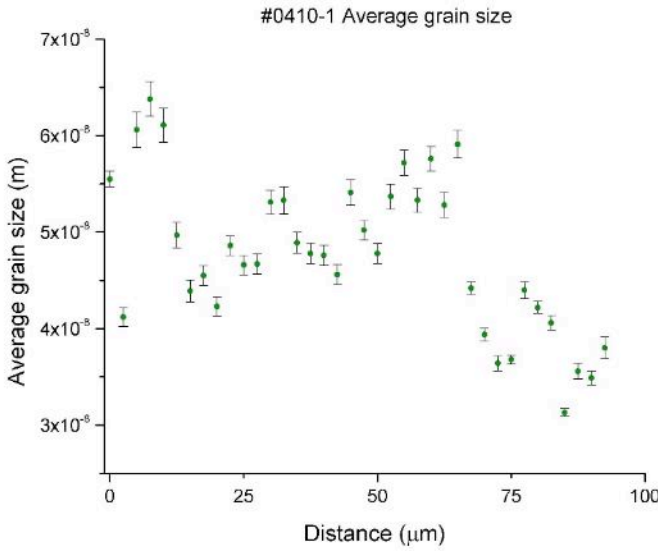

Estimated growth thickness at channel entrance (from SEM image) = 145nm

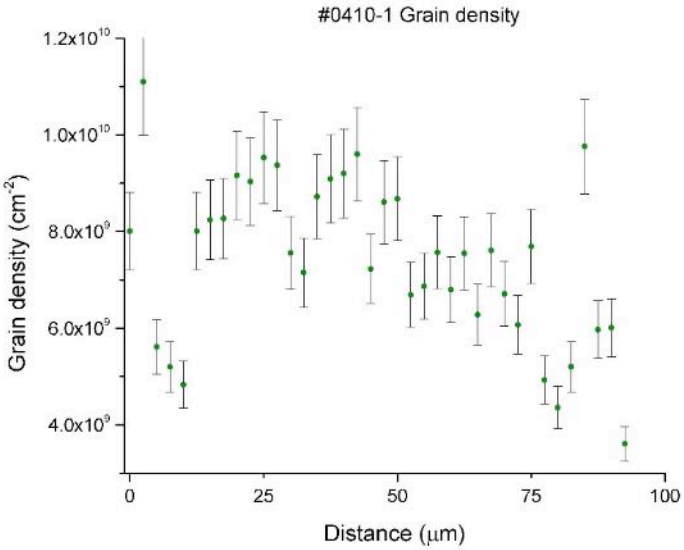

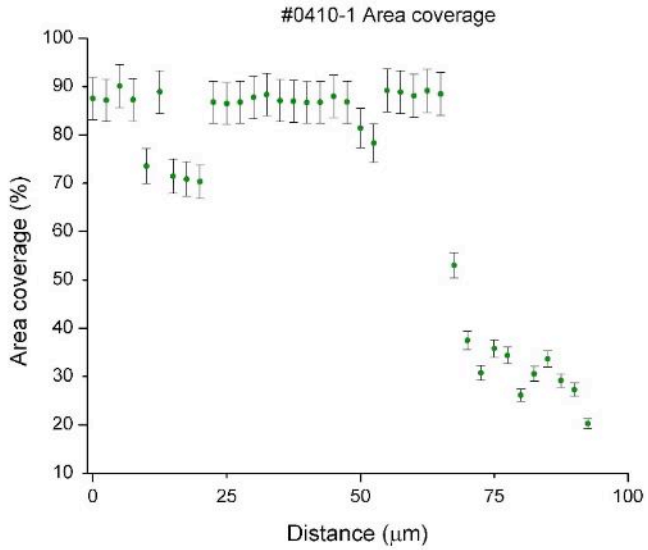

Figure 7.15 Data analysis of sample number 0410-1 (20μl backfill).

#2510-1 (reduced diameter MCP)

Conditions: 10μl backfill, 1 minute US. Base pressure 7.5×10^{-5} mbar, growth power 600 W, growth pressure 20.1 Torr. ½ carbon coated (after taking SEM images on surface). Notes: 10μl seems too low to adequately cover the 6 mm reduced channel MCP as bead formed on jig surface is significantly smaller than 6 mm.

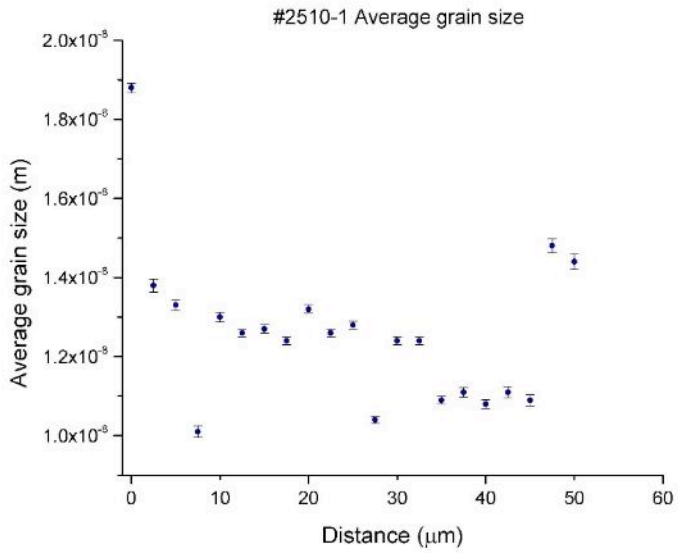

Estimated growth thickness at channel entrance (from SEM image) = 133nm

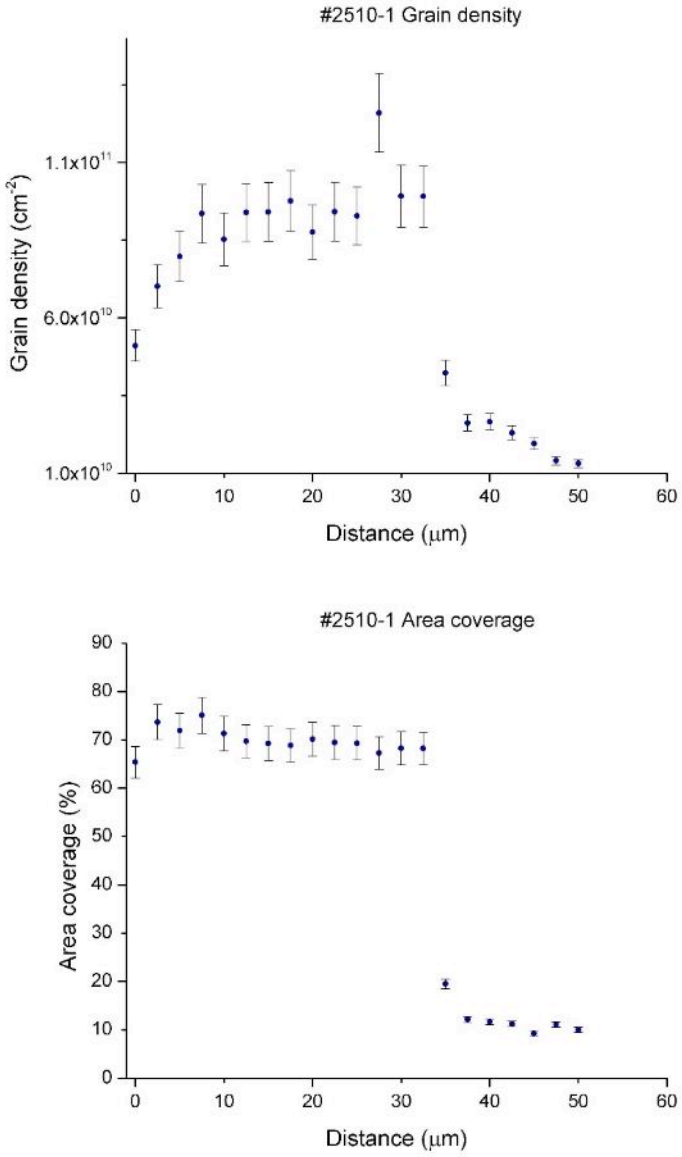

Figure 7.16 Data analysis of sample number 2510-1 (10μl backfill).

Round 2 full sample details

#1411-1 (reduced diameter MCP)

Conditions: 1 minute dip, 20μl backfill. Base pressure 1×10^{-5} mbar, growth power 580 W, growth pressure 22 Torr. Notes: Slight concave warp of MCP apparent. SEM shows low surface roughness of NCD in channel.

Estimated growth thickness at channel entrance (from SEM image) = 136nm

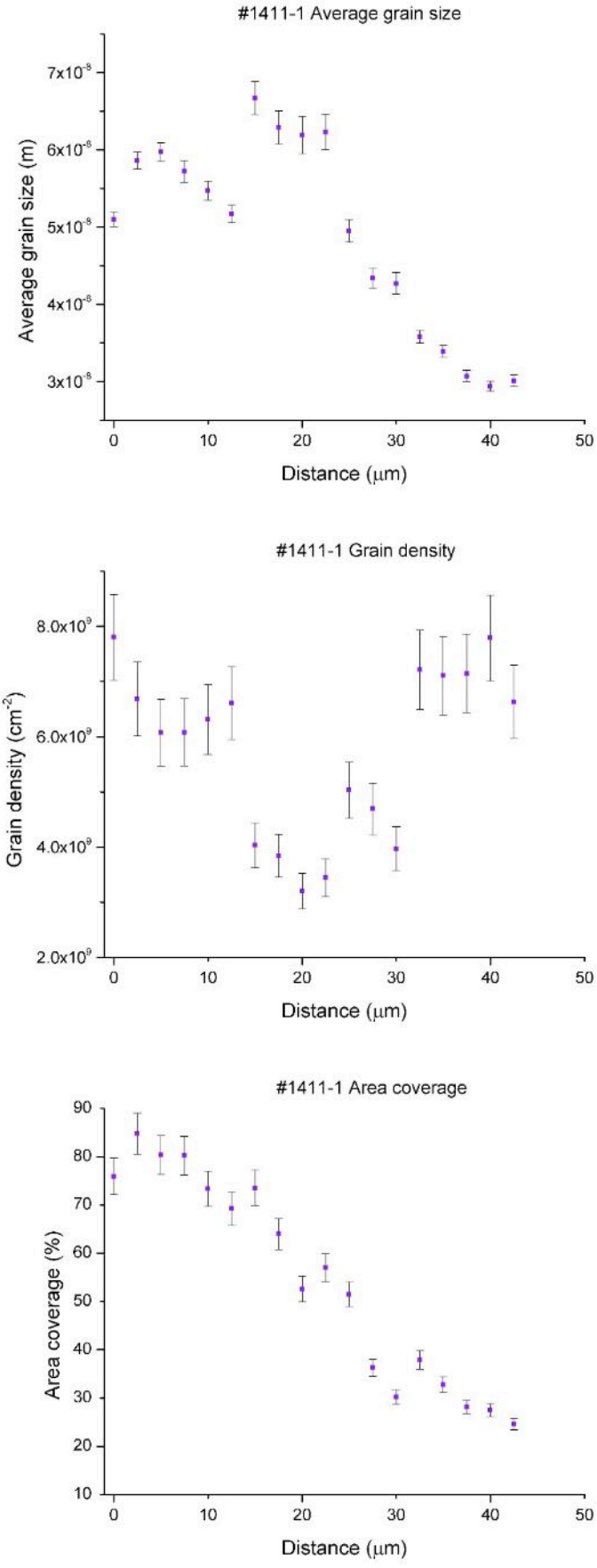

Figure 7.17 Data analysis of sample number 1411-1 (1 minute dip).

#1411-2 (reduced diameter MCP)

Conditions: 5 seconds US, 20µl backfill. Base pressure 1×10^{-5} mbar, growth power 570 W, growth pressure 22 Torr. Notes: SEM shows some ND on cleaved surface.

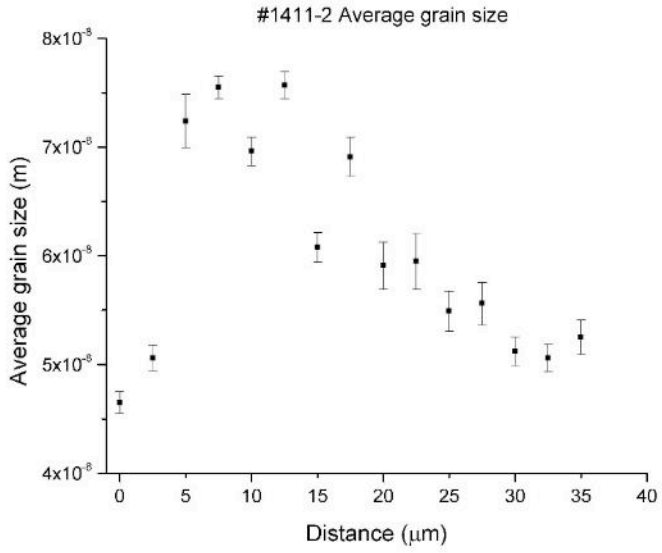

Estimated growth thickness at channel entrance (from SEM image) = 135nm

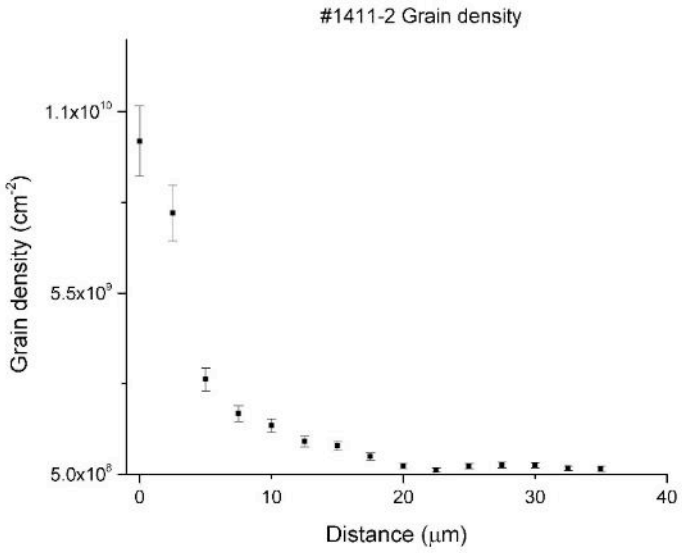

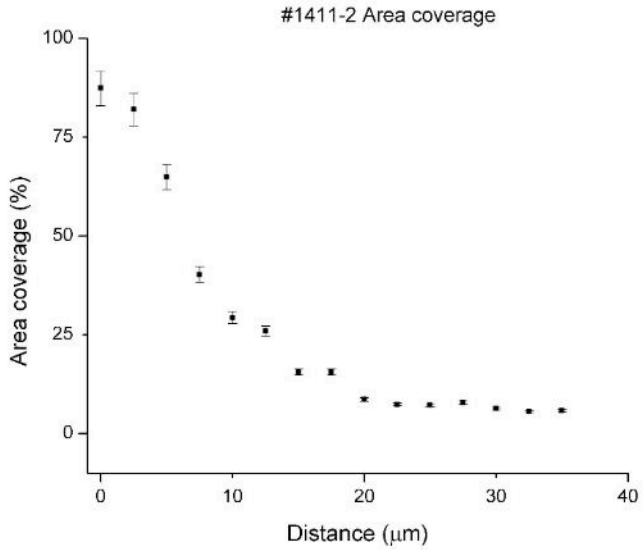

Figure 7.18 Data analysis of sample number 1411-2 (5 seconds US).

#1411-3 (reduced diameter MCP)

Conditions: 30 seconds US, 20μl backfill. Base pressure 6×10^{-5} mbar, growth power 536 W, growth pressure 20 Torr. Notes: Very slight warp of MCP. SEM shows low particle density throughout.

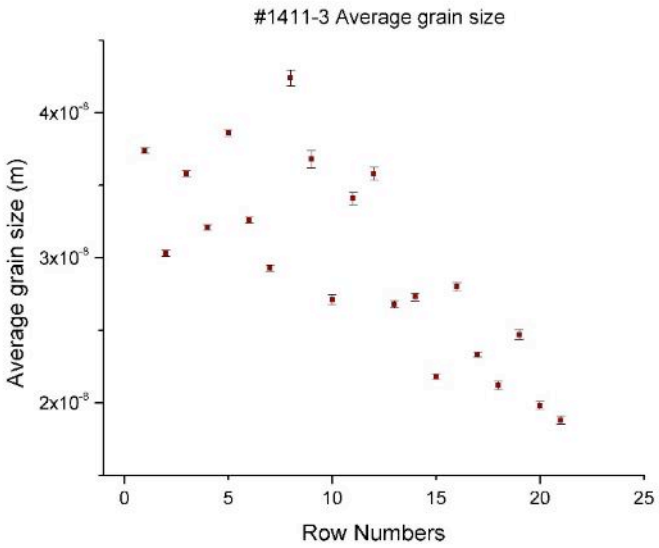

Estimated growth thickness at channel entrance was impossible to distinguish from SEM image.

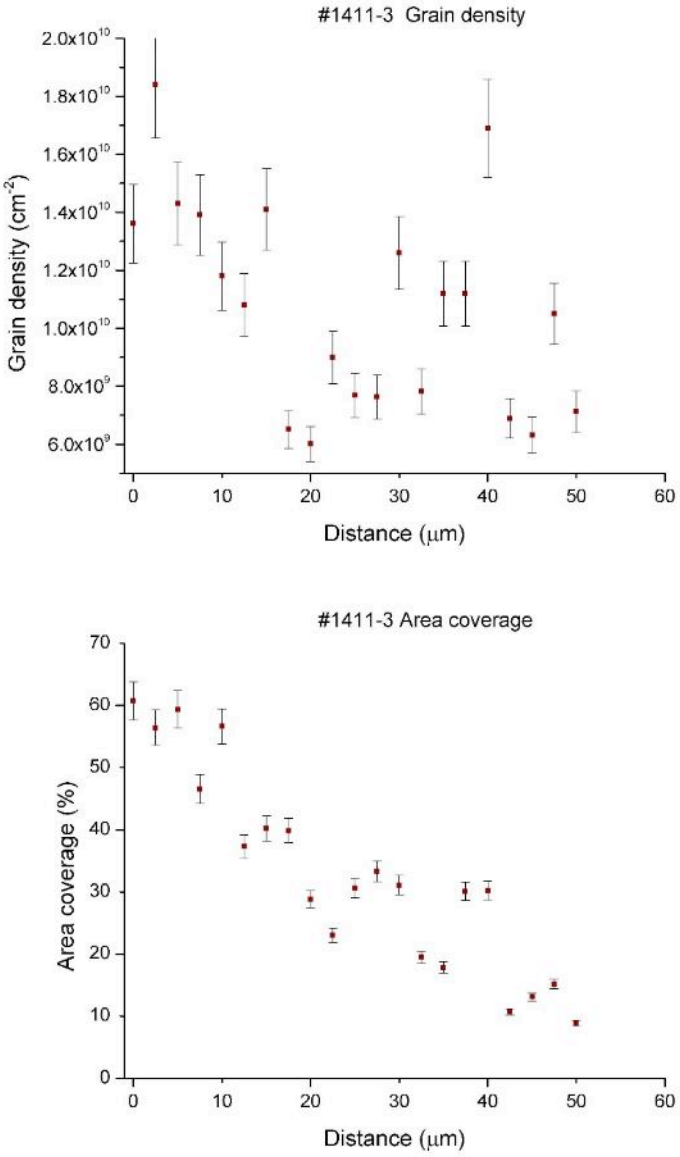

Figure 7.19 Data analysis of sample number 1411-3 (30 seconds US).

#1411-4 (reduced diameter MCP)

Conditions: 5 minutes US, 20µl backfill. Base pressure 3×10^{-5} mbar, growth power 570 W, growth pressure 20 Torr. Notes: As before, very slight warp of MCP. Centre darker than others, suggesting a rougher surface is scattering light more effectively. Otherwise a generally colourful surface. SEM shows good particle density but evidence of slight clumping of NDs.

Estimated growth thickness at channel entrance (from SEM image) = 109nm

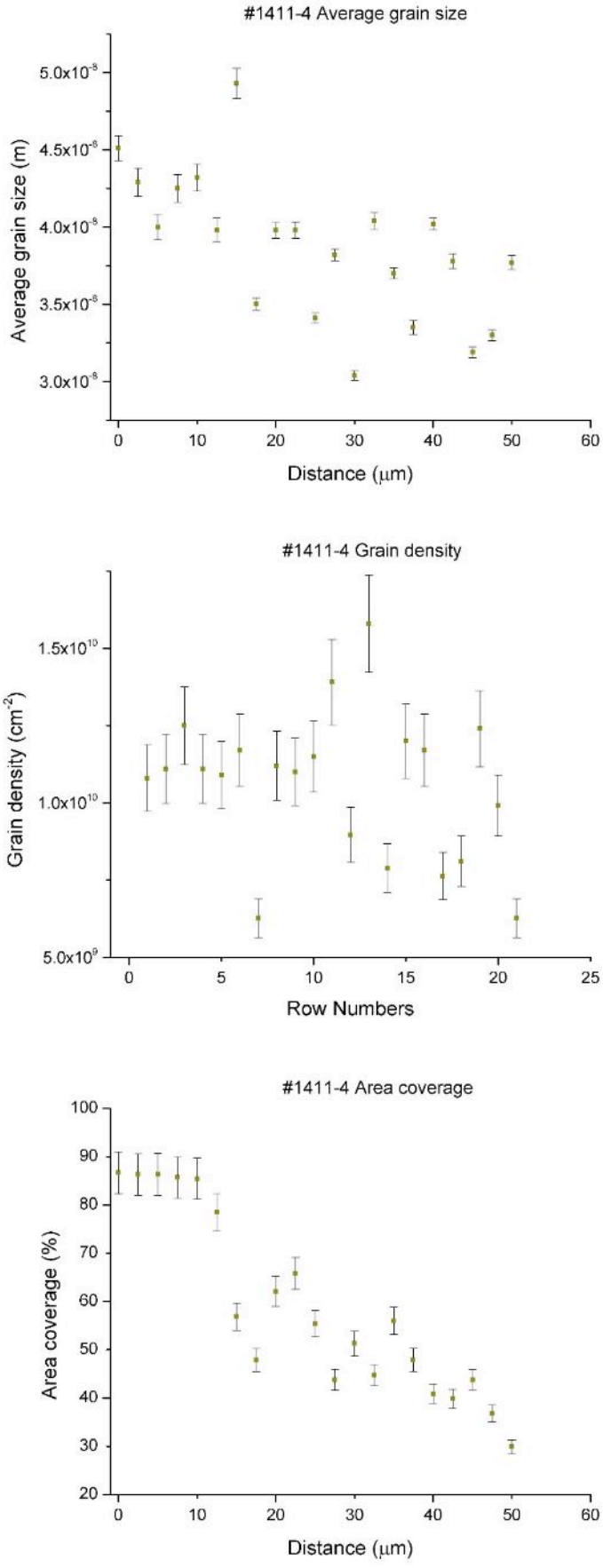

Figure 7.20 Data analysis of sample number 1411-4 (5 minutes US).

#1411-5 (reduced diameter MCP)

Conditions: 10 minutes US, 20µl backfill. Base pressure 7×10^{-5} mbar, growth power 540 W, growth pressure 20 Torr. Notes: SEM shows good coverage (with low roughness) but not perfect – first blank patch at 5µm depth in channel.

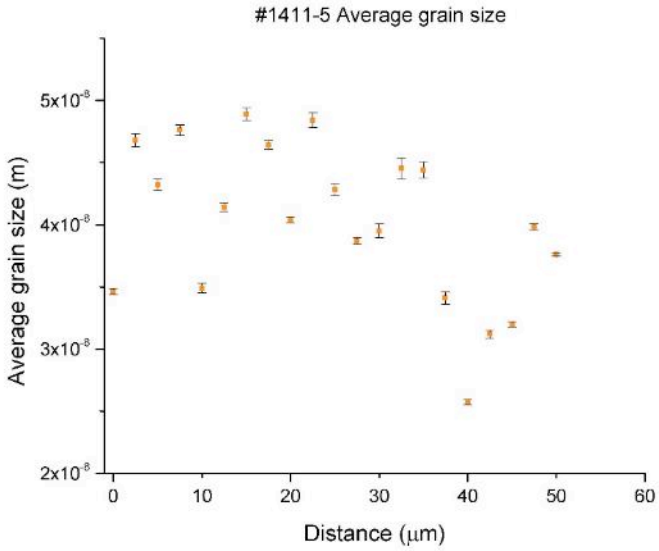

Estimated growth thickness at channel entrance (from SEM image) = 100nm

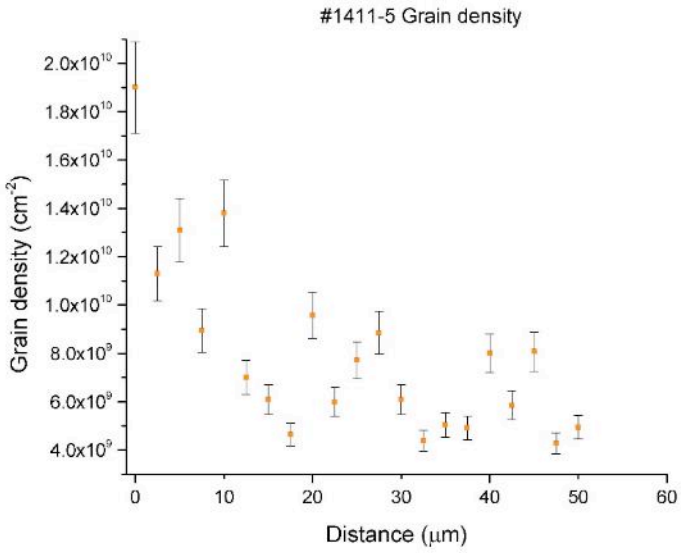

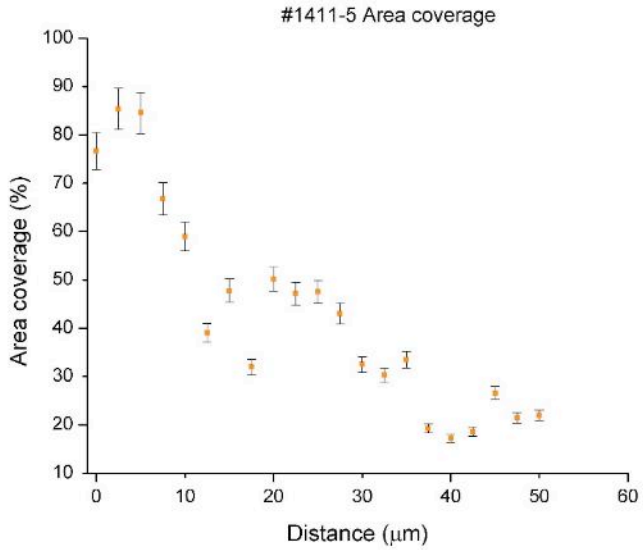

Figure 7. 21 Data analysis of sample number 1411-5 (10 minutes US).

Blank MCP (reduced diameter MCP)

Notes: Taken from same batch as other reduced diameter MCPs used. Some *ca.* 100nm diameter particles are observed very sparsely distributed in the channels. However, these particles are not seen on cleaved surface. The origin of these particles could be residue from cleaving process, cross contamination of grown ND from the others in the sample series, or contamination of the channels during their fabrication at Photonis.

Appendix C: Chapter 8 data

380˚C

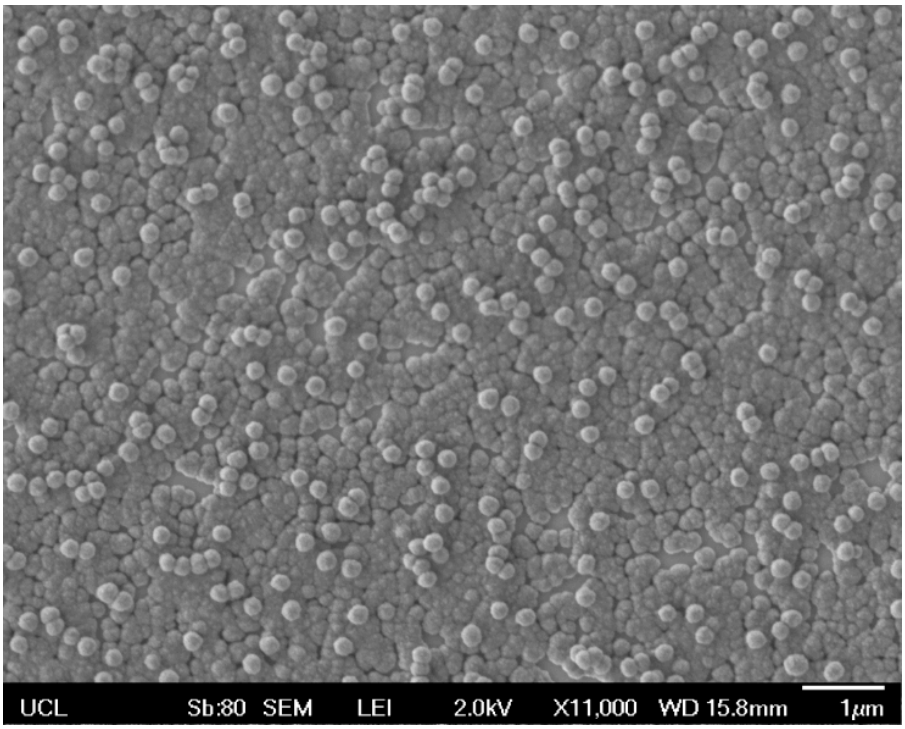

Figure 8.13 Scanning electron micrograph of NCD surface grown at 380°C.

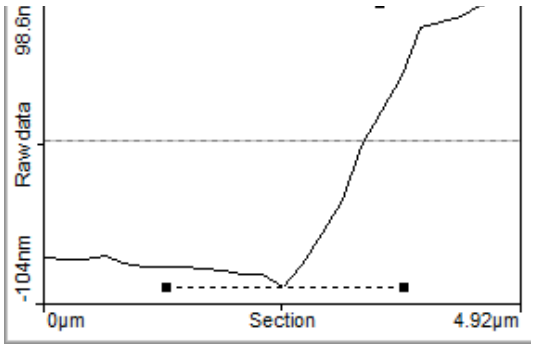

Figure 8.14 AFM line scan of NCD film grown at 380°C. The dotted line represents the limits of the length measurement.

Figure 8.13 shows the surface of the NCD layer grown on silicon at 380°C. The round shape of the crystallites reveals no crystal orientation is favoured, instead all possible orientations grow concurrently, twinning to form what is referred to as 'ballas type' diamond due to its visual similarity to ballas stones.[1] This form of diamond is common in sub optimal growth conditions and is likely due to the incomplete decomposition of the CH_4 into diamond regrowth precursors, causing the inclusion of a high number of twinning and stacking faults.[2] The NCD layer appears to cover almost the entire surface, with some small gaps between grains. The surface pertains to essentially one grain layer with a small number of secondary grains sitting on top of the primary layer. The primary and secondary grains are approximately 100-200 nm although many of the primary grains have coalesced at an earlier stage of the growth, making an accurate determination of the grain size difficult. The film thickness, as determined by AFM, was 193 nm (Figure 8.14), therefore the growth rate is around 64 nm/hr.

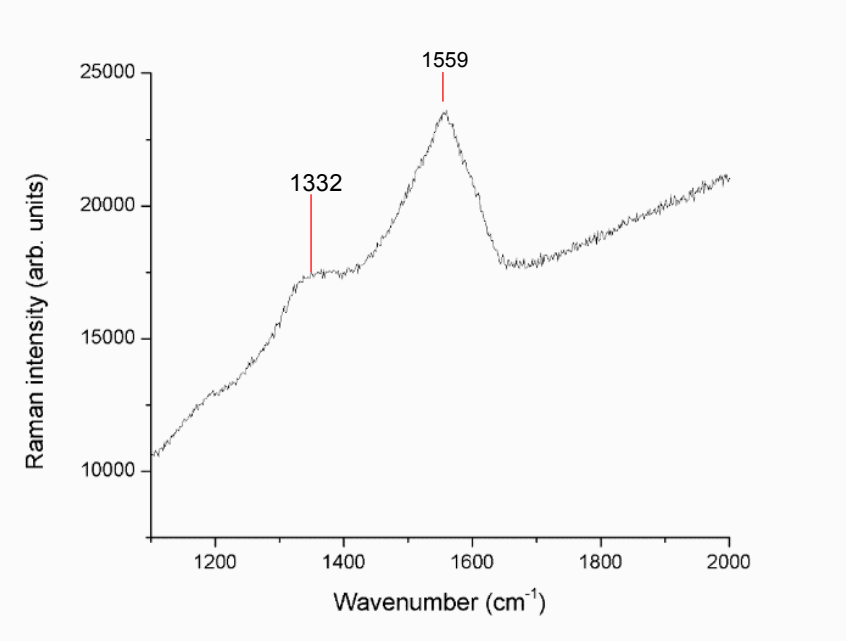

Figure 8.15 Raman spectrum of NCD film grown at 380°C.

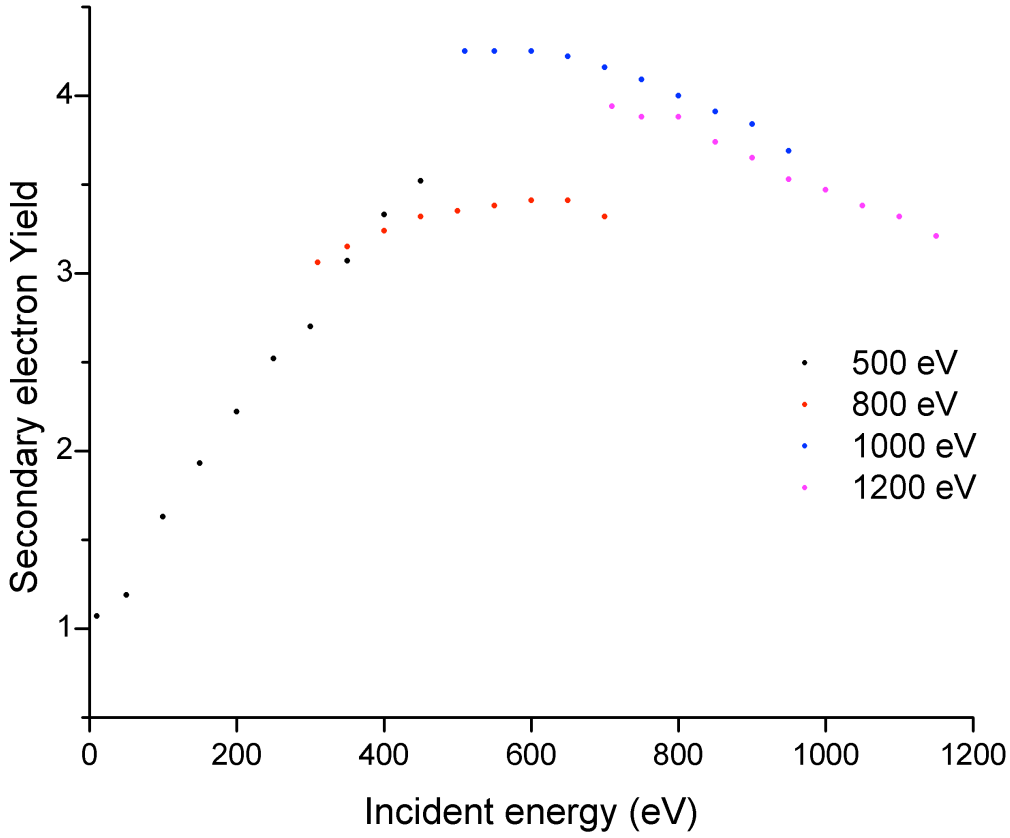

Figure 8.16 SEY of NCD film grown at 380°C as a function of incident electron energy. Beam energies used are given in the legend.

The Raman spectrum presented in Figure 8.15 yields two peaks, the first a broad peak at 1332 cm^{-1}. The second peak is situated at 1559 cm^{-1}, corresponding to the G-band (typically quoted as 1560 cm^{-1}) due to the in-plane stretching mode of sp^2 carbon. G-band peaks seen in NCD are typically associated with grain boundaries, [3] however considering the unusual morphology of this sample, the sp^2 carbon could be situated within the grains. Figure 8.16 shows the SEY of the 380°C film. Here, a maximum gain of 4.2 at an incident electron energy of 500 eV was recorded.

420˚C

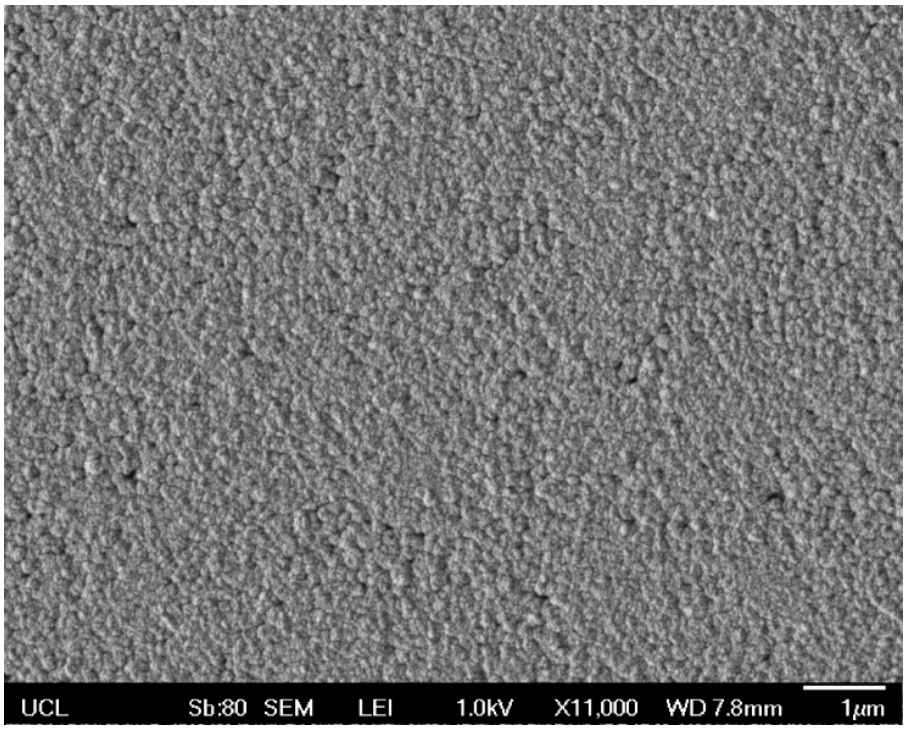

Figure 8.17 Scanning electron micrograph of NCD surface grown at 420°C.

The layer grown at 420°C shows a similar morphology to that seen in the 400°C sample, albeit with a slightly smoother surface, with a grain size on the order of 80-100 nm. Figure 8.18 shows the thickness of the 420°C growth to be 250 nm, which corresponds to a growth rate of approximately 83 nm/hr.

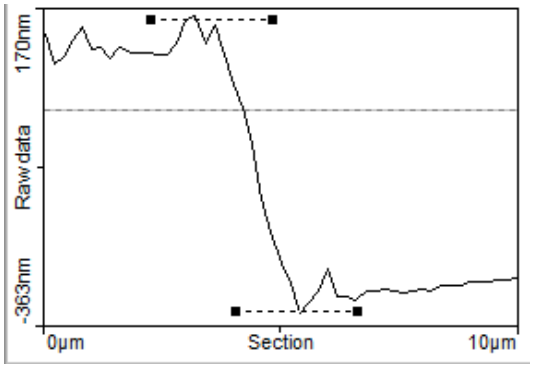

Figure 8.18 AFM line scan of NCD film grown at 420°C.

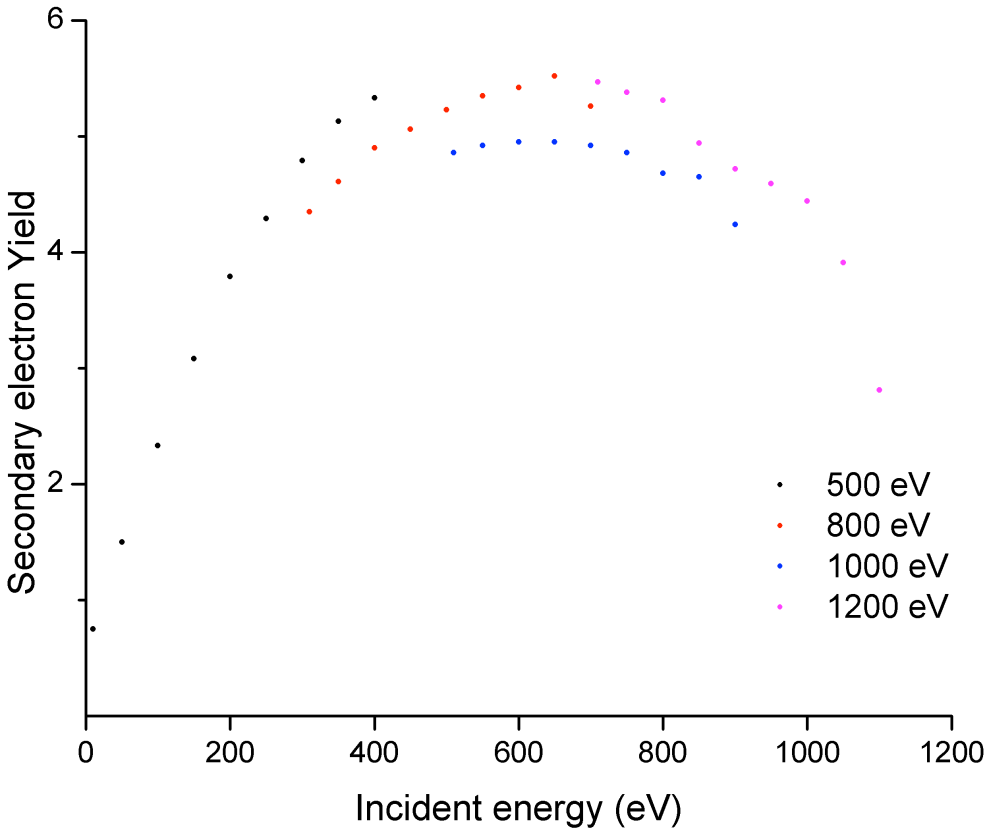

Figure 8.20 shows the spectrum of the film grown at 420°C is very similar to that seen in Figure 8.3, with a more defined pair of peaks. The G peak at 1555 cm^{-1} is slightly redshifted, suggesting greater strain in the graphitic material within the NCD layer grown at 420°C.[6] The maximum SEY for the 420°C growth was 5.5 at ~700 eV, a result very similar to that seen in the 400°C sample.

600˚C

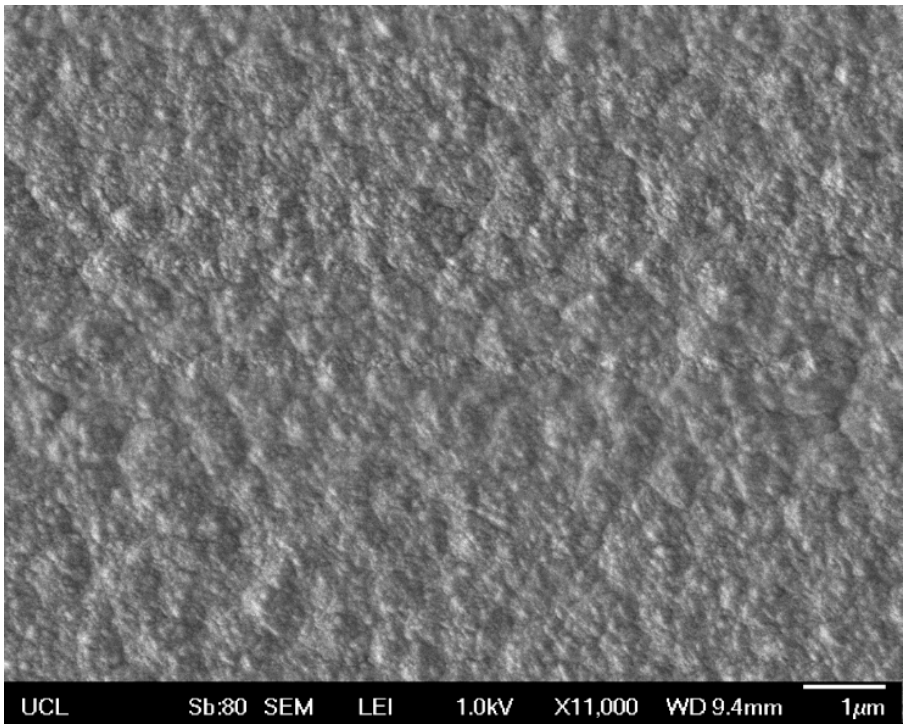

Figure 8.21 Scanning electron micrograph of NCD surface grown at 600°C.

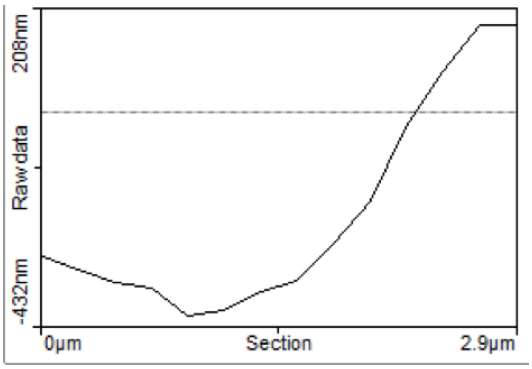

Figure 8.22 AFM line scan of NCD film grown at 600°C.

The surface in Figure 8.21 is a departure from the previous three temperatures. At 600°C a smoother, less granular surface presents itself. This film was measured to be 595 nm, suggesting a large increase in growth rate, up to *ca.* 198 nm/hr (Figure 8.22).

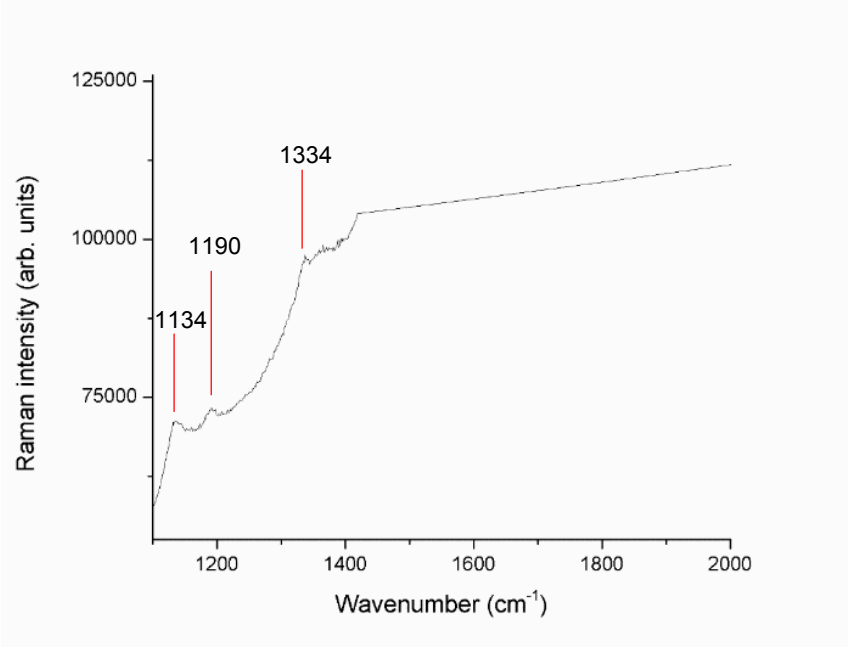

Figure 8.24 Raman spectrum of film grown at 600°C.

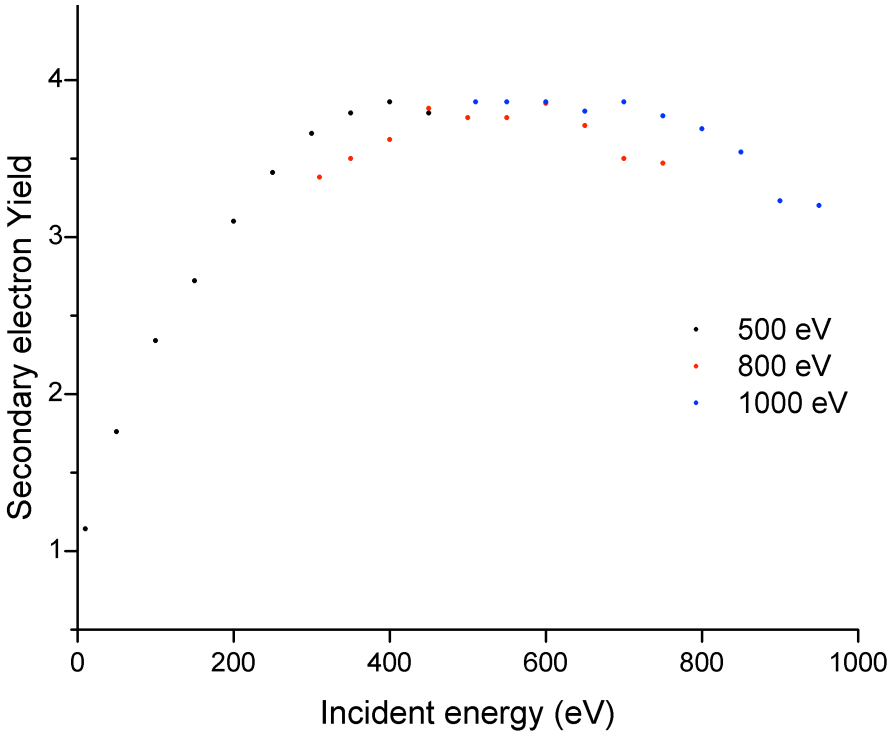

Figure 8.23 Secondary elctron yield of NCD film grown at 600°C.

The spectrum in Figure 8.24 has undergone clipping of the Raman intensity signal due to the very high background luminescence. However some peaks can still be identified at 1134 cm^{-1}, 1190 cm^{-1}, 1334 cm^{-1}. The weak peak seen at 1134 cm^{-1} can be attributed to trans-polyacetelene within the grain boundaries and surfaces of the NCD layer.[4] The very weak peak at 1190 cm^{-1} may be the stretching vibration modes of polyene-like structures.[5] Finally the peak at 1334 cm^{-1} is a slightly shifted away from the value normally given for a diamond peak (1332.4 cm^{-1}), suggesting residual stress in the film,[6] likely on the order of 1 GPa.[7] The SEY maximum was observed in the 400-700 eV region with a yield of 3.8. The broad peak may be due to the increased thickness of the layer giving an increased depth of generation of secondary electrons.[20]

3 hours growth

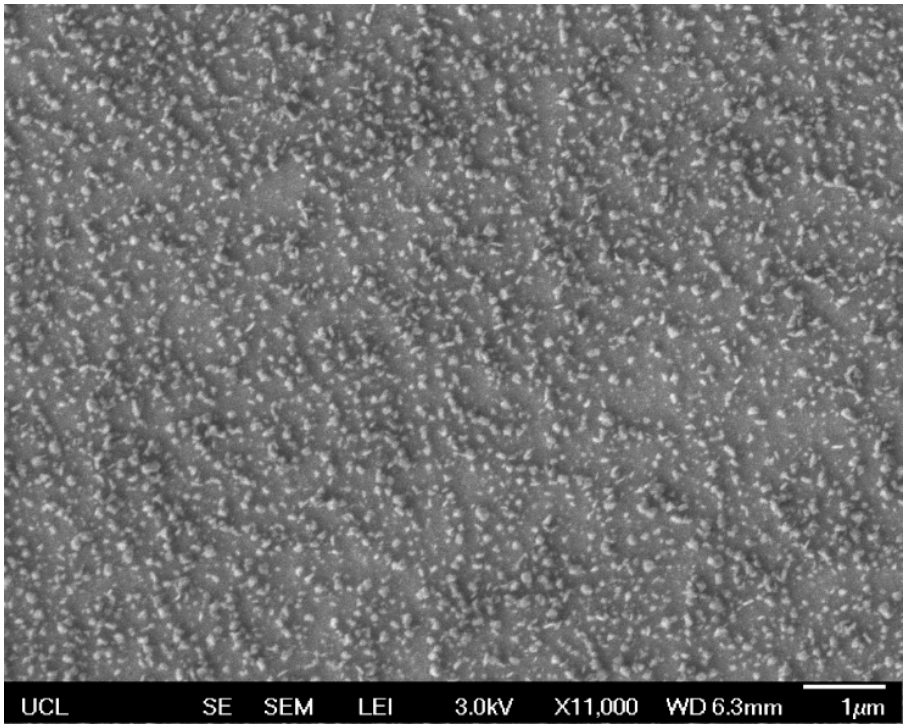

Figure 8.25 Scanning electron micrograph of NCD surface grown at 400°C using the final sample cooler, the 2 pipe reservoir, for 3 hours. The enhanced cooling capability of this cooler enabled the use of microwave powers more than double that used throughout section 8.3.1 (see table 7.1).

The upgraded sample holder resulted in a slower growth rate – after 3 hours of growth the film remains incomplete with large gaps between the enlarged ND seeds. A measurement of the film thickness is therefore not possible, although the grain size can be estimated from higher resolution images to be in the 60-100 nm range. However the micrograph does indicate the initial stages of growth of highly faceted NCD.

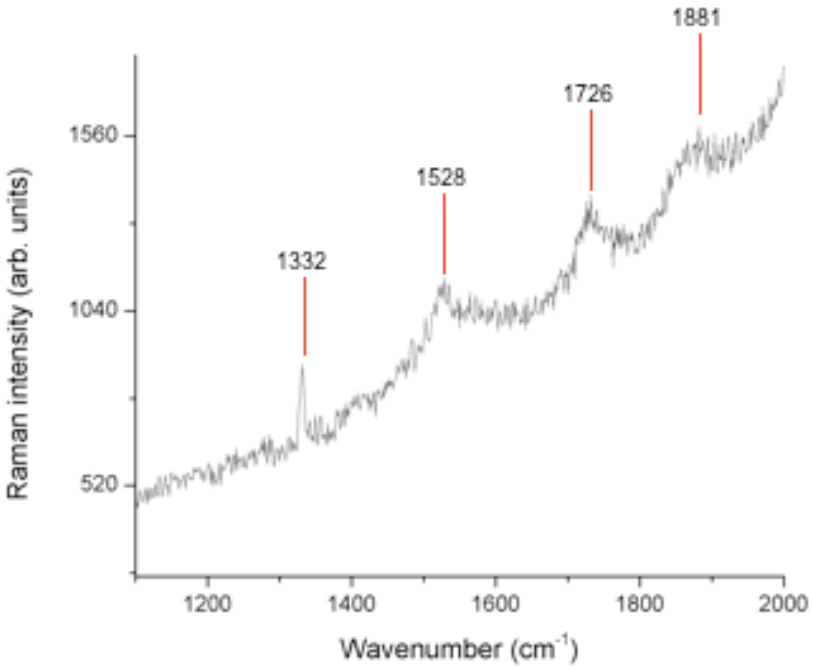

Figure 8. 26 Raman spectrum of NCD surface grown at 400°C using the final sample cooler for 3 hours.

Figure 8.23 shows the Raman spectrum from the 3 hour sample. The first labelled peak, at 1332 cm^{-1}, is a much sharper diamond peak than previously seen, with no additional stress. This is encouraging evidence of the superior growth conditions used. At 1528 cm^{-1} a broad G peak is present with low relative intensity. Next, the peak seen at 1726 cm^{-1} has been tentatively

attributed to defects in the diamond lattice by Prawer *et al.*[8] Finally, the peak at 1881 cm^{-1} is associated with hydrogen passivated silicon,[9] whose inclusion in the spectrum is due to the incomplete film exposing the silicon substrate. This combination of peaks supports the observation from the SEM images that the growth resulted in an incomplete layer containing a low proportion of non-diamond carbon. The SEY seen in figure 8.24 is comparable to that seen in Figure 8.4 in terms of both shape and magnitude. A maximal gain of 5.8 (6.2 if the 800 eV beam energy and 800 eV incident energy data point is taken to be reliable) around 800 eV suggests far more effective NCD growth from a SEY perspective, even without a fully closed film. Therefore the slow growth rate and high applied microwave power can be seen to be a more effective growth regime for low temperature NCD growth, even without a complete film present.

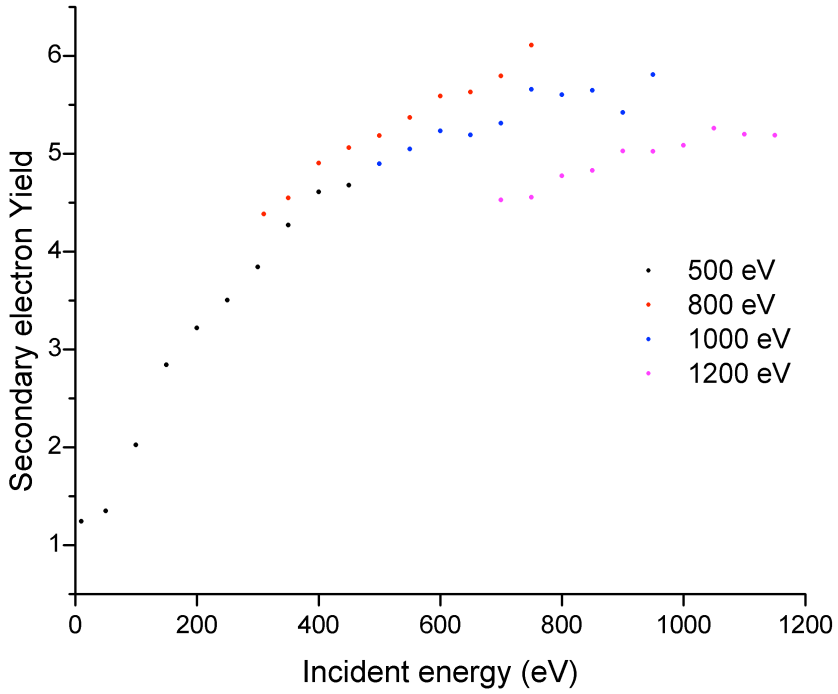

Figure 8. 27 SEY of NCD surface grown at 400°C for 3 hours using the final sample cooler, the 2 pipe reservoir.

[1] S Bühlmann *et al.*, 'Characterization Of Ballas Diamond Depositions'. Diamond and Related Materials 8, 1999, pp. 194-201.
[2] J Michler *et al.*, 'Microstructure Evolution And Non-Diamond Carbon Incorporation In CVD Diamond Thin Films Grown At Low Substrate Temperatures'. Journal of Crystal Growth 172(3-4), 1997, pp. 404-415.
[3] A Ferrari & J Robertson. "Interpretation of Raman spectra of disordered and amorphous carbon." Physical review B 61(20), 2000, pp. 14095-14107.
[4] A Ferrari & J Robertson, "Resonant Raman spectroscopy of disordered, amorphous, and diamondlike carbon." Physical Review B 64(7), 2001, 075414.
[5] B Dippel *et al.*, "NIR FT Raman spectroscopic study of flame soot." Physical Chemistry Chemical Physics 1(20), 1999, pp. 4707-4712.
[6] J Zhang *et al.*, 'Effect Of Boron And Silicon Doping On Improving The Cutting Performance Of CVD Diamond Coated Cutting Tools In Machining CFRP'. International Journal of Refractory Metals & Hard Materials, 2013.
[7] D Knight & W White, "Characterization of diamond films by Raman spectroscopy." Journal of Materials Research 4(2), 1989, pp. 385-393.
[8] S Prawer *et al.*, "The Raman spectrum of amorphous diamond." Diamond and Related Materials 7(1), 1998, pp. 106-110.
[9] M Stutzmann, "Hydrogen passivation of boron acceptors in silicon: Raman studies." Physical Review B 35(11), 1987, pp. 5921-5924.